Dissertation

Development of readout electronics for the RICH detector in the HADES and CBM experiments

- HADES RICH upgrade, mRICH detector construction and analysis -

Adrian Amatus Weber

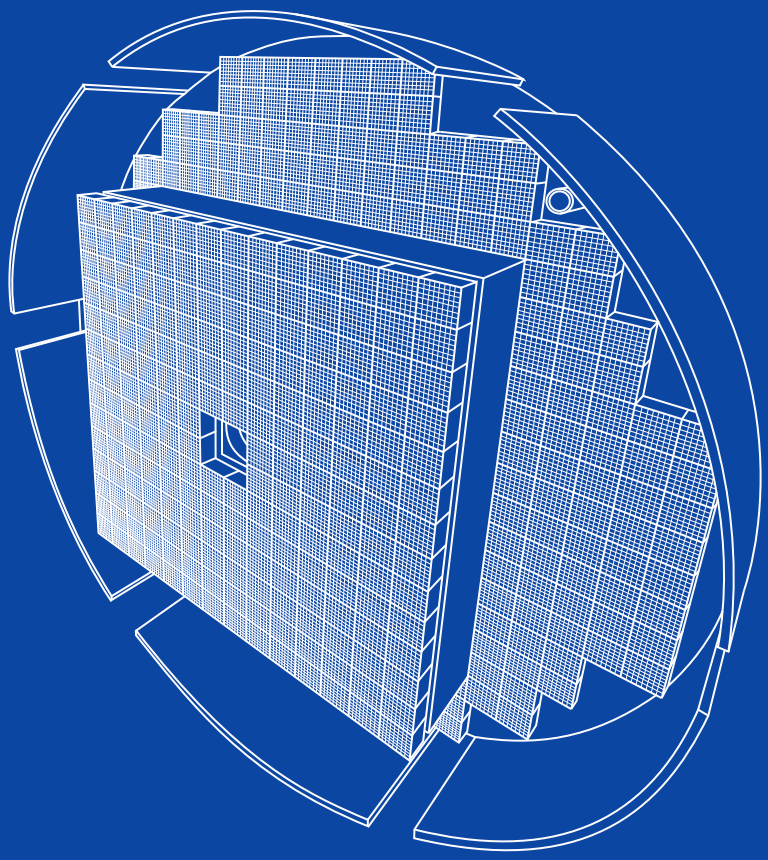

JUSTUS-LIEBIG-
UNIVERSITÄT
GIESSEN

Development of readout electronics for the RICH detector in the HADES and CBM experiments

- HADES RICH upgrade, mRICH detector construction and analysis -

Inauguraldissertation

zur Erlangung des Doktorgrades am

Fachbereich Mathematik und Informatik, Physik, Geographie

der

Justus-Liebig-Universität Gießen

vorgelegt von

Adrian Amatus Weber

aus Biskirchen

Gießen (2021)

Aus dem II. Physikalischen Institut

Dekan: Prof. Dr. Kai-Thomas Brinkmann
Gutachter: Prof. Dr. Claudia Höhne
Gutachter: Prof. Dr. Karl-Heinz Kampert

Erklärung der Urheberschaft

Ich erkläre: Ich habe die vorgelegte Dissertation selbständig und ohne unerlaubte fremde Hilfe und nur mit den Hilfen angefertigt, die ich in der Dissertation angegeben habe. Alle Textstellen, die wörtlich oder sinngemäß aus veröffentlichten Schriften entnommen sind, und alle Angaben, die auf mündlichen Auskünften beruhen, sind als solche kenntlich gemacht. Bei den von mir durchgeführten und in der Dissertation erwähnten Untersuchungen habe ich die Grundsätze guter wissenschaftlicher Praxis, wie sie in der "Satzung der Justus-Liebig-Universität Gießen zur Sicherung guter wissenschaftlicher Praxis" niedergelegt sind, eingehalten.

Datum

Unterschrift

Zusammenfassung

Diese Arbeit trägt große Anteile für die Entwicklung, Installation und Überwachung der auf FPGAs basierenden Auslese der neuen DiRICH boards im HADES, CBM und mCBM Experiment bei. In letzterem wird weiterhin eine Analyse der aufgenommenen Daten in der Strahlzeit Kampagne des Jahres 2020 durchgeführt.

Das HADES und CBM Experiment sind fixed target Schwerionen Experimente an der GSI, Helmholtz Zentrum für Schwerionen Forschung in Darmstadt/Deutschland, bzw. an der künftigen Facility of Antiproton and Ion Research (FAIR). Das HADES Experiment ist ein weltweit bekanntes Experiment am SIS18 Beschleuniger der GSI und wird, zusammen mit dem Compressed Baryonic Matter (CBM) Experiment, den CBM Pfeiler von FAIR bilden. Beide Experimente haben unter anderem das Ziel, Dielektronen und deren Spektren in unterschiedlichen Energiebereichen zu vermessen. Der Ring Imaging Cherenkov (RICH) Detektor, welcher in beiden Experimenten als Subdetektor zum Einsatz kommt, ist essentiell für die saubere Identifizierung von Elektronen. Der HADES RICH Detektor wurde mit einem neuen Photonendetektor basierend auf MAPMTs ausgestattet. Dafür wurde neue Ausleseelektronik entwickelt, die für CBM an SIS100 genutzt werden wird. Die zum Einsatz kommende DiRICH Ausleseelektronik basiert auf der TDC Messung von MAPMT Signalen in den FPGAs der DiRICH boards.

Die vorliegende Arbeit fokussiert sich auf das Upgrade des HADES RICH mit MAPMTs und der neuen DiRICH Auslese. Die Verwendung von 428 MAPMTs mit 856 DiRICH boards verbessert die Effizienz der Elektronen Identifizierung und Erkennung von Doppelringen erheblich. Weiterhin dient dieses Upgrade als Prototyp für den Test der CBM RICH Ausleseelektronik. Die Stromversorgung und die Überwachung des RICH Detektors wurden entsprechend angepasst und erneuert. Der aktualisierte HADES RICH Detektor lieferte in der Ag+Ag Strahlzeit bei 1.58 AGeV im März 2019 hervorragende Ergebnisse.

Ein zweiter Prototyp, basierend auf der gleichen DiRICH Elektronik wie der erneuerte HADES RICH, ist für das mCBM Experiment entwickelt worden. Das mCBM Experiment ist ein Prototyp-Experiment für das zukünftige CBM Experiment um die gemeinsame, kontinuierliche Auslese der Detektoren sowie online Analyse Algorithmen zu testen. Ein spezieller mRICH Prototyp wurde mit einem neuen Auslesekonzept entwickelt, konstruiert und in Betrieb genommen. Die Auslese, basierend auf dem bekannten TrbNet Netzwerk, wurde auf das Konzept der kontinuierlichen Auslese angepasst. Das Auslesekonzept des mRICH in Phase-I von mCBM wurde des weiteren für Phase-II mit der ersten Implementierung der Auslese auf der finalen CBM Hardware weiterentwickelt. Die Weiterentwicklung beinhaltet unter anderem grundlegende Änderungen im Datentransport und der Steuerung der Datenauslese.

Die Daten aus der Phase-I Strahlzeit von mCBM des Jahres 2020 wurden unter Beachtung der Funktionalität des Detektors und der Synchronisation zu anderen Subdetek-

toren analysiert. Hervorragende zeitliche und räumliche Korrelationen zwischen dem mRICH und dem mTOF Detektor wurden herausgearbeitet und in allen Details in dieser Arbeit dargestellt. Eine zusätzliche Analyse der mRICH Ringe und der Hits wurde durchgeführt und belegt das zuverlässige Verhalten des mRICH Prototyp-Detektors in einer Umgebung der kontinuierlichen Auslese.

Am Ende der Arbeit konnte in einem ersten Teststrahl auch eine erste Version der Phase-II Auslese mit einer Synchronisierung zu allen anderen mCBM Detektoren erfolgreich in Betrieb genommen werden.

Abstract

This work contributes large parts to the development, installation and monitoring of the FPGA based readout of the new DiRICH board in the HADES, CBM and mCBM experiments. In addition, an analysis of data taken in the 2020 mCBM beamtime campaign is performed.

The HADES and CBM experiments are fixed target heavy ion experiments at the GSI Helmholtz Centre for Heavy Ion Research in Darmstadt/Germany respectively at the upcoming Facility of Antiproton and Ion Research (FAIR). HADES is a well established experiment at the SIS18 accelerator of GSI and will be completing the future Compressed Baryonic Matter (CBM) pillar of FAIR together with the CBM experiment at SIS100. Both experiments aim for the measurement of di-electrons and their spectrum in different energy regimes. The Ring Imaging Cherenkov (RICH) detector, a subdetector in both experiments, is allowing for clean electron identification. The HADES RICH detector has been upgraded with a new photon detector based on MAPMTs. New front end electronics have been developed which will also be used for CBM at SIS100. The DiRICH FEE is based on TDC measurement of MAPMT signals in a FPGA on the DiRICH board.

The presented work focusses on the upgrade of the HADES RICH with a new photodetection plane based on MAPMTs and DiRICH readout. The use of 428 MAPMTs with 856 DiRICH boards is opening up new capabilities in the electron identification for the HADES experiment and is in parallel a large scale prototype test of the CBM RICH detector electronics. The powering scheme as well as the monitoring of the RICH is upgraded to match the new electronics. The full upgraded HADES RICH performed excellently in the march 2019 Ag+Ag beamtime at 1.58 AGeV.

A second prototype, based on the same DiRICH electronics as the upgraded HADES RICH, has been developed for the mCBM experiment. The mCBM experiment is a prototype experiment of the future CBM experiment for the test of the common free-streaming readout and online analysis algorithms. A dedicated mRICH prototype has been designed, constructed and commissioned with a new readout concept, based on the known TrbNet network and adapted to the free-streaming environment. The readout concept of mRICH in phase-I of mCBM is further developed towards phase-II with the first implementation of the readout concept on the final CBM hardware. The new development includes i.a. major changes in the data transport and the handling of the readout.

The data from the phase-I beamtime 2020 of mCBM is analysed in terms of the readout performance as well as the synchronisation to the other sub-detectors. Excellent time- and spatial correlations between the mRICH and mTOF detectors are found and described in detail in this work. An additional analysis of the mRICH rings and the hits is performed in detail and shows the reliable behaviour of the constructed mRICH prototype detector in the free streaming environment.

Finally, in a first test beam, a first version of the phase-II readout with full synchronisation to the other mCBM detectors could successfully be brought into operation.

Table of Contents

List of Figures

List of Tables

CHAPTER 1

Introduction

Since the earliest days of humanity people are searching for the origin of everything. After thousands of years of thinking, guessing and believing, science gives nowadays the possibility to really measure and explain the state where everything began. From the theory point of view, a very successful model of describing the fundamental particles and forces was developed and tested in many experiments.
The Standard Model of particle physics with its theories of Quantum Chromodynamic (QCD) and Quantum Electrodynamics (QED) are able to predict and explain many of the phenomena that are observed in nature. Nevertheless the Standard Model can not explain everything and has to be extended to explain at some point all observed phenomena.
The interaction of elementary particles in a condition as approximately 10 µs after the big bang can be recreated in the laboratory by heavy ion collisions and the formation of a quark gluon plasma. On the other hand heavy ion collisions could help to improve the understanding of neutron stars and neutron star mergers in the laboratory as many of the conditions are quite similar. Several experiments could measure important properties of the collisions of heavy ions and help to explain the basic structure of known matter.

1.1 The Standard Model

The Standard Model of particle physics is the most successful model describing all elementary particles and interactions of these particles. The model was developed as a renormalizable relativistic quantum field theory, defined by a local

$$SU(3)_C \times SU(2)_L \times U(1)_Y$$

gauge symmetry.
These three factors of the gauge symmetry give rise to the fundamental interactions in the Standard Model of particle physics. It describes three of the four fundamental forces in nature which are transmitted by (virtual) exchange bosons (spin = 1). Until nowadays the gravitational force with the graviton as gauge boson could not be included into the model.

The Standard Model includes 12 fermions, 4 exchange bosons representing the fundamental forces and the higgs boson.
The 12 fermions (spin $\frac{1}{2}$) are divided into two groups, the leptons and the quarks, which

are again grouped into three families. Each family member has charges: electromagnetic, weak and/or color charge. One of the two quarks per family has an electromagnetic charge of $+\frac{2}{3}$ and one has a charge of $-\frac{1}{3}$. The resulting families in the quark sector are up and down, strange and charm, as well as top and bottom quarks. These different types of quarks are being called flavour. As these are also carrying color charge the quarks are interacting with the electroweak as well as with the strong interaction.

The three generations of leptons are divided into electrons, muons and taus with their neutrino partners ν_e, ν_μ respectively ν_τ. Electron, muon and tau are carrying an electrical charge (-1) and are therefore interacting with the electroweak force. In contrast to quarks, they are not carrying a property called color charge and do not interact with the strong interaction which is coupling to the color charge of a fundamental particle.
Neutrinos are in a very prominent position as they are electrically neutral and carrying no color charge. They are only interacting weakly.
The masses of the neutrinos can only be given by an upper limit (see Figure 1.1).

For each lepton and fermion an anti-particle exists. It has the same mass, the same spin but opposite charge.

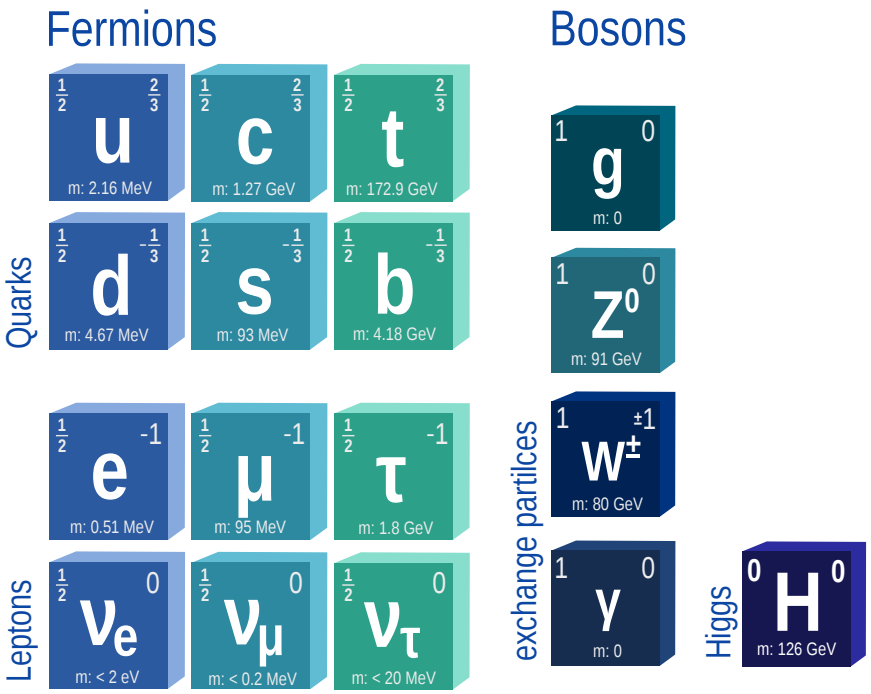

Figure 1.1: Schematic drawing of the fundamental particles of the Standard Model and their families with mass, charge and spin [1].

1.1.1 Electromagnetic Interaction

Interactions in the Standard Model are described by the exchange of particles, the gauge bosons. The range of the forces is defined by the mass of these bosons.
The gauge boson of the electromagnetic interaction is the mass-less photon γ which gives the force a range to infinity. The electromagnetic boson is coupling to electric

charge and consequentially the photon, which is electrically neutral with J^{PC} of 1^{--}, is not coupling to itself but to electrically charged particles as e.g. electrons.
The coupling constant α is given, at least at small momentum transfers, by approximately 1/137 [1].

The electromagnetic interaction is described by the Quantum Electrodynamics (QED) represented by the symmetric U(1) group. The Lagrangian density shows the invariance under gauge transformation of the QED and is given by

$$\mathcal{L}_{QED} = \bar{\psi}\left(i\gamma^{\mu}D_{\mu} - m\right)\psi - \frac{1}{4}F_{\mu\nu}F^{\mu\nu} \tag{1.1}$$

with $D_{\mu} = \partial\mu + iqA_{\mu}(x)$ and $F_{\mu\nu}(x) = \partial_{\mu}A_{\nu}(x) - \partial_{\nu}A_{\mu}(x)$. A_{μ} is the vector potential [2].

The Lorentz invariance and the local gauge invariance results in the existence of a coupling and also defines the coupling. From the symmetry and its Noether current j^{μ} the electric charge Q can be identified as

$$j^{\mu} = q\bar{\psi}\gamma^{\mu}\psi \qquad\qquad Q = \int dx^3 j^0(x) \tag{1.2}$$

in the QED [1, 2].

1.1.2 Weak Interaction

The weak interaction is mediated by a neutral current and a charged current. The charged current interaction is transported by the two charged gauge bosons W^+ and W^-. The neutral current is transported by the electrically neutral Z^0 gauge boson. The corresponding charge is called the weak charge and carried by all fermions as well as the gauge bosons of the weak interaction. Therefore they can interact with each other. The three gauge bosons of the weak interaction are massive with approximately 80 GeV respectively 91 GeV [1]. The coupling constant α_W of the weak interaction is in the same order of the fine structure constant α. Nevertheless the weak interaction is a short range interaction (at momentum transfer q much smaller m_W) due to the mass of the gauge bosons that is directly influencing the propagator term of the interaction as m_W^2.

The charged weak current interaction is the only flavour changing process in the Standard Model of particle physics. It gives the possibility to couple an up-type quark to a down-type quark or to couple a charged lepton to its partner neutrino.
In the lepton sector only transitions within a family with a universal coupling strength are allowed. This, together with the non-zero neutrino masses, finally also results in neutrino oscillations.

In the quark sector the universality of the coupling is not hold any more and the $W^{\pm}$ bosons can change the quark flavour even between families. All up-type quarks can change into all down-type quarks. The change of the flavours was introduced by Cabibbo, Kobayashi and Maskawa with the 3×3 unitary CKM-Matrix that is specified by three Euler angles and one phase angle [3, 4]. The CKM Matrix rotates the mass eigenstates of the d, s and b quarks into flavour eigenstates d', s' and b'. The unitarity of

the Matrix hence gives back a uniform coupling strength between the up-type states u, c, t and the rotated states d', s', b'. The rotation allows only coupling between up-type states and the corresponding flavour eigenstates (e.g. ud') [2, 5].

The charged currents are maximal parity and charge conjugation violating as the $W^{\pm}$ boson is only coupling to left-handed particles and right-handed anti-particles. The possibility of CP-violation is assigned to the imaginary phase of the CKM Matrix.

Neutral weak currents are mediated by the Z^0 boson. They are coupling to electric charge and do not change masses. Like the charged currents, they are violating parity and charge conjugation [5, 6].

1.1.3 Electroweak Unification

A great step towards the grand unification of all forces could be done by the unification of the electromagnetic and weak interaction of Glashow-Salam-Weinberg [7–9]. Glashow-Salam-Weinberg based their theory on the introduction of a weak isospin and a weak hypercharge.
Knowing that three massive bosons and a massless boson are needed, a group for the generation of mass and a U(1) for the electromagnetic interactions are needed in the global gauge group.

A weak isospin I_W is introduced by a $SU(2)_L$ symmetry group and a $U(1)_Y$ group is introduced by a weak hypercharge Y_W resulting in a global gauge symmetry group $SU(2)_L \times U(1)_Y$. The electrical charge is there defined as $Q = I_3 + \frac{Y}{2}$ [2].
All left-handed chiral fermions are grouped together to isospin doublets $I_W = \frac{1}{2}$ ($I_W^{(3)} = \pm\frac{1}{2}$) to connect to the SU(2) gauge bosons. All right handed chiral fermions are grouped to SU(2) singlets of $I_W = 0$ respectively to the family and quark generations.

Three (2^2-1) of the massless gauge bosons are arranged in the weak isospin triplet (W^1, W^2, W^3) and one into a weak hypercharge singlet (B^0).
Introducing a mixing between the triplet and the singlet by a 2×2 matrix and the corresponding Weinberg angle Θ_W connects the B^0 and W^3 massless bosons to the neutral physical bosons Z^0 and γ. The parameter Θ_W is a running constant that is measured in experiment and leading to the unification at high q^2.
The W^1 and W^2 are identified as the W^+ and W^- bosons.
Three of the massless bosons are gaining mass by a spontaneous symmetry breaking via scalar Higgs fields and finally resulting in the known particles W^+, W^-, Z^0 and the massless γ.
The non-zero vacuum expectation value of the Higgs field is resulting in the existence of a Higgs-boson [2, 5, 6].

1.1.4 Strong Interaction

Gluons are the gauge bosons of the strong interaction and are introduced by the Quantum Chromodynamics (QCD). The QCD is a quantum field theory of a SU(3) symmetry group [1, 2, 5, 6].
Each of the six known quarks can carry a color charge of either red (r), green (g) or blue (b), respectively the anti-color anti-red ($\bar{r}$), anti-green ($\bar{g}$) or anti-blue ($\bar{b}$) for the anti quarks. Leptons do not carry color charge and are consequently not participating in the strong interaction.

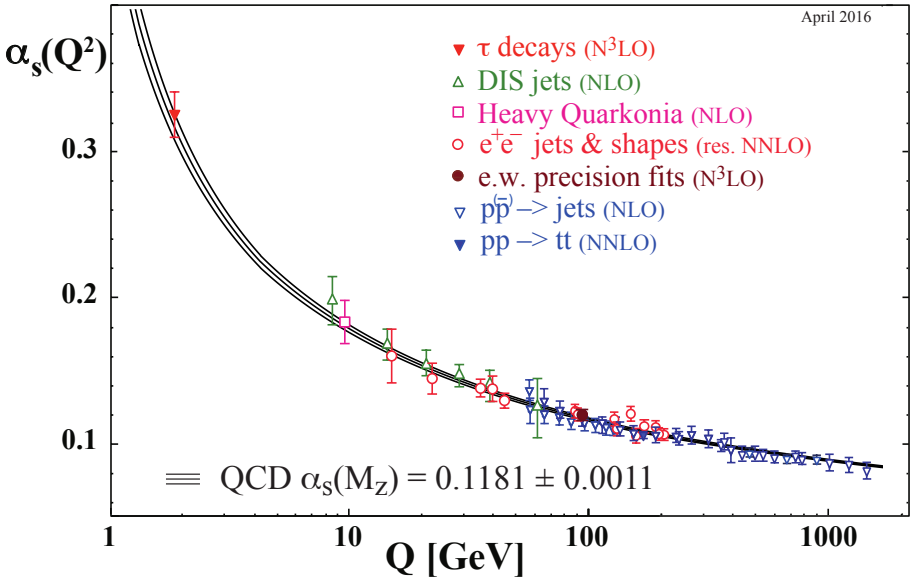

Figure 1.2: Combined world data on the coupling constant of the strong interaction α_S [1].

The gluons as the gauge bosons are coupling to color and anti-color. As a consequence of the fact that the SU(3) is a non-abelian gauge symmetry gluons are self-interacting. They are carrying color and anti-color at the same time.

As no free quarks or colored hadrons (bound states of the strong interaction) were ever observed, quarks are always bound together to color neutral ("white") objects. The phenomena of quarks being always bound together to color-less objects is called confinement [2, 5].
The well known bound objects are baryons and mesons. Baryons are build from three quarks or three anti-quarks. The valence quarks are colored as rgb to be color neutral. The most important baryons are the protons and neutrons as they are the baryons forming the matter on earth.
Mesons are objects formed by two quarks: a quark and an anti-quark. They are color neutral as a combination of a color and a corresponding anti-color is also color neutral.
Other more exotic combinations of quarks that are color-neutral as well are possible too, e.g. the tetraquark [10].

The introduction of a local SU(3) color invariance creates N_c^2-1 = 8 gauge fields, resulting in 8 gauge bosons - the gluons.
The complete Lagrange density of the QCD [2] is

$$\mathcal{L}_{QCD} = \sum_{c=1}^{N_c} \sum_{f=1}^{N_f} \bar{q}_{fc} \left(i\gamma^\mu D_\mu - m_f \right) q_{fc} - \frac{1}{4} F^a_{\mu\nu} F^{a\mu\nu} \tag{1.3}$$

with a field strength tensor of

$$F^a_{\mu\nu} = \partial_\mu A^a_\nu - \partial_\nu A^a_\mu + g f_{abc} A^b_\mu A^c_\nu \tag{1.4}$$

The self interaction of gluons produces divergences in higher orders of the perturbation theory that are renormalized and results finally in a running coupling constant α_S. α_S is decreasing with increasing momentum transfer Q^2 (small distances) resulting in higher precision of the theory with higher Q^2. The decreasing of α_S to a vanishing coupling strength in the limit of $Q^2 \to \infty$ is called asymptotic freedom. At asymptotic freedom (zero distance) the quarks are moving freely (compare Figure 1.2).
For lower Q^2 the coupling is rising, such that perturbation theory is not applicable anymore and other methods are needed [2, 6].

The coupling can be described by

$$\alpha_S(\mu) \approx \frac{1}{\beta_0 ln\left(\frac{\mu^2}{\Lambda^2_{QCD}}\right)} \tag{1.5}$$

with $\beta_0 = 11 - 2N_f/3$ and $\Lambda_{QCD} \approx 0.2GeV$ for $N_f = 4$ which is determined empirically [11].

1.2 Chiral Symmetry Breaking

Protons are baryons with a measured mass of 938.272 081 $\pm$ 0.000 006 MeV and have a quark content of uud [1]. The mass of the up and down quarks are given by $m_u = 2.16^{+0.49}_{-0.26} MeV$ and $m_d = 4.67^{+0.48}_{-0.17} MeV$ [1].

Calculating the mass of the proton just by the pure quark content gives

$$m_{uud} = 2 * m_u + m_d = 8.99^{+1.09}_{-0.55} MeV$$

Even assuming the highest mass of the quarks, the quarks contribute only 1.07 % to the measured proton mass. The hadrons gain most of the mass by a process called chiral symmetry breaking.

In the limit of vanishing quark masses the QCD exhibits a chiral symmetry. Left and right handed quarks transform independently under $\psi_{L/R} = \frac{1}{2}(1 \pm \gamma_5)\psi$ [11].
The resulting flavour symmetry $U(N_f)_L \times U(N_f)_R$ can be decomposed as

$$U(N_f)_L \times U(N_f)_R = SU(N_f)_L \times SU(N_f)_R \times U(1)_V \times U(1)_A \tag{1.6}$$

where the $SU(N_f)_L \times SU(N_f)_R$ is the chiral group. The $U(1)_V$ is an exact symmetry and implies baryon number conservation.

In chiral symmetry the left- and the right-handed quarks decouple completely. The Lagrangian of the QCD (see Equation 1.3) is invariant under global SU(3) flavour rotations of the left and right handed quarks. In case of a chiral symmetry the spectral functions of a vector and an axial vector meson should not diverge. Furthermore the masses of the chiral partners have to be the same.

Measurements of the spectral function of the chiral partners ρ (J^P=1^-) and the a_1 (J^P=1^+) via a mass spectrum from the OPAL collaboration in hadronic τ decays (see

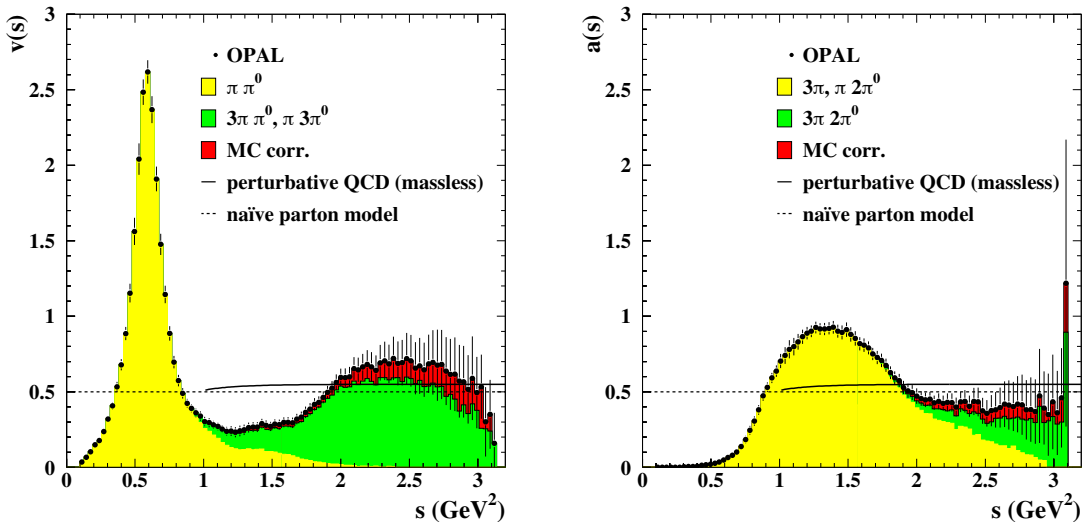

Figure 1.3: Experimental measurements of the vector and axial-vector spectral functions in hadronic τ decays by the OPAL collaboration [12].

Figure 1.3) indicate a chiral symmetry breaking as the two distributions differ significantly. The mass difference of both distributions is on the order of the mass of the ρ-meson. This large discrepancy is not explainable by the explicit breaking of the symmetry due to a finite current quark mass of below 10 MeV for the light quarks.
Comparing the quark masses to the scale of QCD (Λ_{QCD}) of around 200 MeV one can still speak of an approximate symmetry.

The solution is a spontaneous breaking of the chiral symmetry. The symmetry is realised in higher states but in the ground state (i.e. vacuum) the symmetry is not realised any more. A non-vanishing vacuum expectation value has to exist. For chiral symmetry breaking we define a chiral quark condensate [11]:

$$\langle 0|q\bar{q}|0\rangle \cong -(0.23 \pm 0.03GeV)^3 \cong -1.6fm^{-3} \tag{1.7}$$

The existence of a chiral quark condensate allows the transformation of e.g. left-handed quarks into right-handed quarks via the annihilation with left handed antiquarks from the quark condensate. The left and right handed quarks are no longer decoupled.

Figure 1.4 depicts the principle of spontaneous symmetry breaking. The left side of the figure shows a potential with its ground state positioned in the middle. The ground state of the potential as well as the potential itself are symmetric (invariant) under rotations.
The right side shows a "Mexican Hat" potential with a ground state at finite distance to the center of the potential. The center of the potential is a local maximum surrounded by a valley of a minima. As the ground state is obviously lying at some position in the valley of minima, the rotation symmetry is broken whereas the potential itself is still symmetric.

In the picture of chiral symmetry the existence of a non-vanishing vacuum expectation value of the scalar quark condensate generates massless Goldstone bosons π and a massive σ meson. In the case of 2 flavours the Goldstone bosons are identified with

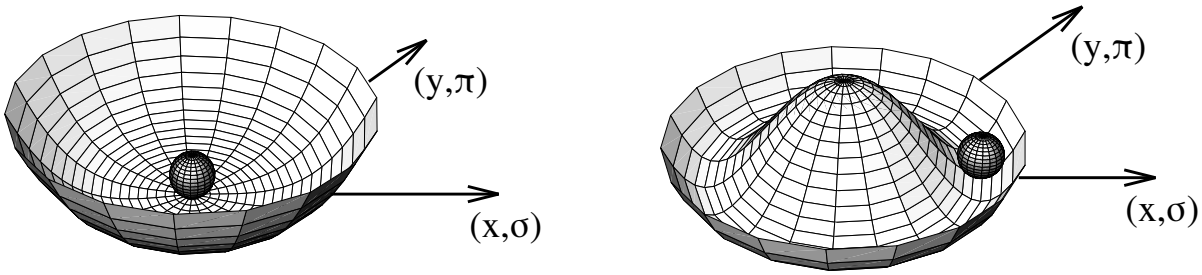

Figure 1.4: Mechanical example of spontaneous symmetry breaking. **(left)** A symmetric potential with its ground state in the center. **(right)** The potential is still symmetric under rotations. The ground state is spontaneously broken as the ball chooses a minimum of the potential that is not in the center of the potential. In contrast to the radial excitations a rotation in the potential costs no energy [13].

the pions. As we inspect a 3 flavour case (u-, d- and s-quarks) the Goldstone bosons will create the mesons of the scalar meson octet.

The existence of a non-vanishing mass of the pions in nature can be understood in terms of the QCD chiral symmetry being only approximate, as the masses of the up-, down- and strange-quarks are very small but non-vanishing. The small but non-vanishing quark masses are breaking the symmetry in addition explicitly. An extremely useful link between the hadron observables and the current quark masses is given by the Gell-Mann-Oaks-Renner relations (GOR) [13, 14]

$$m_\pi^2 = -f_\pi^{-2} \left(\frac{m_u + m_d}{2} \right) \langle 0|\bar{u}u + \bar{d}d|0\rangle \tag{1.8}$$

where f_π is the pion decay constant. The GOR-relation can serve as an indicator for the strength of the symmetry breaking and quantify it by the chiral quark condensate as one parameter.

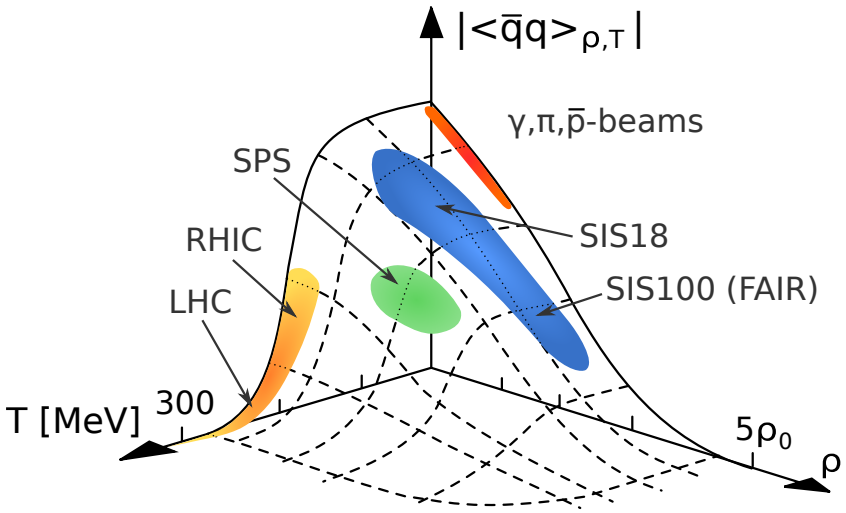

Figure 1.5: Temperature and density dependency of the chiral condensate expectation value based on NJL model calculations. The colored areas indicate the regions accessible by A+A collisions at different accelerator facilities. Figure adapted from [15, 16].

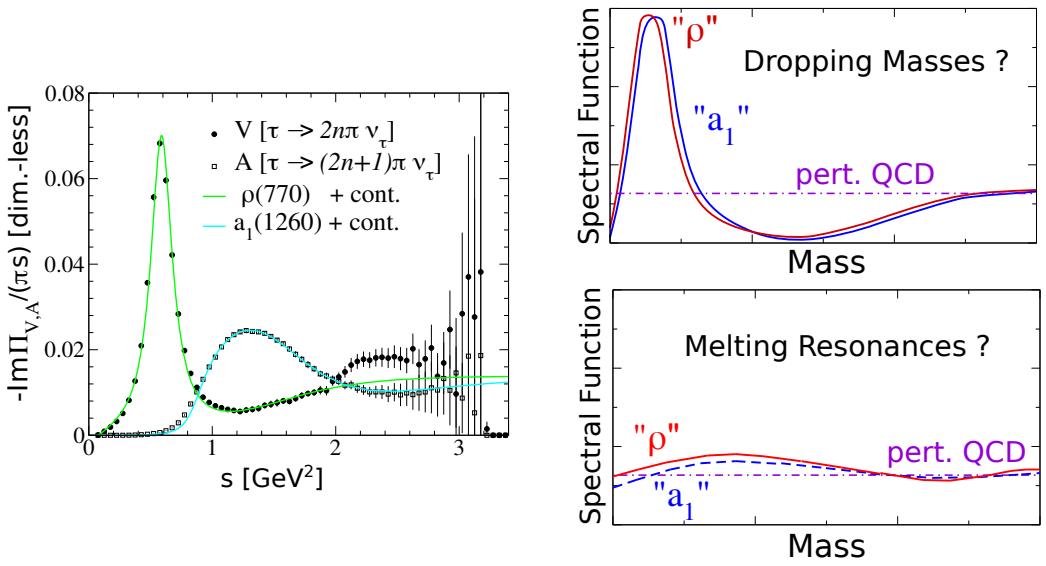

Figure 1.6: **(left)** Vector and axial vector spectral functions as measured in hadronic τ decays from the ALEPH collaboration [17]. **(right)** Schematic scenarios for chiral symmetry restoration in matter [18].

The dependence of the quark condensate expectation value can be calculated in the Nambu-Jona-Lasinio (NJL) model [16]. Figure 1.5 shows the density and temperature relation of the quark condensate based on NJL model calculations.

Starting from a vanishing temperature and density of the matter, the expectation value of the quark condensate is at maximum. An increase of the density as well as temperature results in a vanishing of the quark condensate. The blueish area in Figure 1.5 indicates the region of the SIS18 experiments as HADES and FOPI, but also mCBM. The region at higher densities will be investigated by the CBM experiment at FAIR. In the SIS energy region the chiral condensate is already partially melted, showing that chiral symmetry is also partially restored. As RHIC and LHC are investigating matter at low density but high temperature, the decrease of the chiral condensate is behaving slightly differently. For LHC energies a region is reached, where the chiral condensate is nearly vanished.

The chiral condensate is not directly experimentally observable. A possibility of measuring the chiral condensate is given by QCD sum rules. Integration over hadronic spectral functions (i.e. axial and vector) give a connection between the chiral condensate and the hadronic observables [18].

Figure 1.3 and Figure 1.6 (left picture) are both showing the results of the measurement of the a_1 and ρ spectral function of the OPAL and ALEPH collaborations. The deviation of both spectral functions of the chiral partners and the resulting gap in mass are nicely observed in both experiments. Moving to a region in the phase diagram where chiral symmetry breaking is restored and the chiral condensate is vanishing, the spectral functions are predicted to change its shape and converge to each other, resulting in the same mass for both chiral partners. From theory calculations a dropping mass or a mass broadening (melting resonance) is discussed, but experimental results from the last years are favouring the broadening mass scenario [19, 20] (see Figure 1.6, right figures).

1.3 Heavy Ion Collisions and the Quark-Gluon Plasma

Heavy ion collisions are a perfect tool to achieve conditions in the laboratory with high temperatures and/or high baryon densities such that quarks can not exist as nuclear matter in hadrons anymore. In the limit of asymptotic freedom deconfinement of the hadronic matter is expected and may be leading to a new form of matter of quasi-free moving quarks and gluons, the Quark-Gluon Plasma.

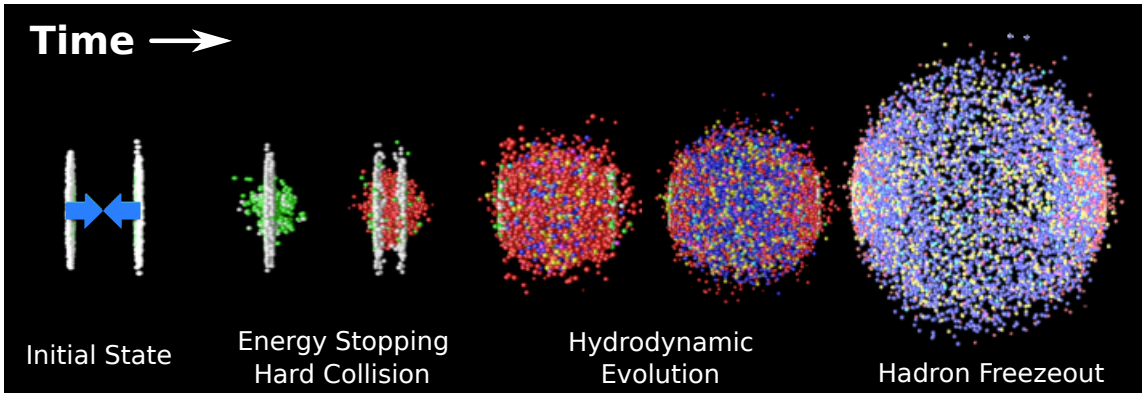

Figure 1.7: The time evolution of a heavy ion collision. The Lorentz contracted ions (left) collide. In the overlap region between both ions first hard collisions take placee with large stopping and high enrgy density. This phase is going over to a hydronamic evolution of quarks and gluons (middle). In the final state the particles freezeout to hadrons (right). [21]

Heavy ion collisions and their final state are quite dependent on the particle types of the collision system and the collision energy as well as the impact parameter b. Depending on these parameters the collision can form different types of matter.
Collisions can take place either with colliding beams or one beam running on a fixed target. The first scenario allows to achieve higher collision energy, the second higher interaction rates. Different facilities offer different possibilities and the detector design is optimized accordingly.

In a collider experiment the detector is most likely positioned symmetrically around the interaction point. Two beams of particles are accelerated in opposite direction to each other and cross exactly at the position of the detector. The resulting collision and development of the collision is strongly dependent on the energy and particle type of the collision. A symmetric setup with same ions and energies in both beams is producing a 4π symmetric interaction. If the collision beams are asymmetric as e.g. one beam has a different energy, the whole system is boosted towards one direction. The detectors are usually designed for one of the two scenarios as they have to cover a certain acceptance in space. Both beams can either share the same beam pipe or use two different ones. The most famous facility using such collisions is the Large Hadron Collider (LHC) at CERN with the dedicated heavy ion program of the ALICE detector.

In a fixed target experiment only one heavy ion beam is accelerated. The accelerated beam is hitting a fixed target in the beam- or at the end of the extraction-line. The target of such a detector is often a foil of e.g. gold. Due to an asymmetric momentum distribution of the two colliding ions, the whole collision is boosted into one direction.

The detectors have to be build to cover only this direction of the collision. This gives even some more flexibility in the design of a detector as a collider experiment is most likely stacked together and all sub detectors have to fit into each other. For fixed target experiments it is more feasible to put the sub detectors in a row what gives some degrees of freedom to the development. The detectors, mentioned in this thesis, are all fixed target detectors as HADES and (m)CBM are all fixed target experiments.

Figure 1.7 is depicting schematically the evolution of a heavy ion collision seen from the center of mass frame. In the initial state two Lorentz contracted heavy ions are about to collide. As these two heavy ions are colliding they are passing through each other with a certain overlap region. In the overlap region of the collision a high energy density is created and a (possibly) new state of matter is formed. This matter survives for only a very short time. The newly formed matter is expanding and at some point freezing out to hadronic matter [18, 21, 22].

Obviously the overlap of the two ions is defining the number of particles participating in such a collision (participants) and the particles that are not part of the collision itself and are just moving on (the spectators). The measurement of the geometry and the so called centrality of a heavy ion collision is very important. In reality collisions are varying from head to head collisions (central) to grazing collisions where only a fraction of both projectiles are interacting (peripheral collision). To characterize the geometry a vector $\vec{b}$, called impact parameter, is introduced as the distance between the centers of two colliding projectile ions A and B perpendicular to the beam axis (compare with Figure 1.8). The magnitude $|\vec{b}|$ of the impact parameter is defining the fraction of the overlap between A and B.
A central collision is defined by $|\vec{b}| = 0$. A peripheral collision with only a small overlap of e.g. 5% leads to a very different collision zone as its shape is far off from a spherical shape as for central collisions. This is directly influencing the momentum distributions and pressure gradients inside the collision zone.
The shape of the collision zone formed by participants has a mirror symmetry with respect to the interaction plane. The interaction plane is a plane formed by the vector $\vec{b}$ and the z-direction of the collision [22].
The measurement of the participants and the centrality is done e.g. by a zero degree calorimeter. The spectators are, in relativistic heavy ion collision, travelling along the beam direction without an influence of the interaction and are depositioning energy in a detector under nearly zero degree to the beamline. From model calculations (Glauber model), the number of participants can be calculated. In Chapter 3 such a detector will be explained in more detail by the example of the CBM PSD detector.

As already mentioned, a heavy ion collision is evolving from the collision of two ions. The collision of the participants leads to an accumulation of high energy in a small volume for a short time. This conditions can produce very high energy densities that lead to the formation of a so called fireball. This fireball lives for less than 10^{-22} seconds [18, 21–23].

The fireball eventually becomes a thermalized system that may include deconfined matter. The evolution can be well described by hydrodynamics as the fireball seems to be a nearly perfect liquid, at least for high collision energies. The expansion and

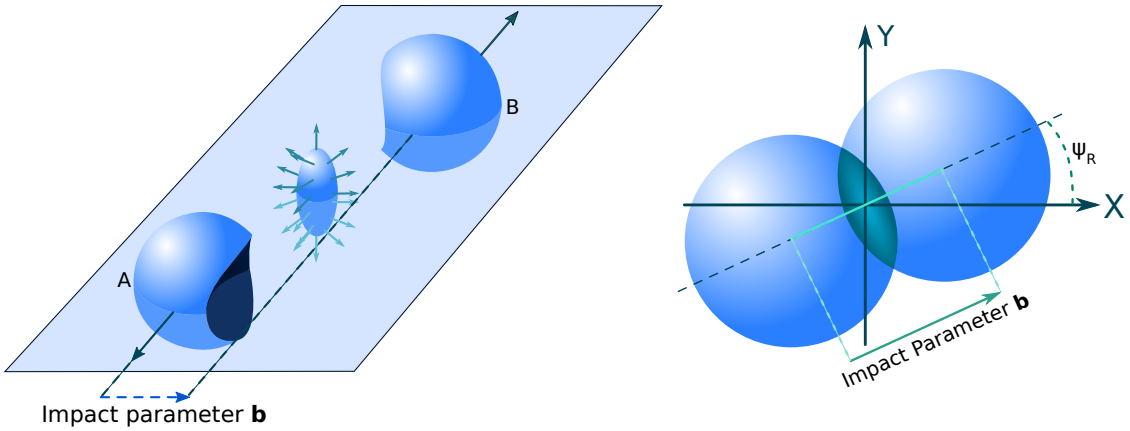

Figure 1.8: Sketch of the interaction geometry of a heavy ion collision. **(left)** Interaction between particle A and B with a small overlap and an impact parameter b. The center shows the interaction region with the participants. **(right)** Alignment of the collision in X and Y with the impact parameter and the tilt of the interaction Plane in space. Figure is inspired by [22].

the cooling of the system results finally in the hadronization of quarks and gluons to baryons and mesons at a certain freeze-out temperature. At this moment the hadrons are formed thus the quark content is fixed but they can still collide elastically and change their momenta (see Figure 1.7).

1.3.1 The QCD Phase Diagram

Collisions of heavy ions can produce different types of matter in the collision process, depending on collision energy and system. Equivalently to the phase diagram of water, a QCD phase diagram is introduced to characterize QCD matter in terms of temperatures and net baryon density (or baryochemical potential μ_B).

Between the phases of QCD matter different phase transitions and potentially a critical endpoint is expected. Figure 1.9 shows a schematic drawing of the phase diagram of QCD matter in the temperature vs. baryon chemical potential (μ_B) plane. Normal nuclei are found at μ_B = 924 MeV at a baryon density n_0 = 0.17 fm^{-3} [24] and a temperature slightly above 0 MeV. From this starting point on, the different experimental facilities can start exploring the phase diagram in heavy ion collisions.

At high temperature T and vanishing net baryon density lattice calculations predict a smooth crossover region between a hadron gas phase and a quark gluon plasma phase [25, 26]. After the transition the quarks are supposed to be deconfined and chiral symmetry restoration is expected ($\langle q\bar{q}\rangle$ = 0). (see section 1.2)

With higher net baryon densities a first order phase transition is expected [27]. The transition from a crossover to a first order phase transition leads to the prediction of a critical endpoint at the end of the first order phase transition line. A critical endpoint would be very interesting for experiments as enhanced fluctuations are expected [24].

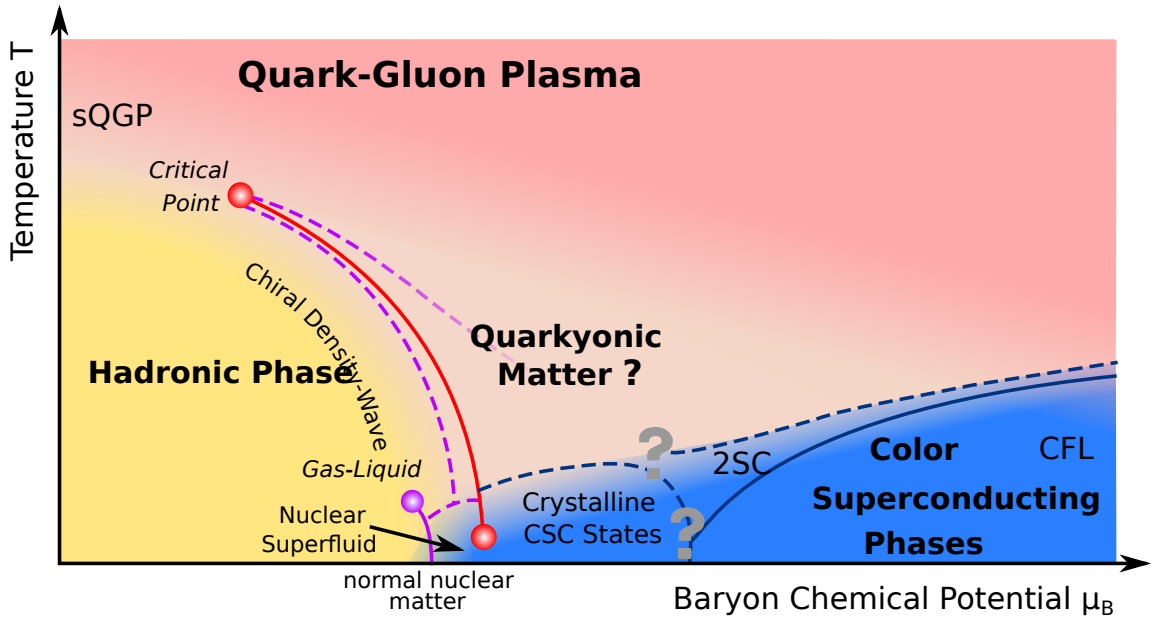

Figure 1.9: Schematic drawing of the phase diagram of hadronic matter. (Adapted from [24])

In addition calculations with high N_c predict a region of quarkyonic matter. The quarkyonic matter has its chiral symmetry restored but is still confined [28]. If quarkyonic matter is found, the confined, deconfined and quarkyonic phase would possibly meet at the critical endpoint and make it a triple point [24].

For nuclear matter with $\mu_B \approx 924$ MeV at T = 0 a first-order transition between a liquid gas phase and a fluid is predicted. At the threshold of $\mu_B = \mu_{NM}$, the nuclear density n varies from zero to n_0 and the nuclear matter is fragmenting into droplets if $n < n_0$ [24]. The end of this phase transition is expected to be marked with a second-order critical point around $\mu_B \approx \mu_{NM}$ and T ≈ 15-20 MeV as indicated by low energy heavy ion collision experiments [24, 29].

In the region of asymptotically large μ_B and low temperature the ground state of QCD matter can be analysed with weak-coupling methods in QCD. Similar to superconductivity for electrons in condensed matter, quarks can form Cooper-Pairs and behave color-superconductive [18, 24].

Different calculations and measurements are trying to determine a critical temperature T_c of the phase transition from hadrons to a quark gluon plasma at vanishing baryon densities. Lattice calculations of the HotQCD collaboration are predicting a critical temperature of $T_c = 156.5 \pm 1.5$ MeV [30] with a remarkable small error. The lattice results are very promising as they are model independent and are in principle only limited by computing power.
Experimental results on the chemical freeze-out temperature of heavy ion collisions lie around 160 MeV [31, 32].

In this regions of high T and low density LHC experiments are taking data. At RHIC a beam energy scan is done to scan over a larger region of the phase diagram. Differ-

ent center of mass energies between 7.7 and 200 GeV are measured providing an almost uniform coverage of the (T,μ_B) plane [33]. Large parts of the central part of the (T,μ_B) plane have also been investigated by previous experiments at the SPS and AGS accelerators.
At low temperature but high density the HADES detector at GSI with SIS18 beams is investigating the created matter, whereas the upcoming CBM experiment at FAIR will be measuring at high baron density and moderate temperatures.

1.4 Probes of the Quark Gluon Plasma

The previous sections gave an introduction to the overall interest of heavy ion collisions and especially to the formation of a Quark Gluon Plasma. Unfortunately it is a very short process in time and thus it is very challenging to get informations about the heavy ion collisions and the state of the matter being created. Therefore indirect measurement of the QGP and/or dense phases via investigating remnants and outgoing particles has to be done. Different methods to probe the QGP are experimentally possible. Especially probes explored by the CBM and HADES detectors will be discussed further on.

1.4.1 Charm

Particles containing charm quarks are expected to be produced in the very early stage of the collision and serve therefore as an ideal probe of the entire collision history. Charm quarks offer access to the degrees-of-freedom during all stages of the collision making them to a very interesting probe of the QGP [34] or dense matter [18].

The charm and anti-charm quarks are interacting with the medium. Depending on the interaction they hadronize to D-mesons, charmonium or charmed baryons. One of the first predicted signatures for a quark gluon plasma phase was the suppression of charmonium due to color screening of the heavy quark potential in the deconfined phase [35, 36].

Measurements of the charm suppression are reflected by R_{AA}, the nuclear modification factor. It is defined as the ratio between the rapidity density of the J/ψ Yield in AA collisions to pp collisions integrated over transverse momentum, scaled with the binary number of collisions for a certain centrality class (see equation 1.9) [18].

$$R_{AA}^{J/\psi} = \frac{dN_{J/\psi}^{AA}/dy}{N_{coll} \cdot dN_{J/\psi}^{pp}/dy} \tag{1.9}$$

The J/ψ suppression is dependent on e.g. the centrality, the transverse momentum, rapidity regions and the energy scale of the collision. Hot and dense matter has different influences than cold matter. At LHC energies a regeneration-effect due to the coalescence of uncorrelated c and $\bar{c}$ quarks is expected and observed, whereas at FAIR conditions this effect is neglectable.

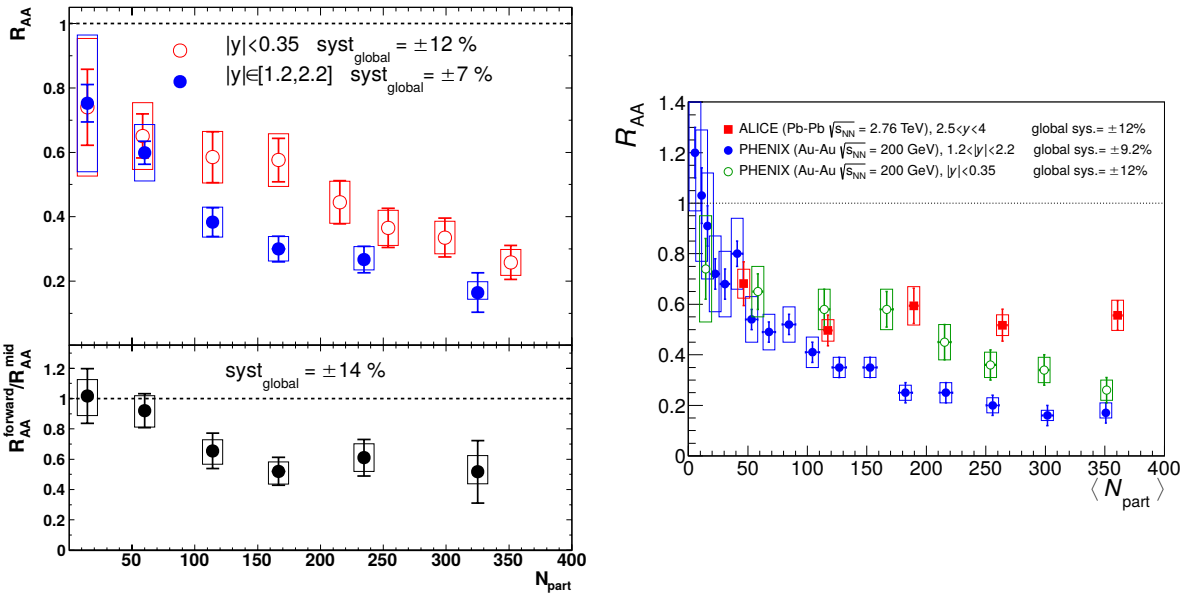

Figure 1.10: **(left top)** Measured nuclear modification factor for mid and forward rapidity in different centralities at PHENIX in Au+Au collisions at $\sqrt{S_{NN}} = 200GeV$. **(left bottom)** Ratios between forward- and mid-rapidity [37]. **(right)** Comparison between PHENIX and ALICE results. Alice is measuring at very high energies and different rapidity [38].

Figure 1.10 shows measurements of the J/ψ suppression at different centralities (represented by N_{part}) and rapidities for PHENIX data in Au+Au collisions at $\sqrt{S_{NN}} = 200$ GeV. The J/ψ suppression is increasing with increasing centrality. Comparisons between mid and forward rapidity show a clear rapidity dependence of the suppression towards less suppression at mid rapidity.

FAIR offers with CBM at SIS100 energies the possibility to study charm production in p and pA at energies close to the production threshold. These measurements will be important as reference for J/ψ production in general and propagation in cold nuclear matter. With a future upgrade of FAIR with SIS300 the investigation of charm in A+A collisions will become possible. At these collisions the time charmonium needs to form is low compared to the medium lifetime. This conditions give unique opportunities to study the interaction of formed J/ψ with the dense medium.

In addition to the previously discussed measurements, the elliptic flow of charm can be measured as well. It gives a measurement of the pressure from the initial stage and whether or not the heavy quarks flow with the medium.

1.4.2 Flow

Flow is an observable more related to the entire fireball of a heavy ion collision. The expansion of the early fireball is driven by the pressure gradients in the collision zone (see section 1.3). The flow as an observable is measuring the angular and momentum distributions of the particles resulting from this pressure gradients. In heavy ion collisions different types of flow are defined.

The anisotropic flow is defined by the Fourier distribution of the Lorentz invariant distribution of the outgoing particles [39, 40]:

$$E\frac{d^3N}{d\phi^3} = \frac{1}{2\pi}\frac{d^2N}{p_T dp_T dy}\cdot\left(1+\sum_{n=1}^{\infty}2v_n\cdot cos(n(\phi-\Psi_R))\right) \tag{1.10}$$

where Ψ_R is the reaction plane angle. Furthermore this defines the coefficients v_n as

$$v_n = \langle cos(n(\phi-\Psi_R))\rangle \tag{1.11}$$

where the brackets indicate an average over all particles in all events [39]. The factor v_1 is associated with the so called directed flow. v_2 is named elliptic flow. These coefficients can be expressed in terms of the particle number distribution as

$$v_1 = \left\langle\frac{p_x}{p_t}\right\rangle \qquad v_2 = \left\langle\left(\frac{p_x}{p_t}\right)^2-\left(\frac{p_y}{p_t}\right)^2\right\rangle \tag{1.12}$$

Directed flow is defined within the reaction plane and influenced by the repulsion away from the beam axis. It takes primary place at the border between spectators and participants. It is also called "bounce-off" [41].

Results on the elliptic flow at high collision energies are seen as a strong hint to the existence of a quark gluon plasma [43] and has been measured for many different particles and their antiparticles.
Elliptic Flow is driven by the expansion due to the pressure gradient in the directions perpendicular to the beam axis. The elliptic flow exhibits a characteristic energy dependency with a sign flip at low energies. This is also predicted by hydrodynamic calculations for energies $E_{Lab} \lessapprox 4-5$ AGeV. In this energy range and below, the spectators

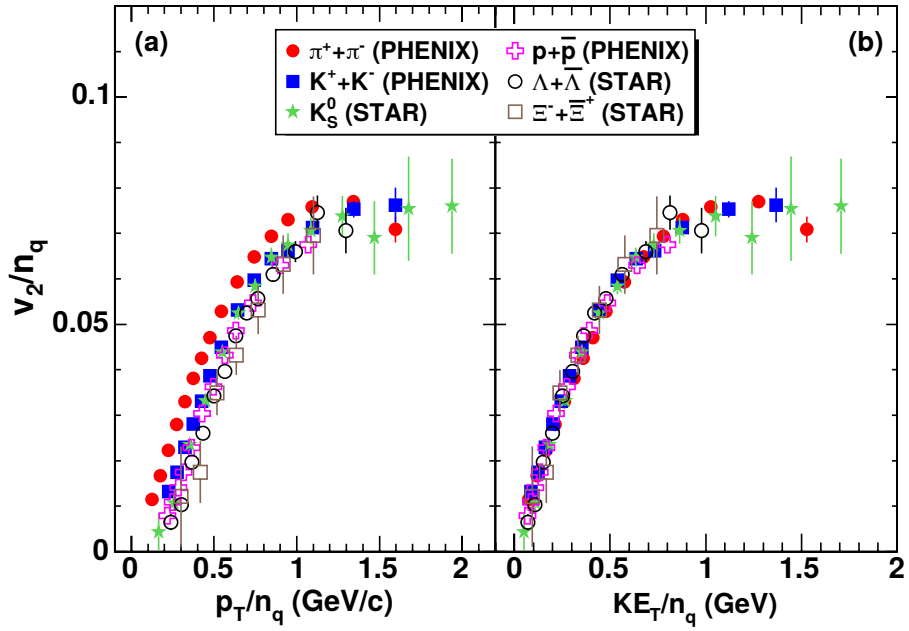

Figure 1.11: Elliptic flow measurement from STAR and PHENIX in transverse momentum (left) and transverse kinetic energy. Both diagrams are scaled with the number of constituent quarks. The flow is measured in identical particle species with minimum bias Au+Au collisions [18, 42].

"shield" the fireball in the reaction plane, guiding the particles towards the direction perpendicular to the reaction plane, called "squeeze-out" [18, 41]. The pressure gradients in the fireball are connected to the equation of state of the created matter, giving a direct link to the flow measurements.

The flow measurement is also predicted to be sensitive to the observation of a phase transition [41]. A combination of the slope of v_1 (negative or positive) in rapidity bins together with the enhancement of v_2 should be an indicator for a first order phase transition respectively a crossover [41].

Measurements of v_2 from STAR and PHENIX are showing a remarkable scaling of v_2 versus transverse energy for a large number of different hadrons if scaled with the number of constituent quarks (Figure 1.11). This measurement amongst others led to a general acceptance of the notion that the initial matter created in heavy ion collisions at the RHIC accelerator is partonic matter. The flow measurement is directly correlated to the degrees of freedom in the initial matter [18].

1.4.3 Event-by-Event Fluctuations

A physical system can also be characterized by the fluctuations of the system regarding certain (conserved) quantities. For heavy ion collisions typical observables would be charge fluctuations, baryon number fluctuations and so on. These fluctuation are an important tool to search for a critical endpoint. To study these fluctuation in HIC, conserved quantities have to be measured on an event-by-event basis. Fluctuations are then derived from the ensemble of the events [44].

If a system is in thermal equilibrium it can be characterized by the partition function

$$Z = Tr\left[exp\left(-\frac{H - \sum_i \mu_i Q_i}{T}\right)\right] \tag{1.13}$$

H is the Hamiltonian of the system. Q_i and μ_i denote the conserved charge and the corresponding chemical potential respectively (strangeness, baryon number, electric charge) [44].

Based on the partition function in equation 1.13 and the assumption of a observable N that is a conserved charge, fluctuations in the system can be identified by a cumulant K_n, defined [45] as

$$K_n = \frac{\partial^n}{\partial(\mu/T)^n} ln(Z) = \frac{\partial^{n-1}}{\partial(\mu/T)^{n-1}} \langle N \rangle \tag{1.14}$$

Furthermore a susceptibility can be defined [45]:

$$\chi_n = \frac{\partial^n}{\partial(\mu/T)^n} \frac{1}{V} ln(Z) \tag{1.15}$$

The use of cumulants of conserved charges is a handy tool to link Lattice QCD predictions from the introduced susceptibility to experimentally measurable values. Rations of cumulants and susceptibilities are used to identify fluctuations in heavy ion collisions giving a volume independent measurement [46]:

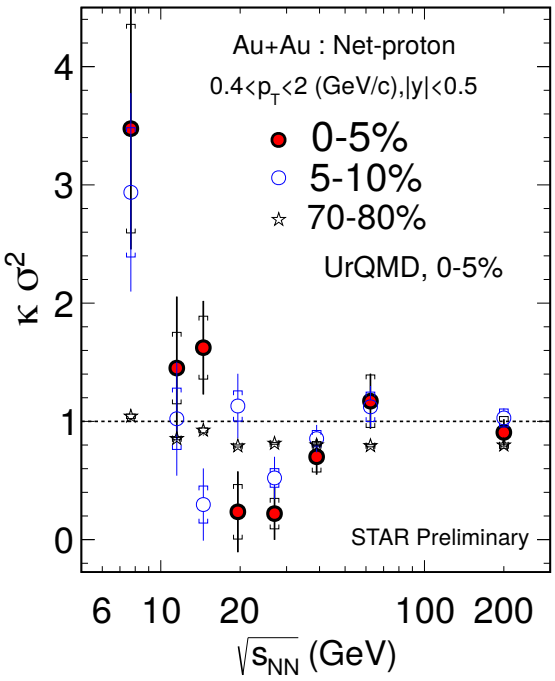

Figure 1.12: Energy dependence of $\kappa\sigma^2$ in Au+Au collisions in the STAR beam energy scan between 7.7 and 200 GeV; centralities of 0-5%, 5-10% and 70-80%, $0.4 < p_T < 2$ GeV and $|y| < 0.5$ [47].

$$S\sigma = \frac{K_3}{K_2} = \frac{\chi_4}{\chi_2}, \qquad \kappa\sigma^2 = \frac{K_4}{K_2} = \frac{\chi_3}{\chi_2} \tag{1.16}$$

with the variance σ^2, the skewness S, the kurtosis κ and the measurable values

$$\begin{aligned} K_2 &= \langle N^2\rangle - \langle N\rangle^2 \\ K_3 &= 2\langle N^2\rangle - 3\langle N\rangle\langle N^2\rangle + \langle N^3\rangle \\ K_4 &= -6\langle N\rangle^4 + 12\langle N\rangle^2\langle N^2\rangle - 3\langle N^2\rangle^2 - 4\langle N\rangle\langle N^3\rangle + \langle N^4\rangle \end{aligned} \tag{1.17}$$

The NA49, PHENIX and the STAR collaborations already measured event-by-event fluctuations searching for the critical point. Figure 1.12 shows the STAR results for the previously introduced $\kappa\sigma^2$ as a volume independent measurement of the net-proton multiplicity distribution for different energies between 7.7 and 200 GeV in different centrality bins in Au+Au collisions for transverse momenta $0.4 < p_T < 2$ GeV and mid-rapidity $|y| < 0.5$ [47].
For a critical point a non-monotonic behaviour is expected. Deviations of $\kappa\sigma^2$ from unity for lower center of mass energies is seen in the STAR data and calls for a more detailed look as well as a measurement of this quantity for lower energies as e.g. available at SIS100 [47].

1.4.4 Hypernuclei

A hypernucleus is a nucleus where at least one hyperon replaces a nucleon. Calculations with statistical models predict a peak of the hypernuclei yield within the SIS100 energy range [48]. On the one hand the production of light nuclei is decreasing with lower energy, on the other hand the hyperon production is increasing with energy, thus the yield of hypernuclei peaks in the SIS100 range [36].

The yield of ${}^{5}_{\Lambda\Lambda}H$ and ${}^{6}_{\Lambda\Lambda}He$ in 10^6 Events of 10 AGeV central Au+Au collisions is predicted to be 5 respectively 0.1. Due to the high rate capability of the CBM detector the

large acceptance and efficiency for double-Λ events will open up a huge discovery potential in the field of light double-Λ hypernuclei [36].

The existence of these exotic nuclei even in heavy ion collisions has been proven: Measurements of the STAR collaboration at RHIC in high energy nucleus-nucleus collisions showed the first results on lightest (anti-)hypernucleus and (anti-)hypertriton [49]. In addition first studies on hypernuclei were done with the HADES detector in Ar+KCl data [50].

1.4.5 Strangeness

Strangeness enhancement in heavy ion collisions with respect to nucleon-nucleon collisions is expected in particular if a quark gluon plasma is formed. In a QGP strangeness can be produced from quarks and gluons in strange-antistrange pair production, especially in the channels of

$$g + g \rightarrow s + \bar{s} \qquad q + \bar{q} \rightarrow s + \bar{s} \quad (q = u, d) \tag{1.18}$$

The Q-value of this process is far lower ($Q_{QGP} = 2m_s \approx 200MeV$) as for a production in nucleon-nucleon reactions via

$$N + N \rightarrow N + \Lambda + K \tag{1.19}$$

with associated $Q_{ass.} = m_\Lambda + m_K - m_N \approx 670MeV$. Thus the production of strangeness is easier in a state of a QGP [51, 52].

The strangeness enhancement is measured in terms of the enhancement factor E_s (here defined at midrapidity):

$$E_s = \left(\frac{1}{\langle N_{AA} \rangle} \frac{dN(A+A)}{dy}\bigg|_{y=0} \right) \Big/ \left(\frac{1}{2} \frac{dN(p+p(Be))}{dy}\bigg|_{y=0} \right) \tag{1.20}$$

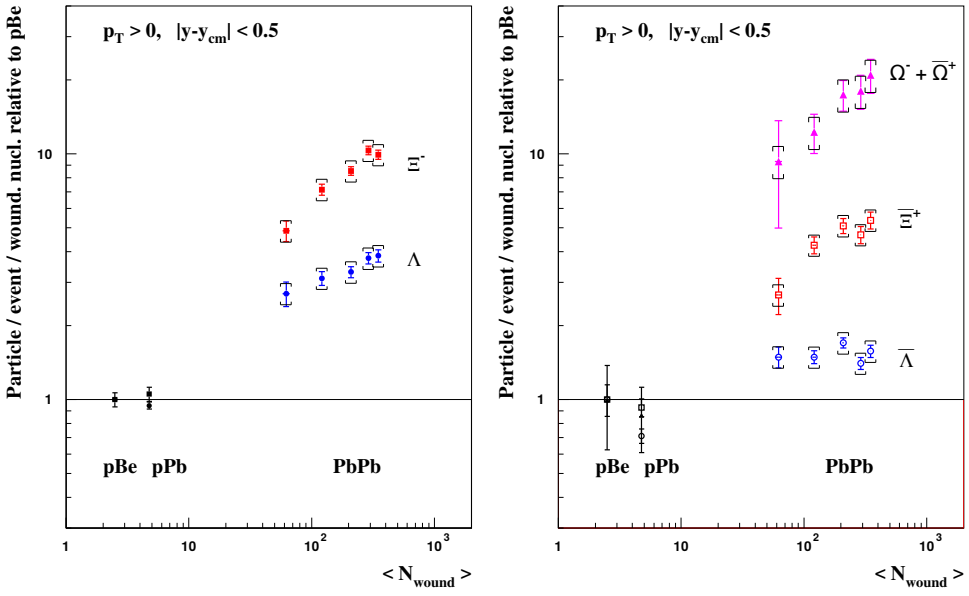

Figure 1.13: Enhancement of strangeness in Pb+Pb collisions at 158 AGeV relative to p+Be and p+Pb for different particles by the NA57 collaboration [53].

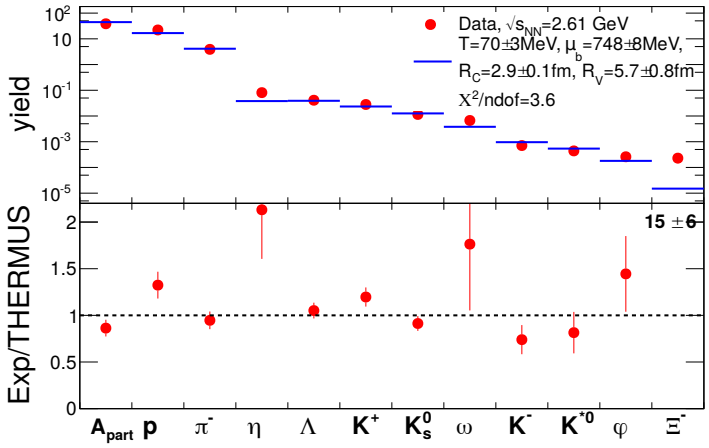

Figure 1.14: Yields of hadrons in Ar+KCl and THERMUS model calculations. The Ξ^- value is deviating from the THERMUS value and is indicated by the value of the ratio [56].

Measurements at SPS, LHC and RHIC energies clearly show an enhancement for strange particles increasing with increasing strangeness (Λ (S=1), Ξ^- (S=2) to Ω (S=3)). The enhancement of the Ω is measured up to E_S = 20 (see Figure 1.13) at top SPS energies [53].

Calculations with thermal statistical model in thermal equilibrium could reproduce the different measured particle ratio as e.g. in top SPS energy [54]. The excess in yield of e.g. Ω^- may be driven by the hadronisation at a phase boundary which comes along with a rapid density change [55].

The well agreement of the thermal model in the high energy regime calls for measurements in the low energy region. The existing SIS18 as well as the future SIS100 accelerators of GSI are covering the low energy regime in heavy ion collisions.

At SIS18 the HADES detector measured yields of hadrons in Ar+KCl at 1.76 AGeV. Figure 1.14 shows the measured yields in comparison to calculations with the thermo statistical model THERMUS. Whereas most of the results are in an excellent agreement with the model, and therefore are also reproducing the well agreement between data and thermal models in high energy data [54], the Ξ^- hyperon yield exceeds the prediction by a factor of 15$\pm$6. This results indicates, that the Ξ^- has not reached chemical equilibrium [56] and that at low energies hadronic processes are becoming more important as in the high energy regime.
Additional measurements of sub-threshold ϕ-mesons at HADES in Au+Au collisions with 1.23 AGeV revealed an enhancement of the rare strange particles, as the ϕ/K^- ratio shows a dramatic increase at this very low energies [57, 58]. All in all, the energy dependence of strangeness enhancement seems to be quite complicated [58].

Strangeness measurements at SIS100 will give new results on low energy enhancements of strangeness and may reveal changes in the degree of freedom of the created matter as well as finding a signal for the onset of deconfinement at high-baryon densities [36].

1.4.6 Lepton Pairs

A key observable to get direct insight into the created matter are electromagnetic probes. They are not interacting strongly but can penetrate the hot and dense matter undistorted. Real and virtual photons are emitted over the full duration of the heavy ion collision. Latter are nearly directly decaying into lepton pairs l^+l^-. The decay of particles into lepton pairs is relatively rare ($\approx 10^{-4}$ for low mass-vector mesons) and consequently a very challenging measurement for particle detectors. Especially a very good particle reconstruction and a low material budged are needed.

The invariant mass spectrum of the lepton pairs is populated by different processes that are dominant in different stages of the whole collision process as shown in Figure 1.15. A detailed understanding of the composition of the dilepton spectra with a distinction between e.g. in-medium l^+l^--pairs and dilepton contributions from hadrons after the freeze-out is essential.

Dileptons are the prime observable for in-medium hadron modification observation as they couple directly to vector mesons (especially the ρ-meson as it decays in the medium). For low invariant masses ($M_{inv} \lesssim 1$ GeV) the spectrum is giving direct access to the ρ, ω and ϕ mesons.
The ρ meson is of special interest: As outlined in section 1.2 the spectral function of the ρ and the a_1 are expected to merge if chiral symmetry is restored. In addition the width of the ρ meson with $\Gamma = 149.1 \pm 0.8$ MeV is huge, compared to the ω and ϕ, due to

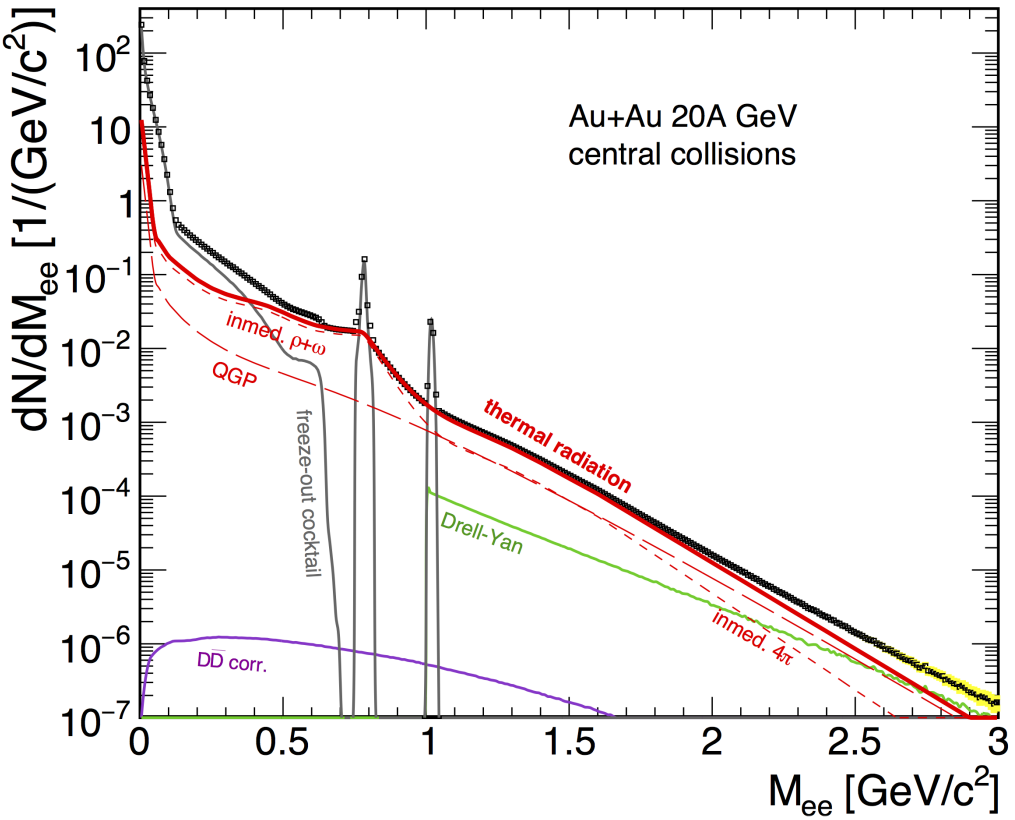

Figure 1.15: Invariant mass spectrum of e^+e^- pairs radiated from central Au+Au collisions at 20 AGeV. The diagram includes different sources of dileptons and its influence for different invariant mass regions [36].

the lifetime of 1.32 fm/c [1]. Compared with the size of the fireball it is quite probably that the ρ decays already in the QCD matter and hence is an ideal probe of in-medium modifications. The dilepton measurements give the possibility to measure the spectral function of the ρ with in-medium modifications and potentially showing a mass dropping or melting of the spectral function.

In the region of low invariant masses the spectra are dominated by N-N Bremsstrahlung and Dalitz-decays of Δ-resonances, π^0, ω and η. In combination with the influence of all stages of the fireball to the measured spectra, it is challenging to clean and interpret the spectra correctly. Nevertheless it is possible as external inputs are required to subtract these contributions.

The intermediate mass region of 1.0 GeV$\lesssim$ M$_{inv}$ $\lesssim$2.5 GeV is primarily populated by thermal radiation from quark annihilation as e.g. $q\bar{q} \rightarrow g\gamma$ and quark-gluon scattering $qg \rightarrow \gamma q$ in the quark gluon plasma, but also pion-pion scattering processes as $\pi\pi \rightarrow \rho \rightarrow \pi\pi$ where the ρ might also decay to l^+l^- [60, 61]. Figure 1.15 shows that the intermediate mass region is additionally populated by correlated pairs from open charm decays as well as Drell-Yan processes [61]. However these sources are neglectible for the CBM energies.

The very low open charm and Drell-Yan contribution for 20 AGeV Au+Au collisions as seen in Figure 1.15 allows a direct measurement of the fireball temperature by the

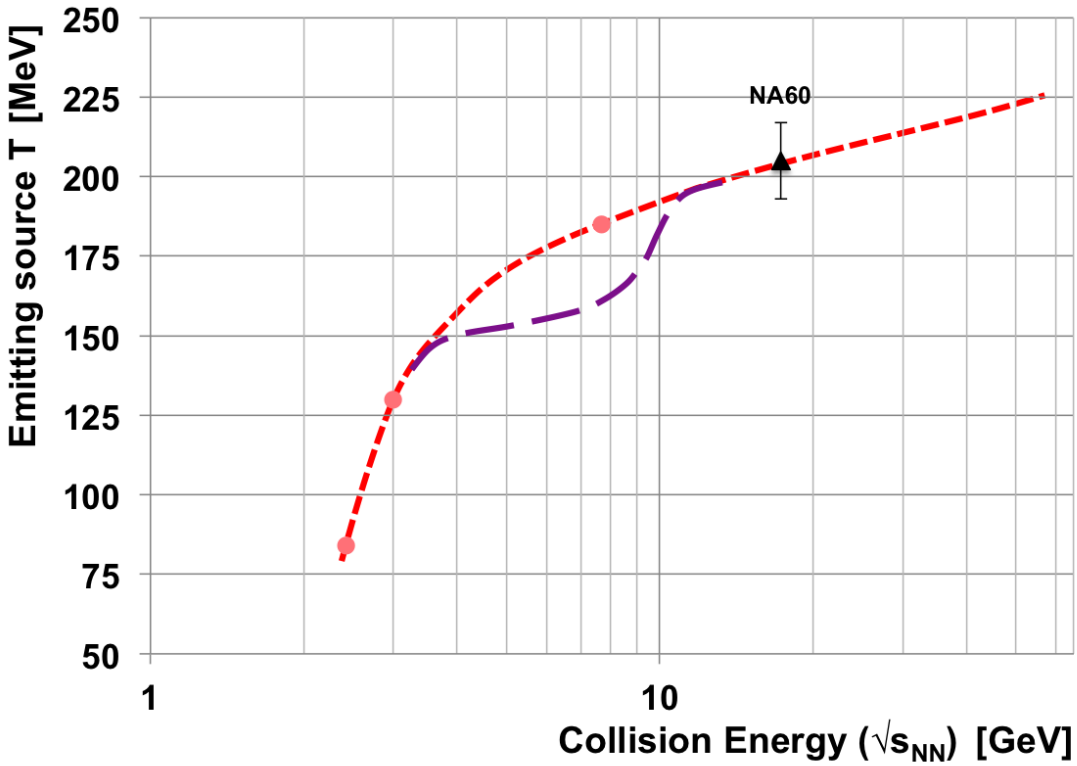

Figure 1.16: Excitation function of the fireball temperature T from intermediate dilepton mass distributions. The red dotted curve represents results calculated within the coarse-grain approach [59]. The dashed violet line represents a speculated shape for a phase transition in the SIS100 energy region [36].

extraction of the spectral slope from the transverse mass spectra. At SIS100 energies the contributions of charm and Drell-Yan are even less, leading to an even cleaner measurement [36].

This opens the possibility of a measurement of the caloric curve. The caloric curve, a measurement of the fireball temperature at different collision energies, would give access to a first order phase transition of the QGP. The first order phase transition would be indicated by a flattening of the caloric curve, as postulated in Figure 1.16.

The determination of the combinatorial and physical background of dileptons is of high importance and notoriously difficult. Due to the difficulty of these measurements it is important to have different and independent measurements. As the sources for background are different in the dielectron and the dimuon channel, it is an excellent cross check to have the possibility to perform the measurements in both channel in the same detector. This possibility is further useful for the understanding of systematic errors.

The Compressed Baryonic Matter (CBM) experiment at the upcoming SIS100 accelerator will be equipped with muon chambers (MuCh) as well as with a ring imaging Cherenkov detector (RICH) and Transition Radiation Detectors (TRD) for excellent muon respectively electron identification in combination with other sub detectors as described in Chapter 3.
The High Acceptance Di-Electron Spectrometer (HADES) experiment at SIS18 and later on at SIS100 is a dedicated detector setup for dielectron spectroscopy with excellent particle identification, a high acceptance and a very low material budget. A more detailed description to the detector setup and the upgrade of the RICH detector of HADES for an even better electron identification is given in Chapter 4 and Chapter 5.

The CBM and HADES experiment are both equipped with a RICH detector to perform high-quality dielectron measurements and improve the existing capabilities in dielectron reconstruction dramatically. The construction, commissioning and readout of the RICH detectors and its prototypes are of high importance to get a precise understanding of their behaviour itself as well as their measured data. Additionally the development of a dedicated but still very reliable and robust data readout as well as data acquisition is a key part in the full chain of steps towards a high-quality dielectron measurement. Finally all these efforts will lead to a better understanding of heavy ion physics and the matter created in heavy ion collisions. The achievement of all these single steps towards a well performing RICH detector and new measurements in physics are the motivation for the work presented in this thesis.

CHAPTER 2

Facility for Anti Proton and Ion Research

The **F**acility for **A**nti Proton and **I**on **R**esearch (FAIR) is a new accelerator facility next to the GSI Helmholtz Centre for Heavy Ion Research in Darmstadt/Germany that is currently under construction. FAIR is extending the existing GSI complex with the construction of a new accelerator ring SIS100 and new experimental facilities.
The acceleration of all types of ions as well as anti-protons with a high intensity is foreseen in the accelerator complex.

The center part of FAIR is the SIS100 ring accelerator with 1100 meters circumference. The synchrotron will be build with a maximum magnetic rigidity of 100 Tm in a dedicated tunnel. The 100 Tm rigidity magnets are fast pulsed superferric (superconducting) magnets with the ability to ramp with 4 T/s and reach peak fields of up to B=1.9 T in the dipole magnets as well as a maximum gradient of T=27 T/m in the quadrupole magnets [62].

The SIS100 will be fed by the already existing, but partially upgraded GSI accelerators UNILAC and SIS18. Adjacent of the SIS100 two storage-cooler rings, a target for

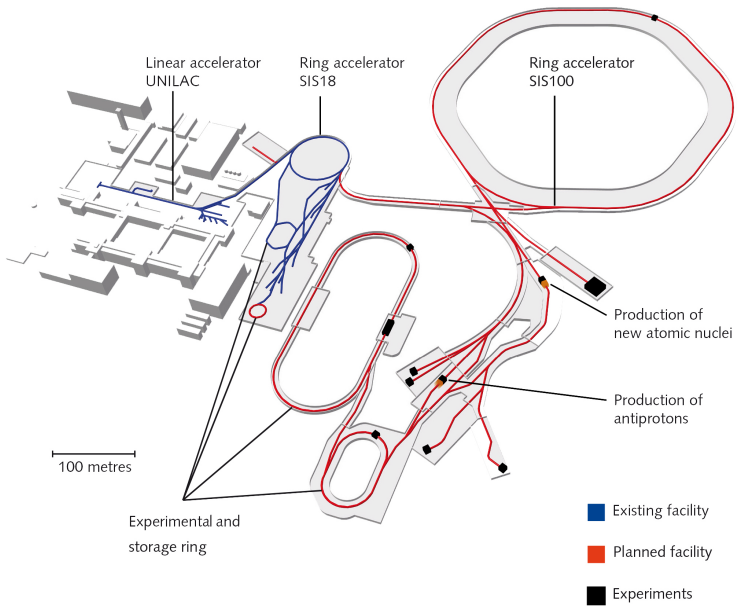

Figure 2.1: Schematic drawing of the FAIR and GSI complex with the existing buildings and facilities (blue) as well as the planned facilities (red) and experiments (black). Picture is taken from FAIR/GSI.

Figure 2.2: Artistic drawing of the planned FAIR accelerator facility with a colored schematic overlay of the 4 modules of the modularized start version of FAIR: **(green)** super conducting synchrotron SIS100 (module 1). **(red)** The experimental area of HADES and CBM (module 1). **(yellow)** NuSTAR facility including the Super-FRS (module 2). **(orange)** Anti-proton facility including PANDA (module 3). The experimental halls of APPA (module 1) are not shown in the overlay in this drawing. The artistic picture is from FAIR/GSI. The colored overlay is an adaption similar to Fig. 1 of [64].

anti-proton production as well as the superconducting nuclear fragment separator, and the experiments are located (see Figure 2.1 and Figure 2.2).

The use of SIS100 gives the opportunity to increase the possible energy and intensity range of the GSI experiments to new areas. For the exploration of baryonic matter this opens new possibilities as baryon densities and temperatures near the expected phase transitions can be achieved. Protons will be accelerated to 29 GeV, whereas e.g. gold ions are getting accelerated to 11 AGeV with a charge state of 79 [18, 62].
A key feature of the FAIR facility is the high interaction rate that can be achieved. Ion beams can reach an intensity of $\approx 10^{11}$ per second, whereas $\approx 10^{13}$ per cycle is expected for anti-protons [62, 63]. The high intensity beam opens the possibility to collect very high statistics and gives the chance to find even rare signals.

Prior to the expected start of the beam operation of FAIR in 2025, the so called FAIR phase 0 is taking place. FAIR phase 0 is an important project for a smooth start of the whole FAIR project and started already in 2018 with first beam operations of the upgraded SIS18 accelerator. In addition, the new CRYRING was operated for the first time at GSI. On the one hand FAIR phase 0 aims to get the full accelerator system with the upgraded accelerator controlling back to operation and undergo a full recommissioning of the upgraded SIS18. On the other hand it gives the young generation of physicists the opportunity to get trained and gain experiences for the future FAIR operation. In parallel further R&D for the full FAIR accelerator and detectors is ongoing. The test of the new control software and the test of detectors of future FAIR experiments is of high importance for a success of FAIR. The experiments R^3B or mCBM, with several prototype detectors, could participate in FAIR phase-0 operations and test the detectors. The mCBM experiment could test the full readout chain for the future operation of the state of the art CBM detectors to pave the path for a successful start of FAIR [65]. Next to research and development for the future, FAIR phase 0 already gives the opportunity to

investigate highly interesting physics project with highly important impact in different subjects of interest [66]. Experiments from the different FAIR pillars are carrying out measurements on their diverse physical topics by the use of all different available accelerator parts from UNILAC over SIS to the experimental storage ring (ESR) [67].

As part of the FAIR phase-0 program the HADES detector fulfilled in march 2019 a complete production beamtime campaign. The HADES experiment took data with an Ag+Ag beam at 1.58 AGeV for 28 days and a total amount of $\approx 15.27 \cdot 10^9$ events [68]. This was the first beamtime of HADES after the upgrade of the RICH detector to the multi-anode photo multiplier (MAPMT) based photo detection including a fully new readout. Additionally the newly installed electromagnet calorimeter (ECAL) was operated in a beamtime for the first time. The phase-0 program offers the HADES experiment the opportunity to investigate highly interesting physics prior to a fully commissioned FAIR facility with its SIS100 accelerator.

The FAIR project is divided into four sub modules that are not all available from the start of beam operation (see Figure 2.2). Module 0 is the SIS100 synchrotron, including the upgraded SIS100 and UNILAC for high intensity operation. The four physical pillars of FAIR are summarized in three more modules. The CBM pillar with the HADES and CBM experiment as well as the APPA pillar are part of module 1 of the FAIR project. The NuSTAR program is organised in module 2 and the anti-proton program of PANDA is part of module 3.

2.1 NuSTAR

The NuSTAR pillar of FAIR is hosting three main experimental subjects: **Nu**clear **ST**ructure, **A**strophysics and **R**eactions. NuSTAR is hosting many different, smaller experiments with the common aim to explore rare isotope beams. The heart of the pillar is the fragment separator Super-FRS. The Super-FRS will accept beams from the SIS18 but also from the SIS100 with up to 1.5 GeV/u at a luminosity of up to 5×10^{11} of $^{238}U^{28+}$ [69, 70]. It will spatially separate exotic nuclei up to relativistic energies and insert the very short lived nuclei into three different branches: A high energy, a low energy and a ring branch with a collector ring for the experimental setups.

Experiments as e.g. R^3B, LaSpec, HISPEC/DESPEC or ILIMA are performed at NuSTAR looking for the limits for the existence of nuclei, the structure of complex nuclei from the basic constituents, as well as collective phenomena [69, 70].

2.2 APPA

The APPA pillar of FAIR is an acronym for **A**tomic **P**hysics, **P**lasma and **A**pplied science. APPA is a collaboration with contributions from a broad variety of interdisciplinary research fields, similar to the NuSTAR group. This huge variety is also reflected in the physics program that is planned. It includes e.g. high-precision QED tests with bound-states in the non-pertubative region, or the exploration of dense plasma for theoretical models of planetary and stellar structures.
A very important physics case of APPA is the further investigation of radiotherapy with

high-energy ions. The development of heavy ion therapy to fight cancer has a long history at GSI and will be moved on to new frontiers with FAIR.

A highly interesting research field is opening in the investigation of matter under harsh conditions as high radiation. This is extremely important for the upcoming human space flight missions to the moon and mars or beyond in order to develop a good shielding of the cosmic radiation during the space flight.

Material science is looking for new insights by the influence of high-energy radiation to materials, new synthesis of materials as well as the creation of nanostructures [71, 72].

2.3 PANDA

The PANDA project at FAIR (Anti**P**roton **AN**nihilation in **DA**rmstadt) is investing $p\bar{p}$-annihilation with all its facets allowing spectroscopic studies of in particular also charmed hadrons with high statistics and precision.
An accelerated anti-proton beam with high intensity (and cooling) will be colliding with a fixed target of hydrogen or a nuclear target with energies from $\sqrt{s}$ = 2.2-5.5 GeV [73].
PANDA allows to study the formation or production of exotic charm states that are connected to the XYZ spectrum as well as investigations of glueballs or hybrids [73]. The charmonium spectroscopy will give new precision on the mass, width and also the decay branches of all investigated states. In addition the possibility of gamma-ray spectroscopy with high precision on single and double hypernuclei will give new informations about their structure and interactions [72].

2.4 CBM

The **C**ompressed **B**aryonic **M**atter pillar of the FAIR facility is formed by the well known HADES detector and the CBM detector. Both detectors aim to study the structure of dense baryonic matter at high baryonic chemical potential and moderate temperatures. The HADES experiment will move from its nowadays location at SIS18 to the CBM cave at SIS100 to a place in front of the CBM experiment. HADES is well suited for reference measurements with proton beams and moderate multiplicity heavy ion collisions as e.g. Ag+Ag with beam energies up to 4.5 AGeV. The CBM experiment will be able to cover also heavy systems with beam energies of up to 11 AGeV as well as proton beams of up to 29 GeV [36, 74]. The combination of both experiments provides excellent conditions to investigate dense baryonic matter.

The physics case of CBM and HADES with the search for a first order phase transition, studying the equation of state of dense baryonic matter as well as searching the critical endpoint, chiral symmetry restoration and possible exotic phases like quarkyonic matter (Chapter 1.4), offers a highly exciting discovery potential and will lead to a deeper understanding of dense baryonic matter [18, 36, 72].

In the following chapters a more detailed description of the detector concepts of CBM, HADES as well as the FAIR phase 0 experiment mCBM is given.

CHAPTER 3

Compressed Baryonic Matter Experiment

The **C**ompressed **B**aryonic **M**atter (CBM) experiment is a fixed target experiment, designed for heavy ion collisions to measure hadronic, leptonic and photonic observables with high interaction rates of up to 10 MHz and charged particle multiplicities of up to 1000 per Event [18].

The physics goal of CBM is the measurement of rare probes like low mass dilepton pairs, multi-strange hyperons, hypernuclei, charm and open charm if possible, but also correlations, fluctuations and collective flow. These probes shall allow to characterize the dense baryonic matter created in the heavy-ion collision. The setup gives the possibility to measure these probes with an unprecedented precision despite of low multiplicities as shown in Figure 3.2. SIS100 gives the chance to scan an energy region that is not well covered by experiments but is highly interesting for new discoveries and promising physics results [18].
Electron-positron pairs and hadrons in heavy-ion collision up to 4.5 AGeV beam energy will also be covered by the HADES detector. HADES will be moved from its nowadays measurement position at the SIS18 facility to a place in front of the CBM experiment (see Figure 3.1).

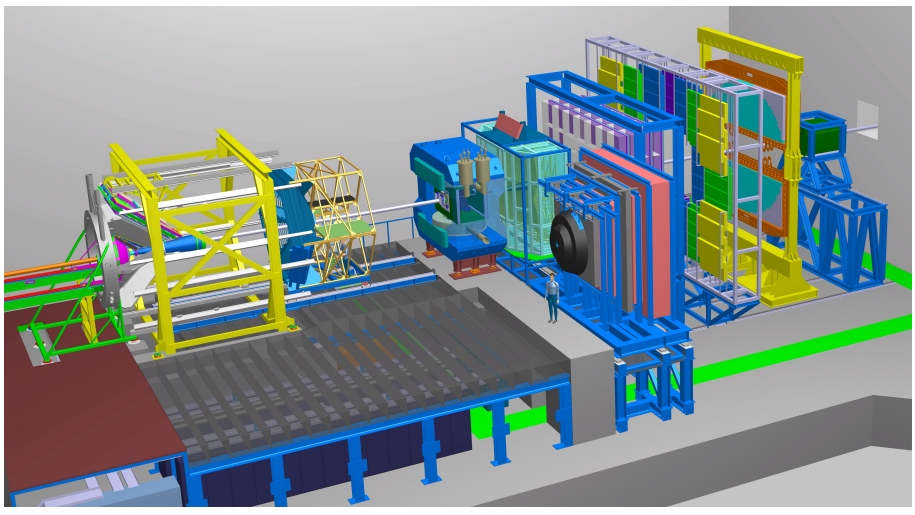

Figure 3.1: 3D model of the CBM cave with the HADES detector (left) and the CBM detector setup (right). The CBM detector is shown in the electron identification setup with the RICH detector in measurement position [75].

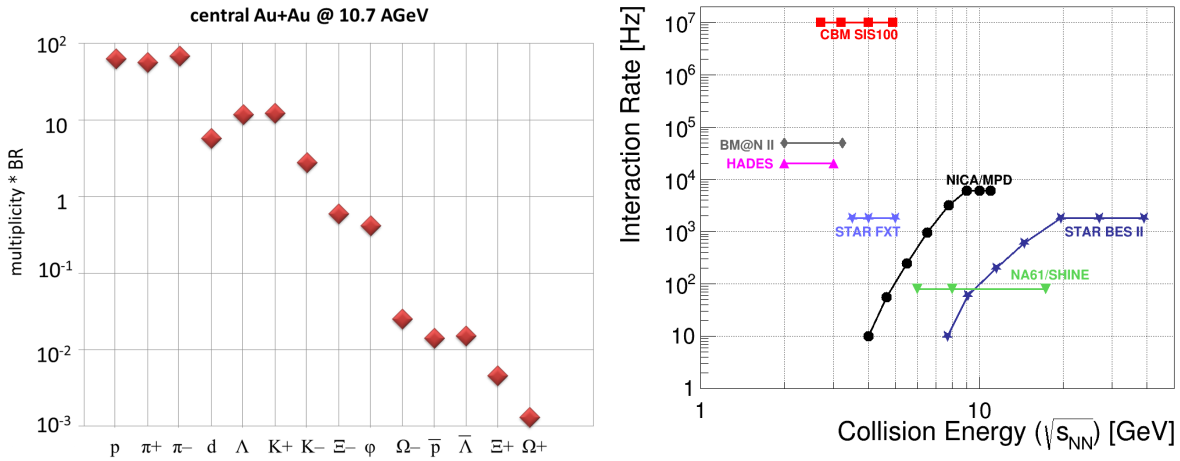

Figure 3.2: **(left)** Model predictions for yields (multiplicity times branching ratio) of probes intended to be measured by CBM at 10.7 AGeV calculated with a statistical model [76]. **(right)** Interaction rates and collision energies of different heavy ion collision experiments [36].

The CBM research program [18], that will be fulfilled e.g. by the probes discussed in Chapter 1.4, is focussing on:

- Search for the equation of state of QCD matter and the relevant degrees of freedom
- Search for a phase transition to a QGP, a coexisting region and an endpoint
- Hadron modification in dense baryonic matter
- Restoration of chiral symmetry
- Production of single and double hypernuclei
- charm production and in-medium properties

Extremely fast and radiation hard detectors are needed to cope with the aims of CBM and the connected high interaction rates (see Figure 3.2 for a comparison to other experiments). To provide an excellent hadron and lepton identification, a high resolution vertexing, high speed (online) trigger and a highly advanced data acquisition (DAQ) are needed. The CBM readout system is a key feature of the whole project and is designed to be free-streaming with an online event reconstruction on multi-core computing farms.

The CBM detector concept foresees the exchange of the RICH and MuCh detectors to optimise the setup for electron respectively muon identification. Therefore the RICH is movable by crane whereas the MuCh detector is located on rails due to its weight and for a reliable movement.

3.1 The CBM subdetectors

The CBM experiment is a combination of seven sub detectors and a superconducting dipole magnet in front of the system. The combination of tracking and particle identification (PID) detectors in a high interaction rate experiment and high radiation environment is quite challenging demanding for high-end detector solutions. In the following, the individual detectors of CBM will be presented in the order of appearance downstream from the target.

3.1.1 Superconducting Dipole Magnet

CBM uses a dipole magnet to bend particles in its field for momentum measurement. The magnet is superconducting with an integrated field of 1 Tm in $\pm$0.5 m around the center and a maximum field of $\approx$1 T. The magnet will have an opening angle of $\pm$25° vertical and $\pm$30° horizontal from the target at the beginning of the magnet. The inner of the magnet has a rectangular opening of 1.44$\times$3.00 m to give the STS and MVD detectors enough space to fit inside the magnet.
The magnet is equipped with a removable field-clamp to reduce the magnetic field for the RICH detector. For the MuCh setup, the field-clamp is removed.
The operation time of the magnet is designed for 20 years with an operation of 3 month per year and 100% duty-cycle [77, 78].

3.1.2 MVD

The reconstruction and tracking of e.g. dielectrons, hypernuclei or multistrange hyperons can be improved by a very good capability in track and vertex reconstruction. To distinguish between the primary vertex and a displaced vertex a detector close to the target is needed. This feature is critical for e.g. background reduction in the dilepton analysis where conversion photons and π^0-Dalitz decays can be reduced by high-resolution tracking close to the target [18].

The **M**icro **V**ertex **D**etector (MVD) is a small pixel detector made of four stations located 5-20 cm downstream inside the magnet. To cope with the high interaction rates, high radiation and to provide a small material budget of 0.3-0.5% X_0, CMOS Monolithic Active Pixel Sensors (MAPS) are used. To distinguish between vertices, a high resolution of the detector is needed. The MVD MAPS will fulfil a resolution below 5 µm. They are mounted on the four stations and can be operated with 100 kHz average collision rate in 4-10 AGeV Au+Au collisions or at 10 MHz in up to 28 GeV p-A collisions [79].

3.1.3 STS

The **S**ilicon **T**racking **S**ystem is located inside the CBM dipole magnet. The 8 stations of STS are used to track particles and determine their momentum by the bending in the 1 Tm dipole magnet. In central Au+Au collisions the typical track multiplicity is expected to be 700 in the STS apertures acceptance of 2.5°< Θ<25° [80].

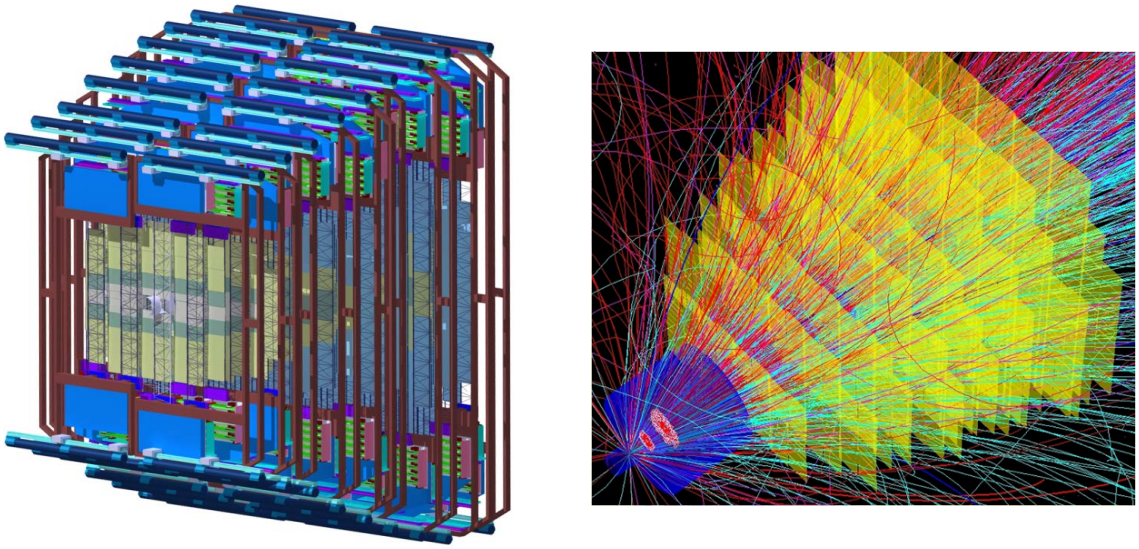

Figure 3.3: **(left)** Schematic view of the STS detector. **(right)** Tracks from a central 25 AGeV Au+Au collision overlaid with the GEANT simulation of the STS tracking stations [82].

The STS is based on silicon micro strip detectors. They are highly granulated and double sided with a thickness of 300 μm, summing up to around two million readout channels [81].

The STS is designed with a single hit resolution of 25 μm and a read-out strip pitch of 58 μm to reach the required momentum resolution of $\Delta p/p \approx 1\%$.

A hit rate of about 10 MHz per cm^2 is expected in the inner region of the STS whereas the rate is dropping by two orders of magnitude to the outer areas. To keep the strip occupancy constant at a few percent, different strip length are chosen.

The signals of the self triggering front-end electronics is used with a shaping time of 20 ns to avoid pile-up of events. For a high tracking efficiency, a very good signal to background ratio for detected hits is important. The track reconstruction efficiency is expected to exceed 95 % for particle momenta above 1 GeV [80, 81].

The position inside the magnet is highly exposed to radiation. Thus the radiation hardness is of high priority. The sensors are replaced if an integrated fluence exceeds 10^{13} 1 MeV neutron equivalence fluence per cm^2. To reduce the damage by induced leakage currents, the STS is operated at 500 V and has to be cooled to around -5°C [80, 81]. The read-out electronics is connected to the micro strips by the use of multi-line cables of ultra-thin aluminium-polyimide. The electronics is dissipating heat and thus a dedicated cooling concept is under development to achieve the aimed -5°C operating temperature [81].

3.1.4 RICH

The **R**ing **I**magine **CH**erenkov (RICH) detector is a key detector for electron identification and pion suppression in a momentum region of up to ≈8-10 GeV. The RICH detector will use CO_2 as radiator gas with an index of refraction of n = 1.00045 (T=0°C,p=1 atm).

The Cherenkov photons from the radiator are reflected and focused on a detector plane by two arrays of mirror tiles. The spherical mirror tiles are build from 6 mm thick glass and are coated with Al+MgF_2. Their radius of curvature is 3 m [83].

The detector planes are symmetrically installed above and below the CBM acceptance area. The photons are focused on Multi-Anode Photo Multiplier Tubes (MAPMTs) which are arranged in an array of 14×7 PMT backplanes per detector plane, one backplane carrying 2×3 MAPMTs. The photo-detection plane with the mounted read-out electronics is positioned such that the influence of the magnetic field of the dipole magnetic is minimized. This is achieved by the additionally mounted field-clamps at the magnet and a shielding box to reduce residual magnetic-field around the detection planes [83, 84].

This thesis will concentrate on the development of the mCBM, CBM and HADES RICH detector and its read-out electronics. More details on the different RICH detectors of HADES and mCBM will be given in Chapter 5 respectively Chapter 6. A precise description of the CBM RICH detector will be found in section 3.3.

3.1.5 MUCH

The **Mu**on **Ch**ambers of the CBM experiment will be exchanged with the RICH and are needed to identify even the low momentum muons from low-mass vector meson decays within the high particle density. The muon chamber is build in a sliced structure where the absorber is sliced in layers with readout chambers in-between. The thickness of the absorber slices, its material, as well as the number of slices, is optimized to the CBM energy range. An absorber of 2.5 m of iron will be passed by muons from J/ψ meson decays nearly without further suppression, whereas e.g. muons from ω mesons are suppressed by a factor of 10. [85].

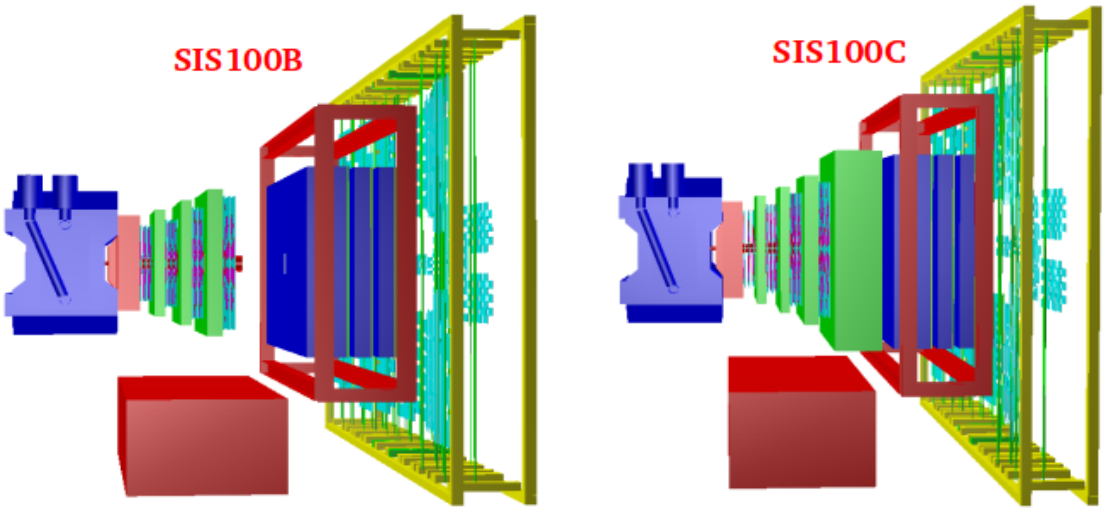

Figure 3.4: **(left)** MUCH geometry with 4 stations and 4 absorbers. **(right)** MUCH geometry with 5 stations and 5 absorbers [86].

The CBM MuCh will be build from up to five detector stations. Each station is made of three layers, making the detector flexible for changes in the detector technology. The first two detector layers will be equipped by Gas Electron Multipliers (GEMs). The GEMs are build as triangular shaped sectors with a length of 80 cm respectively 97 cm and stacked circular around the beam pipe. The third and further stations downstream are planed to be equipped with straw tubes. Newer studies investigating a change to resistive plate chamber technology (RPCs) had been done and results are still under discussion [85, 87].

The first absorption layer is made from carbon with lead inserts, whereas the following absorbers are made from iron with increasing thicknesses. The whole detector will cover an acceptance of $\pm 5.6^{\circ}$ to $\pm 25^{\circ}$, limited by the magnet and beampipe dimensions. Different geometries with 4 stations and 4 absorbers (SIS100B) as well as 5 stations and 5 absorbers (SIS100C), with the TRD as the fifth station are foreseen for different CBM setups (see Figure 3.4) [86].

3.1.6 TRD

For additional electron identification starting from p>(1.5-2) GeV, a **T**ransition **R**adiaton **D**etector (TRD) is used. The improvement in pion rejection helps on the one hand in the low mass vector meson measurements, on the other hand it is essential for the intermediate mass region beyond 1 GeV where thermal radiation from the fireball is accessible. In addition to electron identification the TRD is also used for the identification of light nuclei by the measurement of their specific energy loss. The high space point resolution gives the TRD also tracking capabilities. It is used as a bridge in track finding between STS and TOF and can also be used as a muon tracking station in the MuCh setup [88].

The TRD will be build with 4 detection layers resulting in 216 modules (see Figure 3.5). The whole active area of the detector will measure 113.4 m^2 with a 30 cm thick

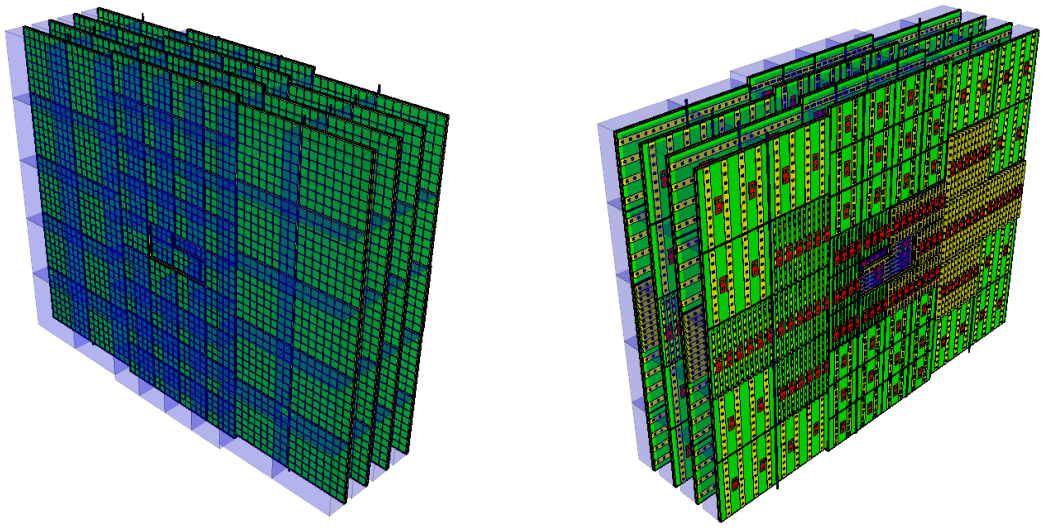

Figure 3.5: **(left)** Front side of the TRD detector with the radiator boxes. **(right)** Back side of the TRD detector with backplanes and the front-end electronics [88].

radiator between each layer.

Four readout pad sizes between 1.2 cm^2 and 8 cm^2 will be used in the TRD to keep the occupancy constant over area and keep the material budget as well as the number of channels at an acceptable amount. Each pad will have a resolution across the pad of $\approx$ 300 µm and 3-30 mm along the pad. Each second layer of the TRD is rotated by 90°. Simulations of Au+Au collisions at 10 AGeV predict a hit rate per read-out pad of around 50 kHz with small localised areas reaching 120 kHz.

The TRD is build as a composition of a radiator material and a Multi-Wire Proportional Chamber (MWPC). Electrons passing the radiator are producing transition radiation (TR) photons with a certain probability, whereas the slower pions are traversing without photons produced. The default radiator material is chosen as a stack of 2 mm thick PolyEthylene foam foils. The TR photons from the radiator are absorbed in the beginning of the readout chamber in a 85% Xenon and 15% CO_2 counting-gas mixture. The TRD is collecting the charge information of the TR as well as the specific energy loss $\langle dE/dX \rangle$. This improves the pion-suppression furthermore.

3.1.7 TOF

The **T**ime-**O**f-**F**light detector is an additional detector for hadron identification. It will be used in all CBM setups in all energy ranges and collision types. The time of flight detector is measuring interactions of the traversing particle with different layers (stacks) of the detector system in different spatial positions. Based on this interaction points, and further informations from STS or even TRD, a tracking of the particles along the CBM detector is performed and the velocity β of the particle is calculated (based on the position and time informations of the detector layers) [82].

$$m^2 = p^2 \cdot \left(\frac{1}{\beta^2} - 1 \right) \tag{3.1}$$

Using the extracted momentum information p from the STS setup in the magnetic field of the dipole magnet, the mass of the particle can be derived by equation 3.1.

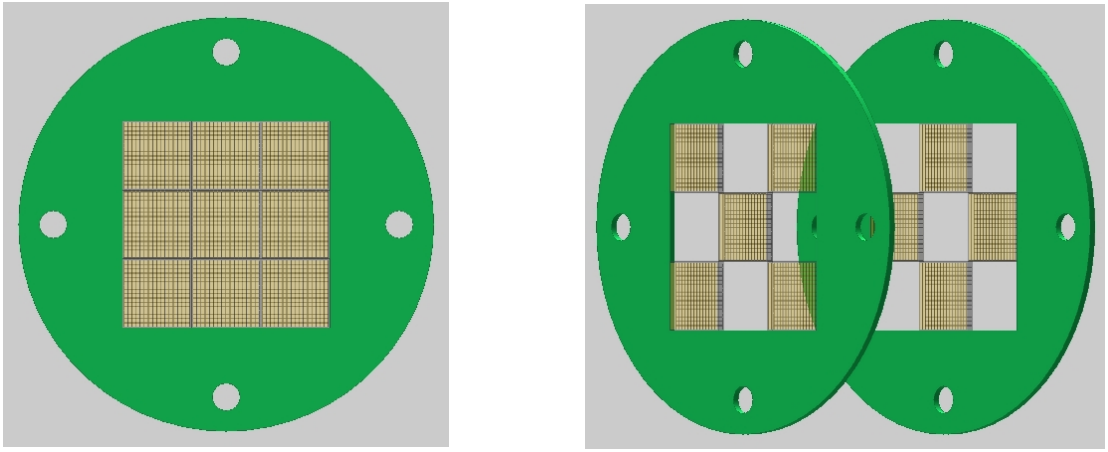

Figure 3.6: **(left)** The start detector with nine scCVD diamond plates and 16 electrode strips on each side vertically and horizontally. **(right)** The nine plates are located on two different PCBs stacked behind each other [82].

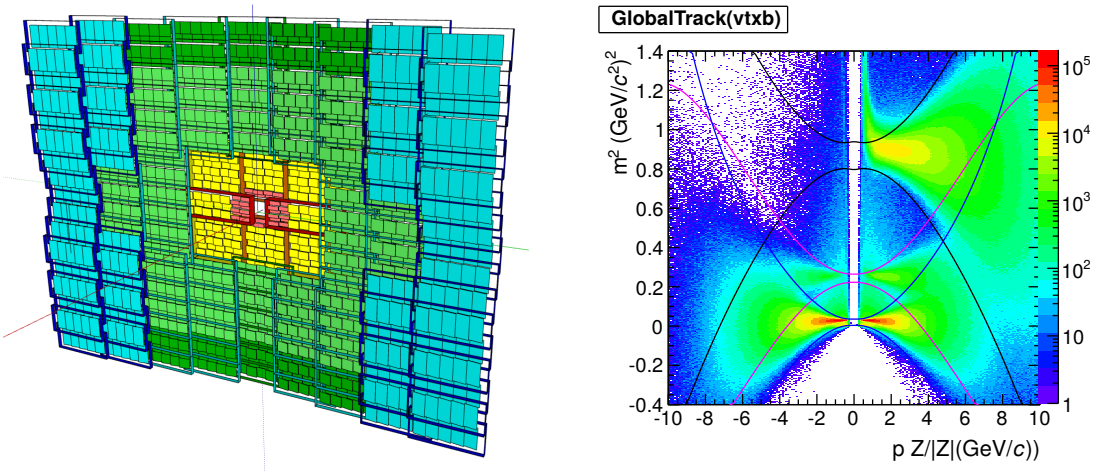

Figure 3.7: **(left)** Schematic view of the TOF Wall with the different module types colored. **(right)** Correlation of the mass squared and the momentum from STS measurements in simulation of 10 AGeV Au+Au collisions [82].

To separate kaons from pions and protons the TOF detector requires a time resolution of better than 80 ps in total and a time resolution per channel of 60 ps with a detector efficiency of at least 95%. To achieve this, the Multi-Gap Resistive-Plate Chambers (MRPC) technology is chosen. In addition a T_0 reference detector is necessary to determine the time of flight. The T_0 is planed to be a high rate start detector (SD). For the heavy ion setup a large area pcCVD diamond plate and metallic electrode strip layers on both sides will be used, whereas scCVD plates will be put together like a mosaic for proton and light ion beams (see Figure 3.6). In addition to the start time, the start detector is a very important tool for online monitoring and beam profile investigations [82].

The time of flight wall (TOF detector) will cover the same acceptance of 2.5°< Θ<25° as all CBM detectors. At a location between 6 m and 10 m downstream from the target, this results in an acceptance area of about 120 m^2. To cover this area effectively, six different modules with five different types of MRPCs are used. The modules are differing in size, number of cells and number of MRPCs. The MRPCs itself are all build with different active areas, granularity, glass thickness and type of glass (for a full list see [82]). All 226 modules respectively 1376 MRPCs are later on arranged with a slight overlap to have a full coverage of the acceptance (see Figure 3.7).

The development of a low resistivity glass gives the possibility to achieve fluxes in MRPC1 to MRPC3a of 1 kHz/cm^2 to 25 kHz/cm^2. The outer MRPCs MRPC3b and MRPC4 are equipped with float glass as they are exposed to fluxes of about 1 kHz/cm^2 only. The modules are flushed with a gas mixture of 85% CH_2FCF_3, 5% C_4H_{10} and 10% SF_6.

3.1.8 ECAL

The CBM **E**lectromagnetic **CAL**orimeter is one of two calorimeters in CBM and planed to be a "shashlik" type calorimeter. It will be used for the identification of (direct) photons and the identification of electrons by a measurement of the energy deposition and spatial position. In addition to the measurement of electromagnetic decay products of

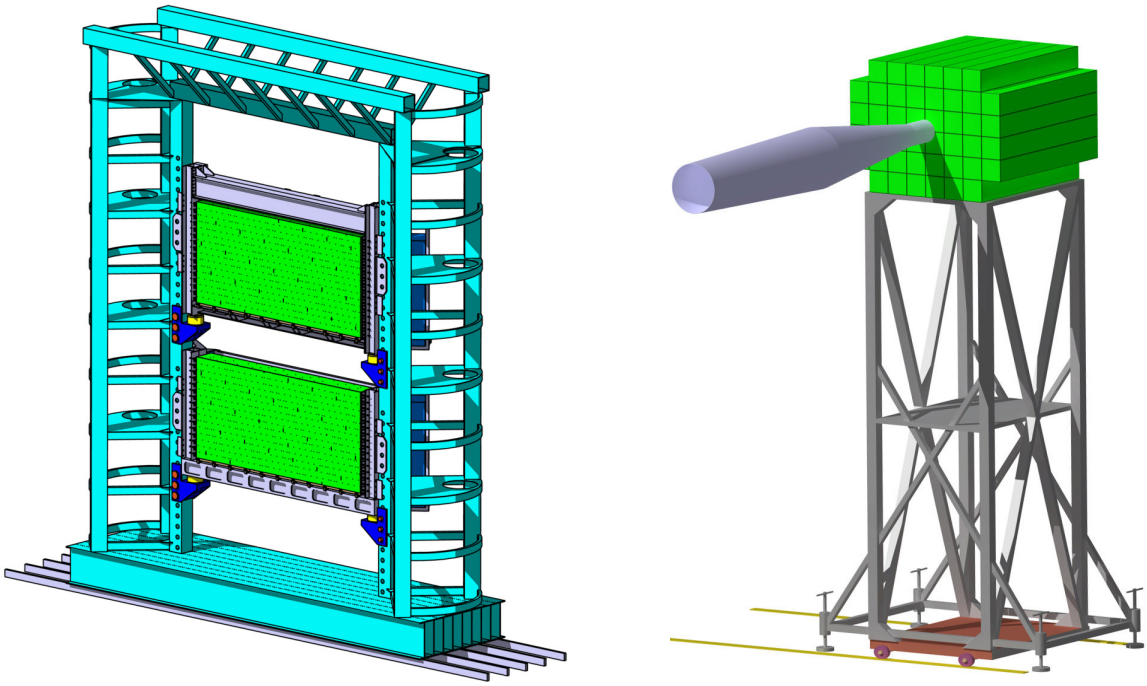

Figure 3.8: **(left)** Schematic view of the ECAL detector with two movable sensitive areas [89]. **(right)** Schematic view of the PSD detector on its mounting structure [90].

hadrons the two photon decay of glueballs in the dense and gluon-rich medium could be measured [89].

The detector itself will be made from lead absorber plates and scintillator tiles, giving the name "shashlik" calorimeter. The 2 mm thick scintillator plates and 1.5 mm thick lead stacks are attached to wavelength shifting fibers, penetrating the stack. Optimised light collectors and the large amount of photons allows to finally connect to conventional photomultipliers and their readout electronics.

The calorimeter is planed as a setup of two rectangular blocks, one below and one above the beamline. Each of the blocks is adjustable to optimise the system for specific measurements (see Figure 3.8, left). The whole ECAL will have 4352 electronic channels in 1088 modules, where each module has cells of the size of 60×60 mm^2 [89].

3.1.9 PSD

The **P**rojectile **S**pectator **D**etector (PSD) is installed for the experimental measurement of the centrality of the collisions as well as for the orientation of the event plane. As introduced in Chapter 1.3, the PSD detector is of special interest for event-by-event measurements as it is needed e.g. in fluctuation measurements in the search for the critical endpoint [90].

The event-plane of a collision is reflected in the position of its spectators which are detected by the PSD far downstream at the end of the CBM detector setup. A good energy resolution in combination with a good position measurement by a modular structure with fine azimuthal segmentation is required. The PSD will be able to operate in a beam energy region from 2-35 AGeV and beam intensities of up to 10^9 Au ions

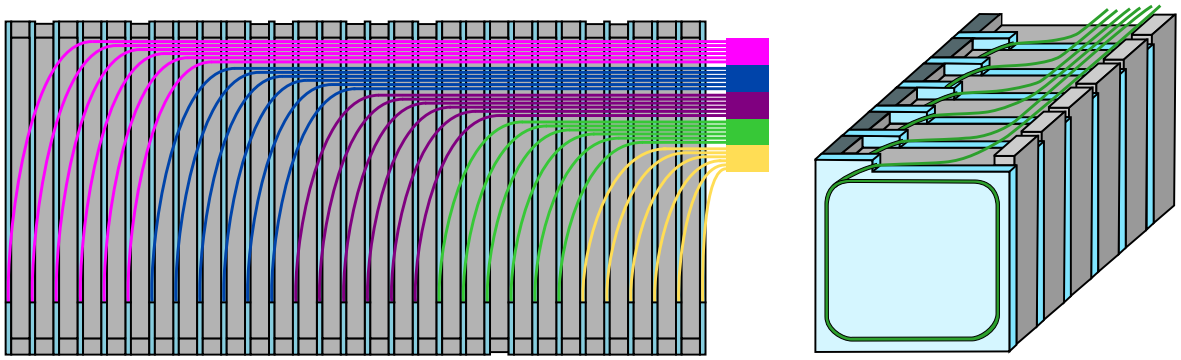

Figure 3.9: **(left)** Stacked PSD module and scintillation tiles with fibers, combined to six per readout sensor. **(right)** Angled view on the PSD module with a scintillator tile in front [90].

per second. The reaction plane is determined with an accuracy of better than 40° and the centrality with an accuracy better than 10%. This is achieved with a transverse area of 1.5×1.5 m^2, a transverse granularity of 20×20 cm^2 and an energy resolution of $\sigma_E/E < 60\%/\sqrt{E(GeV)}$. A schematic drawing of the PSD detector is shown on the right side of Figure 3.8.

Each module of the PSD calorimeter is build in a sandwich like design as the ECAL is proposed. A module is build from 60 lead-scintillator tiles with 16 mm respectively 4 mm thickness. The light from a scintillator tile is readout with wavelength shifting (WLS) fibers, guaranteeing a high efficiency and uniform light collection. A single photodetector is seeing the light from six consecutive fibers that are combined [90]. The inner structure of a single module is shown in Figure 3.9.

The scintillator plates are build from polystyrene based scintillator material. The WLS fiber is glued in a groove on the surface of the scintillator. The readout electronic has to be selected such that 10 photodetectors are fitting in the 20×20 cm^2 back side of a module. This is fulfilled by micropixel avalanche photodiodes [90].

3.2 The CBM Data Acquisition

The **D**ata **Ac**Q**uisition (DAQ) of the CBM detector, as well as for mCBM as a test-bench, is a very challenging project as the data is produced free-streaming in each sub detector. Classically, data readout is triggered by a central triggering system for all sub detectors. In the case of CBM, each detector is self-triggering and has to be precisely synchronized with the other detectors.

Collision rates of 10 MHz are leading to a data rate from the detectors of approximately 1 TB/s. The archiving resources are not able to handle this high rates and thus a compression of the data is necessary. An online event selection will be used to get rid of non-interesting interactions and end up with a data rate that can be written to tape [91].

Each detector setup of CBM is designed with a very fast readout-out concept and in most cases radiation hard front-end ASICS. The CBM RICH detector readout is completely based on field programmable gate arrays (FPGAs) that are located outside the acceptance and inside the shielding box resulting in a less radiation hard environment

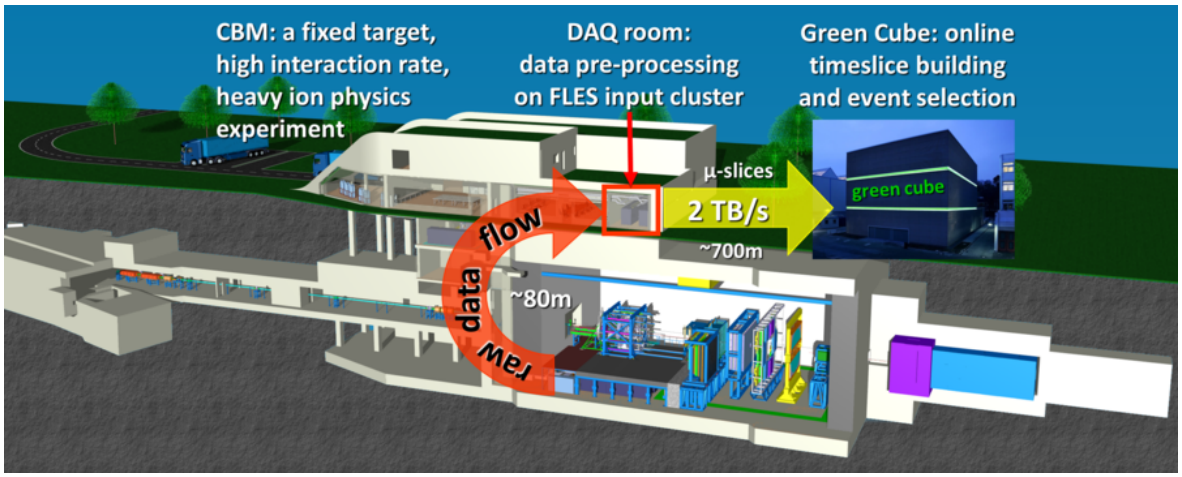

Figure 3.10: Drawing of the CBM building. Raw data from the detectors is transported by optical fibers to the CRI in the DAQ room. Further on, microtimeslices are transmitted via InfiniBand to the green IT Cube for timeslice building [92].

in comparison to FEE ASICS of other CBM subdetectors. The front-end electronics is marking each hit with a timestamp and sends these data information to higher level data aggregation units. Many detectors are using the CERN GBTx-based radiation hard aggregation units [91]. The RICH is combining the informations from its FEE on a dedicated combiner board with an included hub functionality and further advanced features, that will be described in detail in Chapter 7.

Data from the detectors itself will be transported via optical fibers to the DAQ room of the CBM building (see Figure 3.10). The CBM DAQ room is hosting a farm of several ASUS ESC8000 G3 servers. They will be equipped with up to four **C**ommon **R**eadout **I**nterface (CRI) boards and one InfiniBand connection per server. The CRI is chosen to be the FLX-712 (respectively BNL-712) card with a Xilinx Kintex UltraScale XCKU115

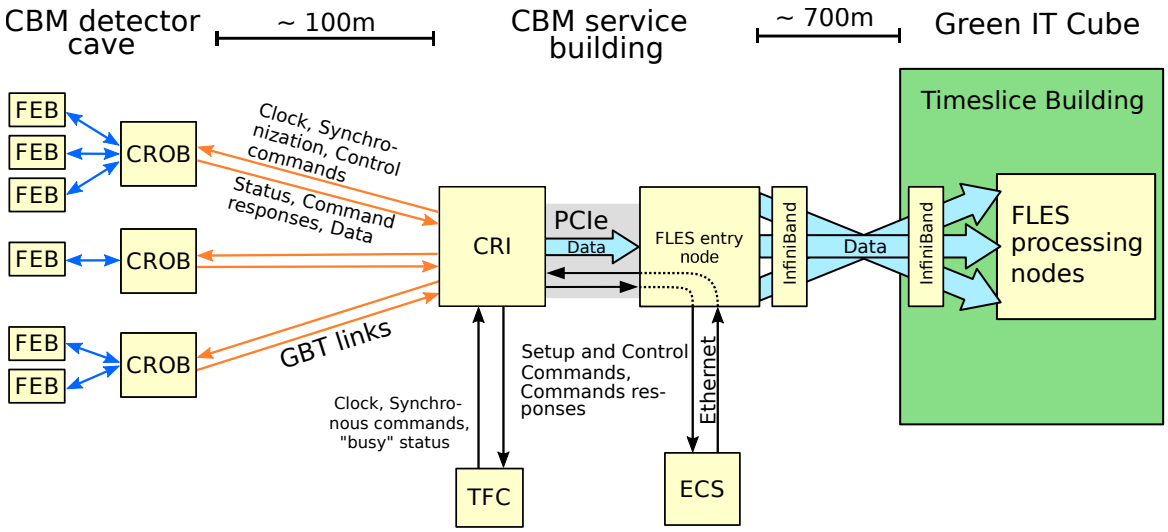

Figure 3.11: Proposed readout chain of mCBM phase II and most probably for CBM. The individual stages are shown with all their types of data connection as well as transmitted informations. The figure is adapted from [93] and [94].

63 55	47 39	31 23	15 7	0
hdr_id	hdr_ver	eq_id	flags	sys_id	sys_ver
idx				
crc		size		
offset				

Table 3.1: The bitwise structure of a microtimeslice descriptor. Adapted from [97].

FPGA, PCIe Gen3 x16 connection, jitter cleaner and 48 bidirectional optical links with up to 14 Gb/s [95, 96], or an update of this card.

The CRI is receiving the data streams from the connected **C**ommon **R**ead**O**ut **B**oards (CROBs) and processes this data. Data sorting, feature extraction as well as the building of microtimeslices can or will be be done on the CRI to prepare the data for further processing and unpacking. The CRI provides a high speed PCI express connection to the First-Level Event Selector (FLES) entry node (Server hosting up to 4 CRIs) [93, 94].

This PCIe connection is used for the data transport, but also as connection to a wishbone interface for slow control on the CRI and its connected CROBs. The FLES entry node itself is equipped with an InfiniBand interface. A single mode fiber is used to transmit the data via long-range InfiniBand to the GSI Green IT Cube with a bandwidth of 2 TB/s. The servers and switches of the Green IT cube are receiving the microtimeslices that are transmitted from the DAQ room by the FLES entry nodes and combines these to so called timeslices. A microtimeslice is a small slice in the time, defined by the control software. For tests in the mCBM setup e.g. a microtimeslice length of 102.4 µs respectively 1.28 ms was used. In the same mCBM setup, 10 microtimeslices were combined to one timeslice. The data in timeslices on the processing

name	size	example	description
hdr_id	8	0xDD	Descriptor format identifier. Fixed to 0xDD.
hdr_ver	8	0x01	Descriptor format version. Set to 0x01 for this version.
eq_id	16	0x1234	Equipment identifier. Specifies the FLES input link.
flags	16	0x0000	Status and error flags. See Tab. 3 for more details.
sys_id	8	0x00	Subsystem identifier. Specifier of the CBM subsystem that has generated this microslice.
sys_ver	8	0x01	Subsystem format version. This specifies the format of the microslice data content.
idx	64	0x0000000123456789	Start time of the microslice in ns since global time zero.
crc	32	0x12ACBDEF	CRC32-C checksum of the data content.
size	32	0x00000000	Content size. This is the size (in bytes) of the microslice data content.
offset	64	0x0000000000000000	Offset in data buffer.

Table 3.2: Short explanation of the acronyms from Table 3.1 [97].

nodes is ready for further online unpacking, event building, reconstruction and finally storage to the filesystem.

The microtimeslice is the basic structure of the CBM DAQ. Each data processing board (DPB) in mCBM phase-I, respectively CRI board in mCBM phase-II and in the final CBM DAQ, is creating slots in time. The data produced in this timeslot is labeled as a microtimeslice and put into a microtimeslice-container. A microtimeslice itself has to be self-contained: All informations that are needed for the event-reconstruction of the corresponding detector have to be found in the microtimeslice [97]. The microtimeslices in the unpacking stage consist of a 32-byte descriptor, defining the content of it, and the experimental data. Table 3.1 shows the bitwise representation of the 32-byte and its content, that is explained in Table 3.2.

The microtimeslice with an index s (may) contain the experimental data of a defined time interval

$$t \in [s - dt_0, (s + T) + dt_1] \tag{3.2}$$

with the global microtimeslice length T and the allowed time uncertainty dt_0 and dt_1 (e.g. 5 ns).

For the identification of a subsystem the 8-bit sys_id is used. Table 3.3 presents the identification numbers of the individual systems of the CBM detector. All detectors have to be operated synchronous to achieve the necessary alignment in time for the building of self-contained microtimeslices.
The synchronous operation of all systems is guaranteed by the implementation of the **T**iming and **F**ast **C**ontrol (TFC) system that distributes a global CBM clock to all subsystems. The TFC system is developed by the KIT and will be build up from a master FPGA, sub-masters and slaves. The TFC-master is generating a global time reference and the master clock of the full CBM system. The master propagates these informations via optical fibres through the TFC network to the slaves. In terms of the CBM DAQ the CRI will behave as the slave and receive the global reference time and the clock. The CRI will run on this clock synchronous to all other systems and knows the global time from the reference time distribution. The CRI has to synchronize the lower readout modules [98].

Subsystem	sys_id
Silicon Tracking System (STS)	0x10
Micro-Vertex Detector (MVD)	0x20
Ring Imaging CHerenkov detector (RICH)	0x30
Transition Radiation Detector (TRD)	0x40
Muon Chamber system (MuCh)	0x50
Resistive Plate Chambers (RPC)	0x60
Electromagnetic CALorimeter (ECAL)	0x70
Projectile Spectator Detector (PSD)	0x80

Table 3.3: Subdetector identification in the FLESnet environment [97].

3.3 The CBM RICH Detector

The **R**ing **I**maging **CH**erenkov (RICH) detector is a well known detector type based on the principle of Cherenkov radiation. Many different types of Cherenkov detectors for different experimental purposes are on the market and under development. Cherenkov detectors are very well suited for the identification of particles.

3.3.1 Theory of Cherenkov Radiation

The discovery of the Cherenkov effect, the basis of all Cherenkov type detectors, was published by Pavel Alekseyevich Cherenkov in 1937 [99]. P.A. Cherenkov discovered the emission of light by particles while travelling through a medium with a speed, higher than the in medium speed of light.

A charged particle moving through a medium is locally polarising the medium. If the particle is slow compared to the in medium speed of light, the polarisation is symmetric around the particle and in a global view no polarisation is visible. If the particle is faster than the in medium speed of light, it is still polarising the medium, but the polarisation is now asymmetric. The local polarisations are not shielding each other on the global scale and electromagnetic waves are radiated along the polarisation (see Figure 3.12).

The radiated waves from the moving particle are spreading in a time ΔT. This is the time between the first position P_0 and P_7 in Figure 3.12, right picture. In this time the particle moves a distance of $\beta \cdot c \cdot \Delta T$ and the electromagnetic wave a distance $c/n \cdot \Delta T$. The constructive superposition of the elemental waves is resulting in a wave front, that defines the Cherenkov polar emission angle θ_C under which photons are radiated [100, 101].

$$cos(\theta_C) = \frac{\frac{c}{n} \cdot \Delta T}{\beta \cdot c \cdot \Delta T} = \frac{1}{\beta \cdot n} \tag{3.3}$$

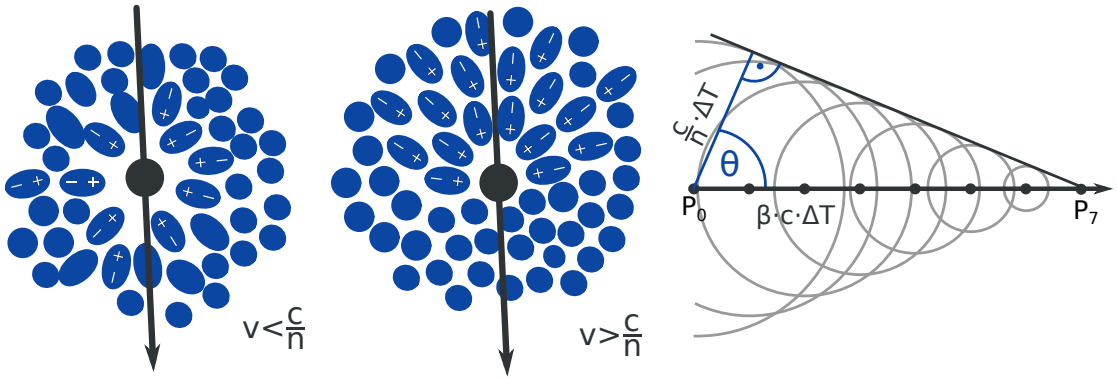

Figure 3.12: Schematic drawing of the Cherenkov effect. A particle is moving with the velocity v through a medium with an index of refraction n and the vacuum speed of light c. **(left)** If the velocity is below the in medium speed of light, the medium gets locally polarised. A global effect is not observed as the polarisation is symmetric and shielding itself. **(middle)** If the particle is faster than the in medium speed of light, the polarisation is asymmetric and the source of radiation. **(right)** The front of coherent waves from the particle is defining the Cherenkov angle θ.

Equation 3.3 is an (rather good) approximation that neglects the recoil by the photo emission [101]. The equation is valid for the conditions of a charged particle travelling through an optical transparent medium faster than the in medium speed of light. In addition the radiator medium has to be much longer than the wavelength of the Cherenkov radiation $\lambda \ll L$.

The emitted electromagnetic radiation is transversally and linearly polarised. Furthermore the equation shows, that only a certain angle and β range is possible. A particle has to overcome a threshold velocity β_{thr} to radiate Cherenkov photons [101].

$$\beta_{thr} = \frac{1}{n} \tag{3.4}$$

This threshold is not exactly constant as the index of refraction n is energy dependent (dispersion). In addition, a particle's velocity is limited by the speed of light. This defines a maximum angle

$$cos(\Theta_{max}) = \frac{1}{n} \tag{3.5}$$

The radiated photons are forming a cone where the opening angle θ_c depends on the velocity of the particles. This cone has the maximum opening angle θ_{max} for $\beta \approx 1$. The Cherenkov angle is thus depending on the energy of the particle. The threshold energy is defined by

$$\frac{E_{thr}}{mc} = \gamma_{thr} = \frac{n}{\sqrt{n^2 - 1}} = \frac{1}{sin\theta_{max}} \tag{3.6}$$

using equation 3.3 [101]. With all this equations it is getting obvious that the Cherenkov angle or the radius of the resulting cone/ring is giving an information about the particle species, if the momentum is known.

Frank and Tamm did successfully find a theoretical description of the Cherenkov effect, resulting in the Frank-Tamm relation

$$\frac{dN_{ph}}{dE} = \left(\frac{\alpha}{\hbar c}\right) Z^2 L sin^2\theta = \left(\frac{\alpha}{\hbar c}\right) Z^2 L \left[1 - (\frac{1}{n\beta})^2\right] \tag{3.7}$$

with the fine structure constant α, the charge of the particle Ze and the path length L in the medium [100]. The Frank-Tamm relation gives the number of produced photons in an energy region from E to $E + dE$. The integration of equation 3.7 is not straight forward as the dispersion of the optical medium $n(E)$ has to be taken into account. This dependency is resulting in an increase of photons in the UV spectrum.

Integration of equation 3.7 with the assumption of a constant index of fraction, yields the following relation for the number of photons

$$N_{ph} = N_0 Z^2 L sin^2\theta \tag{3.8}$$

N_0 is the detector response parameter [100]. The detection of photons includes several efficiency losses as e.g. mirror reflectivity R, quantum efficiency Q of the detector or transmission T of the medium for a imaging detector including a mirror. These effects are summarized in N_0 with

$$\begin{aligned} N_0 &= \left(\frac{\alpha}{\hbar c}\right) \epsilon \Delta E \\ \epsilon \Delta E &= \int (QTR)\, dE \end{aligned} \tag{3.9}$$

with ϵ as the energy average detector efficiency loss in the energy range of ΔE [100].

3.3.2 Cherenkov Detectors

The formation of cones by the Cherenkov photons is used in the concept of Cherenkov detectors. Different types of Cherenkov detectors were build over the last decades. In the following the most important designs for this thesis are presented:

Cherenkov detectors are separated into two types of detectors. The first and most simple type is the threshold Cherenkov detector. No spatial resolution is needed for such detectors, thus it is relatively easy to produce such a detector. Special radiators are selected such that only particles with $\beta > \frac{1}{n}$ produce Cherenkov photons. In case more than one of these detectors with different radiator materials are combined in a row, even the identification of particles is possible (see Figure 3.13).

The threshold momentum of a particle is defined by the mass and the index of refraction [101]

$$P_{thr} = mc^2 \left(\beta\gamma\right)_{thr} = \frac{mc^2}{\sqrt{n^2 - 1}} \tag{3.10}$$

As equation 3.10 shows, only particles with a specific mass are producing photons in a radiator when overcoming the threshold momentum. In combination of a momentum measurement and different index of refraction, the type of a particle can be determined. This principle is sketched in Figure 3.13 where three sub detectors with different radiators are shown. The photons produced by the Cherenkov effect are radiated in the radiator medium. Diffuse reflection by the walls may allow them to be detected by a photon detector (here a Photo Multiplier Tube (PMT)).

The second type of Cherenkov detectors that is introduced here is a ring imaging Cherenkov detector (RICH). In contrast to the threshold detectors, the RICH detectors are using the additional information of the Cherenkov angle of the emitted photons

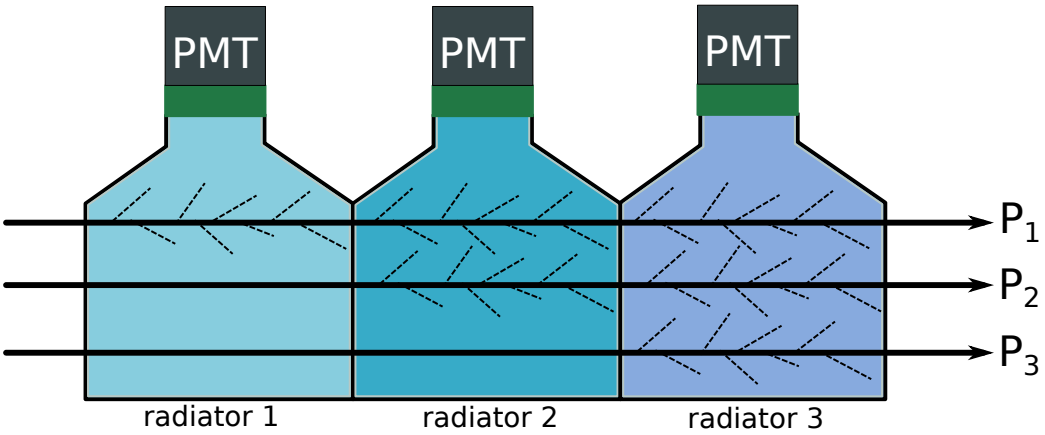

Figure 3.13: Schematic drawing of a threshold Cherenkov detector. Three particles with the same momentum, but $m_1 < m_2 < m_3$, are traversing three sub detectors with different radiators ($n_1 < n_2 < n_3$). Particle 1 has such a mass, that it is above the threshold in all detectors. Particle 2 is as heavy, that it is not creating photons in the first radiator, but in the following. The last particle is producing photons only in the last detector. The combination of these informations gives the possibility to identify the particle species.

to identify different particles. The photons are forced to form a ring by the usage of a defined but rather short radiator length (proximity focussing) or by the use of special optical focussing mechanisms as spherical mirrors. The use of a mirror is on the one hand very helpful as the photons and the photon detectors can be moved out of the acceptance of the beam. Additionally the photons are focussed to sharp rings, in contrast to the proximity focussing RICH with relatively wide rings. On the other hand it is introducing more uncertainties as the mirror is not perfectly spherical and the reflection is not always perfect.

The CBM and HADES RICH detectors are based on the RICH technology with a focussing mirror. The mCBM RICH (mRICH) is based on the proximity focussing concept with an aerogel block as radiator.

A proximity focussing RICH produces a ring of photons, with a defined width of the ring. As particles are only producing Cherenkov photons in the radiator volume, the inner part of the ring is not filled. The shorter the radiator volume is, the tighter is the produced ring. On the other hand a smaller radiator is leading to less Cherenkov photons (see equation 3.8). A compromise between a defined ring and an acceptable number of photons has to be found. The radius of the ring is highly influenced by the thickness of the radiator as well as the distance of the radiator to the photo detection plane and the Cherenkov angle. The granularity of the photo detection plane has to be adapted to the ring size to be able to resolve the rings (see Figure 3.14, left).

A mirror based RICH detector is in general more challenging than a proximity focusing RICH as the focussing element is a mirror. Here even small uncertainties can lead to huge effects on the projected rings. For the CBM and HADES RICH, most of the detector volume is filled with a radiator gas. A particle going through the detector is moving through the radiator medium and emitting photons on its path through the medium as described by equation 3.8. The emitted photons of the particle are flying in the direction of the charged particle towards a mirror. The mirror is spherical, reflects the photons and focusses them towards its focal point. The mirror is in the acceptance of the detector and thus its material budget has to be as small as possible. Nevertheless

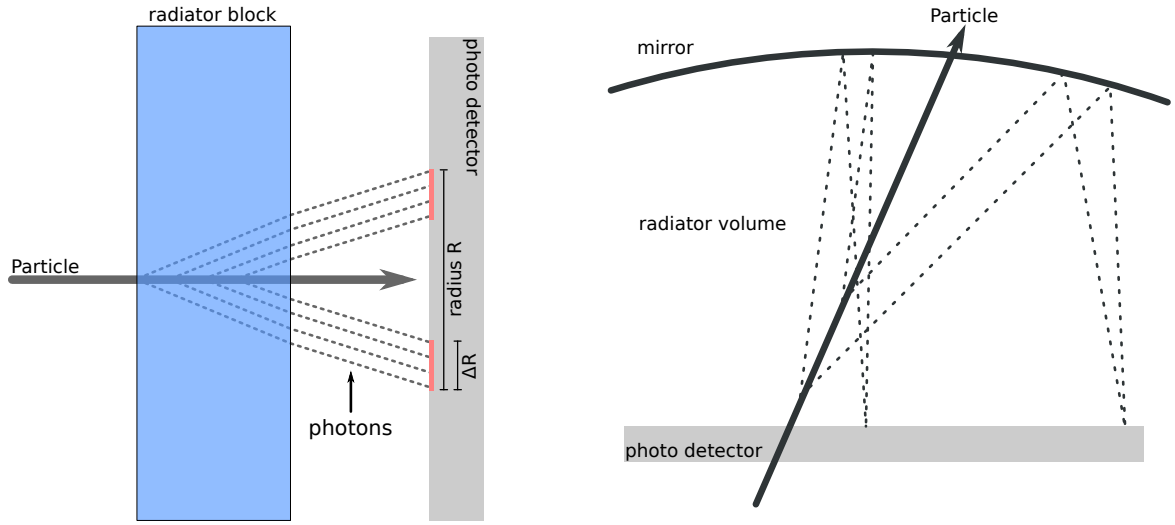

Figure 3.14: Schematic drawing of **(left)** a proximity focussing RICH and **(right)** a (spherical) mirror focussing RICH detector (Adapted from [101]). In both cases a photo detection plane is measuring the projected ring of the Cherenkov photons.

it has to be extremely homogenous on the surface with a high reflectivity and has to be sufficiently strong to conserve its shape in order to preserve its optical parameters.

The reflected and focussed photons are measured at the photo detection plane. In the photo detection plane the cone focussed to a ring is detected and further processed to digital signals. The radius R_C of the rings in a RICH detector with spherical mirror is approximately given by equation 3.11. The radius of the mirror is given with R_S. The focal length is $f_S = R_S/2$ [101].

$$R_C = f_S \cdot \theta_C = \frac{R_S \cdot \theta_C}{2} \Rightarrow \theta_C = \frac{2 \cdot R_C}{R_S} \tag{3.11}$$

Taking into account the momentum $P = mc\beta\gamma$ of a particle the mass of a particle can be expressed as

$$m = \frac{p}{c}\sqrt{\frac{1}{\beta^2} - 1} = \frac{p}{c}\sqrt{(n \cdot cos\theta_C)^2 - 1} = \frac{p}{c}\sqrt{\left(n \cdot cos\left(\frac{2R_C}{R_S}\right)\right)^2 - 1} \tag{3.12}$$

As heavy ion experiments are in general equipped with a magnet and can perform a momentum reconstruction of the particle passing the RICH by a good tracking, the mass of a particle, and therefore its type, can be measured by the radius of the Cherenkov ring R_C.

3.3.3 CBM RICH Concept and Mechanics

The position of the detector is 1.6 m downstream the target, directly after the CBM magnet and before the TRD detector. The location of the detector is constraining many design decisions by e.g the influence of the magnet stray fields on the photo camera or the material budget of the mirrors with supporting structures in the acceptance.

The detector is designed to fulfil its physics requirements in electron identification and pion suppression. The RICH is the key detector to identify electrons in the low

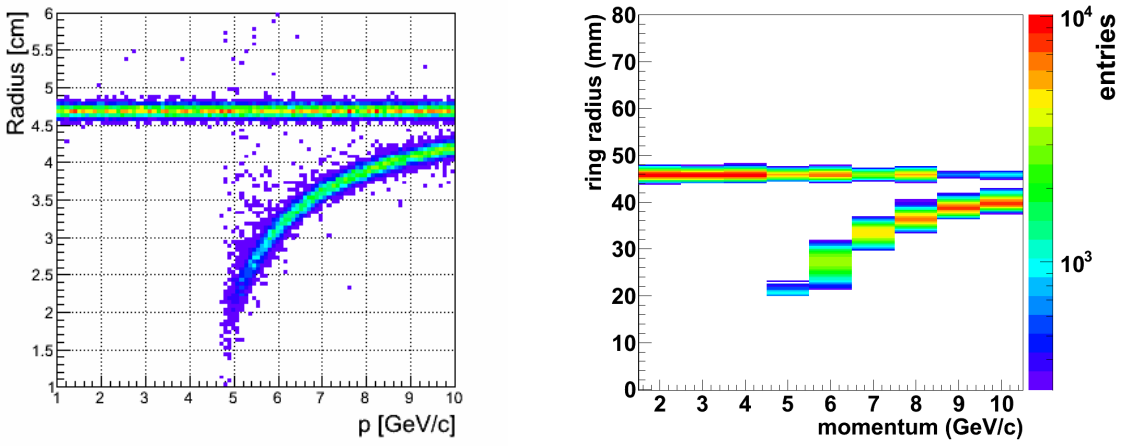

Figure 3.15: **(left)** Monte-Carlo simulation of the CBM RICH. **(right)** Measured CBM RICH prototype data in a test beam at CERN. Both histograms show the radius-momentum distribution of the RICH detector for electrons and pions [83].

momentum region of up to 8-10 GeV. In the region of higher momenta the TRD detector is completing the identification of particles. The electron identification of the RICH is extremely important in the low mass vector meson section and the decay of J/ψ to e^+e^-. To achieve a clean sample with reduced background, a pion suppression of above 100 is aimed by the RICH detector for the di-lepton spectra. In combination with the TRD a suppression of even 10000 should be achieved [83].

For the physics at SIS100 already a pion suppression factor of 1000 is sufficient to have a background that is mostly dominated by π^0-Dalitz decays and γ-conversion.

The CBM RICH detector has to match the acceptance of 2.5-25° in polar angle of the full CBM experiment with a full azimuthal coverage. To compensate the influence of the dipole magnet on the particles, the width of the RICH has to be increased to 35° [83].

The detector will be constructed from aluminium alloy in separated parts to improve the installation process. The complete RICH detector will be movable by a crane which makes the existence of an especially strong supporting frame below the detector itself indispensable (see Figure 3.16). The supporting frame will ensure the stability of the detector, but also provides an adjustable positioning of the detector with respect to the beam axis. Three hinged supports will be mounted on the RICH/MUCH foundation and the counterpart on the support frame, where each of these supports can carry 6 tons of weight. A possible movement within 15 mm in y, 100 mm in x and 580 mm in z improves the safety of the craning process as the detector can be moved in the best suited position [102].

The movement is realised by two different types of supports as shown in Figure 3.17. Type 1 is optimised for a transverse and vertical movement, whereas type 2 regulates the longitudinal and vertical direction. Both types provide a full rotational degree of freedom [102].

The detector itself is separated in three main parts that are later on introduced in more detail: A radiator volume, a mirror structure and a photo detection plane.

The radiator vessel is the main body of the detector. It is build from aluminium parts that are sealed together and mounted to the global support structure shown in Figure 3.16. Next to the function as a gas- and light-tight vessel of the radiator gas, the aluminium vessel is the main structure of the detector, providing the stiffness for crane

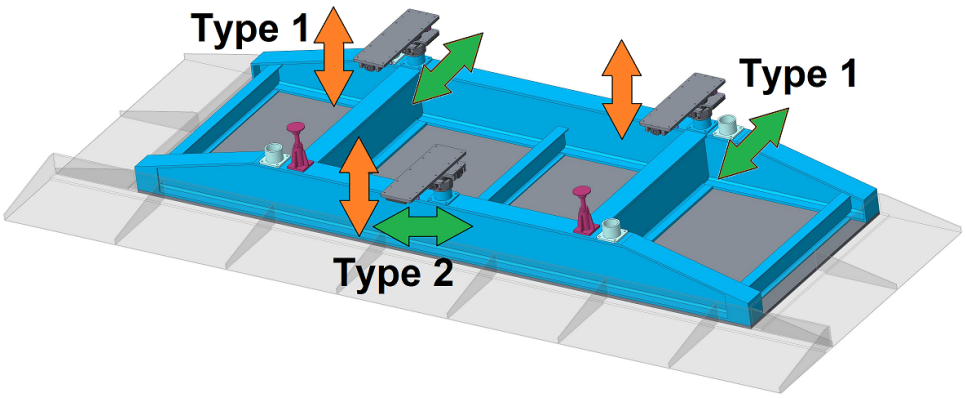

Figure 3.16: CAD drawing of the support frame (bottom view) with the connections to the hinged supports, that is mounted on the RICH foundation [102].

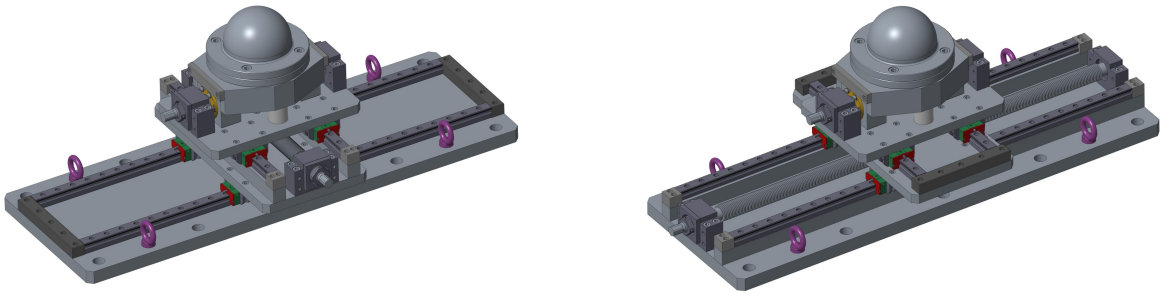

Figure 3.17: CAD drawing of the adjustable hinged support. **(left)** Type 1 with a transverse and vertical movement. **(right)** Type 2 with a longitudinal and vertical movement [102].

movement and the supporting structure for two magnetic shielding boxes around the two photo cameras with a weight of roughly 1400 kg per shielding box with attached camera [103]. The full vessel will be about 6 m in width, 2.2 m in length and 5 m in height [102]. These huge dimensions make it hard to produce and transport the full structure. Therefore the detector is separated in smaller parts that can be produced more easily and will be later bolt and sealed with rubber gaskets in the CBM cave. As a reduction of material budget, the entrance window to the detector (see Figure 3.18, left) is made of Kapton foil or a similar material. The rear side of the detector, adjacent to the TRD, will be closed with a thin plastic sheet (see Figure 3.18, right).

The whole vessel will be operated with a slight overpressure of the radiator gas of 2 mbar and an allowed leakage of maximum 3 standard liters per minute.

In the inside of the CBM RICH detector the focussing mirror is located. The mirror will be made from arrays of smaller mirrors. Each of the mirror tiles has to be positioned individually in all three dimensions to form an in global perspective homogeneous and, even more important, a common spherical surface without further distortions. The mirror tiles are positioned on a mirror supporting structure that can with-

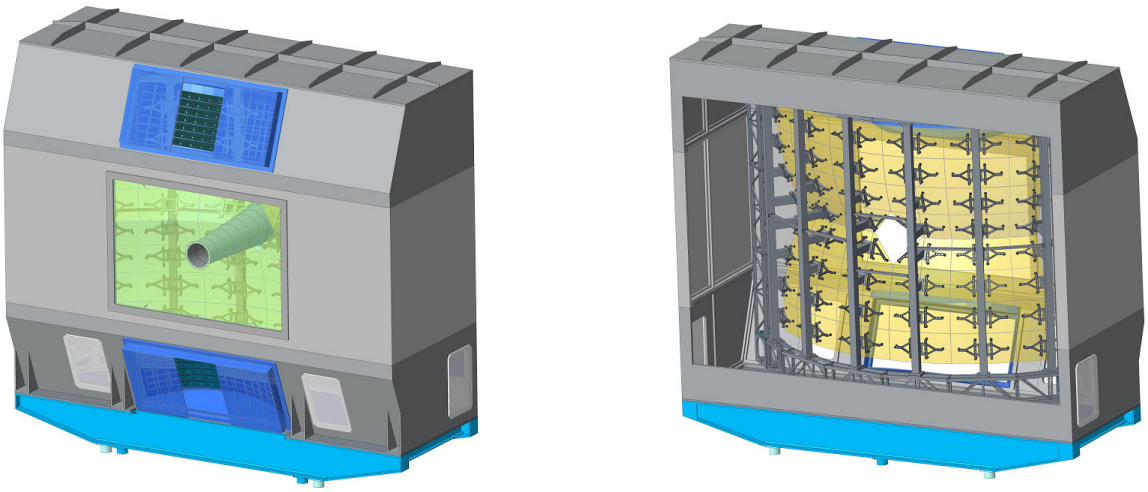

Figure 3.18: **(left)** Drawing of the CBM RICH detector in beam view. The central opening with the beamtube (mid) and the shielding boxes (blue) are visible. **(right)** The backside of the detector with a view on the mirror wall with the mounting structure [102].

stand the forces of the mounted mirror without a huge deformation and that allows a movement of the RICH without destroying mirror tiles. This all has to be achieved with a sufficient low material budget in the acceptance region.

The mirror surface will exceed an effective area of 6.5 m^2 per half with four different types of mirror tiles. Each type of mirror tile has a different size and gaps of 3-4 mm between the corners of adjacent mirror tiles. In total 80 mirror tiles will be mounted in the RICH detector. The mirror holding structure will be made from thin walled aluminium alloy AD31 (EN AW-6061) pillars. Each pillar holds mirrors from two vertical rows of the mirror wall with a dedicated mirror mount. Analysis on the stiffness of the pillar show a deformation of less than 0.06 mm (see Figure 3.19, right). Each pillar is designed to carry eight mirror holding structures with different distances between the mirror and the pillar. The measured deformation of the pillar under load is reflecting the increased deformation with increasing lever arm.

Each of the holding structures is designed to hold mirror tiles on a tripod construction. The tripod mount concept is foreseen to allow a full adjustability of the mirror tiles in space in the design limits and guarantee a perfect alignment. The alignment of the mirror tiles is done with screws on the mirror holders. The holders itself are glued to the mirror with a radiation proof glue that reduces the stress to the mirror on the glueing positions to a minimum. The gravitational force will produce some stress to the mirrors. The resulting deformation by gravity is shown in Figure 3.20, right figure. The result of a deformation analysis is comparable with the expectation.

The pillars with their attached mirror holding structures are mounted in a frame that surrounds the full mirror array [102]. The frame is not mounted to the whole vessel to ensure the lowest possible stress on the mirrors while lifting and movement (compare Figure 3.19).

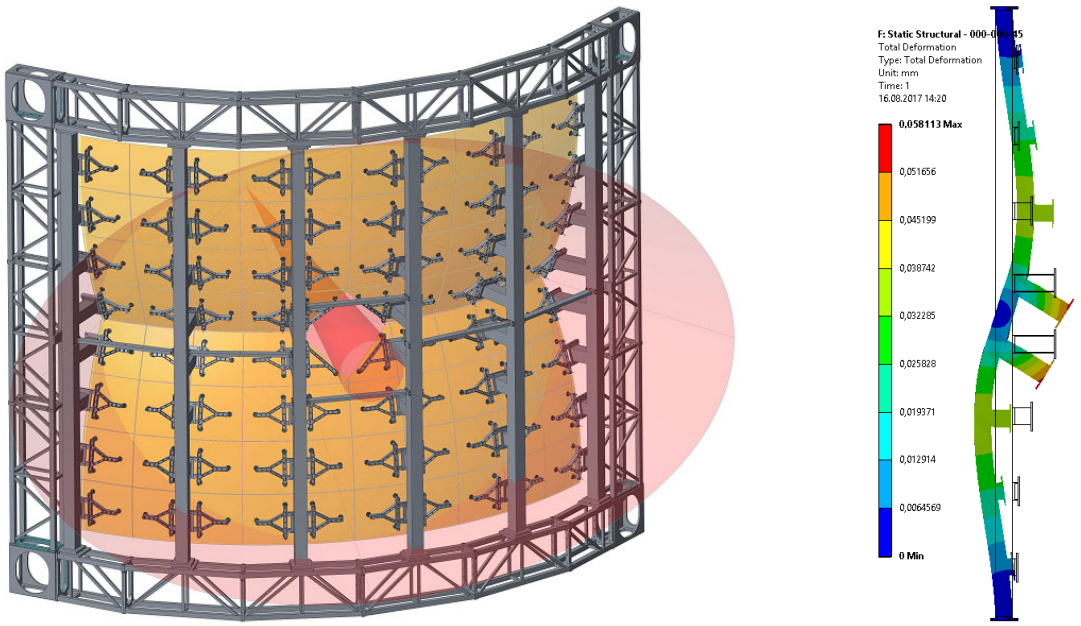

Figure 3.19: **(left)** Aluminium holding structure for the mirror array with the surrounding support frame. **(right)** Exaggerated drawing of a deformation analysis of a pillar under load [102].

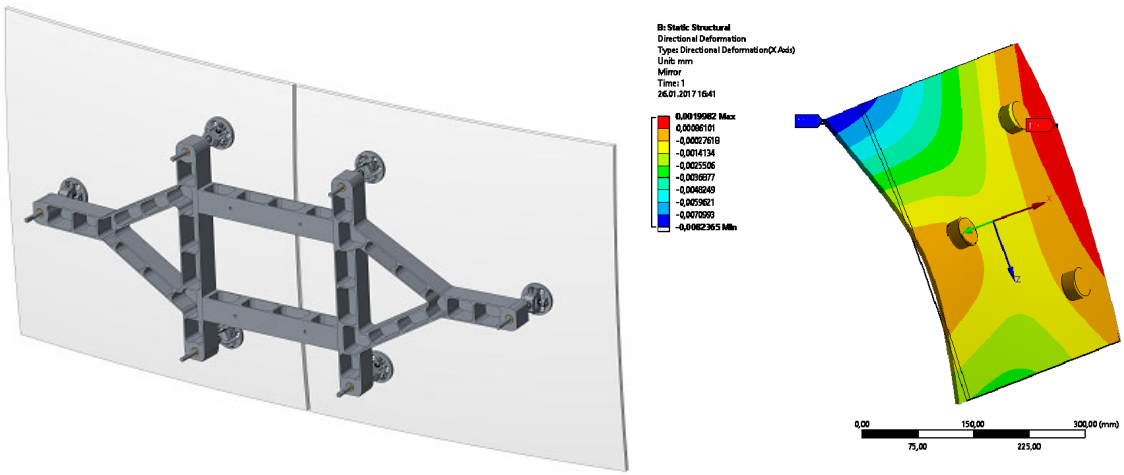

Figure 3.20: **(left)** Mirror holding structure with its three mounting points for one of the attached mirror tiles. **(right)** Exaggerated drawing of the deformation analysis of a mounted mirror tile under gravity [102].

The CBM RICH detector is exposed to the remnants of the magnetic field of the dipole magnet. Dedicated field clamps are mounted to the magnet to reduce the influence of the magnetic field to the RICH detector. Unfortunately an additional reduction of the field in the position of the photodetector plane is needed as measurements of the MAPMT H12700 showed an efficiency drop for magnetic fields of above 2-3 mT (see section 3.3.6). In addition to an effect on the MAPMTs, the magnetic field has to be small to assure straight particle tracks in the RICH detector. Bended tracks in the RICH would lead to smeared rings and harm the performance of the RICH detector.

Simulations with ANSYS, OPERA and COMSOL are executed to find the best geometry and material to reduce the stray field in the photodetection plane. The shielding boxes are planed to be made of magnetic iron and will reach a weight of about 1 ton

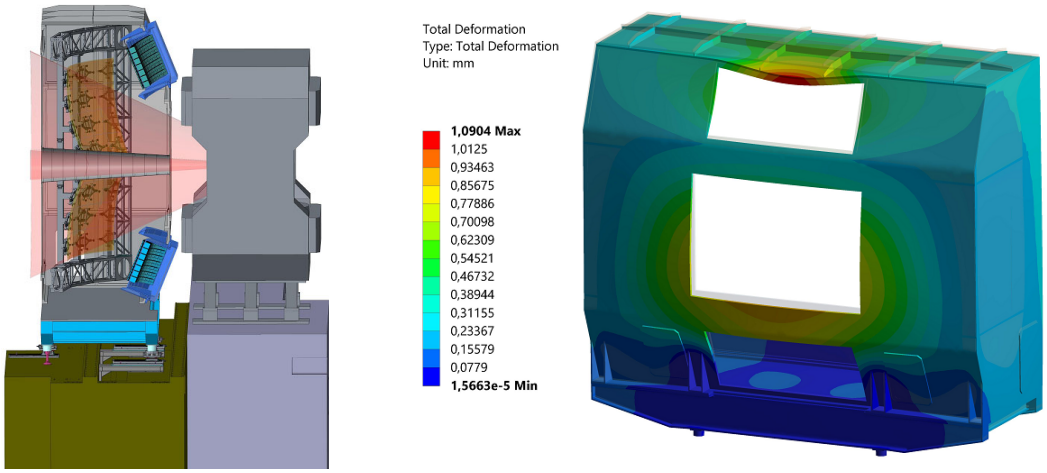

Figure 3.21: **(left)** CBM RICH design with attached shielding box in blue. **(right)** Exaggerated drawing of the deformation of the CBM RICH detector vessel under gravity with attached shielding boxes of a maximum weight of 5 tons (estimate of an upper limit) [102].

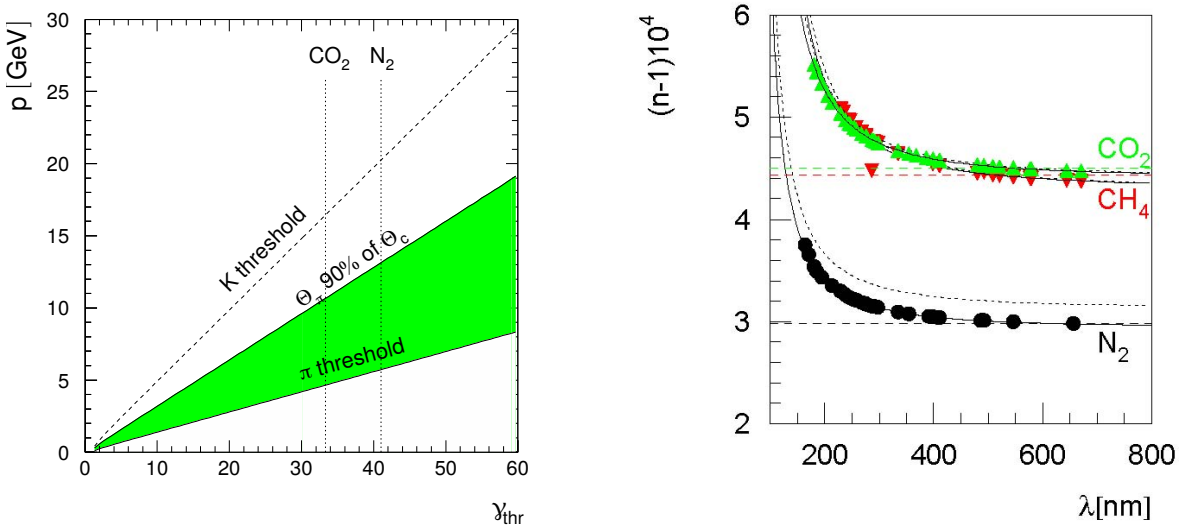

Figure 3.22: **(left)** Threshold momentum of the pions and kaons for different threshold Lorentz factors γ_{thr}. Green indicates the region of possible pion identification up to 90% of the Cherenkov angle. **(right)** Dependence of refractive index on wavelength for N_2, CO_2 and CH_4 for T=0° and p=1 atm [83].

each. Figure 3.21 shows the CBM RICH design with attached shielding boxes and the expected deformation of the vessel due to the gravitational force from shielding boxes with a maximum weight of 5 tons (for an estimate of an upper limit). The current design foresees the attachment of the readout electronics to the shielding box with a later on combined insertion in the detector vessel.

3.3.4 CBM RICH Radiator

The CBM RICH detector is planned as a gaseous RICH detector with CO_2 as radiator gas. CO_2 has an index of refraction of $n = 1.00045$ (T= 0°, p=1 atm) [83], a resulting γ_{thr} of 33.3 (see equation 3.6) and a maximum Cherenkov angle of 1.72° (see equation 3.5).

The vessel will be filled with ≈ 63 m^3 of the gas with a radiator length of 1.7 m. In-beam tests with a prototype measured a number of N≈22 hits per ring [83]. Referring to equation 3.8, a figure of merit N_0 of 171 cm^{-1} is expected.

The chosen gas provides a good electron to pion separation until high momenta. The threshold momentum of pions in CO_2 can be calculated with equation 3.10 and gives a value of P_{thr}=4.65 GeV/c. A separation between electrons and pions is assumed to be possible for Cherenkov angles of up to 90 % of the maximum Cherenkov angle, i.e. up to momenta of about 10 GeV. Figure 3.22, left, illustrates the possibility of the RICH detector to separate pions and electrons even at high momenta above 5 GeV/c. The threshold momenta of kaons is located at ≈ 16 GeV .

The CO_2 radiator is absorbing photons at a wavelength below 180 nm. Above this value it is nearly completely transparent. In the region of small wavelength the chromatic dispersion becomes more important as the changes in the index of refraction become more significant (see Figure 3.22, right) [83].

The scintillation of CO_2 is fortunately only a small contribution to the detected photons. Estimates based on central Au+Au collisions expect a contribution of 250 measured photons homogeneously distributed over the photo detection plane [83].

3.3.5 CBM RICH Mirror

The mirror of the CBM RICH detector is one of the key elements for a precise electron identification as the reflection is influencing the shape of the Cherenkov rings. It is designed as a spherical focussing mirror separated into two halves, focussing the Cherenkov photons to one of the two photon detection planes. Each of the halves will be equipped with a mirror array of ≈40 individual smaller trapezoidal mirror tiles, adding up to a total mirror size of 13 m^2 with a focal length of 1.5 m (radius of curvature: 3 m).

The splitting of the mirror in separate smaller mirror tiles is necessary to reach a reasonable size with the needed precision of the full mirror for the CBM detector and to be still manufacturable. Small gaps of 3-4 mm in between neighbouring mirror tiles are needed to keep the mirror flexible enough for the craning process to minimize the risk of cracking mirrors. On the other hand, the gap is chosen reasonable small to reduce losses of Cherenkov photons to a minimum. As mentioned earlier, each of the tiles will be attached to a tripod mounting structure that allows the alignability of each individual tile to better than 1 mrad. This is needed to get a common spherical surface over the full mirror as well as an eventually needed correction of the position after e.g. craning.

In addition to the alignment via screws on the holding structure, a software based mirror alignment correction system was developed and tested [104]. A dedicated equipment for the measurement of mirror misalignments is positioned in the detector (Continuous Line Alignment Monitoring (CLAM)). Based on the measured misalignment by the CLAM method, a correction of the data can be applied.

The mirror tiles will be produced by JLO Olomouc. The tiles are made from SIMEX, a special borosilicate crystal. The full glass mirror is polished and later on coated with a 110 nm aluminium film. Oxidation of aluminium is critical for the reflectivity of the mirror, as it absorbs photons in the UV region strongly. A 110 nm coating of MgF_2 is applicated on the Al coating as a protective layer [83].

Measurements of different mirror types were performed by the RICH group and summarized in [83]. The measurements of the chosen mirror type from JLO Olomouc provides a relatively flat and constant reflectivity of above 85% over the full wavelength down to 200 nm (see Figure 3.23). In addition the mirrors show a very good focussing and optical surface quality.

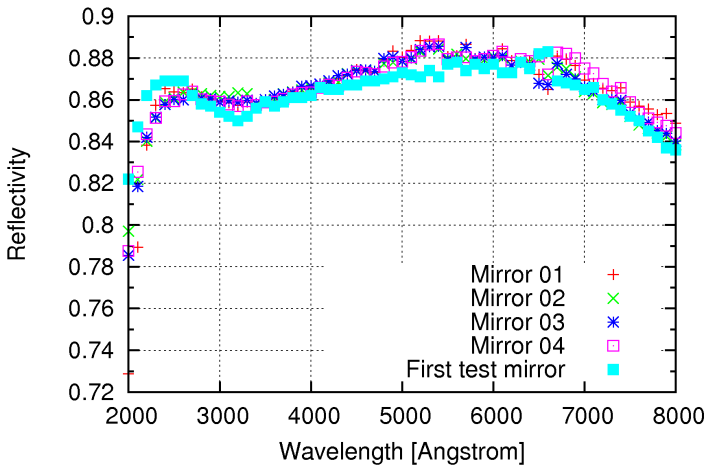

Figure 3.23: Reflectivity of different JLO Olomouc mirrors showing the reproducibility of the coating quality [83].

3.3.6 RICH Detection Plane

The photon detection plane of the CBM RICH detector is separated into two cameras, one on the upper and one on the lower half of the detector, as previously shown in Figure 3.18. Each of these cameras is positioned around the focus point of the mirror system and follows the radial shape of the mirror in the X-direction. The camera position is tilted to match the focal plane of the mirror. The mirror and photodetection plane are tilted to minimize the influence of the magnetic field on the photodetectors.

The basic concept of the photon detection plane is the same for all three RICH detectors discussed in this thesis. The main difference in the discussed cameras is the geometrical positioning of the MAPMTs. The RICH detectors photon detection is based on the multi anode photo multiplier tubes (MAPMTs) Hamamatsu H12700B. The H12700 is a quadratic photo sensor with an effective sensor area of 48.5×48.5 mm^2 and a full device area of 52×52 mm^2. The effective area is divided in 8×8 pixels. The outer pixels have a length of 6.25 mm whereas the inner pixels are only measuring 6 mm.

Figure 3.24 is showing the dimensions of the Pixels and the full MAPMT as well as the basic principle of the MAPMTs function. The H12700 is chosen after several tests of different MAPMTs as it is combining the large size of 52x52 mm^2 from the H8500 MAPMT with the beneficial single photon properties of the R11265 tube [106]

Several parameters are playing a very important role in the use of a MAPMT. One of the key parameters is the quantum efficiency of the PMT. The quantum efficiency (QE) is defined as the probability to produce a photoelectron from an incoming photon in the photocathode. Additionally to the QE, the photo electron collection efficiency and entrance window transmittance are playing an important role. The use of a Superbialcali photo cathode leads to a significantly higher quantum-efficiency of the H12700, compared to the H8500. In addition, the entrance window of the H12700 is made of UV glass instead of standard borosilicate glass, enhancing the wavelength transmission range down to 185 nm with a maximum of 600 nm (H12700B-3) [108], to match the op-

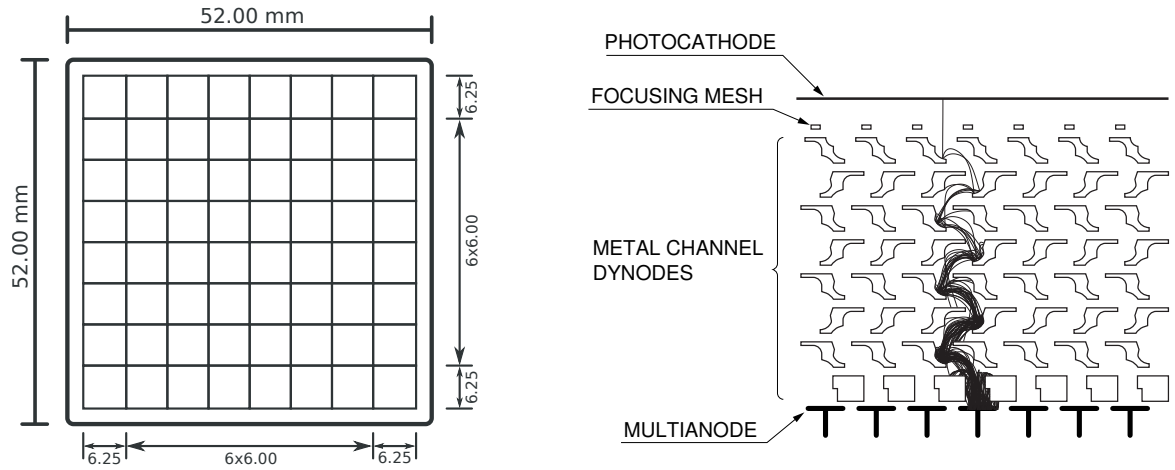

Figure 3.24: **(left)** Schematic drawing of an H12700B MAPMT with its dimensions and pixel size. The outer pixels are 0.25 mm wider. The full effective area is surrounded by a small non-sensitive area. **(right)** Electrode structure and electron trajectories for a multi anode PMT [105].

tical properties of the CO_2 radiator gas. Furthermore the UV glass is more radiation hard than the standard borosilicate glass.

In the CBM environment the photo detection plane has to cope with high interaction rates and thus with a high hit rate per pixel. A maximum hit rate on the order of 700 kHz/pixel is expected in the inner most regions (see Figure 3.25). Calculations with a gain of 10^6 for single photons result in a signal current of 0.1 μA per pixel, respectively ≈5 μA per MAPMT which is far below the maximum rating of the H12700B-3 [83].

Each of the 1100 acquired MAPMTs have been tested in a laboratory setup. The quality assurance test focussed on parameters as gain and efficiency of the MAPMTs (as well as individual pixels). The gain measurement is necessary to later selected groups of six MAPMTs by gain to operate them with a shared high voltage on a common backplane of the RICH detector [109].

Next to the possibility to work at maximum rates it is important to have a low noise level in the photo detector. The targeted dark rate of the CBM RICH detector is below 100 Hz/pixel. This low dark rate is even more important in the free-streaming CBM environment than in the HADES detector, as all detected photoelectrons are entering the read out chain and thus can slow down the reconstruction as well as lead to buffering issues on the front-end electronics. The trigger free environment also requires a very good time resolution as the events can partly overlap and as the event building in the time stream is based on time window cuts. The higher the time resolution is, the tighter the cuts can be chosen and the better the event reconstruction is working.

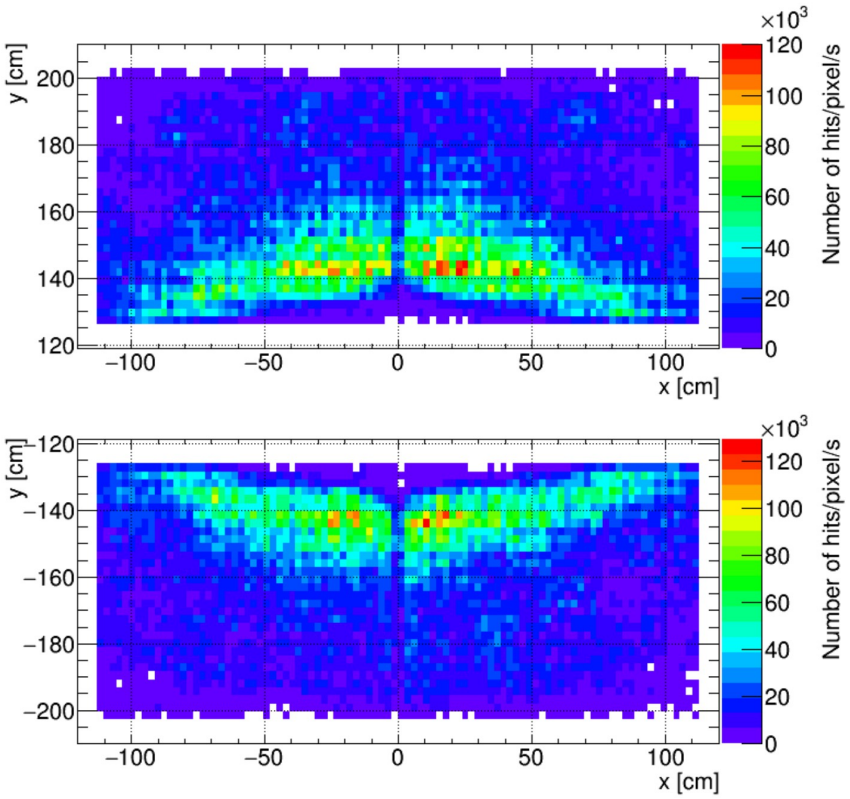

Figure 3.25: Expected single photon hit rate per pixel in the photo detection plane for minimum bias Au + Au collisions at 10 AGeV and 10 MHz interaction rate [107].

3.3.7 RICH Front-End Electronics

The Front-End Electronics (FEE) of the CBM RICH detector is mostly identical to the FEE of the mRICH and HADES RICH detector. Only changes in the firmware and updates in the layout due to production processes are different between the experiments.

The FEE is designed as a composition of submodules. The basic structure is a backplane. The backplane is a PCB of $156 \times 105\ \mathrm{mm}^2$. It is designed to be as light tight as possible to be used as the connection part between radiator volume and readout volume of the detector. The side of the PCB pointing to the radiator gas is hosting the H12700B-3 Hamamatsu MAPMTs with their recommended Pin Header for PMT signals, ground and high voltage connection. The inner side of the PCB is equipped with SAMTEC connectors. At these connectors the FEEs, the DiRICH boards, a data combiner board (Combiner board) and a power distribution board (power module) are connected. One standard backplane can host 6 MAPMTs in a 3×2 array. Two of the six MAPMTS are rotated by 180° relative to the others. On the readout side, one PMT is connected to two individual DiRICH boards, resulting in 12 DiRICH boards per backplane (see Figure 3.26 and Figure 3.28).

The backplane is connecting the Serializer/Deserialize (SERDES) data lines of the DiRICH boards and additional low voltage differential signal (LVDS) lines with the combiner board. As the RICH FEE is used in triggered and self-triggered experiments, a trigger signal distribution is needed. The trigger signals are distributed from the combiner board to a trigger fanout chip on the power module and further on to the individual DiRICH boards.

Next to the trigger distribution the power module's main use is the power distribution of the high and low voltage. A high voltage LEMO connector is used to connect to a 3.2 mm diameter HV cable. The HV is distributed via the backplane to the HV connectors of all six MAPMTs. MAPMTs have to be pre sorted in bunches of six by gain to match the high voltage needs as a backplane provides only one common high voltage.

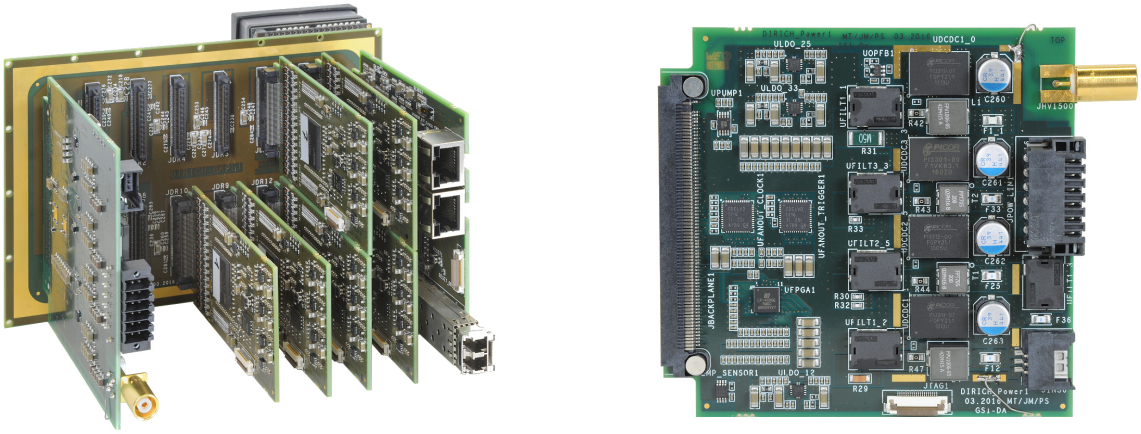

Figure 3.26: **(left)** A partially equipped backplane with one MAPMT, DiRICHes, Power and Combiner module. **(right)** A power module with fully equipped on-board DCDC converter stage.

The low voltage connection is highly challenging as low voltages with high currents are needed to operate the FEE. Two scenarios are currently implemented and under discussion as improvements are planed for CBM:

The standard option is the usage of on-board DCDC converters. The power module is connected to a supply voltage of up to 36 V and filtered on board. Further on, four different DCDC converter ICs are regulating the input voltage to the four needed output voltages for all connected FPGAs and pre-amplification stages in the RICH FEE. 3.3 V and 2.5 V are needed in a low current regime. The 1.2 V and 1.1 V voltages, needed for the amplification and FPGA operation, are problematic due to high currents: The 1.1 V line has to cope with up to 15 A of current. The draw back of the DCDC converter solution with its lightweight cabling is radiation of electromagnetic noise to the DiRICH boards, influencing the measurements by an increased noise bandwidth (compare to Figure A.8).

A connection of pre-regulated voltages is foreseen as a bypass of the converter, however on the cost of thick power lines going in. Twelve power cables with a core diameter of 1.5 mm have to be connected to a Weidmüller connector. Such a cable implies huge forces on the PCB and the connectors and is not as flexible as a cable used in the on-board solution. In addition this solution suffers dramatically from a voltage drop on the supply line. Nevertheless this method has the huge advantage of excellent noise behaviour on the detector.

As the RICH group puts emphasis on the optimum experimental setup, the already measuring experiments of mCBM and HADES are using pre-regulated input voltages. In detail, the concept of supplying the voltage is different and will be explained in more detail in Chapter 5 and Chapter 6.

With respect to the future CBM RICH, the powering scheme is under discussion and not finalised. Different measurements with external DCDC converters in different positions with respect to the power module were done (see appendix A). These measurements clearly confirmed the dependence of the noise in the FEE with respect to the power supply mechanism.

The heart of the RICH front-end electronics is the DiRICH board. One of these cards is 100×47 mm^2 in size and hosts the pre-amplification stage of 32 MAPMT pixels, threshold setting infrastructure for all channels and the Time-to-Digital Converter (TDC) including the TrbNet based data transport.

A typical signal output from a single photon amplification of the H12700B-3 is shown in Figure 3.27. This signal has a width of 2-3 ns and a rise time of 0.52 ns. The small signal has to be amplified by an amplification stage as the TDC of the DiRICH is operating in a region of $\approx$1-2 V. The negative input signal is shaped to a positive signal with an overshoot in the falling edge to improve the measurement of the falling edge of the Time-over-Threshold (ToT) signal.

All experiments have to deal with the influence of noise, crosstalk or electrical influences on the signal detection. In the case of the RICH detector's MAPMTs and FEE, fake signals are generated by crosstalk in the MAPMT, random darkrate of the MAPMT or e.g. radiated noise from the DCDC power board. A very robust method to get rid of such signals in order to clean up the data samples is the application of a threshold to the input signal to move the sensitivity of the TDCs further apart from the baseline of the noise. In the case of the DiRICH, the already existing LVDS inputs of the central

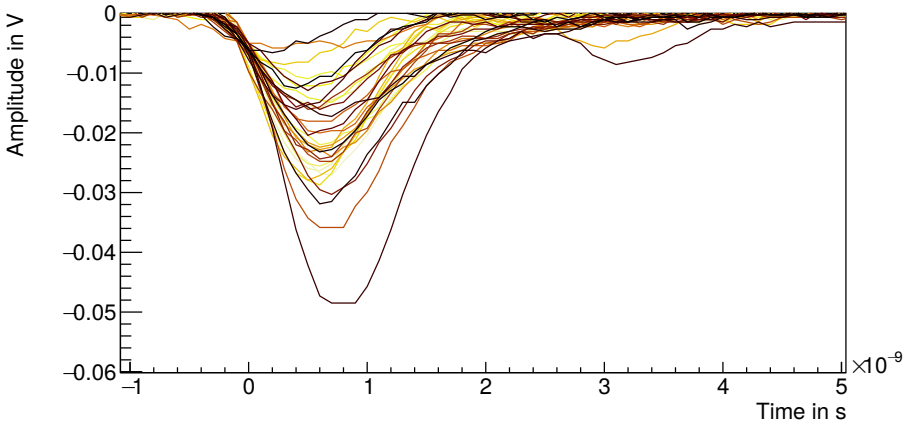

Figure 3.27: Typical signal of MAPMT pixels before amplification of the DiRICH board [110].

Lattice ECP5 FPGA are used to filter the readout stage input for signals above a certain threshold. The threshold of each channel is configured individually with two additional Lattice MachXO3 FPGAs, supplying the LVDS inputs with a threshold voltage.

The central FPGA of a DiRICH supports 32 input- and a reference-time TDC channel. A tapped delay line TDC is implemented on the FPGA, giving a resolution of roughly 10 ps and precision of around 12-30 ps, depending on the calibration method. The TDC data is locally buffered in a ring buffer until a trigger signal is arriving. The size of the ring buffer and the trigger rate is limiting the possible data rate of the TDCs. The data transport over SERDES from the DiRICH to the combiner board is running with 2 Gb/s (2.4 Gb/s in CBM) and thus not limiting the throughput.

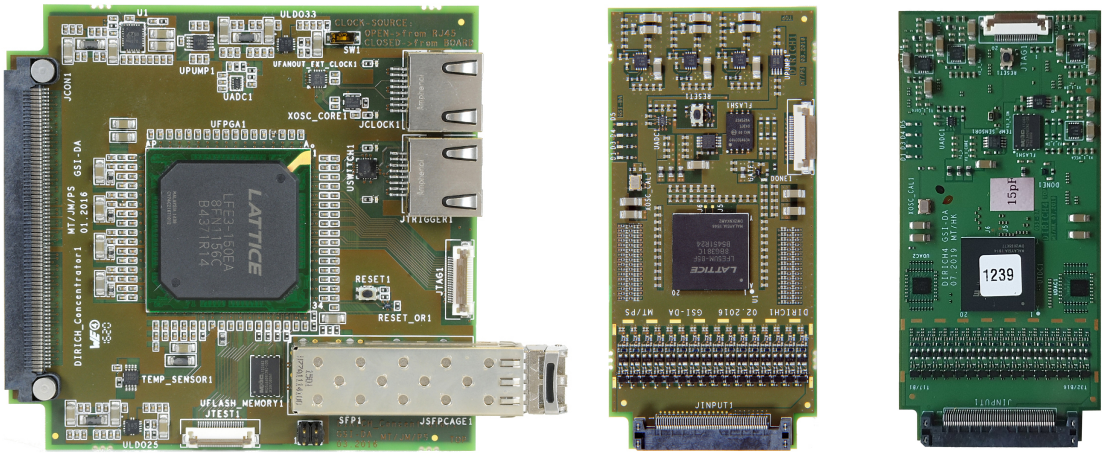

Figure 3.28: **(left)** The RICH combiner module with its central Lattice ECP3 FPGA, the SFP+ cage for the fiber connection to the upper readout stages and two RJ45 connection for Trigger and Clock distribution. **(middle)** A DiRICH version 1 with one central Lattice ECP5 FPGA and the 32 channel amplification stage near the SAMTEC connector. **(right)** A DiRICH version 4. It has two small Lattice MachXO3 FPGAs for threshold settings, an improved layout and easier FFC connection.

The DiRICH and all other RICH FEE is based on TrbNet. More details to TrbNet are given in section 4.6.

All 12 DiRICH boards on a backplane are sending data via their SERDES media interfaces to the combiner board. The combiner board is the central component on a backplane for the data connection to the higher level readout structures. The firmware of its ECP3 FPGA is the main difference between all RICH detector setups and the key part of the firmware development presented in this thesis. The core usage of the combiner board is the hub functionality. Data from an uplink port is distributed to all downlink ports (DiRICH boards) and back. Next to the distribution of the trigger information from the central trigger system (CTS) and the data from the front-end, also the slow control is distributed to all DiRICH boards. The combiner is equipped with a 200 MHz clock that is distributed to all connected DiRICH boards. Its is used as the base clock for the TDCs an the system clock of TrbNet. The use of an external clock source is also foreseen.

3.4 The mCBM Experiment

The mCBM experiment is a prototype experiment of the SIS100 CBM experiment at the SIS18 accelerator. It started operation in 2018 with first small prototypes and developed further in the past years to the nowadays full mCBM detector setup with prototypes of most of the CBM detectors and readout. The aim of the experiment is a test of the full detector chain including the final CBM readout with full online data reconstruction

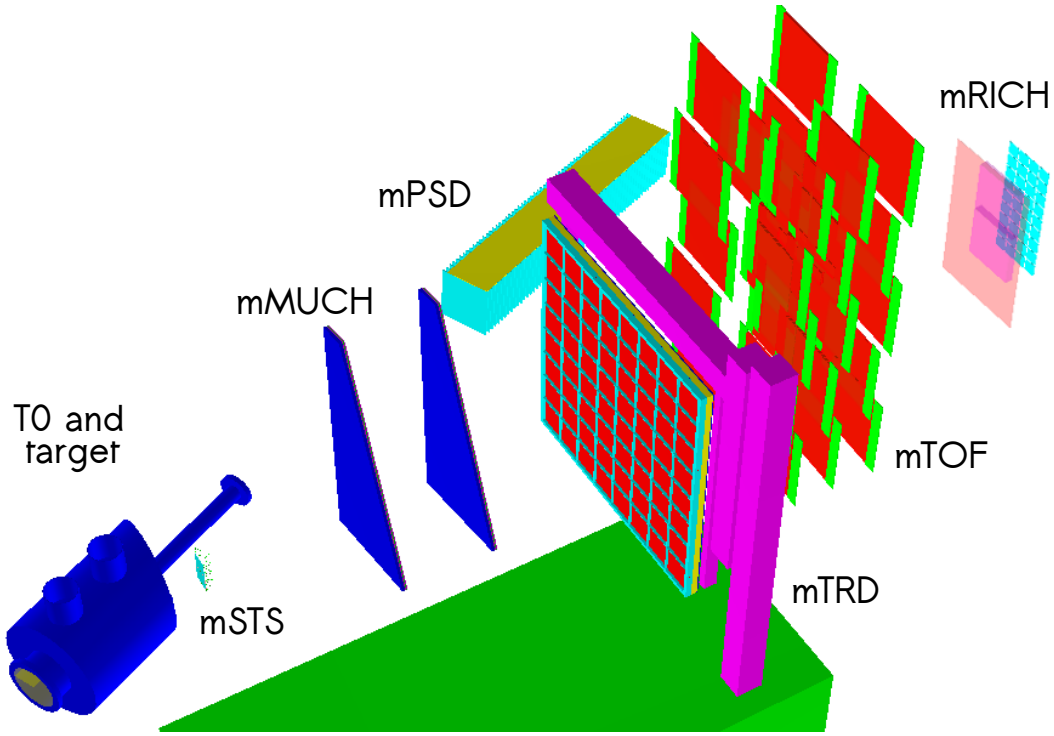

Figure 3.29: The mCBM experiment geometry of march 2020. From left to right: target box with T0 included, STS ladders, MUCH, TRD, TOF, RICH. In the background the PSD is positioned next to the beampipe. All detectors (except PSD) are rotated by 25° with respect to the beampipe.

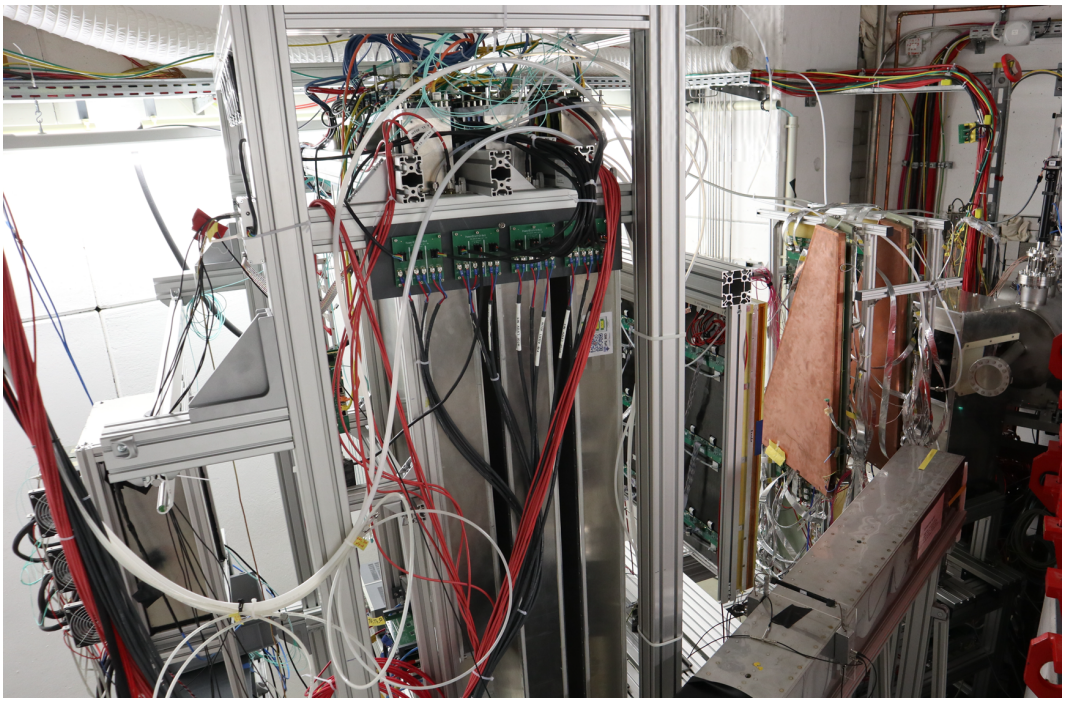

Figure 3.30: Real life photography of the mCBM detector setup in the cave in march 2020 [94]. The beam comes from the right.

capabilities. Next to the extensive test of the detector prototypes in real CBM environments, the mCBM experiment helps to find structural problems from software to hardware and monitoring issues.

mCBM is located in a cave next to the HADES cave at GSI. It is operated with the Heavy Ion SIS18 beam of different beam types at different interaction rates. Six different prototypes of the CBM detectors are located in a row under a 25° angle to the primary beam axis without a dipole magnet. The absence of a dipole magnet unfortunately limits the capabilities of momentum reconstruction. Nevertheless, the reconstruction of Λ baryons and the production of e.g. a beta spectrum is possible.

Figure 3.29 shows the geometrical setup of mCBM from march 2020 as it is used in all analyses. The T0 detector is located in the vessel on the left shortly before the target. It is followed by the mSTS ladders and two MUCH chamber prototypes. The mTRD prototype is located after the MUCH detector on a holding arm structure. mTRD was added to the mCBM system in the beginning of 2020 and is the newest part of the mCBM experiment. The mTOF is located behind the mTRD with a triple and a double stack next to each other. The mRICH detector is positioned directly behind the triple stack of the mTOF. The 25° line, defining the origin of the mCBM system, is nearly in the center of the mRICH detector. The geometry in Figure 3.29 shows the mRICH entrance window, the two aerogel blocks and the active area of the 36 MAPMTs. The last detector in the mCBM setup is the mPSD prototype. It is located next to the beampipe and is therefore not part of the mCBM acceptance. Figure 3.30 shows a photography of the full mCBM experiment in 2020.

3.4.1 mSTS

The mSTS detector is a demonstrator detector for the full size Silicon Tracking System with the full integration of the sensors, microcables, ASICs and front-end boards. Especially the full operation under real conditions with the full powering scheme, noise, etc. are tested in this setup. The detector is build from half ladders with two or three modules attached to it. The ladders are attached to the C-frame mechanical structure, providing cooling with cooled water. During the march 2020 beamtime one ladder with two modules was mounted in the mSTS box [94].

3.4.2 mMUCH

The mMUCH detector is based on the GEM technology. Each of the two chambers is a sector-shaped triangle with the dimensions of the first CBM MuCh station. The stations are positioned with a maximum overlap to the the nearby detectors to allow time and spatial correlations to these detectors. The readout of the mMUCH is based on the STS-XYTER-2.1 like the mSTS and the final CBM experiment. mCBM allows the mMUCH a test of the rate capabilities of the chambers, with a test of the full bandwidth of the readout under optimum noise performance. In addition the detector is tested in a radiation environment, showing the radiation tolerance of all components [94].

3.4.3 mTRD

The mTRD will be a combination of four layers with one module each. Until the march 2020 beamtime only the first layer was available. In future the first layer gives a x-coordinate and the second layer a precise y-coordinate. Each of the foreseen layers is comparable with the large, outer region modules for the SIS100 CBM TRD. Each of the modules is segmented into 6 rows of 128 rectangular shaped pads. The readout of the mTRD is based on SPADICs on Quad-FEBS (four ASICs each). Each ASIC is able to readout 32 channels, combining to 128 channels per Quad-FEB [94].

3.4.4 mTOF

The mTOF detector is build from five full size modules of type 4. They are combined to one triple and one double stack as shown in Figure 3.29 and Figure 3.31. In addition to the two stacks, test counters are mounted in front of the double stack. Each of the five modules is equipped with five MRPC2 counters. These counters are arranged with a slight overlap between neighbouring MRPCs, showing up in correlation measurements of the mCBM detectors as presented in Chapter 8.

10 Get4 TDCs with 32 channels each are used with two readout boards and a GBTx chip per module, summing up to 1600 channels in total. Each of the used MRPC counters are build with 32 strips, 1 cm pitch and 27 cm in length with a 0.8 mm thick low resistivity glass. The 32 strips are read out on both sides. The MRPCs are constructed to cope with rates of about 5 kHz/cm^2 as they are foreseen for the intermediate rate regions of the CBM TOF. All in all this sums up in an active area of 150×125 cm^2. The full mTOF is positioned with the double stack near the beampipe ($\approx12^\circ$) where the particle flux is higher with respect to the triple stack, that is centred at 25° to the beam. An event display of a measured collision in Pb+Au with a technical drawing of the M4-module is shown in Figure 3.31 [94].

As the completion of mTOF, the T0 detector is mounted as a part of mCBM near the target. The in-beam T0 detector is build as a polycrystalline diamond plate of 0.3 mm thickness. It is placed upstream in the beampipe vacuum and readout with a precision of 50 ps. The signals are getting preamplified on the PCB and are fed to the outside to an additional FEE board, sending out the data with GBTx chips. T0 is synchronised to the same reference clock as the TOF detector. The segmentation of the T0 is giving the possibility of a beam quality and position monitoring [94].

3.4.5 mRICH

The mRICH detector is a small prototype detector of the CBM RICH detector with the same front-end electronics as the future CBM RICH as well as the upgraded HADES RICH. It is positioned in the center of the 25° position of mCBM and therefore directly behind the mTOF triple stack. More detailed information to the mRICH detector is provided in Chapter 6.

3.4.6 mPSD

The mPSD detector tests one module of the final CBM PSD. The module is $200 \times 200\,\mathrm{mm}^2$ with a weight of 500 kg. It consists of 60 individual lead/scintillator assemblies with included optical WLS fibers as described in section 3.1.9. Six consecutive fibers are connected to a Hamamatsu MPPC S12572-010P and read out.

The mPSD is located with an angle of 5° to the beam axis and is therefore in an outstanding position relative to the other mCBM detectors. The usage of mPSD in mCBM gives the unique possibility to test the readout electronics in a real environment with high rates and the possibility of correlation measurements with other subsystems [94].

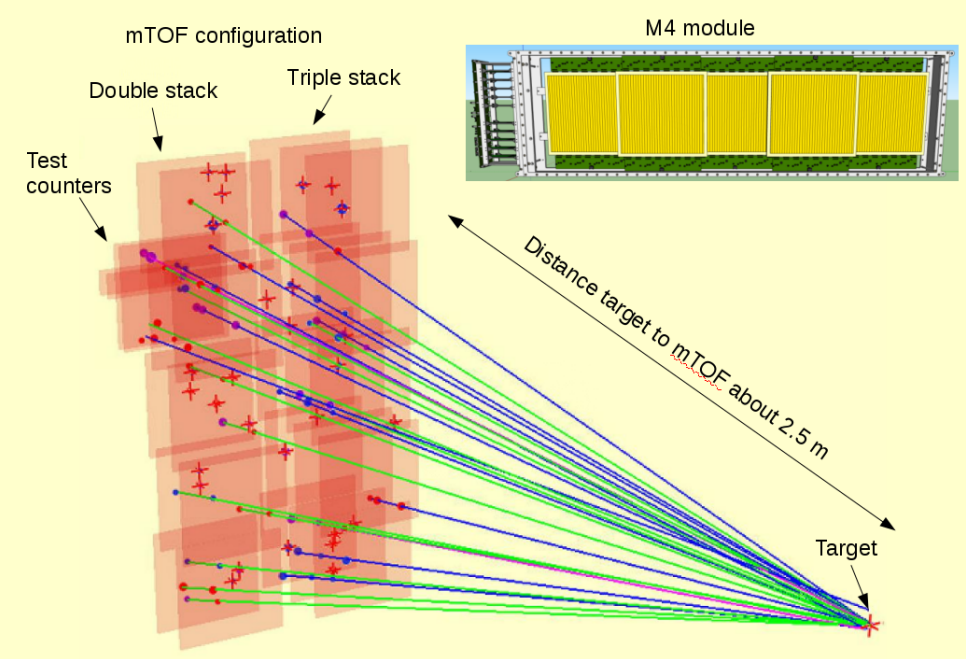

Figure 3.31: Technical drawing of a type 4 module with its five MRPC2 counters inside (top). In addition an event display of a measured high multiplicity event in Pb+Au collisions is presented [94].

3.4.7 DAQ

The DAQ of mCBM is the main part of the experiment as the interplay and integration of all CBM detectors in a common experiment are tested. The CBM readout is mostly based on GBTx, with additional TrbNet based detectors as e.g. the RICH detector. The readout chain of mCBM was first build to concentrate on the GBTx based systems (phase I) and is undergoing a conceptional change to the first DAQ prototype system of CBM with the CRI board (BNL-712/FLX-712) as key element for 2021 and beyond (phase II). The readout concept of the mRICH detector as used in this thesis (Chapter 6) is concentrating on the DAQ concept with an AFCK board (phase I). Based on this, Chapter 7 introduces the further developments of the RICH readout towards the CRI based readout as it will be used in phase II and later on in CBM.

The CBM DAQ concept is based on splitting the readout stages in three physical locations. The detector specific front-end boards as e.g. DiRICH boards and the readout boards (e.g. combiner boards) are located near or at the detectors in the mCBM detector cave. The optical connections from the sub detectors are connected to the DAQ container, located outside the cave with a distance of roughly 50 m. The optical fibers connect TrbNet, GBT or even UDP links. This outside part of the DAQ is common in all phases of the mCBM experiment. The further steps of the readout in the DAQ container and the GSI green IT cube, are differing for the individual phases.

3.4.7.1 Phase I Readout

Phase I is based on the use of a dedicated data processing board (DPB) that is located in the mCBM DAQ container. These DPBs are realised as AFCK boards in microTCA crates. The DPB is used to process the data already at this early stage (data sorting, feature extraction or other operations). Data from different downstreams (CROBS/FEE) is packed into micro-timeslices at the AFCK and transmitted via a 10 Gbit/s single mode optical fiber connection to the green IT cube. The FLES entry node in the IT cube is equipped with a FLIB board, receiving up to 4 FLIM links from the AFCKs. The FLIB is

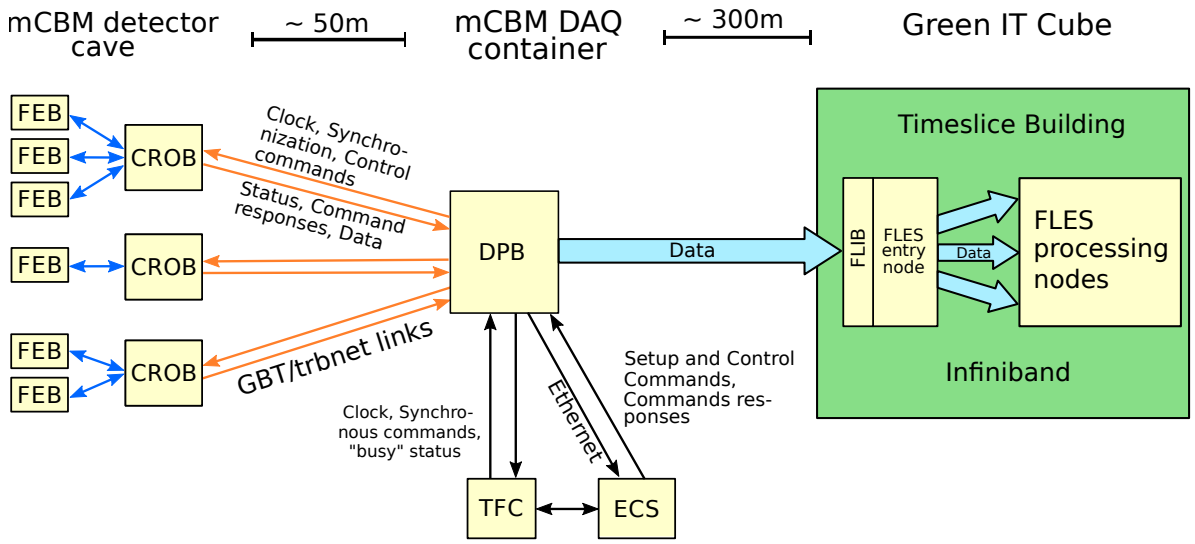

Figure 3.32: Schematic readout of the mCBM DAQ phase I with an AFCK board as DPB. Adapted from [94].

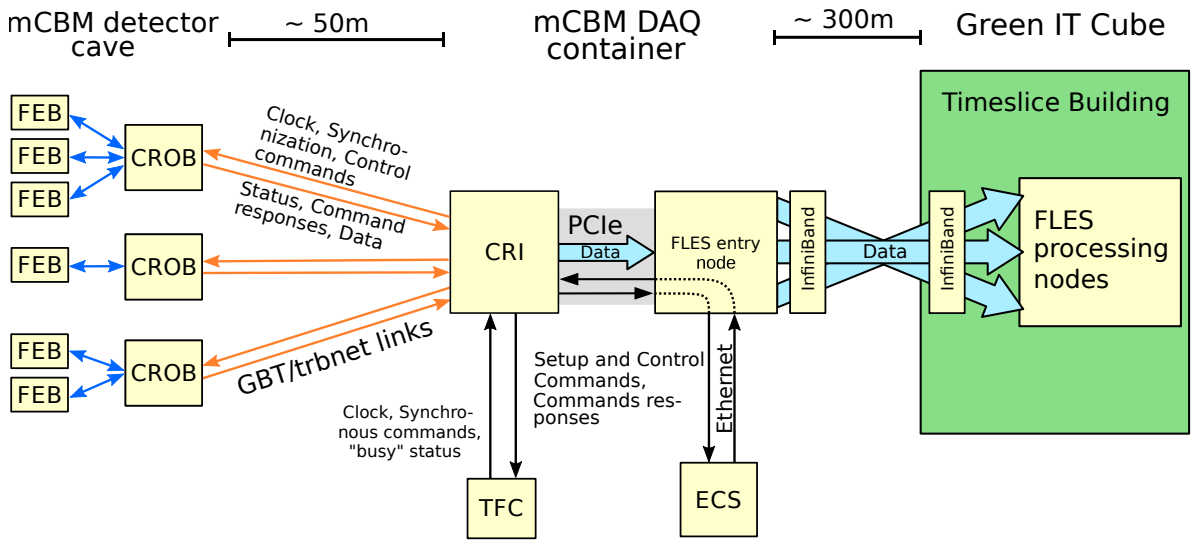

Figure 3.33: Schematic readout of the mCBM DAQ phase II with a CRI as substitution of the DPB and FLIB boards. Adapted from [94].

a Xilinx Kintex 7 based HTG-K700 board with a PCIe Gen2 x8 connection. It indexes the data and forwards it via PCIe to the entry node itself. From the entry node on data is distributed via InfiniBand network to the FLES processing nodes where micro-timeslices are processed to timeslices. These produced timeslices are ready for further online or offline reconstruction and analysis stages [94]. The full chain of data transport in phase I is shown in detail in Figure 3.32.

3.4.7.2 Phase II Readout

In Phase II of the mCBM experiment, the DAQ is changing to the first prototype of the final CBM DAQ. The data transport from the CROB to the mCBM DAQ container is quite similar to phase I. The huge difference between both concepts is the introduction of the common readout interface (CRI). The CRI is a BNL-712 board with 48 optical connections (see Chapter 7 for more details) and combines the functionality of the previously used DPB (AFCK) and FLIB. The FLES entry node is now moving from the IT cube to the mCBM DAQ container. In mCBM two CRI boards and an InfiniBand card are attached to a server via PCIe Gen3 x16. This server is the FLES entry node and allows the communication to the CRI and CROB/FEE boards. The CRI combines the data preprocessing, micro-timeslice building and PCIe functionality to one board. The data from CRI is transmitted via long range InfiniBand cables to the IT cube, where timeslice building is processed on the FLES processing nodes (see Figure 3.33) [94].

CHAPTER 4

High Acceptance Di-Electron Spectrometer

The **H**igh-**A**cceptance **DiE**lectron **S**pectrometer (HADES) is a general purpose, fixed target detector located at the SIS18 accelerator at GSI. It is participating in the FAIR phase-0 program at SIS-18, continuing with its state of the art physic program. Upgrades of the existing detector systems, the DAQ and the introduction of new detectors are preparing HADES for the future as part of the CBM pillar of FAIR at SIS100. HADES will be reallocated from its position in the SIS18 cave to a position in front of the CBM detector in the CBM cave, to continue with its physics program and extend to higher energies.

HADES is designed with emphasis on di-electron measurements in heavy-ion, but also proton and pion induced reactions in an energy range of 1-4 GeV [112]. The detector has to deal with high track densities in heavy ion collisions as Au+Au, but also with high interaction rates to achieve high statistic data samples for studying highly suppressed leptonic decays. In addition, the fixed target HADES experiment has to cover

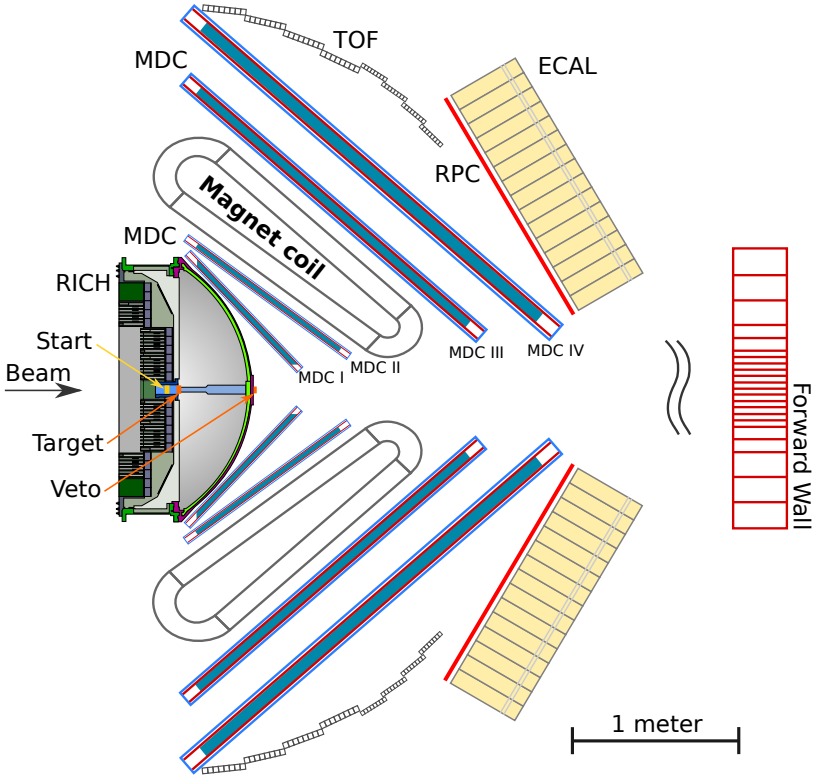

Figure 4.1: Schematic overview of the sub detectors of the HADES experiment in Z direction. In particular the picture shows the new RICH detector and the new ECAL detector. Figure is adapted from [111] and further improved.

a very high acceptance of 18°-80° in polar and almost full azimuthal angles to achieve a high probability to detect lepton pairs. Next to a high invariant mass resolution, a low material budget for the reduction of background from secondary particles (e.g. γ-conversion) or multiple scattering [113] is of high importance.

HADES is build from different sub detectors, focusing on particle identification and tracking. A hadron blind RICH detector is located in the field free region around the target, followed by a low mass tracking system surrounding a superconducting toroid magnet. The magnet coils are defining 6 symmetric sectors of the HADES experiment. Behind the magnet the META detector, a combination of an RPC detector in the inner polar angles and a TOF in the outer region, a Forward wall detector for centrality determination and the newly constructed electromagnetic calorimeter (ECAL) are completing the HADES detector (see Figure 4.1 for a schematic drawing of the full HADES with upgraded detectors).

4.1 Start-Target-Veto

The start and veto detector system of HADES is a combination of two dedicated detectors before and behind the target area. The start detector is made of single crystal chemical vapor deposition (scCVD) diamond sensors, glued to a PCB. The start detector is metallised with 16 strips and bonded to the PCB. This layout allows an exact monitoring of the beam profile and positioning on the sensor [114].

The use of a scCVD diamond allows a time measurement with 50 ps precision. The start detector is located in front of the target section and detects the particles traversing it. The target is designed to reach an interaction possibility of 1 %. A polycrystalline chemical vapor deposition (pcCVD) diamond sensor behind the target is used as veto detector. This allows the detection of particles, that were not interacting in the target. A combined readout of both detectors can thus be used to trigger the HADES experiment on real collisions [114].

4.2 RICH

The HADES RICH detector is an hadron blind Cherenkov detector whose main duty is the identification of electrons and positrons in collisions with an incident energy regime of E_{kin}=1-2 AGeV [115].

A detailed description of the HADES RICH detector with focus on the upgrade to a MAPMT based photon detector is given in Chapter 5.

4.3 MDC

The **M**ini **D**rift **C**hamber (MDC) is providing tracking capabilities to the HADES experiment. It is build from 24 chambers in four layers. Each of the layers consists of six trapezoidal, planar chambers representing the six sectors of the super-conducting magnet. The first two layers are in front of the magnet whereas the last two are behind the magnet. This arrangement allows the calculation of the momentum of particles by the deflection angle measurement. In addition, particles have a certain energy loss in

the MDC chambers. The measurement of the MDC energy loss is an additional parameter for the particle identification of charged particles [113, 116].

The MDC is build to match the ambiguous requirements of the HADES detector on material budget, high rate and track multiplicities in heavy ion collisions. The polar angle coverage from 18 ° to 85 ° implies an increased surface from layer one (0.35 m^2) to layer four (3.2 m^2) with 1100 drift cells per layer.

The cathode and field wires are made from aluminium with 80 µm (MDC I-III) and 100 µm diameter (MDC IV). 20 µm, respectively 30 µm thick gold-plated tungsten wires are mounted as sense wires. Each chamber is build from six layers of sense/field wire layers with different stereo angles of ±0 °, ±20 ° and ±40 ° (see Figure 4.2, left). The different angles between the layers in combination with a thin mylar entrance window and a nowadays argon based counting gas are ensuring a high track reconstruction efficiency, spatial resolution and long lifetime of the MDCs [113].

4.4 Time of Flight Particle Identification

The HADES detector uses two different detectors for time of flight based particle identification. A resistive plate chamber (RPC) detector is used in the inner region (18°<Θ<45°) of the acceptance, whereas a scintillator rod based time of flight detector is used in the outer region (44°<Θ<85°). Both detectors require the Start-detector as T_0 detector for the start time information. Together with the tracking capability and the reconstructed track length, the time of flight detectors are able to provide a β-information of the particles (see Figure 4.2, right). In addition, both detectors, in combination with the start detector signal, are providing the readout of HADES with a multiplicity trigger.

4.4.1 TOF

The **T**ime-**O**f-**F**light wall is a scintillator based TOF detector. The TOF is build from 384 scintillator rods, that are arranged in modules of eight rods. Each sector consists of 8

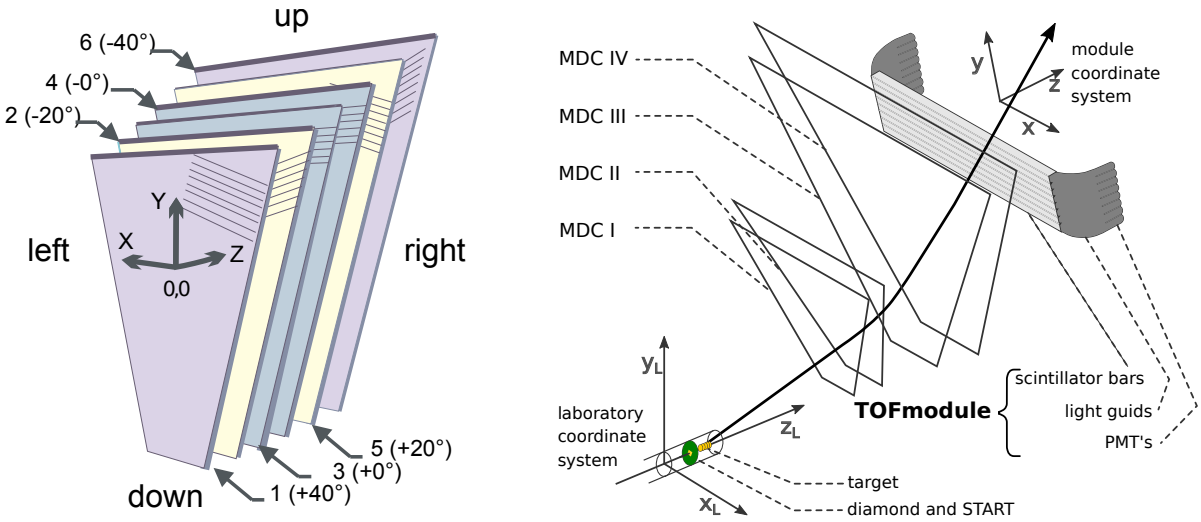

Figure 4.2: **(left)** Schematic drawing of the six layers in an MDC chamber with their differing wire orientations [113]. **(right)** Schematic drawing of track reconstruction in HADES using the MDCs and the TOF detector [117].

such modules, where the inner most 192 rods have a size of 20×20 mm^2 and the outer most a size of 30×30 mm^2. The rods are made of Bicron BC408 plastic scintillators with a length from 1475 mm to 2365 mm, depending on the position [118]. A light guide with a length of 200 mm and a bending angle of 65 ° is attached to the outer rods (see Figure 4.2, right). The inner rods are attached to a light guide with a length of 100 mm and a bending angle of 67.5 °. This light guide is changing its shape from the squared shape to a cylindrical shape for the attachment of a PMT. PMTs are attached on both sides of each rod, giving the possibility to determine the hit position in the rod.

4.4.2 RPC

The **R**esistive **P**late **C**hamber of the HADES detector is an upgrade of the previously used TOFino detector. The new RPC provides a higher rate capability with an excellent time precision in the order of 72 ps and better [119], that is needed for the operation in Au+Au collisions. The detector is made of 1116 cells, divided in six sectors with an active area of around 8 m^2. Each of the trapezoidal shaped sectors is build with 3 columns and 31 rows in two overlapping layers (see Figure 4.3,left). Each row and column is adjusted in size between 2 and 52 cm, respectively 2.2 and 5 cm, to fit the resolution requirements in the individual regions of the HADES acceptance [120].

Each cell is a stack of 3 aluminium cathodes/anodes with 2 glass plate electrodes (2 mm thick) and a 0.27 mm gap filled with a 90% $C_2H_2F_4$ + 10% SF_6 gas mixture in between. Each cell is surrounded by an aluminium shield, that is insulated with a Kapton laminate. A PVC plate with springs is giving a constant pressure on the chambers insides to hold everything in place (see Figure 4.3,right) [119, 120].

4.5 ECAL

The **E**lectromagnetic **CAL**orimeter (ECAL) replaced the previously used Pre-Shower detector. It is in operation since the 2019 beamtime and gives new capabilities in energy measurements to the HADES experiment.

The full ECAL is mounted on rails that allow a movement along the beam axis. It covers an acceptance of $16°<\Theta<44°$ and almost full azimuthal angle as it follows the six sectors of HADES. Each sector hosts 163 lead glass crystals with dimensions of $92\times92\times420$ mm^3, summing up to an active area of 8 m^2 and a weight of 15 tons. The lead glass has an index of refraction of 1.708, a radiation length of X_0=2.51 cm and a Molière radius of 3.6 cm. The photons, created by charged particles passing the ECAL,

Figure 4.3: **(left)** Schematic drawing of a full HADES RPC sector [120]. **(right)** Schematic drawing of a single HADES RPC cell [119].

are mostly measured with EMI 9903KB photomultipliers. In addition to these PMTs, Hamamatsu R6091 PMTs are planed to be used in ≈400 modules. An optical fiber is attached to the ECAL module to allow for calibration [121]. The complete module is fixed in a brass container to give the needed strength to each module. The six sectors of ECAL are equipped one after another in symmetric acceptance. During the march 2019 beamtime, four sectors were equipped.

4.6 HADES DAQ and Event Building

The HADES data acquisition is a combination of a dedicated field programmable gate array (FPGA) based readout directly at the HADES sub detectors and a commercial Ethernet network for the data transport to the server farm. The FPGA-based DAQ hardware are multi-purpose Trigger and Readout Boards (TRBs) in different versions (TRB3, TRB3sc, DiRICH, . . .) that implement the custom network TrbNet, utilizing optical links [122].

Standard TrbNet is running on 2 Gb/s links between different TRB boards. The data transported on these 8Bit/10Bit encoded SERDES connections are separated into three virtual channels: trigger channel, slow control channel and event data channel. In case of the triggered HADES experiment one dedicated central trigger system (CTS) is controlling the readout of the full detector with all subsystems. The limiting factor on the achievable data rate is defined by the round trip time of the trigger signal and the busy-release signal from the endpoints. To achieve high rates of 100 kHz, the TrbNet was developed [122].

The virtual channels in TrbNet are treated separately with individual buffers for each channel on a network node. An arbiter logic switches between the virtual channels, even within a running transfer on one channel, after a complete packet. This is needed to guarantee the smallest possible latency for trigger channel messages. These TrbNet data packets have a size of 80 bit (16 bit of header and 64 bits of data) to allow a low granularity. The transfer of data has to be answered from the receiver to prevent buffer overflows. In addition safety layers as error detection are implemented in the TrbNet nodes [122, 123].

More details on the implementation of TrbNet can be found in [123] and in Chapter 7.

A trigger signal for the HADES detectors is generated from different possible sources. A combination of start detector signals and multiplicity as well as e.g. a trigger pulse from the RICH laser input are trigger generators. Trigger generators are used to supply the CTS with a fast input signal. Based on the input CTS is deciding whether a trigger is accepted. An accepted trigger leads to the output of a reference time signal via dedicated differential cables to all sub detectors. In parallel a LVL1 trigger message is transmitted via the trigger channel to provide additional information as the trigger type, the trigger number or a random code. Based on the trigger, the FEE is read out and all available data is written to buffers. The endpoint boards are all sending a busy release signal back to the CTS to clear for the next trigger.

The data readout of the FEE buffers is controlled by the CTS, too: It sends a readout request via the data channel to the FEE readout handler. The readout handler controls

the readout of the data from the buffers based on the CTS readout package informations as e.g. the information about the event builder where the data has to be send to. The data is transmitted over (mostly) optical fibers to hubs. Hubs are dedicated TRB boards merging the TrbNet data from all connected downlinks (front-end boards, but also other hubs) to one combined data stream. The combined data stream is sent to the next level of hubs.

Each sub detector has a dedicated layer of hubs that is transmitting the combined data via commercial Ethernet network switches to the event builder servers. Therefore the TrbNet data is packed into the HADES common event structure and later on equipped with UDP headers [122, 123]. The use of a commercial network allows the use of standard servers and switches that are well tested and could be purchased out of the shelf.

The HADES event builders are receiving the UDP packets, calibrating and combining the data to actual events that are written to tape for further data analysis. The HADES event building is based on the Data Acquisition Backbone Core (DABC) software [124].

All TrbNet based boards are accessible via slow control. The slow control is implemented in the third virtual channel, that has the lowest priority in data transfers. Each board is equipped with a 1-wire temperature sensor or an I^2C UID integrated circuit (IC). These ICs are giving an unique ID to each of the boards. TRB boards are accessible via 16-bit addresses that are matched to the unique IDs of boards based on a database for each sub detector. Next to the TrbNet address of a TRB board, broadcast addresses are implemented to allow the read out of different clusters of boards and registers in one slow control package. The access of the flash memory and the possibility of a reboot of TRB boards based on slow control messages is a powerful tool for fast updates of the firmware of boards, as well as to restart boards individually. The access of SPI and I^2C interfaces via slow control registers is provided, too. The slow control of TrbNet gives a high power in monitoring and control capabilities of the subsystems as presented in the case of the HADES RICH upgrade in Chapter 5.

CHAPTER 5

Upgrade of the HADES RICH Detector

The HADES RICH detector is part of the HADES experiment since the earliest days and of outstanding importance in electron identification. The detector is located in the field free region of HADES around the target with a full acceptance in azimuth angle, except of six holding structures matching the six magnet sectors, and a polar angle acceptance of 18°<θ<80°.

The combination of the information from the RICH detector with tracking and momentum information from the other sub detectors with the very low material budget and the high acceptance of HADES gives access to the di-lepton spectrum measurements.

The RICH detectors radiator gas was chosen to be C_4F_{10}. C_4F_{10} has an index of refraction of n=1.00151 resulting in γ_{thr} ≈18 [125]. Leptons with momenta p_e>9.3 MeV (see equation 3.10) are above the Cherenkov threshold and can produce Cherenkov photons in the radiator volume. However, hadrons can produce Cherenkov photons starting from 2.5 GeV, muons from 1.9 GeV on, making the HADES RICH an especially hadron blind detector.

The RICH detector is a very compact detector with a diameter of 1580 mm. Depending on the polar angle of the electron track, the radiator provides a radiation length of 36 cm at θ=20° to 65 cm at θ=80°. Cherenkov photons are reflected and focused by a spherical mirror with low material budget but excellent optical properties such as high reflectivity. The focus of the mirror is matched by a CsI based photo detector plane in a methane atmosphere. The geometry of the mirror and the photo detector was chosen to keep the ring diameter at an almost constant value.

A CaF_2 window is separating the C_4F_{10} radiator gas from the CH_4 counting gas for the CsI photodetector. A detailed overview on the schematic setup of the original HADES RICH detector is given in Figure 5.1.

The following chapter will give an full overview of the upgrade of the existing RICH detector. Nevertheless it will simultaneously present developments and measurements for the upgraded RICH, that are key parts of the work behind this thesis: The flashing, testing and bookkeeping of the 856 DiRICH boards with its different FPGAs as well as the improvement of the firmwares are a major contribution to the full upgrade of the RICH (see section 5.2.2). Next to the preparation of the hardware of the RICH, the RICH related DAQ software with different scripts and settings was developed to make a successful beamtime of the HADES RICH detector possible. Furthermore a system for the measurement of the magnetic field and its monitoring inside the RICH vessel near

the MAPMTs was developed and integrated into the overall TrbNet readout and HMON monitoring (see section 5.2.1.1). The additional installation of a temperature monitoring between the MAPMTs and the backplane itself was a key part of the safe operation of the detector, but also for the quality of the taken data. Based on these temperature measurements, a low voltage interlock system was developed to protect the MAPMTs from high temperature, increasing noise and accelerated ageing (see section 5.2.1.2). The installation, connection and the control of the high voltage system is an additional part of the work behind this thesis and a very important part for the data quality of the RICH detector as the HV directly influences the measurement of the Cherenkov photons (see section 5.3.1). Related to all the previously mentioned projects, the monitoring and control of the HADES RICH detector, from temperatures over the gas and powering towards readout features was developed from scratch, based on the general HADES monitoring (HMON) (see section 5.5).

5.1 Overview of the HADES RICH Detector

5.1.1 Mirror

The Cherenkov photons form the radiator gas are reflected and focused by a spherical VUV-mirror. The mirror is segmented into 18 individual tiles in 6 sectors. The low radiation length in the compact RICH is limiting the number of produced photons. In order to achieve a good ring reconstruction with more than 10 hits per reconstructed ring [113], emphasis was put on a very high quality of the optical components while a low material budget was aimed at [126]. The full mirror plane is enclosed by a thin carbon fibre shell of 0.4 mm thickness to increase the detectors stability, while minimizing the material budget [113]. The requirements of the mirror's substrate material

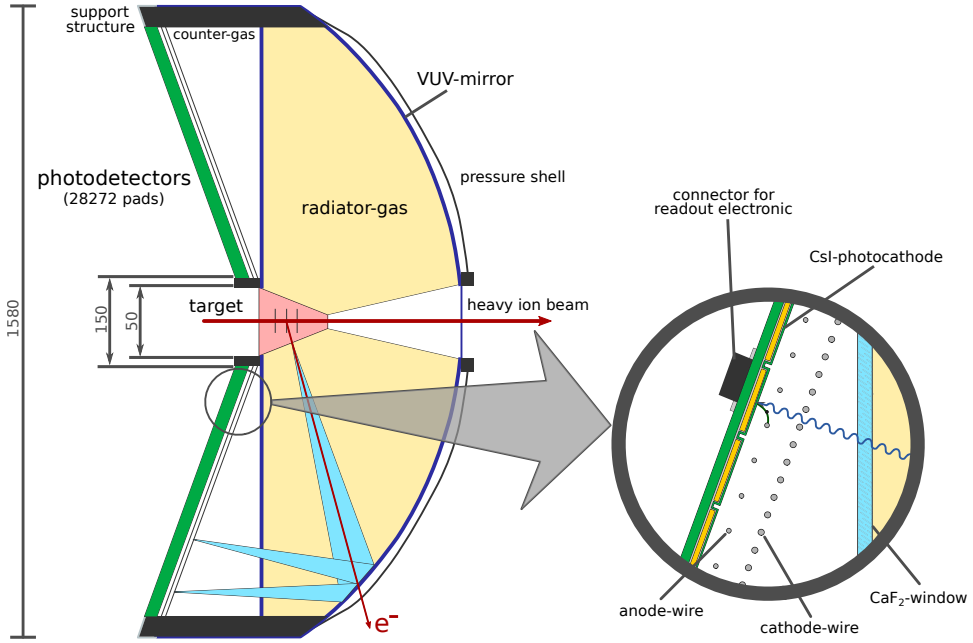

Figure 5.1: Schematic view on the RICH detector before the update. A zoom in the photo detection region is provided for a more detailed view. The figure is adapted from [126, 127].

parameter	value
Outer diameter D	1440 mm
Radius of curvature R_i	872 mm
Substrate thickness d	$\leq$ 2 mm
Radiation length X_0	$\geq$ 20 cm
Reflectivity R (λ=150 nm)	$\geq$ 70 %
Surface roughness σ (rms)	$\leq$ 3 nm
Surface slope error SSE_{80}	$\leq$ 1 mrad
Areal density ρd	$<$ 0.3 g/cm^2

Table 5.1: Optical and geometrical parameters of the HADES RICH mirror [113].

was defined to be $d/X_0 \leq 1$ % with the substrate thickness d. A high reflectivity as well as a high precision on the surface was needed to compensate the back-draw of a short radiator length and limited wavelength acceptance.

Three of the 18 mirror pieces are combined to fill one of the six sectors of the HADES magnet coil. A support structure in between the sectors is holding the single mirror parts in place and allows for exact positioning. Glassy carbon is used as mirror substrate to minimize background from external pair production, multiple scattering and energy loss due to bremsstrahlung [113]. Nevertheless, the mirrors of two out of six sectors are glass mirrors.

All tiles are grinded to 2 mm thickness as listed in the mirror parameter Table 5.1. The surface of the carbon was polished to a roughness according to Table 5.1 and afterwards cut to the final dimensions of its position in the mirror plane. These high quality mirror tiles are coated with a 20 µg/cm^2 aluminium reflective layer. A protective layer of 12 µg/cm^2 MgF_2 was coated on top to keep the achieved reflectivity of R$\approx$ 80 % constant over years. The achieved reflectivity is in good agreement to float glass mirrors. A surface slope error SSE_{80} was measured between 0.5 and 0.8 mrad, whereas the surface roughness is $\sigma \approx$2-3 nm [113].

5.1.2 Window and Gases

The separation between the photo detection volume, filled with CH_4, and the radiator volume is the second critical item for the optical properties. The window was build as a combination of 64 hexagonal discs of monolithic CaF_2 crystals that are glued together to a disc of 1500 mm diameter.

The 5 mm thick crystals are individually polished and measured to achieve the best transmittance. The transmittance reaches from 70% at λ=145 nm to above 90% at λ=190 nm. A stainless steal support structure in the position between sectors and an additional sealing is protecting the window from gravitational forces as well as from mechanical stress due to e.g. thermal expansion or gas pressure gradients [113, 126].

The detector is filled with around 700 litres of gas at a pressure of $\approx$ 10-40 mbar above ambient conditions. The purified C_4F_{10} radiator gas was circulated in a closed system with liquidisation and a liquid buffer reservoir. The complete gas is controlled by a PLC-controlled gas supply system that regulates the pressures and keeps the pressure difference between the radiator and photo detector below 3 hPa to protect the fragile CaF_2 window [113].

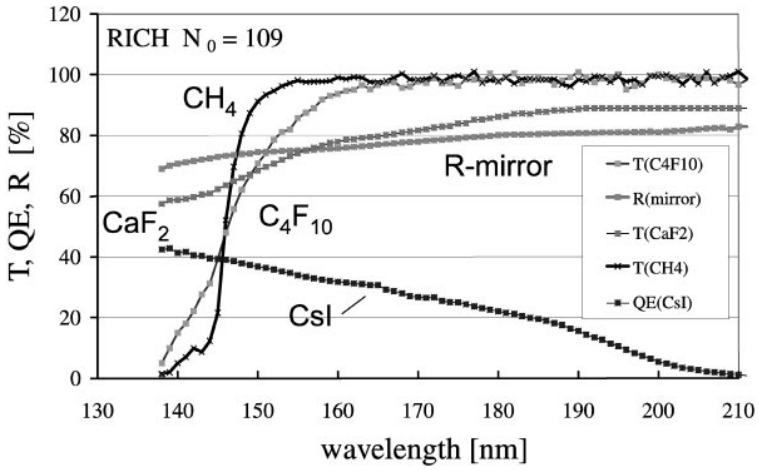

Figure 5.2: Quantum efficiency QE of CsI photo converter, mirror reflectivity R and the transmission T of the radiator and detector gas as well as the CaF_2 window is shown [126].

5.1.3 Original Photodetection Plane

The original RICH detector used thin-gap multi-wire proportional chambers (MWPC) with CsI cathode pads as photo detection plane. Six individual MWPCs were positioned in a pyramidal shape to match the focal plane of the mirror as good as possible. Each MWPC had a PCB based photosensitive cathode plane. A triangular shaped PCB is segmented in 4712 pads and gold plated conductive layers. All pads are individually coated with a Resin Stabilized Graphite (RSG) as well as a reflective CsI coating. The CsI layer converts photons into electrons that are amplified by a high voltage between the cathode plane, cathode wires and anode wires. Cathode wires are made from d_C=50 µm, the anode wires from d_A=20 µm, thick Gold-plated tungsten. Voltages of 2450 to 2550 V were used to achieve a visible gas gain in the CH_4 of $(3-9)\cdot 10^4$ [113]. The 28272 pads of the full RICH detector were readout by custom front-end electronics, attached to the backside of the CsI-PCB.

The CsI has a quantum efficiency of about 40% at 140 nm wavelength, decreasing to 0% at 220 nm. Figure 5.2 illustrates the counter play between the quantum efficiency of the readout and the transmittance of the radiator gas. This results in a small window between $\lambda_{min} = 145$ nm and $\lambda_{max} = 220$ nm, where the RICH was able to detect photons. All the efforts in a high optical quality and a dedicated photo detection result in a figure of merit $N_0 \approx 109$, corresponding to 12-21 detected photons per ring [126].

5.2 Towards a RICH future

The HADES RICH detector is in operation since 1999. Over 20 years of operation in heavy ion collisions are resulting in the signs of ageing, resulting in a significant reduction on Cherenkov photon statistics. Especially the 2014 Au+Au beamtime suffered in the ring identification from a reduction in statistics of 40-50% over the last decades [128].

With respect to the future operation of HADES in FAIR phase-0 beamtimes as well as an important part in the FAIR CBM pillar at SIS100 an update of the RICH is needed. The development of the CBM RICH detector with a newly developed front-end electronics based on TrbNet and the existence of already purchased Hamamatsu H12700B-3 MAPMTs offered the unique chance of an upgrade for future FAIR operation (see Figure 5.3). In parallel the upgrade is a large scale prototype test of the upcoming CBM RICH detector.

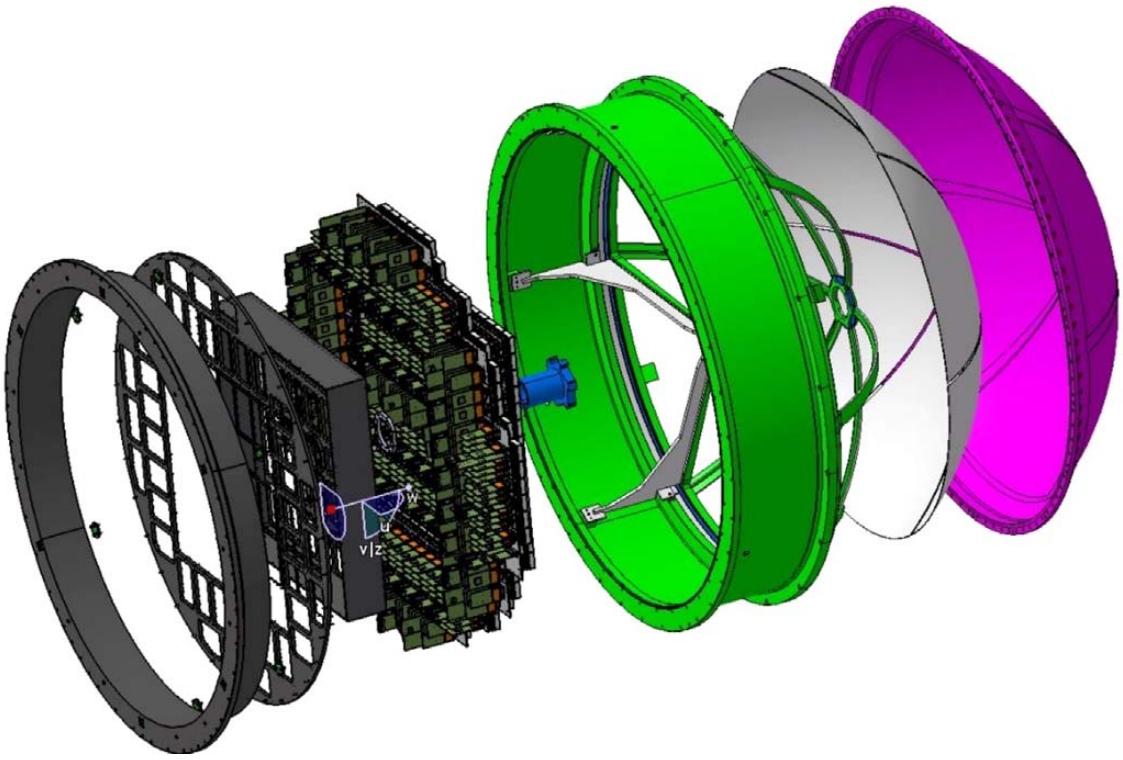

Figure 5.3: Explosion drawing of the upgraded HADES RICH detector geometry with the new TrbNet based front-end electronics and the new MAPMT photo detection plane [128].

The upgrade towards a new photon detection as well as a new readout concept comes with great synergies between the two future CBM pillar experiments, but also PANDA as additional user of the FEE. On the one hand the functionality of the concept of the DiRICH FEE can be verified and improved. On the other hand a lot of progress in the understanding of the new detector, its parameters, peripherals as power supplies and the training of young scientists in the harsh environment of production beamtimes could be done.

5.2.1 Photodetection Plane

The joined effort of the CBM RICH and HADES RICH team resulted in an upgrade of the old CsI photon detector camera to a new state of the art MAPMT based camera. The upgrade is an interplay between the new MAPMT technology and the newly developed DiRICH FEE. As introduced in section 3.3.7 the MAPMT photo detector is connected to a PCB backplane. The backside of the backplane is equipped with the corresponding FEE including power and trigger distribution as well as data transport. The backplane PCB of the DiRICH system is the connection between the inner gas volume of the detector and the outer environment. Therefore the backplane has a pronounced position as the sealing for the gas volume.

Each backplane is screwed to an aluminium flange with M2x8 screws at a torque of 0.6 Nm. A 1.5 mm diameter NBR70 sealing rubber band is inserted in a notch in the aluminium flange. This rubber ring seals the connection between each PCB and the aluminium. The sealing is needed for the gas volume but also improves the light tightness of the detector. The individual PCBs are arranged symmetrically around the beampipe (compare to Figure 5.4) with a gap of 1 mm in between.

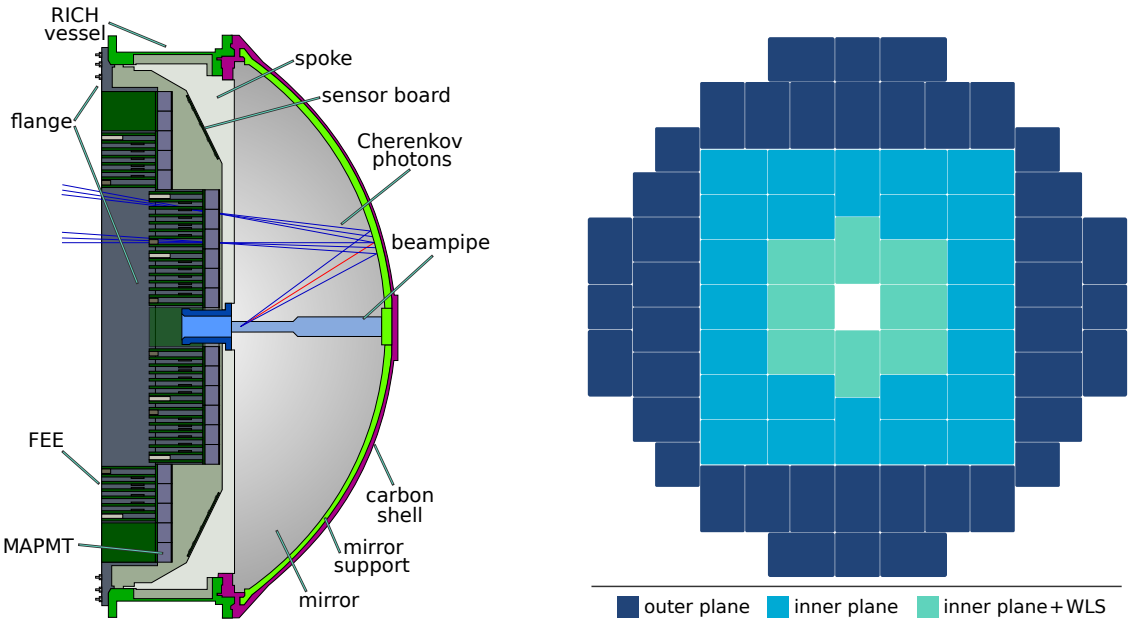

Figure 5.4: **(left)** Schematic drawing of the upgraded RICH detector in side view. The position of the PMTs in two planes with respect to the spokes and the mirror is shown. **(right)** Scheme of the backplane of the RICH detector with the different backplane orientations and the additional WLS coating in the innermost region. The inner and outer plane are shown in different colors.

The positioning of the photodetector is constrained by the rectangular size of each PMT respectively each backplane and the focal plane of the mirror. The detection plane is separated in an inner and an outer part to match the mirror focus sufficiently good with the available rectangular backplanes.

Figure 5.3 indicates on the left side the aluminium flange with the PCB cut outs in its three pieces. The inner plane is screwed and glued to a rectangular aluminium frame with 100 mm depth. The frame is glued and screwed to the outer aluminium plane, forming the complete sensitive plane. An additional ring was constructed that matches the geometry of the old RICH vessel. This ring is the adapter plate between the old RICH vessel and the new camera. In parallel, the depth of the ring is controlling the distance to the mirror and therefore the correct positioning in the focal plane. A second vessel with the same mounting interface as the old RICH was build as a test stand for electronic measurements. Later on this vessel was used as a mount for the then replaced CsI photodetector. The geometry of the RICH spokes, that match the six sectors of HADES, is changed to fit to the new camera. In addition, a flat middle part is prepared to hold an additional custom PCB.

The inner aluminium parts of the new photo detector are painted with NEXTEL Velvet-Coating 811-21. This black color provides an absorption of up to 98% of all photons. This is needed to absorb nearly all of the produced photons that are not reaching the MAPMTs and prevent from reflections towards the mirror or even the MAPMT plane.

The full upgraded camera structure is equipped with 66 standard backplanes with 2×3 MAPMTs attached. The outer regions of the RICH detector are limited by the geometry of the old RICH. In order to maximize the active area, an additional backplane was developed. 8 backplanes with a squared shape for the connection of 2×2 MAPMTs

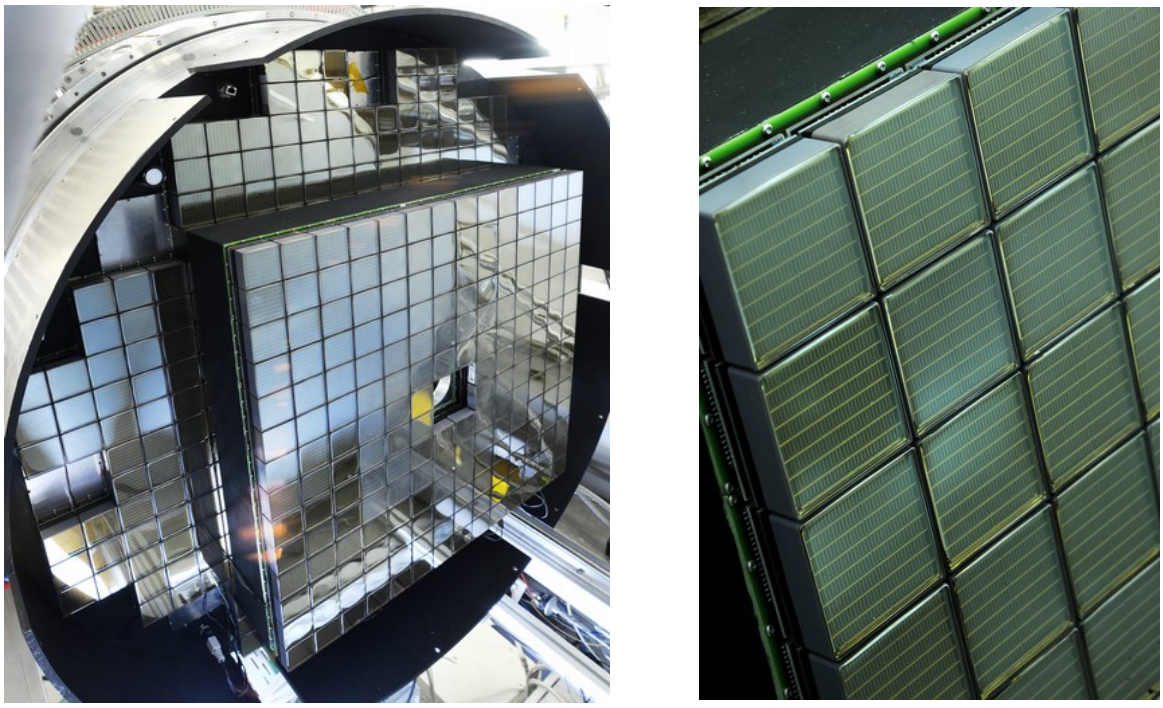

Figure 5.5: MAPMT plane of the upgraded HADES RICH detector. **(left)** Picture of the equipped MAPMT photodetection plane. The 2×2 backplanes are still missing. In the inner part, the WLS coating is visible by a less shiny surface. **(right)** Zoom on a corner of the MAPMT plane. The individual pixels of the MAPMT as well as the backplane PCB and its screws to the aluminium are visible. Photos by G. Otto, GSI.

are added to the RICH. Consequently this backplane holds one combiner, one power module and 8 DiRICH modules (see Figure 5.4, right).

After the exchange of the old CsI based photodetection plane with the new MAPMT based camera the MAPMTs are inserted. The Camera is mounted on a rail structure. This structure allows the movement in beam direction and therefore the opening of the RICH vessel. The maximum space between the camera and the vessel in the open state is roughly 1 m. This space is needed to connect the 428 H12700B-3 MAPMTs to the backplanes and, with respect to future CBM beamtimes, to unmount the MAPMTs as it is planned to use these in the CBM RICH, too. The MAPMTs are grouped by gain to one common backplane. This ensures a constant gain for all PMTs on one backplane and is needed for the high voltage control. The usage of a custom made mounting tool for the H12700 improves the safety of inserting the MAPMTs. This tool prevents local pressure on the MAPMTs entrance window and makes an unmounting possible.

The innermost part of the MAPMT plane is covered with a wavelength shifting (WLS) coating (see Figure 5.4) [86, 107, 129]. The WLS coating is limited to the innermost region only as the radiator length is the shortest in this region and thus the lowest amount of Cherenkov photons is produced. The coating with p-terphenyl counteracts the shorter radiator length and shifts photons from the ultra violet wavelength region into the sensitive wavelength of the MAPMTs. Previous tests of the WLS coating have been done in a beamtime test at COSY, Forschungszentrum Jülich. Analysis of the beamtime data revealed an increase in number of hits per ring of 10%−20%. The WLS coatings fast decay constant was measured to 2.35 ns and is in good agreement with

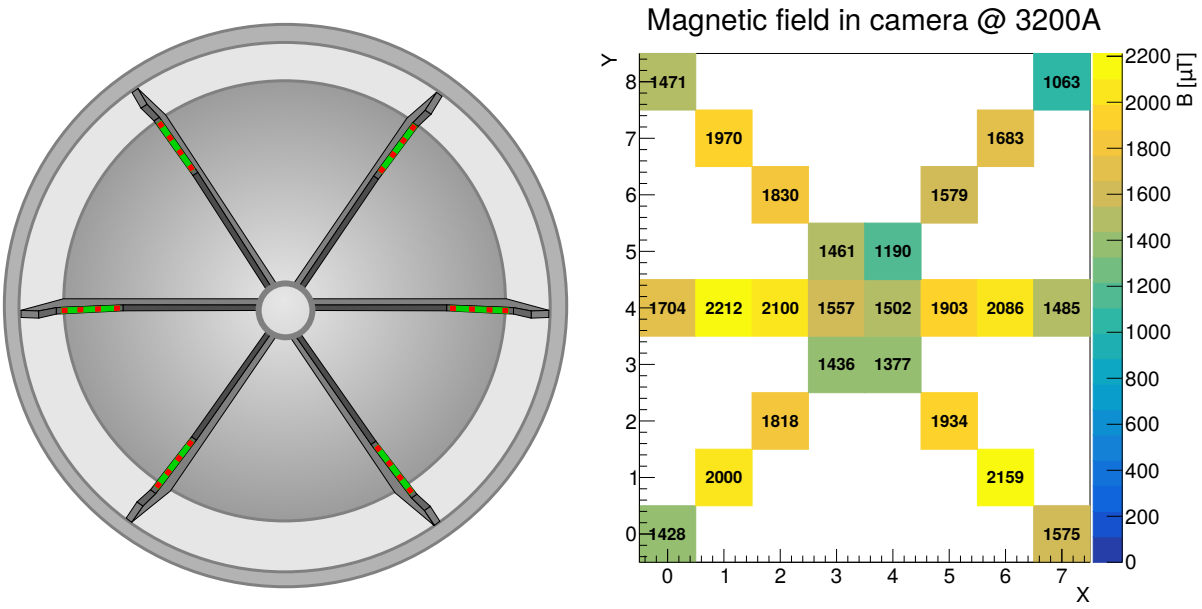

Figure 5.6: **(left)** Schematic drawing of the positions of the spokes and the mounted sensor boards (green). The position of the four Melexis MLX90393 ICs are indicated with a red square. **(right)** Measurement of the magnetic field in µT in the HADES RICH at full magnetic field (3.2 kA current). The diagram is reflecting the individual positions to the schematic drawing on the left side.

time-resolved fluorescence measurements in the laboratory. For more details on the WLS coating and its analysis see [129].

The nearly fully equipped MAPMT plane is shown in Figure 5.5. The inner part of the plane is less shiny, indicating the WLS coated MAPMTs. The full photodetection plane consists of 428 MAPMTs with 27392 pixels in total. Figure 5.5, right picture, shows an enlargement of the plane such that even single pixels of the MAPMTs are visible.

5.2.1.1 Magnetic Field Measurement

MAPMTs are constructed with a dynode chain for electron multiplication. The existence of a magnetic field has a direct influence on the charge multiplication process in the dynode chain as the electrons are bent by the field. Measurements in the laboratory revealed an efficiency reduction of the MAPMTs in magnetic fields, especially in the outer pixels and primarily in the Z-direction of the MAPMT. In the HADES RICH a maximum field strength below 3 mT in the region of the MAPMTs is a central requirement. A soft iron shield is screwed in a radial shape around the MAPMT plane with cut-outs in the region of the spokes. The cut-outs are visible in Figure 5.5, left picture. The application of soft iron and its influence on the magnetic field at the MAPMTs was simulated. A sufficient reduction of the magnetic field in the MAPMT plane was seen in the simulations, leading to a simulated maximum field of below 3 mT.

In order to verify the real magnetic field at the position of the MAPMTs, custom sensor PCBs were produced and mounted to the inner spokes of the RICH detector. The mounting position of the sensors is in the region with the highest field and the closest position to the MAPMTs, see Figure 5.6, left. The positioning on the spokes is

chosen, as on the one hand the field is measured between the magnet coils and the MAPMTs. On the other hand, the location of the PCB is not reducing the acceptance. The sensor PCB is equipped with four Melexis MLX90393 sensors. An ATmega168PA microcontroller is used for the readout of the temperature and magnetic field values of the sensors and the data transmission. The measured values are transmitted to a dedicated TRB3sc via UART. The connection to the TRB3sc is realised by RJ45 feedthroughs in the aluminum frame of the photodetection camera and standard Ethernet cables. A special UART entity is used to readout the magnetic field boards and parse the measured float values to 32-bit register values, which are available via TrbNet slow control. A more detailed introduction in the sensor board is given in [130].

A detailed study of the sensor behaviour in a magnetic field, including calibration, has been done in the laboratory with a Helmholtz coil in a climate chamber with different temperatures (see appendix B). All measured values are further corrected to the earth magnetic field strength and the 3-axis values are combined to the total magnetic field.

Figure 5.6, right, represents the measured magnetic field in the individual sensors at a magnet current of 3200 A, the maximum current of the HADES dipole magnet. Figure 5.7 represents the measured values for all 24 sensors at 1000 A, 2000 A, 3000 A and 3200 A. As expected, the measured values show a linear behaviour between the measured magnetic field and the applied magnet current.

A maximum magnetic field of 2.21 mT was measured at a magnet current of 3.2 kA at arm 4, sensor 1. A maximum field of 2074 mT was measured in the y-axis of the sensor, matching the y-axis of the MAPMT plane. The x- and y-axis of the MAPMT is less

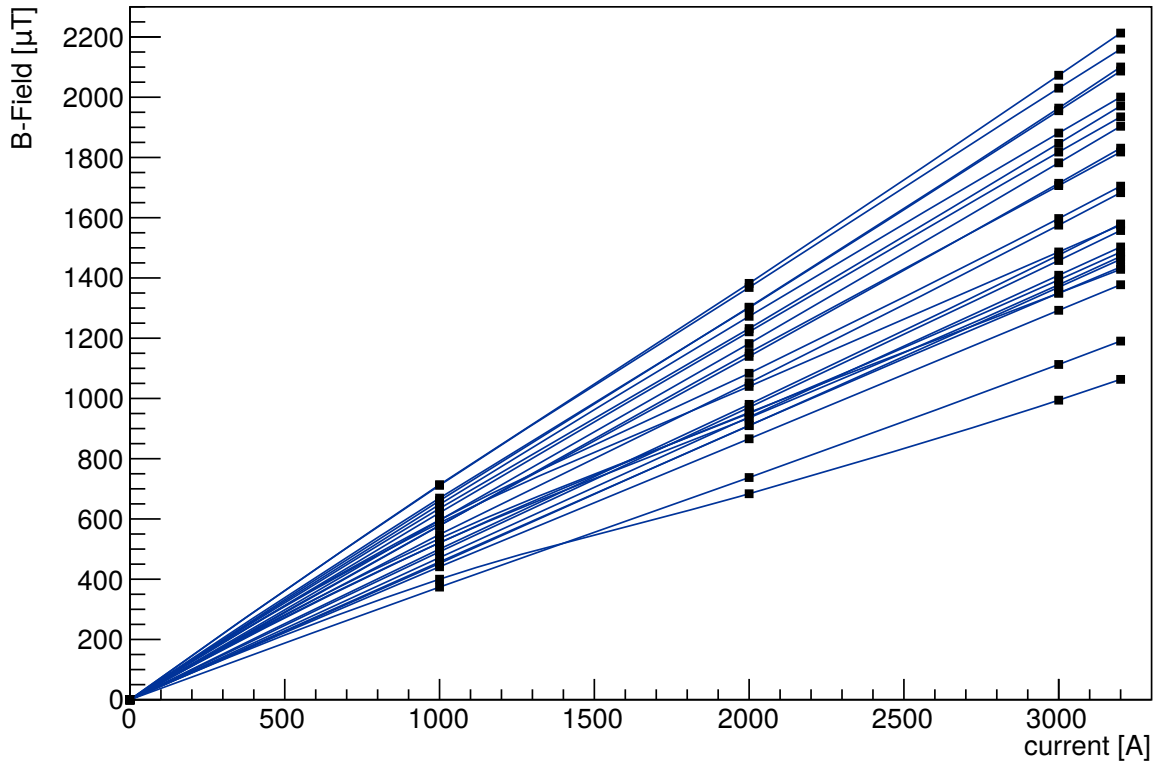

Figure 5.7: Measured magnetic fields in the HADES RICH on all sensors at different magnet currents (1 kA, 2 kA, 3 kA, and 3.2 kA). The measured fields are proportional to the current.

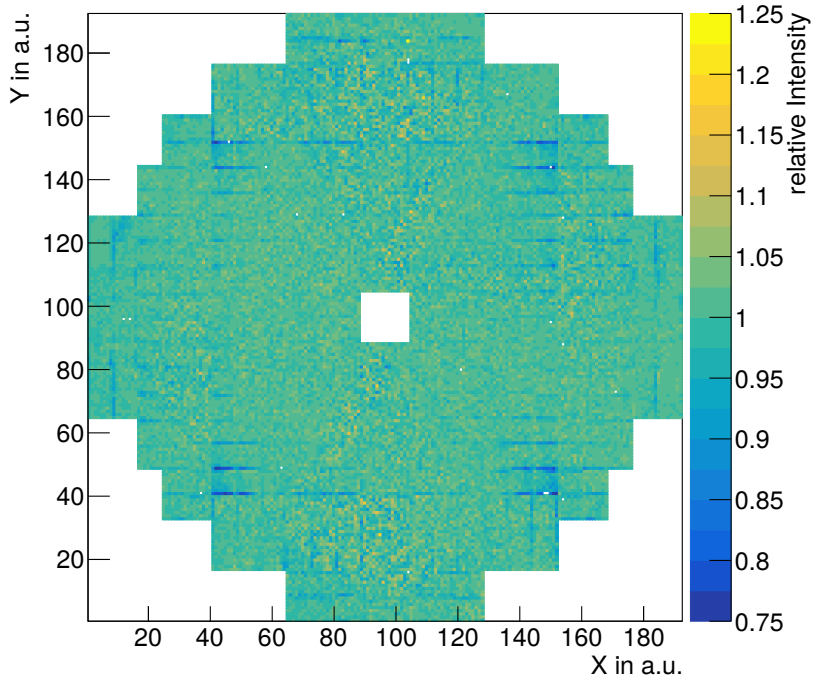

Figure 5.8: Ratio between the RICH detector rate with the influence of the magnetic field at 3kA and a magnetic field at 1 kA. A reduced measured rate is observed in the corners of the inner plane, where the MAPMTs are closest to the magnet coils. The figure is shown in the electronic view of the HADES RICH. The analysis was done by Jörg Förtsch [131].

sensitive to the magnetic field than the Z-Axis. Hence the influence of the magnetic field in the main detector region is acceptable for the detector operation. The closest distance between the sensors and the MAPMTs is near the corners of the inner MAPMT plane. Measurements of the field in this special region result in 2 mT. Unfortunately the corners of the inner plane protrude further to the magnetic field than the sensors. Therefore no reliable upper limit from a sensor measurement can be given in this region. Due to the closest distance to the magnetic field and a magnetic field most likely above 2 mT, the highest influence of the MAPMTs efficiency is expected in this regions.

Figure 5.8 shows a ratio of RICH pixels based on pixel rate measurements with a laser as light source under influence of the magnetic field of the dipole at 3 kA and with a magnetic field at 1 kA. The shown figure represents the view from the RICH electronics. A reduction of the rate of up to 30% is measured at the inner corners of the RICH, where the nearby sensor measurements already predicted the strongest influence of the magnetic field. The reduction is most prominent at the corner rows of the MAPMT pixels. The measured ratio confirms the expected decrease at the measured rates for an increased magnetic field.

To summarize, the use of magnetic field sensors in the radiator volume of the RICH confirmed the influence of the field on the MAPMTs and confirms the feasibility of a operation at the full magnetic field of HADES. An upper limit on the field in the main part of the RICH detector plane of 2.2 mT was measured at the maximum magnet current of 3.2 kA. The magnetic field in the corners of the inner region could not be evaluated with the available measurement techniques and is expected to be a bit larger.

As a trade of from the measurements, the decay time of the magnetization of the soft iron shield could be measured as $\tau = (21.61 \pm 6.05)$ days. Therefore the magnetic field was measured over several days after the magnet was switched off. The decrease of the magnetic field in the measurement period was fitted with an exponential function and the decay time was extracted.

5.2.1.2 Interlock

Next to the influence of the magnetic field, the MAPMTs can suffer from increased dark rates. The integrated charge of a MAPMT over the operation under high voltage defines the lifetime of a MAPMT. An increase in dark rate by a factor of two would lead to half the lifetime as under normal dark rate and furthermore an increase of noise in each event. The dark rate of a MAPMT is increasing with temperature. Measurements on the temperature dependent dark rate of the H12700 unveiled roughly a doubling of the rate at a temperate increase by 5°C. A temperate of the MAPMTs above 30°C has an increased dark rate, but is still on an acceptable level. A temperature above 35 °C is critical for the operation of the detector. Next to the increase of the dark rate, the measurement shows spikes in the rate and therefore an unpredictable behaviour. More details on the temperate dependent behaviour of the MAPMTs can be found in [84, page 74f.].

A temperature based interlock system is implemented in the HADES RICH detector as a protection of the MAPMTs. The interlock system is measuring the temperature in between MAPMTs and the backplane at different positions on the detector (see Figure 5.9, left). As the first step towards an interlock, these additional temperature sensors are needed as a standard backplane has no temperature measurement IC. Standard 1-wire digital thermometer sensors DS18B20 in TO-92 package are used for the temperature determination. The gap between a MAPMT and the backplane is limited by the pin-header connectors distance and height (free space W×L×H:8×36×7 mm^3).

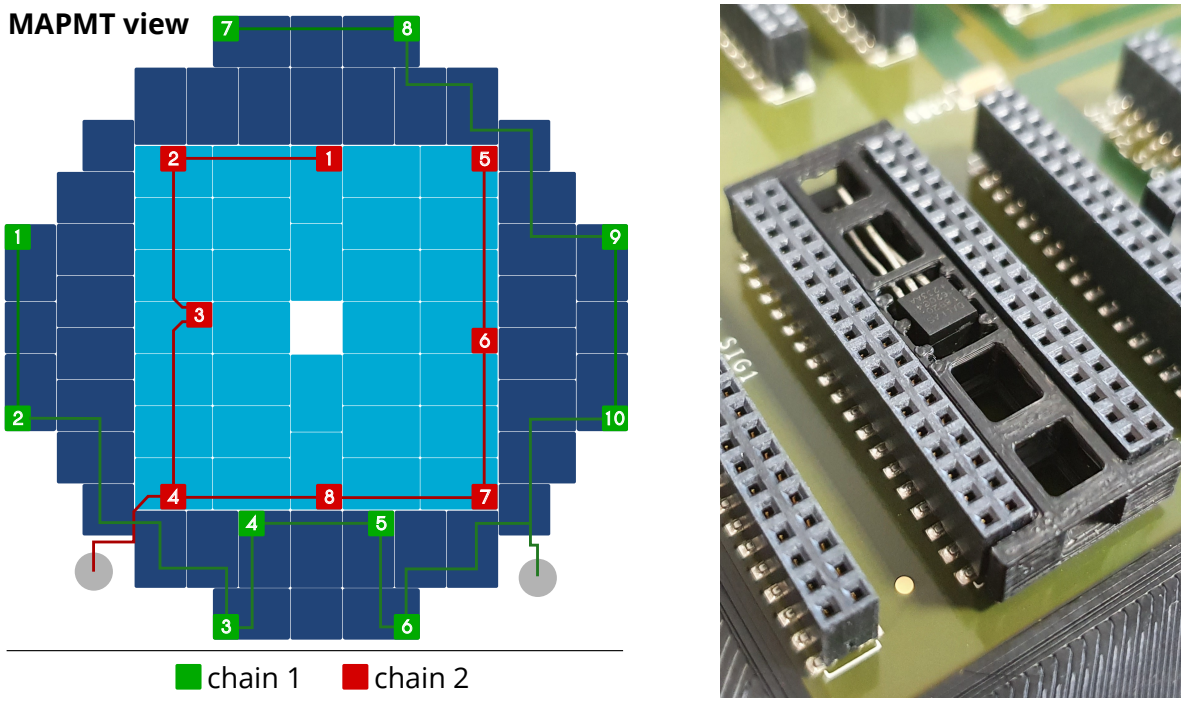

Figure 5.9: **(left)** Schematic view from the MAPMT side on the backplanes. Green indicates the position of all temperature sensors from chain 1. Red represents the positions of the sensors from chain 2. The feed-throughs of the 1-wire lines are indicated by grey circles on the bottom of the detector. **(right)** A close up photography of the DS18B20 holding structure with an attached sensor. This pictures shows a dummy without attached cables and isolation of the pins.

The DS18B20 is mounted in a 3D printed open support structure to get the best temperature flow to the sensors. Sensors are soldered in a chain with thin wires. All conducting parts of the connections are later on isolated.

The HADES RICH is equipped with two chains of sensors, the first is carrying 10, the second 8 sensors. The unique IDs of the DS18B20 are read out before mounting the sensors and mapped to the sensor position on the chain. An overview on the UIDs of the sensors in the RICH detector is given in Table 5.2. Figure 5.9, right, shows the mount of a single temperature sensor in between the MAPMT headers on a backplane. The 3D-printed holding structure is matching exactly this free space and is holding in place by friction forces. The sensor is hold in place by a hole in the mounting structure. Three thin bridges are used as a stabilisation in the mounting structure to keep the sensor in place and still allow an exchange of the heat. The left side of Figure 5.9 shows the location of the 18 sensors on the photodetection plane, including the separation in two chains.

The supply and data wires of the 1-Wire sensor are connected to the pins of the sensor, inside the mounting structure. The final three bus wires of the bus are always guided from sensor to sensor in the central tunnel between the two MAPMT rows on a backplane. The feed-through of the wires from the sensors to the readout board are realised by RJ45 inserts in the aluminium frame of the RICH photo detector plane. The soft iron shielding is prohibiting a direct access to the feed-through in the inside of the detector. As the sensors are connected to the feed-through while the detector is getting closed, an additional lockable plug connector is installed in between the wiring from the sensors to the RJ45 feed-through.

The two chains are using separate feed-throughs and are completely separated on different wires to avoid a loss of all sensors in case of a broken wire or anything comparable. Standard RJ45-Patch cables are used as a connection from the feed-throughs to the readout and control board. Separate RJ45 breakout boards are used to connect the RJ45-cables to the read-out board. A pull-up resistor is soldered in place on the short path between the breakout and the readout board.

A dedicated TRB3sc (TRB3 **s**ingle **c**rate) with a central Lattice ECP3 FPGA is used for the readout of the sensors. The sensor TRB3sc is powered separately to the detector and therefore running stand-alone. Dedicated VHDL Entities are instantiated with the UIDs as generic input to read out the DS18B20 sensors. The temperature values of all sensors are accessible via slow control registers via TrbNet and presented in the

Position	UID chain 1	UID chain 2
Sensor 1	530416523728FF28	3B0000092C430228
Sensor 2	BB04165233BFFF28	BB0000092A30D028
Sensor 3	52031646CD5FFF28	B60000092D9D3C28
Sensor 4	EC0416525116FF28	0E0000092C30AF28
Sensor 5	050416523379FF28	E40000092D682028
Sensor 6	E2041651AEA5FF28	E70000092C430628
Sensor 7	940000092C3B2F28	800000092AE74728
Sensor 8	4B0000092D22BD28	6E0000092AF8EF28
Sensor 9	C30000092B07EA28	
Sensor 10	780000092A277628	

Table 5.2: UIDs of the backplane DS18B20 temperature sensors in the two chains.

online monitoring (see Section 5.5). The FPGA is internally filtering the temperature values for invalid measurements and compares the measured valid temperatures to an interlock value. A hardcoded threshold value for the interlock is hardcoded to 37.0°C in the VHDL code. This value is accessible via slow control at register `0xe120` and can be adjusted as needed by the operator. A restart of the FPGA resets the adjusted interlock threshold to the hard coded value.

In case a measured temperature of at least one sensor exceeds the threshold value, an interlock signal is generated. The generated interlock signal from the FPGA is forwarded to a dedicated interlock PCB that is located next to the sensor TRB3sc in the same rack. A picture of the boards in the crate below the RICH detector next to the hubs of the FEE is provided in Figure 5.13. The interlock PCB is a very simple control board with two relays. Two relays are used to be protected against failures in the relays mechanics. The control signal from the TRB3sc is controlling the switching of the relays with a NUD3105 IC as relay driver. A capacitor is used as a buffer to bridge problems or reloads of the FPGA for several seconds. Consequentially the interlock has a delay of several seconds with respect to the measured temperature. In addition, the

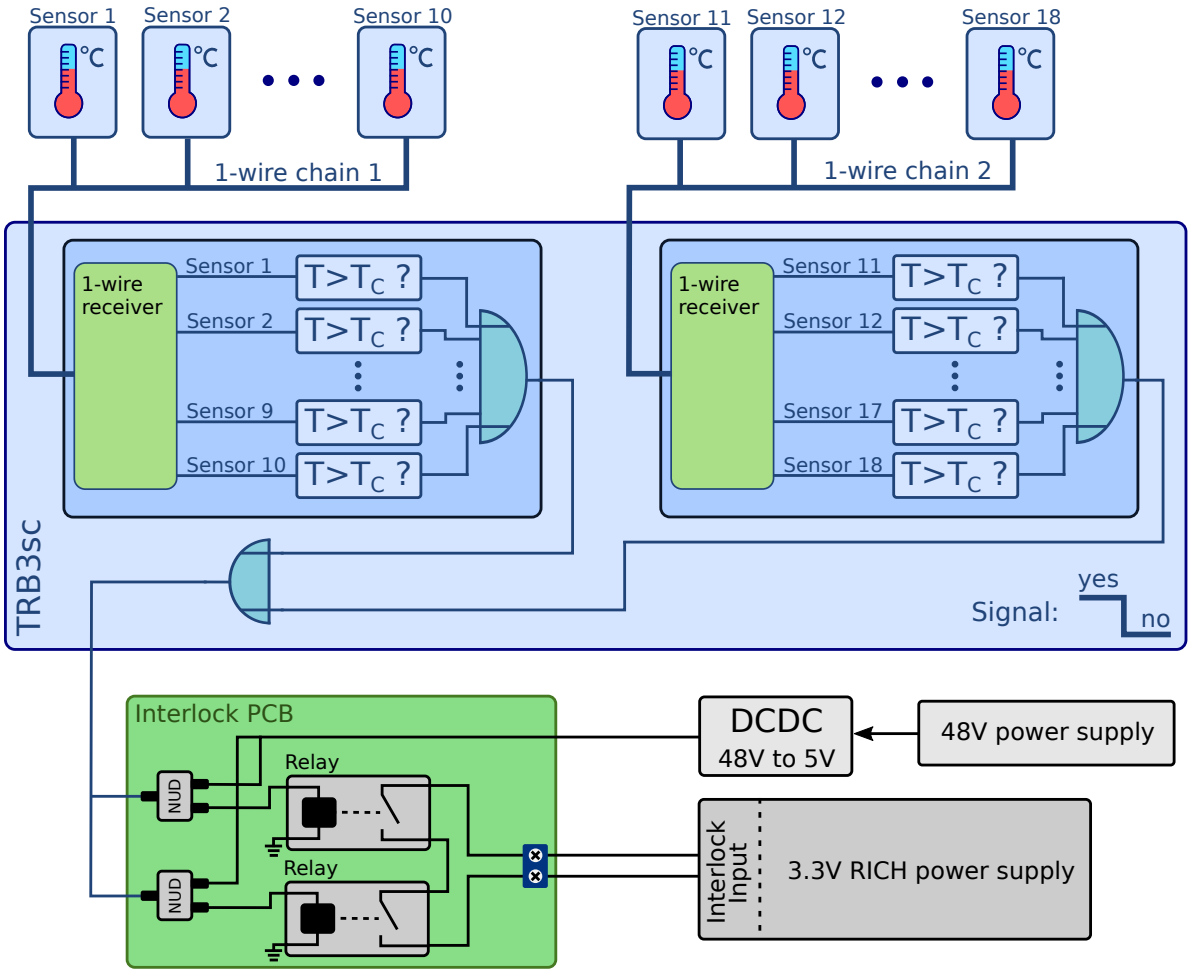

Figure 5.10: Schematic overview of the interlock of the HADES RICH detector. The two DS18B20 chains connect to a TRB3sc. In case a temperature exceeds the threshold temperature T_C, a high signal is generated. Two layers of OR gates generate an output signal, that controls the relays of a dedicated interlock PCB.

PCB is equipped with a switch to bridge the interlock. This switch is only for experienced users and is only a backup for potential problems!

The interlock PCB is connected to the 3.3 V power supply of the RICH detector. In case the measured temperature between the backplane and the MAPMTs is above the threshold value, the 3.3 V power supply interlock is activated and the full FEE of the RICH is switched off. This is the most effective way of an interlock as the FEE is the main source of heat. The voltage has to be switched on by hand if the temperature is back at an acceptable value. In case the readout FPGA is not working or not powered, the interlock is automatically activated.

Next to this hardware based approach a software interlock is implemented. The full low voltage of the RICH detector is accessible via EPICS. The HADES monitoring (HMON) is reading the temperature values from the slow control connection of the sensor board TRB3sc. If a critical temperature, to be set via the HMON script, is reached, the 3.3 V LV is switched off via EPICS interface. The standard software interlock threshold value is 36.0°C. Therefore it should be active before the hardware interlock activates. The hardware interlock is a backup in case of problems with EPICS or other software related issues. The configured threshold values of the hardware and software interlock as well as the status of the hardware interlock are presented in the HMON tactical overview.

The layout of the interlock PCB, as well as a more advanced second version of it, are presented in appendix C.

5.2.1.3 Picosecond Diodelaser

A picosecond diodelaser with 405 nm wavelength is attached to the camera frame as an additional, controllable light source for off-beam measurements and calibrations. A single mode laser fiber is splitted into four fibers by the use of three 50/50 splitters. The splitted fibers are connected to laser inserts, which are screwed into feed-throughs at the photodetection plane aluminium frame with two different depth inside the detector. The front of such a feed-through is covered with an optical diffuser to reach a sufficiently homogenous illumination of the VUV-mirror. The HADES DAQ is triggered by a synchronous differential output signal from the laser, providing an own trigger ID for the laser data.

5.2.2 FEE Wiring and Readout

The backside of the RICH camera is outside of the RICH vessel and equipped with the front-end electronics. The HADES RICH detector FEE is in some sense a prototype of the CBM RICH FEE. DiRICH, combiner and power modules are used on 66 2×3- and 8 2×2-backplanes to read out the MAPMT photoelectron signals with an FPGA based TDC, as introduced in section 3.3.7.
The full detector is equipped with 74 combiner, 74 power modules and 856 DiRICH boards. The FEE of the RICH is this equipped with all in all 2716 FPGAs for different purposes, excluding the higher readout levels of hubs. Section 5.2.1 introduced the layout of the backplanes in the RICH camera. The exact orientation of a backplane and its readout electronics is defined by the beampipe. In order to maximize the distance between the combiner boards and the target as the main radiation source, all backplanes are mounted with the combiner connector pointing to the outside of the detector. The power module is less radiation sensitive. Its FPGA is not needed for the data transport.

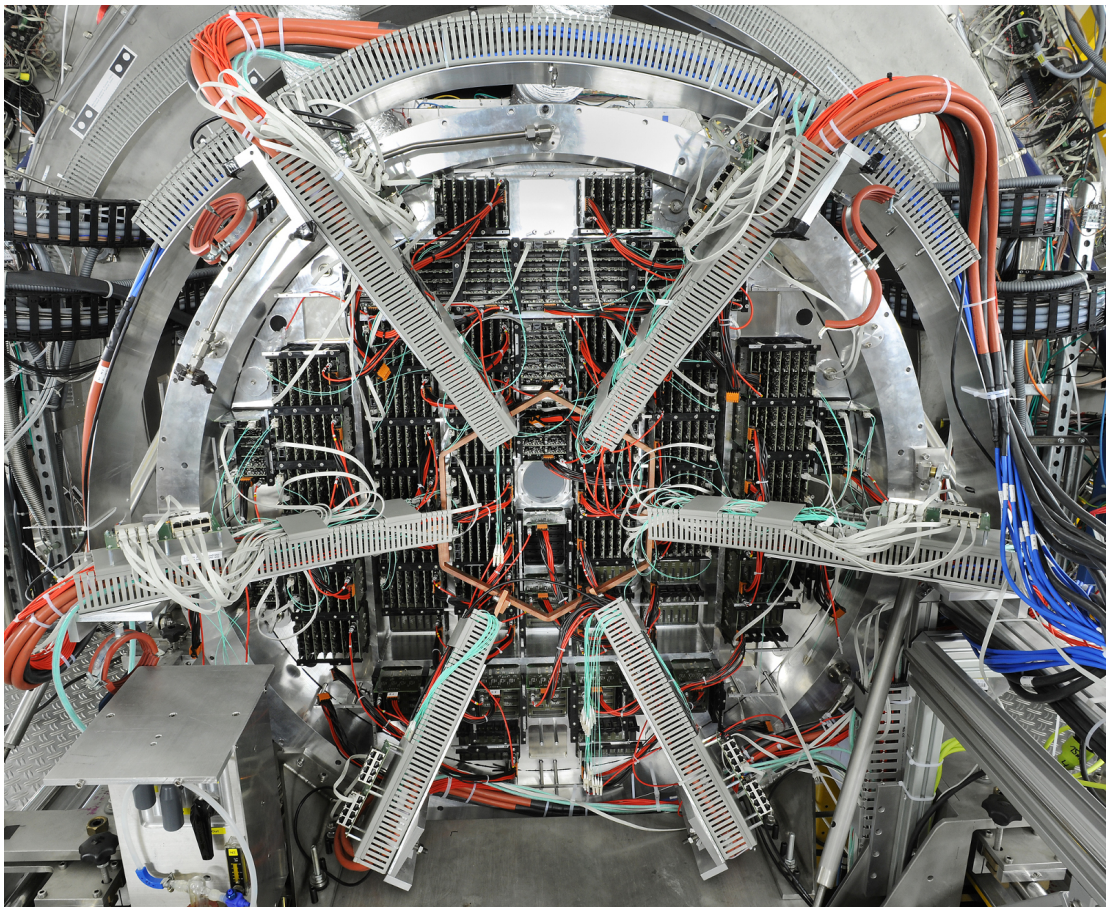

Figure 5.11: Photography of the upgraded HADES RICH detector plane FEE. Photo by G.Otto/GSI

The power module FPGA is only connected to the analog-to-digital (ADC) IC for the monitoring of the voltages and currents on a backplane.

The twelve DiRICH modules on a 2×3 backplane are connected via SERDES to the combiner module. The combiner module uses the already introduced three virtual TrbNet channels: Trigger, Data and Slow Control. Each of the DiRICH boards, as well as the combiner is identified by its unique Id and a serial number, that is written on the FPGA board. The LVL1 trigger signal to the combiner is transmitted via copper on RJ45 cables and further distributed over the backplane. The CTS trigger information, data and Slow Control is transmitted via optical fibers to each combiner board. In combination with the high and low voltage, four cables are connected to each backplane.

Figure 5.11 shows the upgraded HADES RICH electronic side with FEE and the support arms for the cabling. The arms on the RICH detector are used as a cable management system and provide the 0.9 mm diameter optical fibers, RJ45 trigger cables, high and low voltage. The low voltage is playing a special role in the arm design. This will be discussed in detail in section 5.3.2. Due to the unique Id of a DiRICH, no special selection of optical fibers to a backplane is needed. Each board provides an identification by itself. Optical fibers are routed from a crate below the detector in a relatively easy accessible position (see Figure 5.13) around the vessel to the arms. A cable canal is mounted on the outside of the aluminium frame as a guide for all the cables for the FEE. The position of the cable mounting structures is matching the symmetric shape of the detector as well as the six sectors of the HADES detectors. The full cable structure

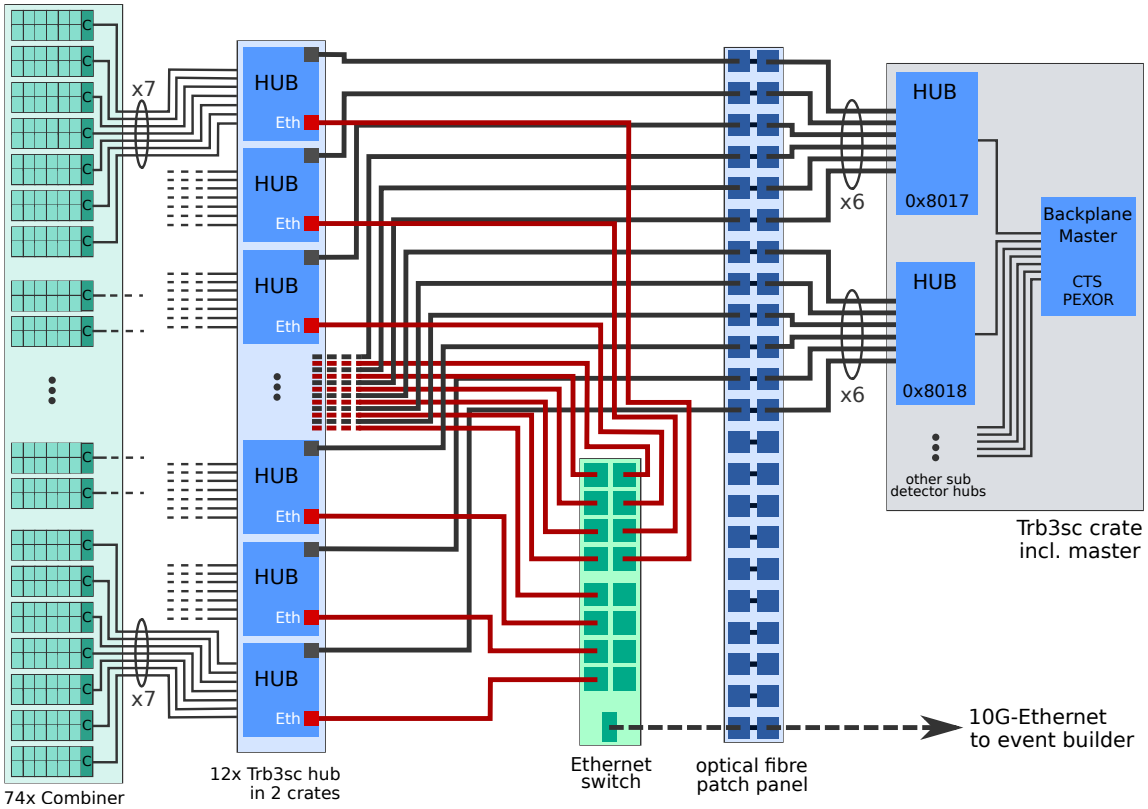

Figure 5.12: Overview on the HADES RICH readout system: Data from the 74 combiners is transmitted to 12 hubs. The hubs are transmitting UDP packages with the TDC data (red lines) from the DiRICHs to the event builder servers via 10G-Ethernet. The TrbNet uplink (grey lines for slow control and trigger) is further transmitted via optical patch panels to two hubs in the DAQ rack, providing a connection to the master of the crate with a connection to PEXOR and CTS.

is fixed to the RICH photo plane to allow for a movement of the full camera without a complete disassembly of the FEE and cables.

The low voltage power supplies are placed near the detector on the same height (to the right in Figure 5.11 (not seen)). All other cables are fed to the RICH detector level from below through a gap near the mounting rails. The thin optical fibers as well as the trigger cabling and sensor readout is attached to a crate, placed in a 19" rack below the detector. This rack is attached to the camera frame, minimizing the stress on the thin optical fibers of the RICH.

A detailed plan of the full detector FEE cabling is shown in Figure 5.12: Each combiner of the 74 backplanes provides a SFP+ cage for the attachment of LC optical fibres for the TrbNet network. In order to reduce the data lines, typically seven combiner are attached to a TrbNet hub. The TrbNet hub is a TRB3sc board with an SFP AddOn. In contrast to a standard TRB3sc, the hub version is built without RJ45 connectors and therefore provides enough space to be equipped with an 8-SFP AddOn. This AddOn is attached to the TRB3sc via a SAMTEC QMS connector and provides eight SFP connections. Six of the connections are on the top, two on the bottom of the AddOn at the place where normally a RJ45 connector is soldered. The standard two SFP connectors of the TRB3sc are usable as well. This configuration of the TRB3sc hub allows the con-

nection of up to eight downlinks to combiner boards and a TrbNet uplink to a higher level readout board. The SFP2 connector of the TRB3sc is used as a Gigabit Ethernet connection and is equipped with a SFP-GbE module. The Gigabit Ethernet connection is used for data output: All the TrbNet data from a combiner module is transmitted to the attached hub. The hub with Gigabit Ethernet is splitting the data paths of slow control and trigger from the data path. While the Slow Control and trigger messages are further transmitted to other TRB boards by the uplink connection, the data path from all up to eight attached combiners is combined to a HADES Event message, that is finally transmitted in UDP packages to a 10G-Ethernet switch and further transmitted with a 10 Gbit Ethernet connection via optical fiber to the event builder servers. A more detailed description of the data transport and TrbNet functionality is available in [123, 132].

Each hub in the RICH system is connected to up to seven combiner boards. Some cables are provided to the FEE as spare for potentially broken cables. In total, twelve TRB3sc hubs with Gigabit Ethernet and TrbNet upstream are located in the crate below the RICH to send out the TDC data to the event builders and to connect to the CTS system. The TrbNet uplinks of the 12 hubs are connected to a LC patch panel. At the patch panel the optical fibers are combined to two thick, more robust bunches. These two bunches comprising the optical fibers from the 12 hubs are further connected to two hubs in a dedicated 19" rack (DAQ rack) on the HADES cave wall. The crates in this DAQ rack are equipped with TRB3sc boards from all HADES detectors. The RICH hubs with the Ids `0x8017` and `0x8018` are further combining the CTS trigger and slow control data and sending the data to the crate master. The master board provides the connection to the central trigger system (CTS) and a connection to the PEXOR computer, which is the (slow) control computer of the TrbNet in HADES, equipped with a PCI-EXpress Optical Receiver (PEXOR).

The front-end electronics of the RICH, especially the DiRICH boards, have to be configured well to operate in the RICH detector with the correct functionality. The TrbNet provides the possibility to send slow control commands to each FEE board and

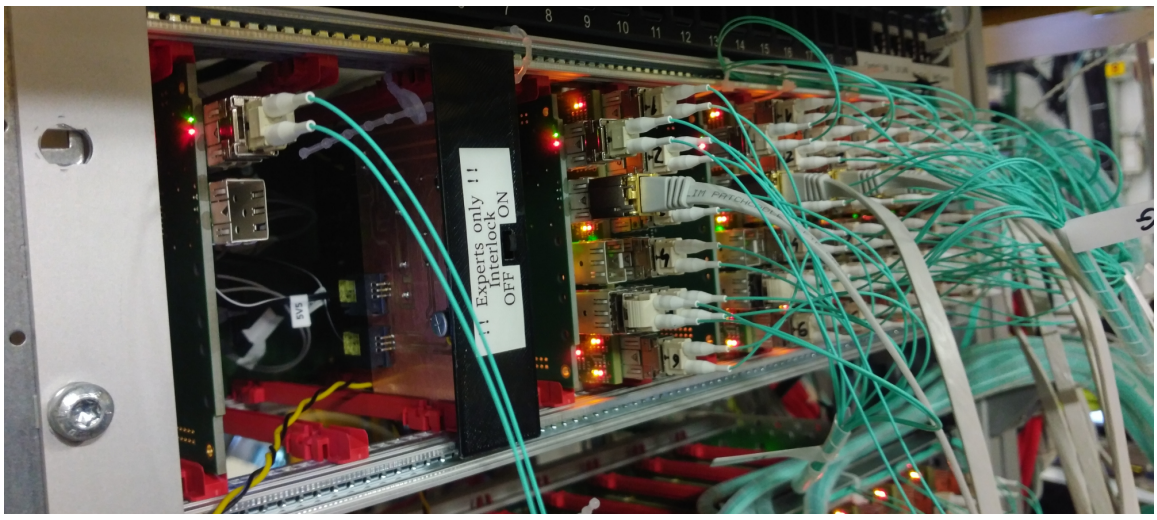

Figure 5.13: Crate below the RICH detector with TRB3sc and Interlock PCB. Left two boards: The sensor board TRB3sc and the interlock PCB with 3D printed mounting. To the right: Hubs for the RICH Combiners and data output.

write values to registers. In HADES the full startup of the detectors and the DAQ is based on a scripted startup procedure. While the startup is processed, the TrbNet addresses are assigned to the corresponding boards and many different settings are loaded to these. On each DiRICH the following settings are done by the startup script:

- invert TDC channel inputs
- enable each TDC channel
- set trigger window from -800 ns to -200 ns
- limit TDC ring buffer size to 10 words (32-bit each)
- limit the maximum event size of one DiRICH to 170 words
- minimum event size of 5 words

Each TDC word, i.e. a TDC message or an EPOCH marker, is written to the ring buffer of the corresponding TDC channel and read out in case a trigger signal arrives. A ring buffer in a DiRICH can store the last 10 words of the corresponding channel. If the trigger window of a DiRICH is enabled, only the data matching the trigger window relative to the trigger time are written to the endpoint buffer.

A maximum of 170 words is allowed in the DiRICH event buffer at the data handler. This limitation on the DiRICH event size is used to keep the total data size at the following Gigabit Ethernet hub below the UDP package limit of 65 kByte.

These subEvents comprise data from up to 7 combiners, thus up to 12·7 DiRICHes. Full event buffers of 170 words in all DiRICHes would lead to 57.12 kByte subEvent size leaving enough space to the 65k Byte for additional headers. Events with less than 5 words on a DiRICH are discarded to reduce the overall data stream. Those events only contain a reference time with header information but are empty otherwise.

The distribution of the trigger signal from the CTS to the RICH detector is based on trigger fan-out boards. The trigger is sent on RJ45 patch cables to the six arms of the RICH. Each arm is equipped with an additional trigger fan-out board (visible in Figure 5.11). The fan out can connected to up to 15 combiner boards and provide the trigger signal to these boards.

5.2.2.1 DiRICH Address Scheme

The control of the detector and mapping of the TDC data to pixels needs an unique address for each DiRICH and combiner board. The TrbNet network foresees a 16-bit address space for all connected Trb based boards. The unique ID of each Trb board is known and accessible in a database. While each boards' firmware is flashed, the UID in combination with the boards serial number is added to the database. The startup procedure of the HADES detector is mapping a system specific address to the UID of a board. The mapping is provided by the RICH group as each serial number of each DiRICH is noted in the correct position and mapped to the TrbNet address scheme of the RICH detector.

The addressing scheme of the 856 DiRICH boards is readable in hex and still provides a high density in the address range. Figure 5.14 is a schematic overview of the addressing scheme of the DiRICH boards with an example address. The 16-bit address of a DiRICH is constructed as follows:

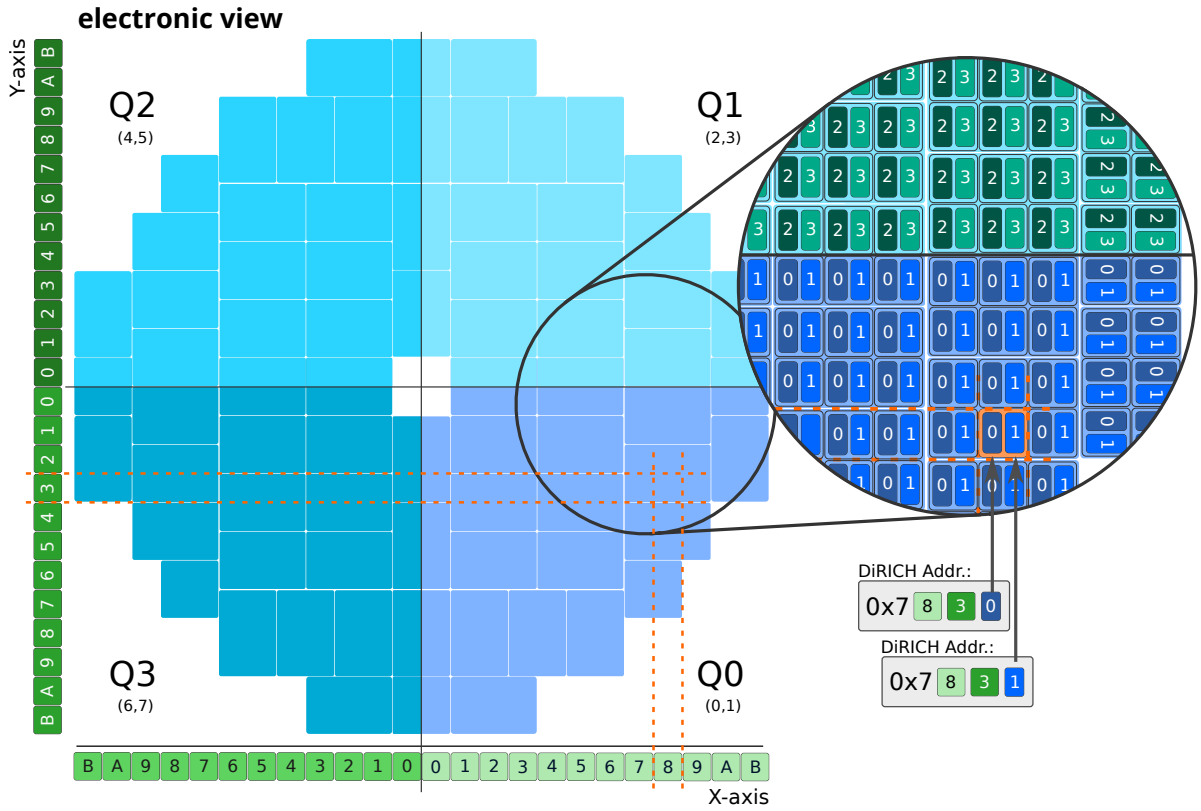

Figure 5.14: Addressing scheme of the HADES RICH DiRICH boards. The RICH is separated in quadrants and subdivided in MAPMT positions. The position of each MAPMT in the XY plane is defining the main part of the address. The quadrant in combination with the information which DiRICH on a MAPMT is addressed, is finalising the addressing scheme.

- Bits `[15:12]`: Representation of all DiRICH boards. In the HADES RICH, this is always `0x7`.
- Bits `[11:8]`: Decoding of the X position of a MAPMT in a quadrant.
- Bits `[7:4]`: Decoding of the Y position of a MAPMT in a quadrant.
- Bit `[3]`: fixed to 0.
- Bits `[2:1]`: Decoding of the quadrant 0 to 3.
- Bit `[0]`: DiRICH of a MAPMT that is addressed.

The addressing of the combiner boards is based on the XY coordinates defined by the position of combiner boards. All combiners of the RICH are identified by bits `[15:8]=0x82`. Bits `[7:4]` represent the X and `[3:0]` the Y coordinate. Starting in the bottom right with 0, the combiners are labelled in rows and columns in the plane. In the example of Figure 5.14, the selected DiRICHes are on combiner `0x8213`.

A help for the identification of the DiRICH and Combiner boards is given with the monitoring webpage. A mouse hoover unveils the address of each DiRICH and combiner board (see Section 5.5).

5.3 Power and Cooling

The HADES RICH powering scheme consists of the low voltage and high voltage systems with the full cabling. Especially the low voltage and a good grounding scheme is of high importance for a reliable and well working RICH detector. The previously introduced limits on the temperature of the MAPMTs are mainly in direct relation to the low voltage, but also to the high voltage, as it increases the inner RICH temperature by up to 2°C. Consequently a cooling concept is needed to operate the RICH over a long period of time at a stable, low enough temperature.

5.3.1 High Voltage

The high voltage system of the HADES RICH is the same as for the CBM RICH detector and thus both experiments will share the infrastructure in the future SIS100 operation. H12700 MAPMTs are operated at a voltage of around 950 V, depending on the gain of the MAPMT. Each backplane hosts MAPMTs of similar gain and is supplied by an individual HV channel set to a voltage meeting the average gain of the MAPMT. The high voltage is distributed from the LEMO EPL.0S.116.DTL connector on the power module to the backplane in a separate PCB layer and supplied to each of the 6 MAPMTs. The ground of the High voltage and the low voltage is connected directly at the FEE.

A Draka CEH50 HV cable with an outer diameter of 3.2 mm and a semiconductive layer is used as the supply line to the power module. This cable is thinner than the standard SHV cables and reduces on the one hand the forces on the power module and its connector and on the other hand the cable volume on the detector supply lines and cable arms. A self made patch panel, made from a PVC plate and SHV patch panel adapters, is located below the detector on a 19" rack. The Draka cable is connected via SHV connectors to the patch panel.

The rack is fixed to the floor of the HADES cave. A drag chain in the main metal structure of the HADES detector is used as a cable guide to provide enough flexibility to the HV connection for a movement of the detector in beam direction. Standard SHV cables are connecting the patch panel to the HV power supply in a separate rack.

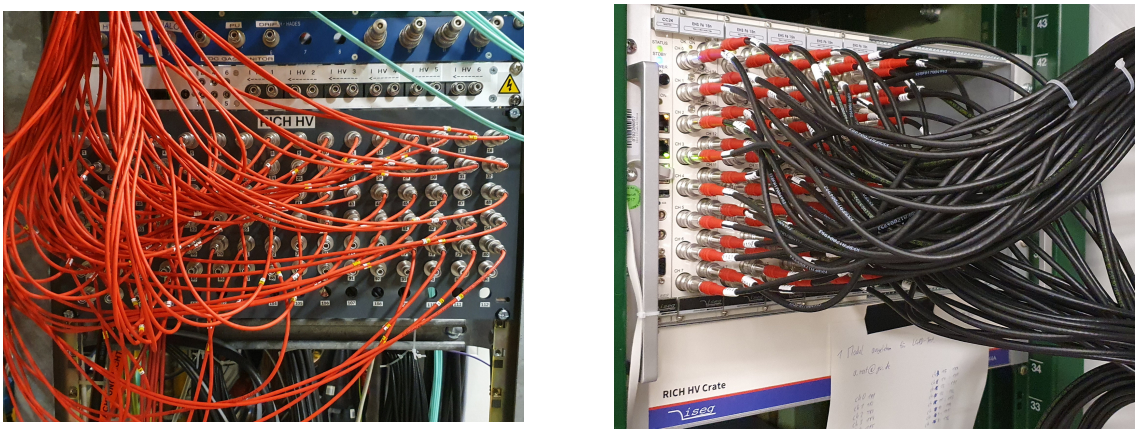

Figure 5.15: **(left)** HADES RICH HV patch panel below the detector with Draka CEH50 HV cables (red). **(right)** RICH HV power supply crate with all channels connected to the patch panel (black standard HV cables).

An ISEG HV power supply crate ECH 44a is used for the HADES RICH detector. This crate provides internal cooling, fits into a 19" rack with 8 HU and offers space for a CC24 master controller and 10 additional HV modules. Six ISEG EHS F6 15n_SHV modules are used in the HADES RICH HV rack for the supply of all backplanes. Each of the modules offers 16 channel with single-channel-floating ground. Each channel can provide up to 1.5 kV negative voltage with a maximum of 4 mA of current. The maximum output voltage is limited by a potentiometer to 1.2 kV as a protection for the MAPMTs. The current per channel under operation conditions was measured to be about I=1.1 mA, respectively I=0.8 mA for the 2×2-backplanes.

The 6 modules are controlled by an CC24 master controller with integrated EPICS and web interface. The HV control is based on a custom IOC. A mapping between the backplane and the HV crate channel is provided in appendix D.

5.3.2 Low Voltage

The low voltage power supply and the power distribution of the upgraded HADES RICH is challenging. The use of in total 2716 FPGAs, the pre-amplification of the MAPMT signals and the data transport with SFP-ports demands for a power consumption of approximately 2120 W. The front-end electronics demands in total four separate voltages. 3.3 V and 2.5 V are required by all boards. A dedicated voltage of 1.2 V is needed for the ECP3 FPGAs on the combiner board. A voltage of 1.1 V is used on the DiRICH boards for the ECP5 FPGA and the pre-amplification of the MAPMT signals. An overview of the currents per kind of voltage is given in Table 5.3.

The increased noise seen in the MAPMT signals in the operation mode with an on-board DCDC converter led to the choice of an external DCDC voltage supply. The high currents on the 1.1 V power line in combination with the low voltage, and following low operation voltage window, restrict the powering scheme. Thick copper cables and a short distance between the power supply and the FEE had to be chosen to minimize the voltage drop on the supply line.

The low voltage is provided by 9 power supplies. Each arm of the RICH is supplied with 1.1 V from a dedicated power supply (six power supplies for the 1.1 V). The other three voltages are provided by one power supply each. All 9 power supplies are located in a 19" rack next to the RICH detector on a rail system and move along the beam direction with the RICH camera to ensure a constant distance between rack and detector to reduce the movements on the cables and the forces on the connectors. TDK Lambda Gen 6-200 are chosen as the power supplies of the RICH detector. The TDK Lambda can provide up to 200 A at up to 6 V (1.2 kW) per power supply and offer an Ethernet

supply voltage	total current	eff. current/backplane
1.1 V	865.9 A	12.14 A
1.2 V	156.5 A	2.11 A
2.5 V	86.0 A	1.21 A
3.3 V	35.0 A	0.49 A

Table 5.3: Overview of the RICH currents for different supply voltages. An effective current per 2×3-backplane is calculated.

Figure 5.16: Low voltage power supply rack with running RICH FEE next to the detector. The voltages (left) and drawn currents (right) of each power supply are visible. All power supplies are connected to LAN and are accessible via EPICS.

connection for remote control. In addition, an interlock interface is provided and used on the 3.3 V line for the RICH interlock system.

Figure 5.16 presents the low voltage power rack with all 9 TDK Lambda devices in operation. The drawn currents and used voltages per power supplies are visible and remotely controlled via an EPICS IOC.

Each of the power supplies allows to screw in the cable plugs of the cable connection to the FEE. The 3.3 V, 2.5 V and 1.2 V power supplies are connected to all arms. Each voltage is connected to six cables (1 per arm). Each of these six cables is crimped to a 50×1.5 mm^2 cable, providing a fanout of the voltages to up to 50 1.5 mm^2 cables. All three voltages are supplied via these 50×1.5 mm^2 cables to the arms and finally with the 1.5 mm^2 output wires to the individual power modules on the backplanes.

The 1.1 V and all GND connections are distributed via 1×70 mm^2 cables. The cables are guided to the arms and connected to copper bars with cable shoes. A 200 mm^2 copper bar for the 1.1 V and a 300 mm^2 copper bar for GND distribution are positioned in the arms of the RICH. The copper bars are manufactured with threaded inserts to connect the power module connectors individually with 1.5 mm^2 cables to the copper bars. The GND bars are all connected in the center of the detector with a ring like copper bar to provide an ideal grounding and give additional stiffness to the arms.

5.3.3 Cooling

Cooling of the RICH detector is very important to keep the MAPMTs below a critical temperature. Different ideas of cooling were discussed and tested. The final cooling concept is based on the usage of fans to blow the cooled cave air into the detector plane and thus remove the hot air from the camera. The cooling fans are arranged such to maximize the cooling on the camera plane.

All 3 cooling fans are connected to a separate HMP4040 power supply and can be controlled remotely via scripts. In addition to the fans a pipe provides additional cool air from the bottom of the detector. The air in the HADES cave is cooled to below 20 °C and thus is cool enough to get the RICH into an operational temperature condition that is constant over time.

5.4 Radiator Volume

Previously to the upgrade of the RICH camera, a CaF_2 window divided the inner part of the RICH vessel into a radiator and a camera volume. The radiator volume was filled with C_4F_{10} radiator gas, whereas the separated camera volume was filled with CH_4. A sophisticated gas system controlled the pressures between the gas volumes and prevented the inner window from high pressure gradients. The gas system had to liquidize the C_4F_{10} and keep a reservoir of it. The old radiator and counting gas was chosen for the operation of the CsI camera. The camera was able to detect photons in the wavelength range of 145 nm to 220 nm. The optics and radiator volume was optimized to this conditions.

The update of the camera to H12700B-3 MAPMTs is a complete change in the readout and therefore the selection of the radiator gas, in terms of optimization of the transmittances and scintillation effects, had to be rethought for the upgraded camera with the new sensitive wavelength range of 185 nm to 650 nm. The new camera has the advantage of an increased sensitive range where more photons can be detected, although Cherenkov photon production increases to lower wavelengths.

A big disadvantage of the increased sensitivity comes with the inner separation window and the radiator gas. CaF_2, the material of the separation window, scintillates in the wavelength regime of roughly 220 nm to 400 nm (compare Figure 5.17, left). This wavelength was beyond the sensitivity of the old camera and was therefore not an issue before the upgrade. Unfortunately, now the scintillation is in the sensitive range and thus acting like a light torch to the detector. Estimates on the scintillation light yield from the CaF_2, based on measurements as reported in [133, 134], were approximately 300 kPhotons per event [135]. This number is comparable to 100 kHz per pixel. A test under beam conditions with the RICH detector reproduced this number. A measurement of the decay time from the in-beam measurement results in τ=0.995$\pm$0.112 μs [136]. This is in perfect agreement with the literature value of τ=0.96$\pm$0.06 μs [133] and confirms the scintillation light influence of the CaF_2 window on the measurements.

These rates would have been a show stopper for the measurement of Ag+Ag collisions and beyond. As consequence the CaF_2 window was removed in the upgraded HADES RICH detector.

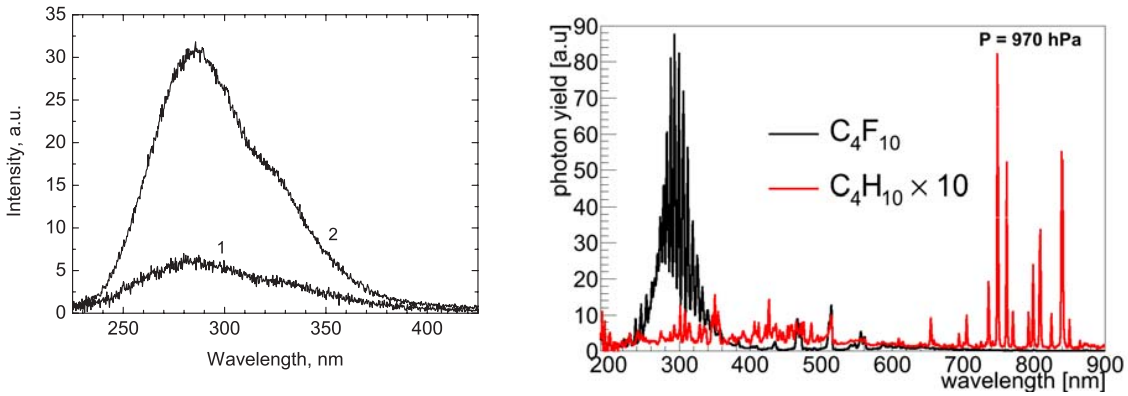

Figure 5.17: **(left)** Luminescence spectra of CaF_2 measured under excitation with 31 eV photons at 300 K (1) and 9 K (2) [133]. **(right)** Spectral distributions of scintillation light emitted from purified C_4F_{10} and C_4H_{10} gas samples [137].

The resulting increase of the radiator volume enforced the choice of a new radiator gas: The existing C_4F_{10} gas system could not be operated with an enlarged volume because the reservoir of liquid C_4F_{10} was too small. Fortunately, a second gas with nearly the identical optical parameters as C_4F_{10} is available: C_4H_{10} has an index of refraction of n≈1.0015 and thus is identical to C_4F_{10} (γ_{thr} ≈18). In addition C_4H_{10} has nearly no scintillation in the sensitive wavelength region of the new camera (see Figure 5.17).

A long-term test of the H12700B-3 MAPMTs under a C_4H_{10} atmosphere showed no significant influence on the photon detection capabilities. Therefore both volumes can be filled with the radiator gas and the separation of both volumes by a CaF_2 window is redundant.

However, C_4H_{10} is a flammable and highly explosive gas, if it is mixed with oxygen at a certain ratio. Luckily, this gas has already been an option for the use as a quenching gas from the very beginning. Thus the usage of C_4H_{10} was already foreseen and most safety standards were already existing. Additional sensors and control on the gas flow as well as the gas mixture were added into the monitoring of the detector to allow for a safe operation.

The change of the radiator gas simplifies the usage and control of the new gas system in comparison to the previous system. The gas system is now operated as an open system (atmospheric follower) and flushed with pure isobutane gas during beamtimes. In between beamtimes the detector volume is flushed with nitrogen (N_2).

5.5 Slow Control and Monitoring

Nearly all parts of the slow control of the HADES RICH detector have been reconstructed during the upgrade. Based on the HADES Monitoring (HMON) a web based monitoring interface has been developed. The QT5 based HADES control graphical user interface (GUI) provides the most important control interfacer for the operators of the RICH but also for the full HADES detector in the control room.

The HADES control GUI provides an interface to the most important scripts of the HADES control (see Figure 5.18). It automatically builds the interface at startup from the folder structure in its main directory and provides a reduced but also an advanced

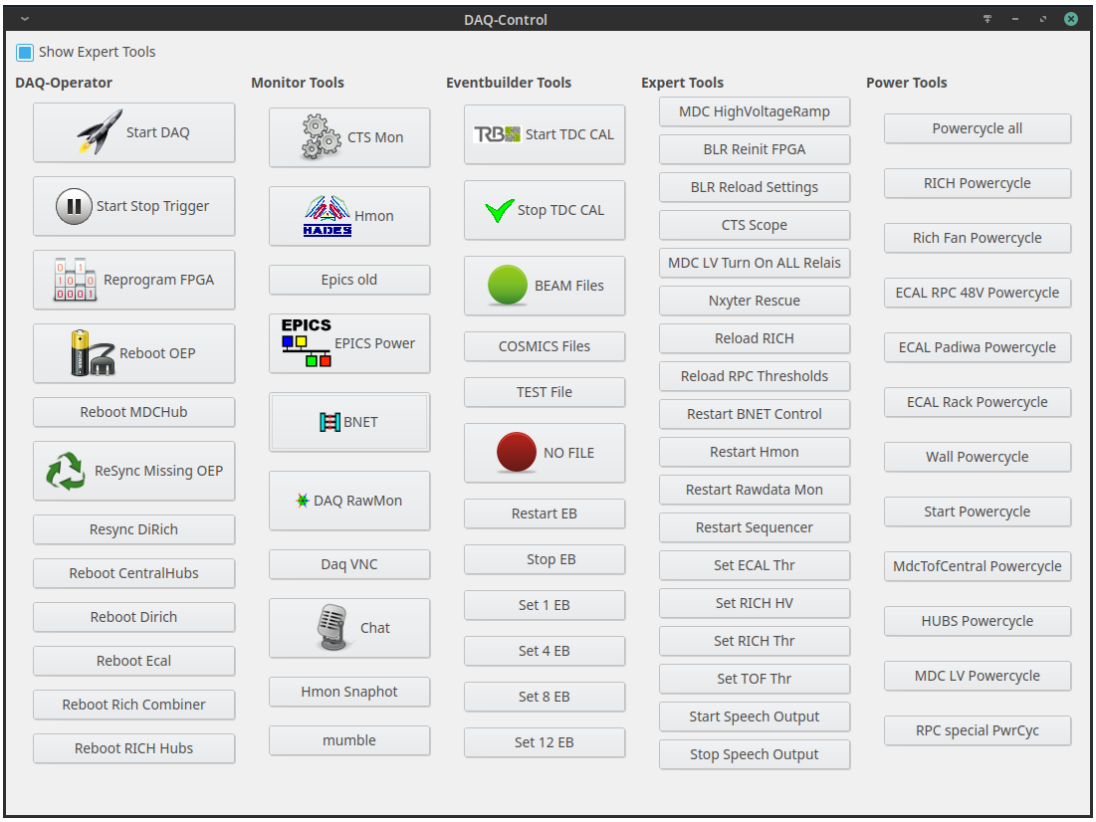

Figure 5.18: The HADES DAQ control GUI is the central control interface for the detector operation and provides a simple and effective control to the detectors and the DAQ itself. The individual sub detector provide several buttons for an easy and fast first level problem solving.

interface. The advanced interface gives access to the control of e.g. the threshold setting of the RICH. The standard interface is used for the control of the detectors by non experts. A bunch of tools for a smooth DAQ operation is provided. Next to the start of the DAQ scripts, a resynchronisation script of the DiRICH boards is available. In case of a larger problem in the RICH DAQ, reboot buttons for the main parts of the detector FEE, DiRICH, combiner and the hubs below the detector, are available. This option opens the possibility to restart the RICH without a power cycle: The reboot reloads the firmware of the FPGAs and brings them back into a clean state.

The monitor tools section provides a fast access to higher level monitoring and control interfaces as well as an access to voice and text chats. The monitoring can directly open the DAQ operators view, open the HMON web appearance, open the event-builder web interface or give access to the EPICS based power control interface.

The operation of the RICH DAQ is based on the FPGA time to digital converters. The tapped delay chain of the TDC is implemented in the circuits of the FPGA. Its core principle is the delay of signals between two FPGA part. The delay is correlated to the position on the FPGA, the applied voltage and most important, the temperature. The TDC has to be calibrated for the operation conditions. The event builder tool provides an easy access to the calibration of all TDCs in the HADES detector system. In the case of the HADES RICH, a linear calibration is applied. The FEE is running with a calibration trigger and the DiRICH TDC inputs are fed with signals from a separated 125 MHz clock source. A linearity between the minimum and the maximum fine-time

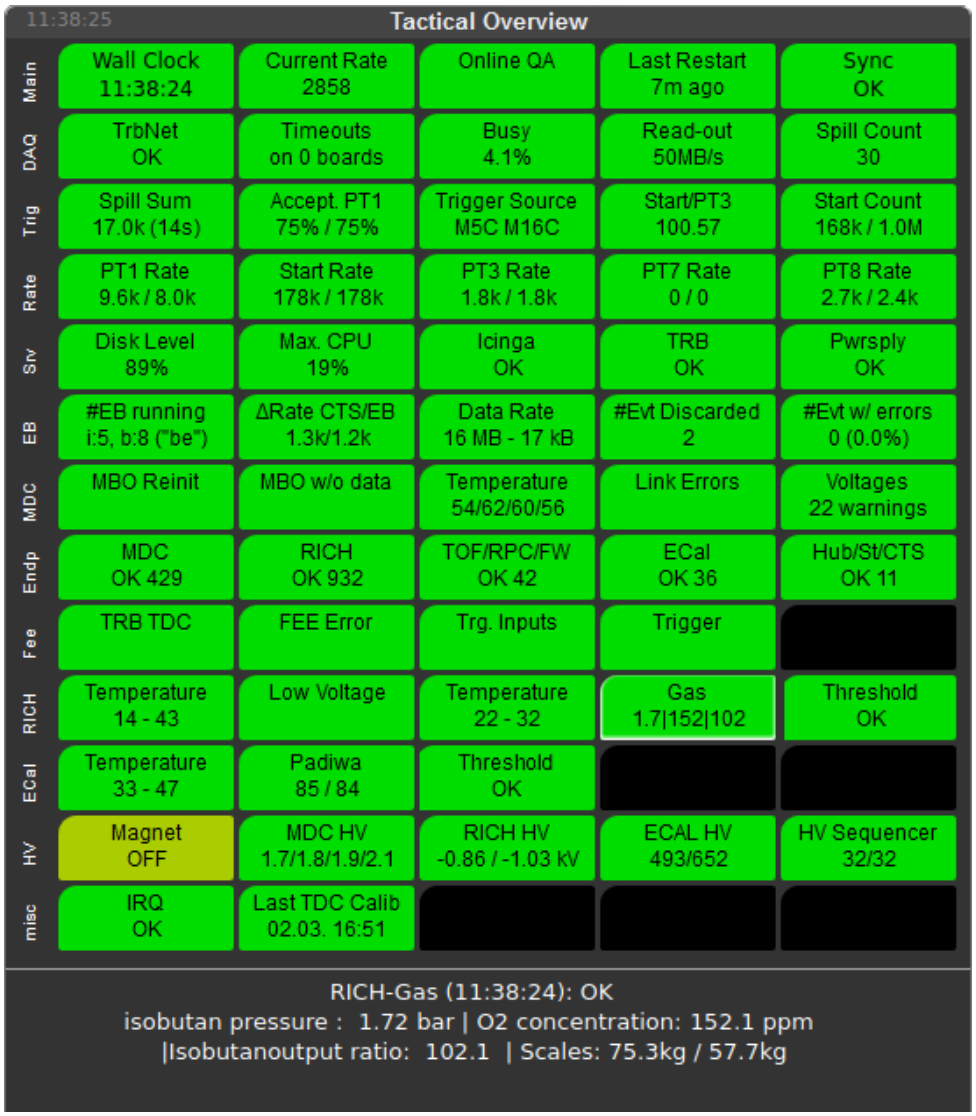

Figure 5.19: HMON tactical overview of the upgraded HADES detector. A hoover of the RICH gas field is shown with the detailed status informations of the main parameters of the gas system, including the values of scales of the two C_4H_{10} gas bottles.

bin of each TDC channel is assumed and extrapolated to the coarse time step size of 5 ns. During production runs the event builder is applying the calibration on the real data [130, 138].

The application of the DiRICH threshold values is of high importance for the operation of the RICH. A dedicated software[1] has been developed for the DiRICH system to search for the baseline of the TDC channels [139]. The baseline with an additional threshold offset value is stored to the MachXO3 FPGAs on all DiRICH boards to provide the correct threshold to all channels. The predefined threshold values are loaded to the FEE after each powercycle of the RICH. A button in the DAQ control GUI is executing this procedure to bring the RICH in an operational condition. In addition the HMON tactical overview indicates whether the thresholds are correctly loaded or not.

The expert tools provide a button for the high voltage setting of the RICH detector. The button is executing a script, that sets the values of each HV channel to the calcu-

[1]Baseline scan by Jörg Förtsch: `https://github.com/joergfoertsch/trb_dirich_threshold`

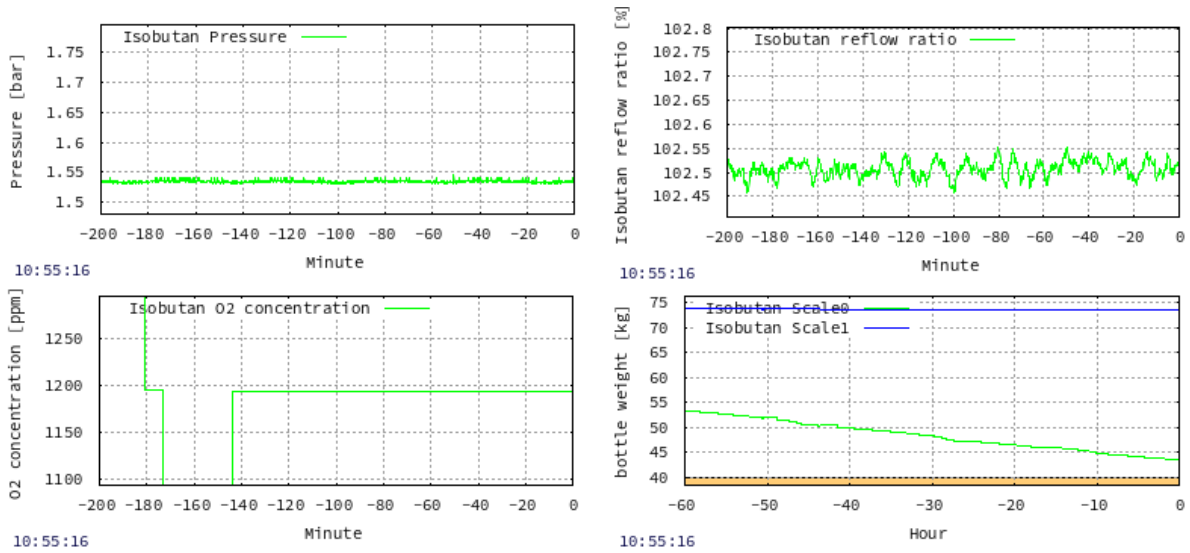

Figure 5.20: HMON webpage with gas system monitoring. The pressure, O_2 concentration, isobutane reflow ratio and the weight of the two isobutane bottles is presented.

lated value from the gain measurements. In addition, the channels are activated and ramped to nominal voltage. The button is used as a toggle switch. The exact status of the HV is additionally provided in an HMON website and indicated with colours in the tactical overview (see Figure 5.19).

The tactical overview is the main overview of the DAQ status (see Figure 5.19). The state of all sub detectors and parameters of these is indicated by colors with additional text support. The RICH detector presents the most important informations of the detector in the tactical overview. The temperature values of the DiRICH boards as well as the temperatures of the backplane sensors are given by the minimum and maximum values. The color of the fields indicate the status of the parameter. In case of a dangerous temperature, the color changes to yellow and further on to red, with a blinking red in the fatal error state.

The status of the low voltage as well as the high voltage is given by two fields. The LV status indicates measured voltage ranges on all four power lines in the text field in the lower section of the window, if a mouse is hoovered on the status field. The high voltage field is representing the minimal and maximal voltage of the channels and indicates the status of the voltages of the individual channels. The color is changing in case of over or under voltage or e.g. a crate being in standby mode.

Figure 5.19 shows the tactical overview with a mouse hoover on the gas status field of the RICH detector. The gas field is indicating the status of the isobutane radiator gas as well the weight of the gas bottles itself. Problems are indicated in the color code already at a very conservative level to keep the detector in a safe condition and be prepared quite early in case of upcoming problems.

The web interface of HMON provides access to different monitoring pages, from temperatures over high voltage to rates per pixel. Figure 5.20 shows the RICH gas monitoring histograms from HMON. The measured values from the last hours are presented and indicate the total trend of the gas system behaviour. The last histogram is a graphical representation of the weight of the isobutane gas bottles. The scales are indicating the weight loss and the latest point of exchanging the bottle. A decrease of the weight

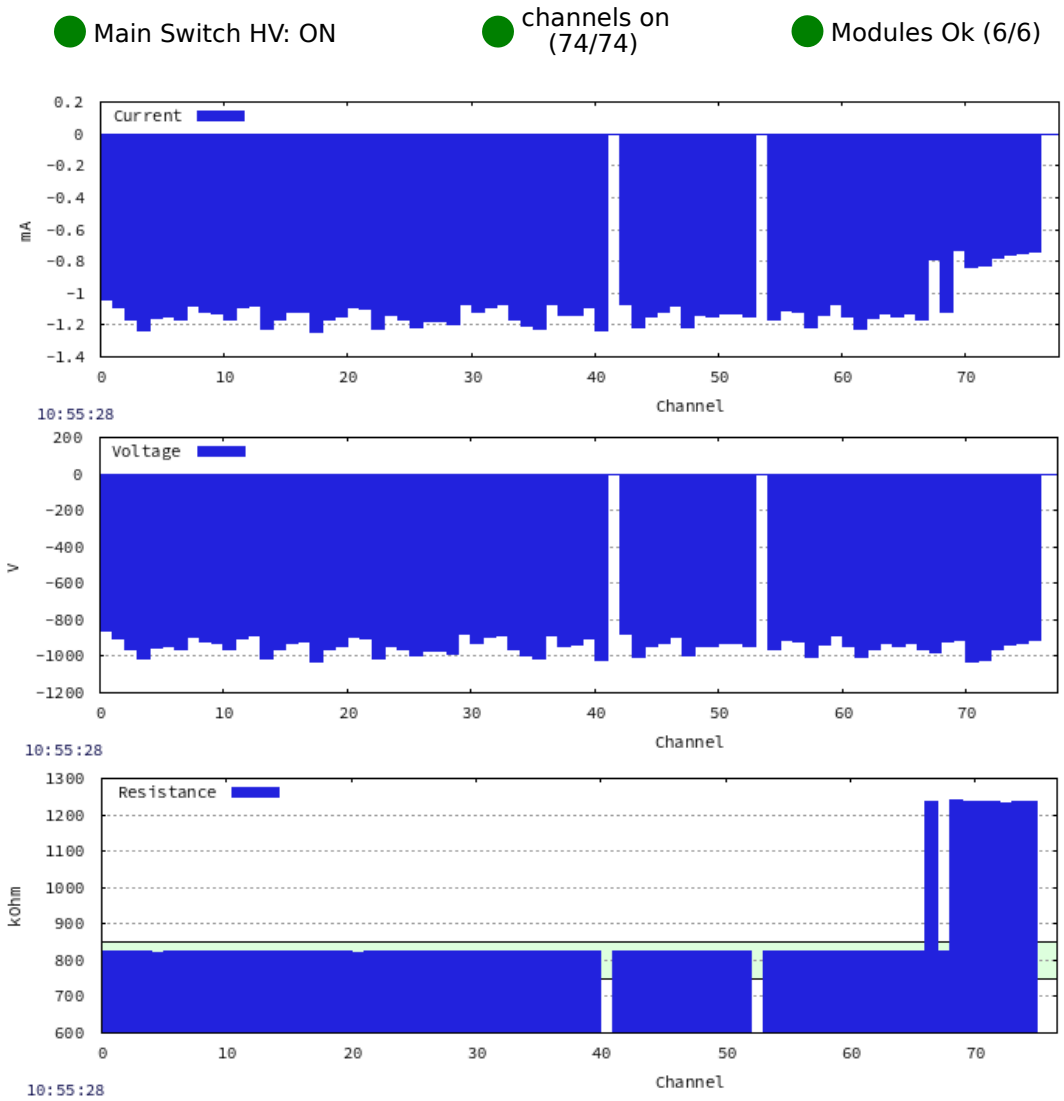

Figure 5.21: HMON webpage with high voltage system monitoring. The measured voltage and current of all individual channels of the HV are provided in one overview page. A calculated resistivity gives a fast and reliable feedback on the functionality of all channels. A text line indicates the status of the crate, channels and modules.

below a certain threshold value indicates the operators an exchange of the empty bottle. The switch between the empty and full bottle is automatically done at the bottles' valves.

The HMON monitoring is based on PERL scripts and is running stand-alone. It provides access to the TrbNet slow control daemon, an EPICS interface and the full range of PERL modules. The representation in histograms itself is based on Gnu-plot and a HADES specific wrapper of it. The access to TrbNet is used in various monitoring scripts. The temperature of e.g. the DiRICH and combiner boards can be read via broadcast addresses and directly visualized in histograms or in a webpage. Gnu-Plot provides a very fast histogram generation. A generation of a 2-dimensional representation of the pixels of the RICH detection plane is possible and provides a powerful tool for online monitoring. The pictures in the monitoring are typically shown in the

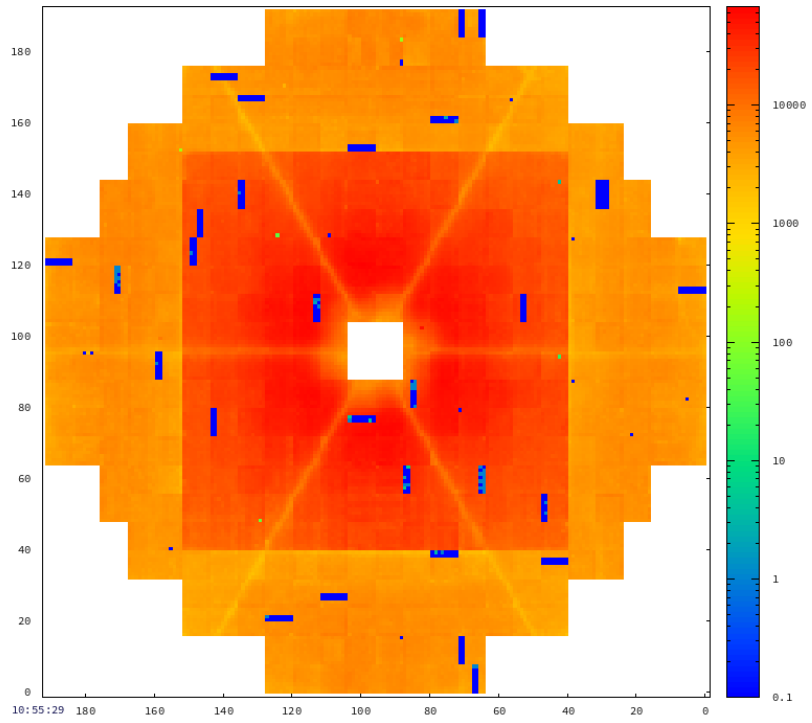

Figure 5.22: An overview of the scalar pixel rate of the RICH channels in Hz. The inner and outer plane as well as the shadowing from the spoles is visible in the rate display. The blue rectangles are related to channels, unfortunately beeing dead due to a misconfiguration in the threshold FPGA's flash memory. The figure shows the data in beamview. (Day 12 of March 2019 beamtime; Run 352557294; Mean event rate ≈10.3 kHz)

beamview that is identical with the electronic-view.

Figure 5.21 shows the web page status of the high voltage system based on EPICS process variables (PVs). Histograms with the measured current and measured voltages of all channels of the high voltage crate are provided. A third histograms shows the calculated resistance of the channels with an indication of the expected value range in light blue. The higher channelnumbers of the histograms are deviating from the

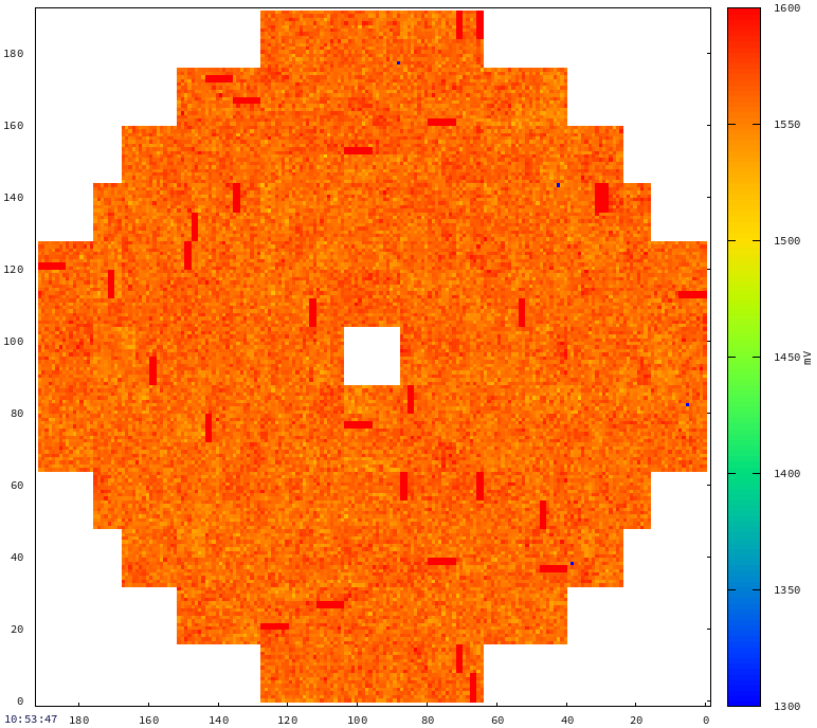

Figure 5.23: Overview on the individual threshold values of all RICH channels from the baseline scan with constant offset in mV. The homogeneous distribution is an indication of the correctly loaded flash settings to the operators. The figure shows the beamview. It represents the thresholds setting at 10:53 of day 12 of the March 2019 beamtime.

rest. These channels are connected to the 2×2-backplanes and therefore draw less current at a comparable voltage. A basic overview of the status of the high voltage crate, channels and modules is given in the upper part of the figure. An additional CSS-studio GUI is available for a more detailed control with single channel or even grouped control of the PVs. The start or shutdown of the HV as well the change of e.g. the ramp speed are controlled only via the CSS-studio interface to prevent from accidental changes on the high voltage by non-experts.

Figure 5.22 shows the full scalar rate display of all 27392 pixels with an update interval of 2 seconds. This plot indicates the functionality of the FEE TDCs and gives an overview on potential problems as missing DiRICH boards. The figure perfectly shows the shadows of the inner spokes of the RICH detector and the separation of inner and outer camera plane. The blue fields are related to misconfigured threshold FPGA's flash memory on individual DiRICH boards. These channels were not functional in the march 2019 HADES beamtime but fortunately homogeneously distributed over the camera and are not disturbing the ring finder functionality. The channels got repaired after the beamtime.

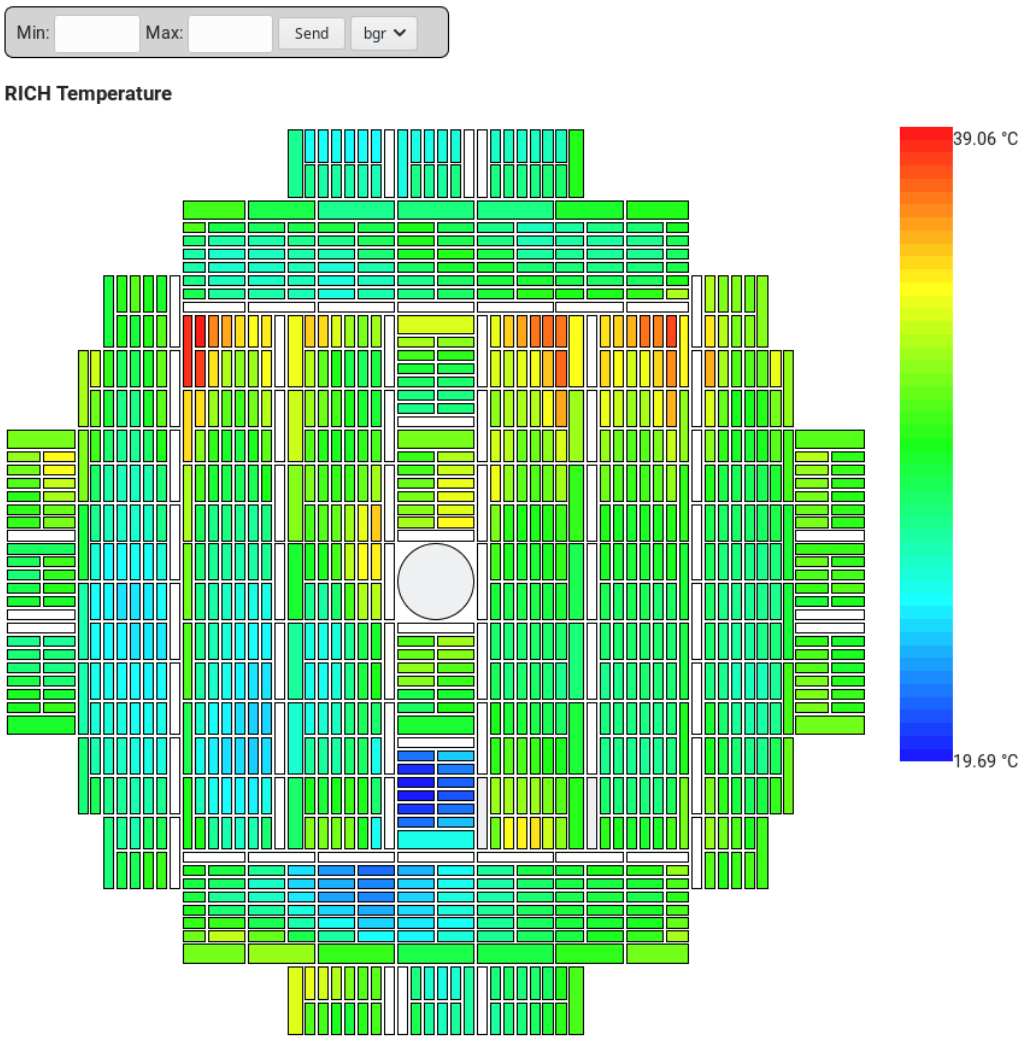

Figure 5.24: HTML based HADES RICH FEE temperature overview in the beamview. The figure shows the exact positions and orientations of all FEE boards. The shown temperatures were typical during the March 2019 beamtime.

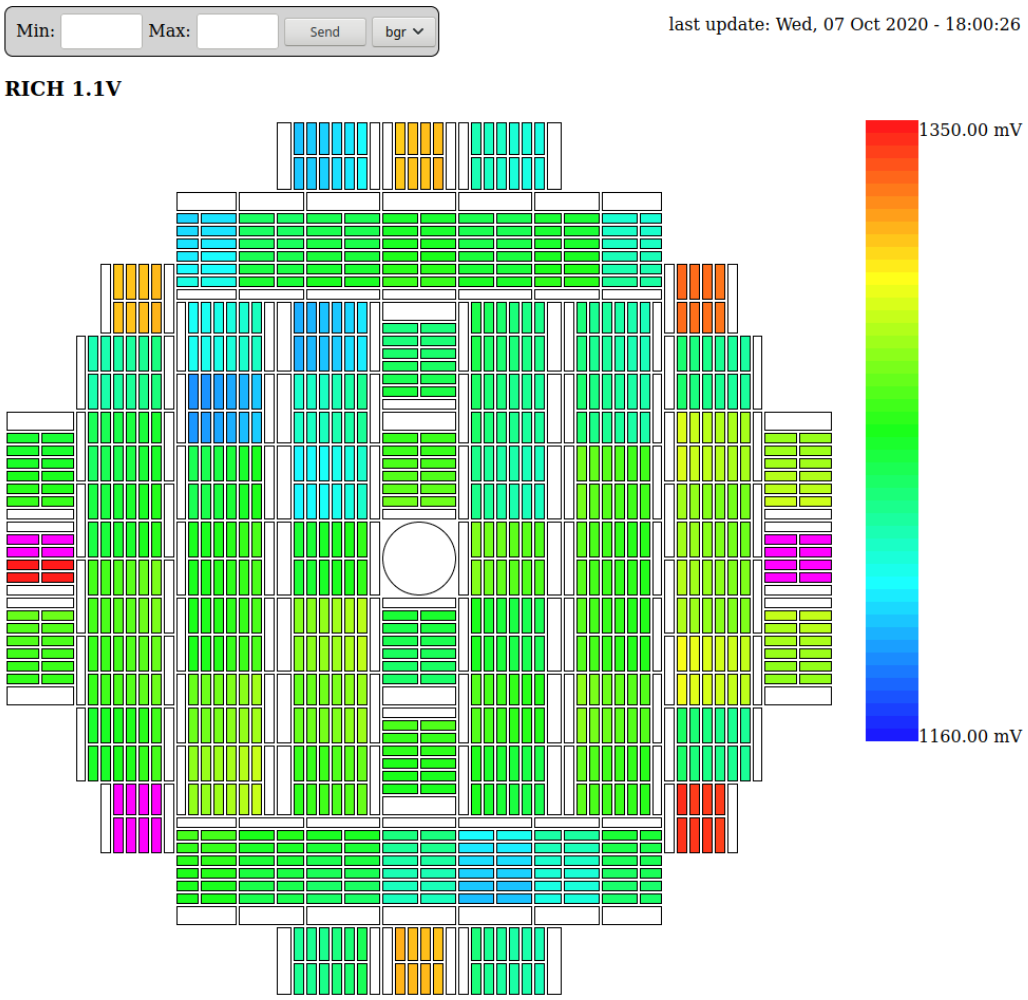

Figure 5.25: HTML based HADES RICH overview showing the 1.1 V power line as measured on the DiRICH boards. Values shown are typical for the March 2019 beamtime.

Figure 5.23 shows in the same 2-D presentation the individual threshold value of each channel of the RICH detector. The correct threshold setting of all channels is very important for a high quality measurement, therefore this histogram is essential. It is updated all 2 minutes and provides a fast overview to the operators on the detector's functionality.

Figure 5.24, Figure 5.25 and Figure 5.26 show a HTML, CSS and JavaScript based monitoring of the RICH detectors front-end electronics. This concept was also exported for the HADES ECAL monitoring. Each FEE module of the RICH with a connection to TrbNet is represented in the web appearance. The values are provided by JSON files and loaded via JavaScript. The webpage provides an interactive change of the minimum and maximum values to highlight a specific range. In addition, a selection between three different color palettes is possible. A mouse hoover at a FEE position unveils a label with the TrbNet Address of the board and the corresponding exact value. This feature is ideal for the search of specific boards and helps to quickly identify potential problems.

Based on the webpage url, a custom command can be executed. This is a very powerful tool for the graphical representation of nearly all slow control values of TrbNet

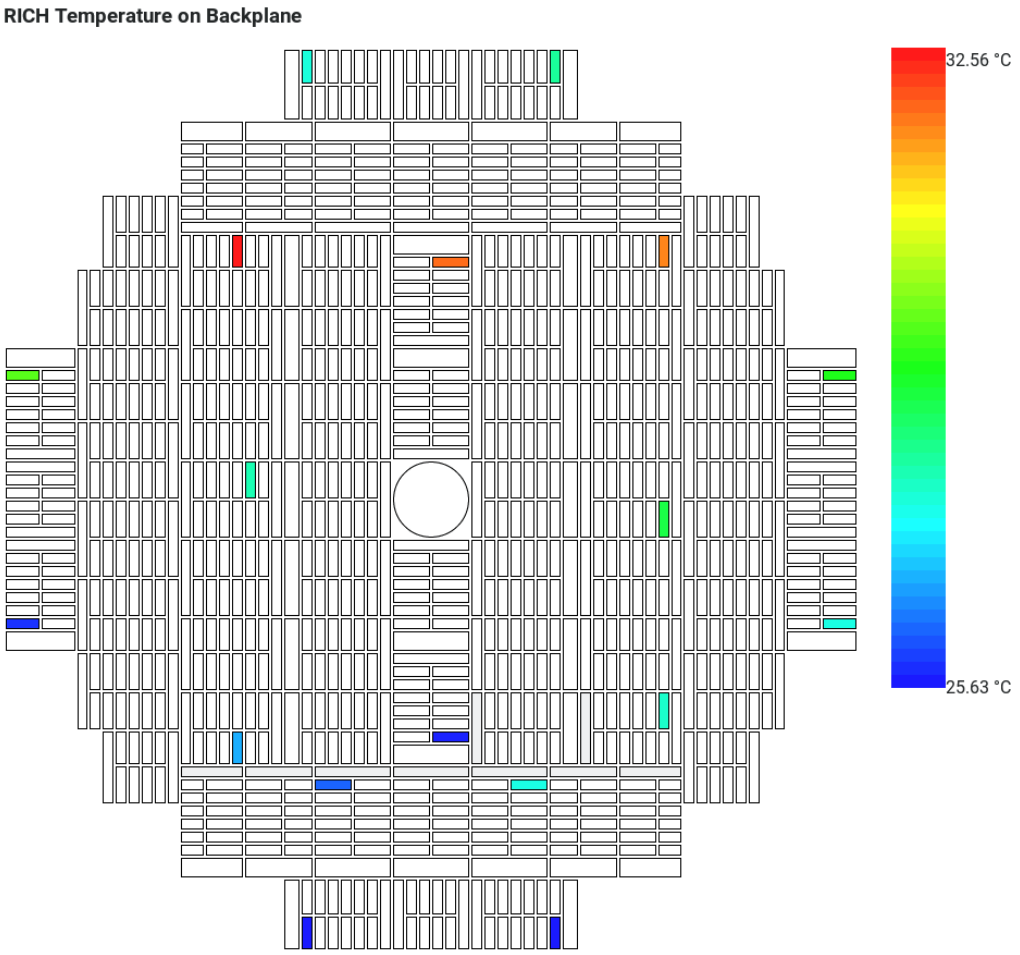

Figure 5.26: HTML based HADES RICH backplane temperature overview with indication of the TrbNet register address of the individual sensors.

like reset counts, hardware versions or scalar rates with an information of the latest update time.

Figure 5.24 shows the temperatures of all DiRICH and combiner boards of the HADES RICH from the internal measurement on the boards. The representation in the scheme of the beamview unveils hot spots in the corners of the inner detection plane. However, overall a smooth distribution of cool air from the cooling fans in front of the detection plane is achieved resulting in an otherwise rather homogenous temperature distribution. The webpage is also used while positioning the fans to maximize the cooling effect, but mostly serves as a detailed detector overview. Figure 5.25 represents the measured low voltages of the 1.1 V power line at the DiRICH FEE. The monitoring unveils the slightly different voltage on the six arms and the higher voltage on the 2×2 backplanes. Individual problems with single backplanes, e.g. a bad connection of the low voltage connector, becomes immediately visible in this monitoring page.

Figure 5.26 is similar to the representation of the full RICH FEE. This figure is representing the positions of the DS18B20 temperature sensors between MAPMTs and backplane in the beamview (see Figure 5.9,left). A mouse hoover unveils the TrbNet register address of each sensor with the latest temperature value. The hot spots from Figure 5.24 are seen here as well. Temperatures are slightly lower because this measurement is inside the radiator volume. These temperature measurements are used

for the interlock system as explained in section 5.2.1.2.

All these monitoring features for the RICH detector give a high confidence to the operators and experts about the functionality and status of the detector. The monitoring is a tremendous relief for solving problems with the detector fast. It was essential for the successful beamtime in March 2019 and showed an excellent performance.

CHAPTER 6

Development of the mRICH detector

The mCBM experiment is a prototype experiment for the future CBM detector, focussing on the combined free streaming data readout and acquisition including finally also online event reconstruction. The main prototype detector of the CBM RICH detector concerning the readout is the upgraded HADES RICH. The overall concept of the CBM RICH including mirrors and radiator has been tested in several CERN beamtimes with a real-size prototype in length [106, 140–143]. The HADES RICH confirms the functionality of the front-end electronics, the MAPMTs and provides an enormous benefit in the running and understanding of the detector. Also ring reconstruction routines can be tested on real data. The readout of the HADES experiment is triggered and completely based on the TrbNet network on dedicated FPGAs. The future readout of the CBM RICH with e.g. synchronisation and free streaming data transport cannot be tested in the HADES experiment.

For the CBM RICH development, the mCBM experiment is the perfect counterpart to the experience from HADES and opens up the possibility of development and test of the full readout chain under beam conditions. A dedicated mRICH detector has been built for participation in the mCBM beamtimes and test of the newly developed CBM

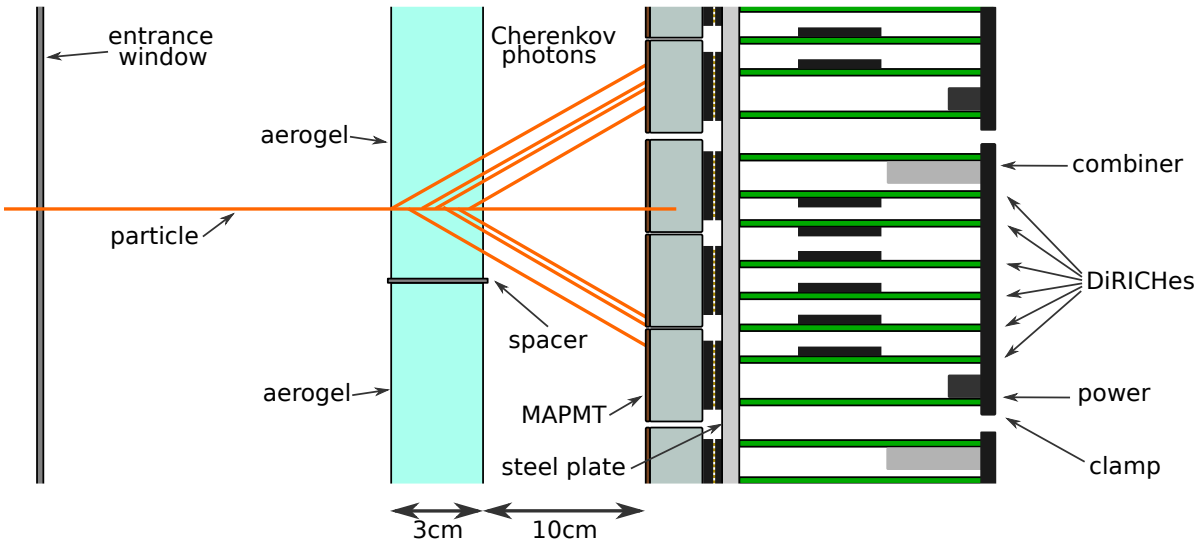

Figure 6.1: Schematic drawing of a side view of the inner mRICH detector. All main parts of the detector as well as the production of Cherenkov photons in the aerogel block are shown.

RICH readout concept in its staged phases. This chapter will concentrate on the construction of the mRICH detector with the first readout stage based on the data processing board (DPB) (phase-I). Chapter 7 will treat the upgrade of the mCBM and mRICH readout to the future common readout interface (CRI) of the CBM experiment (phase-II). Chapter 8 will present an analysis of the mRICH data in the phase-I mCBM beamtimes.

6.1 The mRICH Detector

The mRICH detector is a proximity focussing RICH detector (see section 3.3.2 for a details). Two $20\times20\times3$ cm^3 aerogel blocks are installed in a 3D printed support frame and serve as the radiator volume. The aerogel is positioned with a 10 cm gap to the entrance windows of the photodetection plane of 36 Hamamatsu H12700B-3 MAPMTs. In between the two aerogel blocks, a 1 mm thick ABS spacer is inserted. The aerogel and MAPMTs are inside a box, made out of ITEM profiles, that is flushed with Nitrogen to protect the Aerogel. A detailed overview on the position of the mRICH in the mCBM experiment as well as a introduction of the other sub-detectors and DAQ concepts is presented in section 3.4.

The readout of the mRICH detector is based on the DiRICH readout electronics and from the hardware point of view identical to the readout of the HADES RICH. Six 2×3 backplanes with 12 DiRICH boards, a standard combiner and power module without on-board DCDC converter are combined to form the camera plane of the detector. An aluminium plate is used as mounting plane of the PCBs. Similar to the HADES RICH, all backplane PCBs are screwed to the camera and sealed with a rubber band.

All backplanes are aligned in a symmetric geometry with two backplanes next to each other in horizontal and three backplanes in vertical direction, as indicated in Figure 6.2, left, as well as Figure 6.3,right. Each backplane is oriented such that the combiner points to the upper side and the power module to the bottom side. This arrangement is chosen as it slightly improves the voltage drop on the power line to the backplanes.

The MAPMT position on the aluminium plate is not symmetrical in order to provide enough space on one side of the camera to access PMTs in the mounted state. A 3D printed backplane inlet and additional 3D printed holding structures are attached to the PCBs from the outside. In combination with aluminium bolts they are giving stiffness to the attached DiRICHes, combiner and power boards.

The readout camera itself is screwed to a custom box of ITEM profiles. The box measures $W\times H\times D=382\times597\times250$ mm^3. The side walls are filled with aluminium plates and sealed with rubber band. All connections between ITEM profiles and the walls are sealed with additional LOCTITE SI5368 adhesive and sealant to provide gas and light tightness. The entrance window of the detector is filled with a plastic plate to minimize the material budget in the beam acceptance. All inner parts of the detector are painted black with NEXTEL Velvet-Coating 811-21.

The complete box is mounted to a holding construction. It provides the possibility to mount the detector box in standard vertical position but also in a horizontal position. The ITEM based support is attached to horizontal ITEM profiles that are screwed to the mTOF detector frame. In vertical direction the center of the sensitive MAPMT

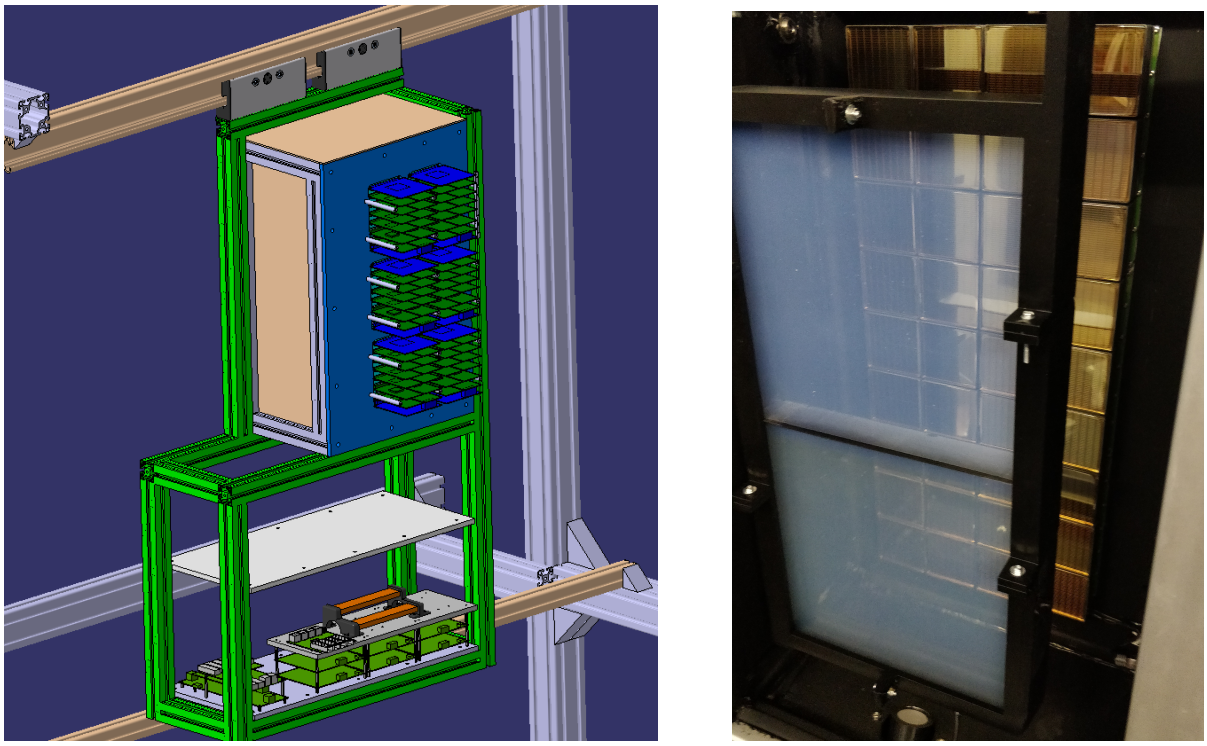

Figure 6.2: **(left)** CAD drawing of the mRICH detector with support structure and connection to the mTOF frame (to the left). **(right)** View into the inside of the mRICH. The two aerogel radiator blocks are mounted with 10 cm distance to the MAPMT detection plane.

plane is at the same height as the beam axis. The mRICH support structure is moveable in horizontal direction and connected with ball-bearing guide bushes to a shaft. The positioned detector is screwed to the bottom ITEM support profile to hold everything in place. The support structure is equipped with PVC inlets to provide nearby mounting space for the low voltage and DAQ boards.

parameter	value
detector concept	proximity focussing RICH
detector volume (W×H×D)	382×597×250 mm^3 (outside)
radiator material	aerogel
index of refraction (n)	1.05
γ_{thr}	3.27
P_{thr} (e^-)	1.6 MeV
P_{thr} (π)	436 MeV
P_{thr} (p)	2930 MeV
camera active area (X×Y)	206.6×470.1 mm^2
camera	36 Hamamatsu H12700B-3 MAPMTs
channels	2304

Table 6.1: Overview on the main geometry and physics parameters of the mRICH detector in the mCBM experiment.

Aerogel is a well know radiator material in Cherenkov detectors. It is an amorphous solid network of SiO_2 nano-spheres. The material has a low density and can be produced with a range of different index of refractions. The mRICH aerogel tiles are identical to the aerogel used by the CLAS12 collaboration RICH detector and come with high light transmittance. Measurements of the CLAS12 collaboration result in an index of refraction of n=1.05 at 405 nm [144]. This index of refraction results in γ_{thr}=3.27 and e.g. a threshold momentum for pions of p_{thr}=436 MeV. A full overview on all important detector parameters can be found in Table 6.1.

The aerogel blocks in the mRICH are hydrophilic. As a protection of the aerogel in the detector box, a dry atmosphere is required. The full detector volume is flushed with dry nitrogen (N_2) and in addition silica gel is placed on the bottom of the detector. An environment sensor board, based on the spoke sensors of the HADES RICH detector (see section 5.2.1, appendix B and [130]), is placed inside the detector volume on the bottom side of the aerogel holder to record the pressure, temperature and most importantly the humidity. The sensor is connected to the CTS and hub TRB3sc board that is also controlling the sensor readout. A gas and light tight RJ45 feed through is mounted in a sidewall of the detector box and provides the connection to the TRB3sc.

A second feed through is placed to connect DS18B20 temperature sensors between the MAPMTs and backplane, identical to the HADES approach (see section 5.2.1.2). The chained 1-wire temperature sensors are connected to the same TRB3sc as the humidity board. The temperature readout sensors are placed in the middle of a MAPMT at the positions indicated in Figure 6.3. It additionally shows the backplanes with all 36 MAPMTs attached (Figure 6.3, middle) and no radiator in front of it. The corre-

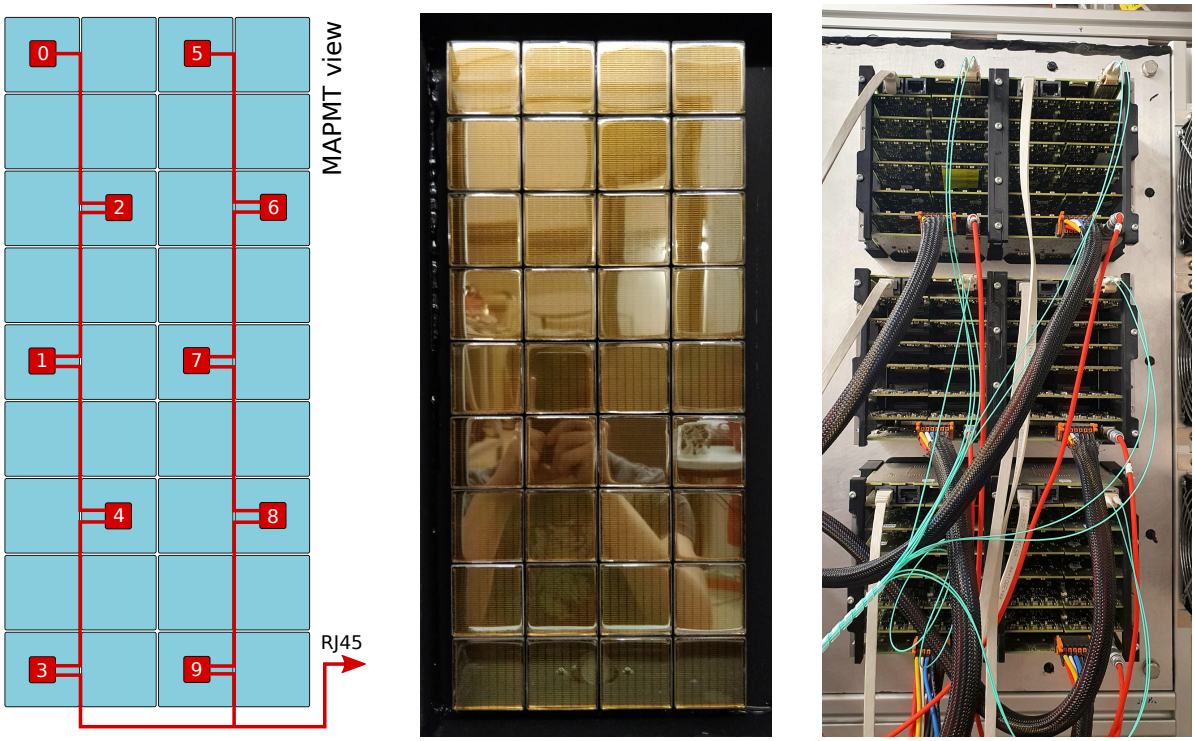

Figure 6.3: **(left)** Schematic overview on the location of the daisy chained backplane DS18B20 temperature sensors. **(middle)** View on the equipped MAPMT plane with sensors below the MAPMTs. **(right)** View on the FEE of the mRICH with all power and data connections.

sensor number in chain	UIDs of DS18B20
Sensor 0	2B0416524E83FF28
Sensor 1	F9041651C3F7FF28
Sensor 2	9E0000092C4AFD28
Sensor 3	F20000092C509F28
Sensor 4	D90000092C890E28
Sensor 5	A90000092C88F428
Sensor 6	EC0000092ACAE828
Sensor 7	430000092AC40728
Sensor 8	630000092ADF4428
Sensor 9	450000092C355A28

Table 6.2: UIDs of the mRICH backplane DS18B20 temperature sensors as indicated in Figure 6.3.

sponding UIDs to the sensor numbers are listed in Table 6.2. The 10 temperature sensors are soldered to a daisy chain with two arms. Sensors 0 to 4 and 5 to 9 form one arm each and are connected below the MAPMT plane to one bus cable, that is later connected to the readout.

The FPGA readout of the sensors is based on an One-Wire temperature readout entity. The UIDs are hardcoded to the entity as generics. This simplifies the matching of readout register to backplane positions and is in parallel a documentation of the readout chains UIDs. The same entity is used for the HADES RICH and mRICH readout. A future usage of the entity in the CBM RICH detector setup is most likely and easily possible.

The MAPMTs are mounted in front of the temperature sensors. The center of the MAPMT plane is matching the 25° degree line, with respect to the beam line, of the mCBM experiment (see section 3.4). Differently to the HADES and CBM RICH detectors, the mRICH detector's photo multiplier plane is located in the particle acceptance. Particles are traversing the MAPMT plane and create signals in the MAPMT channels. Next to an increase of hit signals on the MAPMTs and resulting differences in the detected ring structure (see Chapter 8), this influences the mRICH detector readout. The DiRICH readout is based on the FPGA technology, that is not radiation hard. An increased radiation, in mCBM due to the generated particles in the acceptance, increases the probability of single event upsets in the FPGA and increases instabilities of the FEE. More details on the final readout implementation are given in Section 6.2.

The HV power distribution to the mRICH is coordinated with the other mCBM detectors. The six backplanes are connected to an ISEG high voltage power module that shares a crate with the mMUCH detector in the mCBM DAQ container. The applied high voltage of the backplanes is calculated based on the individual gain of the MAPMTs and is controlled via a scripted Simple Network Management Protocol (SNMP) connection. A common mCBM HV patch panel serves as the connection between the standard SHV cables, used between the DAQ container and the patch panel, and thin RICH specific Draka HV wires. The Draka wire connects to the backplane via a LEMO connector. The HV channels are matched to the correct backplane position and tested individually to guarantee the optimal measurement environment.

The mRICH low voltage power distribution is based on an approach adopted to the experience in HADES and serves as a test bed for the final CBM RICH powering. In the CBM experiment, the low voltage power cables will be to long for a 1.1 V supply

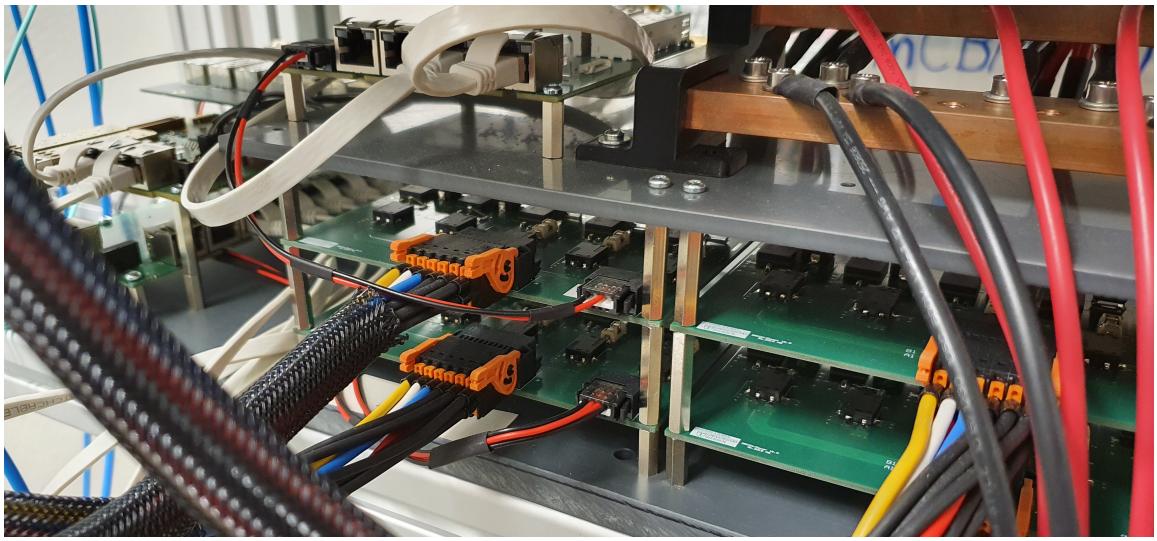

Figure 6.4: View of the low voltage distribution via copper bars and the first four DCDC converters of the mRICH detector. In the foreground, the 1.2 m cables for the connection to the backplanes are visible (orange plug).

line with high currents. As a compromise between a low noise and a reasonable cable length of especially the 1.1 V supply line to the FEE, dedicated DCDC converters as well as a power distribution, are mounted to the PVC inlets in the mRICH support structure below the detector box as shown in Figure 6.4. The DCDC converters are based on the DCDC conversion part of the power modules (see section 3.3.7) with an additional 5th converter for 3.6 V respectively 5.5 V. This 5th voltage is used to power the TRB3sc, the trigger Fanout as well as the optoLink board. The schematic of the DCDC board as used in mRICH phase-I is shown in appendix E.

An HMP4040 power supply is located in the mCBM low voltage niche. The four channels of the HMP4040 power supply are connected with AWG 16 cables from the niche to a dedicated copper bar for power distribution at the mRICH. One copper bar is connected to the +24 V of the power supply, whereas the other copper bar serves as the GND distribution. Each copper bar is produced with threaded inserts to distribute the full current from all four power supply channels to the six newly designed dedicated DCDC converter boards. Thus the +24 V are converted to the necessary four FEE voltages about 1.2 m apart from the backplane, therefore not adding noise to the signals. The voltage drop on the 1.2 m power line has to be taken into account and therefore a higher voltage after conversion, compared to the design with a conversion directly on the power module, is required.

Unfortunately one of the phase-I DCDC boards provides a to low voltage on its 1.1 V power line. Thus one backplane has to run with a reduced amount of DiRICH boards, to reduce the current and finally reduce the voltage drop. The low voltage on the 1.1 V line of this particular backplane is mainly limiting the ToT measurement capabilities of the FEE. The voltage drop, and as a result the reduced input voltage, is limiting the ToT measurement capabilities of the FEE. In phase-II of the mRICH, this problem is solved, as a new programmable DCDC converter (see appendix A) is added to the place, where the optoLink was placed during phase-I. This new DCDC board solves the power issue with the one backplane, while the old DCDC board is still providing the 5.5 V of the TRB3sc.

The FEE of the mRICH detector is cooled by three 120 mm fans. They are powered by a separate 12 V supply line from the mTRD LV-crate and are mounted vertically on the side of the FEE on the ITEM profiles of the box. Thus the fans are pushing air along the rows. The geometry of the backplanes allows the flow of the air from one side to the other and keeps the inner backplane temperature below 33°C.

6.2 mRICH Readout

The mRICH readout is the beginning of the journey towards a TrbNet based, free streaming CBM RICH readout. In section 6.1 the mRICH was introduced with the position of the six backplanes of the mRICH FEE, including the low voltage power connections. One backplane of the detector is forming the smallest readout unit of the mRICH FEE. The DiRICH boards themself are flashed with the exact same firmware as in the HADES RICH detector. Nevertheless, the configuration of the firmware is slightly different. In contrast to the HADES RICH DiRICH boards, which are using a trigger window for readout, for the mRICH DiRICH the readout window is disabled. Data in the ring buffer are not read out with respect to the arrival time of the trigger signal anymore, but the full ring buffer of each DiRICH TDC channel is read out with the arrival of a pseudo trigger and transmitted. In the standard beamtime configuration, each DiRICH is configured to a ring buffer size of 9 words per channel and an event size limit of 245 words per DiRICH.

Disabling the trigger windows is the principle providing the path to a free streaming data readout. The key point of the TrbNet based RICH readout in CBM environments is the generation of a pseudo trigger, forcing the readout of the full TDC ring buffers. A pseudo trigger is generated on a TRB3sc board by CTS, based on a signal synchronous to the start of a microtimeslice. The TDC hits in the ring buffer since the latest readout are all transmitted to the trigger Handler and later on combined with the data from the remaining 11 DiRICH boards of a backplane, identical to the HADES RICH readout.

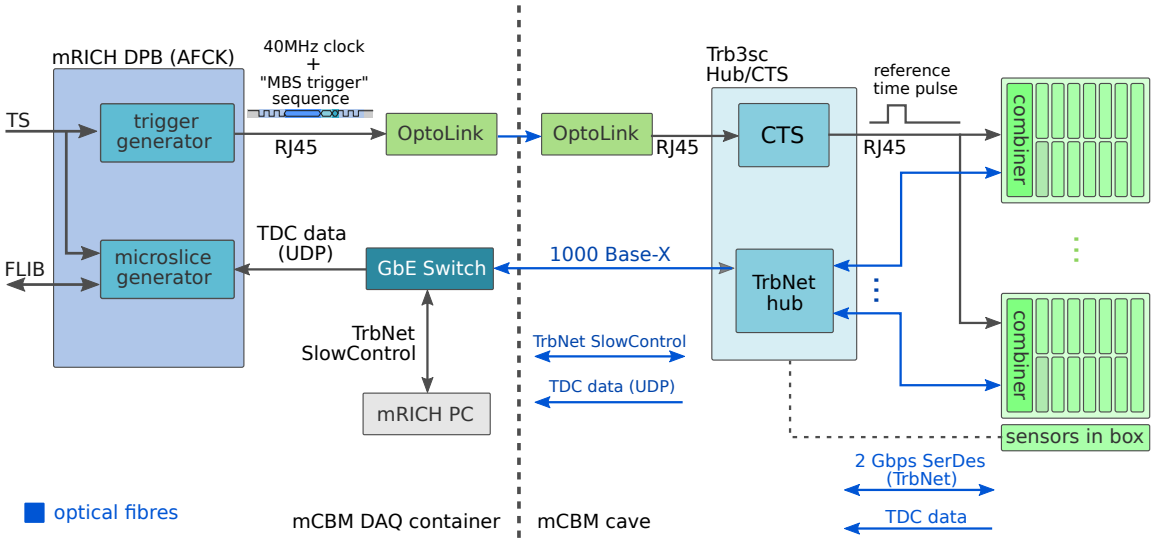

Figure 6.5: Schematic overview of the mRICH readout concept. The blue lines represent optical fibre connections between the readout boards. The readout is spatially separated between a part in the DAQ container (left) and the cave (right).

A microtimeslice splits the time during data taking into discrete packages of a defined length in time. The length of the microtimeslice is defined by the operator and was e.g. set to 1.28 ms during the 2020 beamtime campaign.

6.2.1 TrbNet in the CBM Environment

A dedicated TRB3sc is installed next to the low voltage distribution on the mRICH holding structure and completes the TrbNet based readout part. On the one hand, this TRB3sc provides the readout of the backplane sensors, as well as the humidity monitoring below the aerogel radiator. On the other hand, it is the central trigger system and hub of the TrbNet part of the mRICH readout system. A 6-SFP hub-AddOn is attached to the TRB3sc and provides SFP connections for the optical fibers of the six downlinks towards the combiner boards. A dedicated trigger distribution board is installed below the TRB3sc to get a dense packaging below the detector. The trigger distribution board is a fan-out of the generated CTS trigger signal from the TRB3sc towards the six backplanes via RJ45 cables. A flat RJ45 cable is installed between the fan-out board and each backplane of the mRICH detector. Thin 0.9 mm optical fibre cables with LC-connectors are connecting the data uplink of the combiner boards with the six downlinks of the hub-AddOn on top of the TRB3sc.

6.2.1.1 Combiner and FPGA Based Online Calibration

The optical fiber and the RJ45 trigger connection are providing the full TrbNet functionality to the combiner boards. A virtual slow control connection, data and trigger channel is provided between the combiner and the TRB3sc. The combiner board firmware[1] is utilising a TrbNet hub to combine the data from all 12 connected DiRICH boards, based on the readout command of the CTS. The data from all DiRICH boards is further transmitted to the CTS/Hub TRB3sc. The mRICH combiner firmware is calibrating the TDC data on the FPGA and transmits fully calibrated data towards the CTS/hub board. The TDC based online calibration is needed to correct the TDC tapped delay chain for temperature changes and to match the fine time bins of the TDC to the actual coarse time window of 5 ns (see [130]). The use of an online calibration directly on the combiner board simplifies the later unpacking of the data, as no further calibration of the data is needed. Only small adjustments to the startup procedure of the mRICH DAQ are needed to prepare the online calibration.

The online calibration in the mRICH detector is a progression of the calibration introduced in [130]. The random access memory type is changed to embedded RAM and further optimised in the handling. Several small changes in terms of cross platform usage are included and a more advanced monitoring is introduced. The calibration entity can cope with data from a TrbNet streaming entity (hub) as well as pure TDC_record data. Data from the streaming hub have to be prepared in terms of the correct data size and the extraction of e.g. the trigger type. Nevertheless, the basic principle of the linear online calibration stays untouched: Data from the DiRICH board is fed into the calibration. Based on the incoming data, the minimum and maximum fine time bin per channel (also referred to as limit) is extracted. A configurable statistics for the creation of the limit is needed to use the extracted limits for the calibration. If the limit is

[1]The mRICH phase-I combiner project including data calibration is available at: `http://jspc29.x-matter.uni-frankfurt.de/git/?p=dirich.git;a=tree;f=combiner_calib`

reached, the values are saved in a dedicated RAM and a new limit generation starts in parallel to the calibration of the data. All the TDC fine time data is calibrated, based on the generated limits. In case of a cold start of the board, standard values are used for the calibration. The calibrated data is further fed back into the normal data path and handled like normal TDC messages. All non TDC finetime messages are also carried through the chain, but without calibration, to keep the order of the data constant.

The online calibration can be configured in several modes. A calibration of all, but also of just one dedicated trigger type, is possible. The calibration can be active, while the limit generation is deactivated and vice versa. A high configurability is essential as the calibration entity is used e.g. on the TRB3sc (to calibrated the TDC, that matches the overall CBM time to the local mRICH time), where different requirements have to be fulfilled. An important requirement is the possibility to generate limits only with calibration triggers. In some cases e.g. channels are fed with signals, generated with a clock synchronous to the TDC clock. As the timing of these signals is not random anymore, no meaningful limits could be generated by a physical trigger.

6.2.1.2 CTS and Hub

The mRICH detector readout structure of phase-I is shown in Figure 6.5. It shows, that a dedicated TRB3sc board is required to combine the data coming from the six connected combiner boards at the downlinks and transmit the data as UDP packages via a GbE connection at the uplink. This connection provides the data packages for the DPB as well as the slow control interface, including DHCP and ping support. In addition, the pseudo triggers for the readout itself have to be generated on the same board while the readout of the data has to be controlled. Therefore a central trigger system (CTS), as it is also used in other TrbNet applications, is used.

The TrbNet hub entity of the TRB3sc is essential for the data merging from all connected combiner boards. It is a logic, that controls the data flow between all connected TrbNet boards as well as local endpoints of all available virtual channels (trigger, data, slow control). Slow control commands are transmitted and received via UDP packages on the GbE link and distributed to the FEE via the hub logic. An mRICH control and readout computer is located in the mCBM DAQ container and connected to a GbE switch to receive the packages from the TRB3sc (see Figure 6.5). The computer is equipped with the full software for slow control, monitoring and baseline determination as well as threshold writing. A DABC event builder is available for the analysis of pure TrbNet data. The computer runs the TrbNet daemon, the arbiter of the TrbNet messages. All slow control or flash commands for the TrbNet boards are using this connection. Data to the DPB is routed via the switch by the MAC and IP address of the UDP packages. The GbE data connections are configured via slow control on the Hub/CTS board.

The CTS is the main readout control of TrbNet. In a standard TrbNet environment exactly one CTS is existing in the system of TrbNet boards. CTS is controlling the data readout on the endpoints (DiRICH) and the readout of the hubs. A reference time signal is distributed to all endpoints. Next to the separate physical signal, a LVL1 trigger packet is distributed on the virtual trigger channel of TrbNet via optical links. The packet contains all trigger informations which the endpoints require, as e.g. trigger type and trigger number. The trigger system is stopped until all FEE boards acknowledge the trigger information with a trigger release message. A trigger handler entity

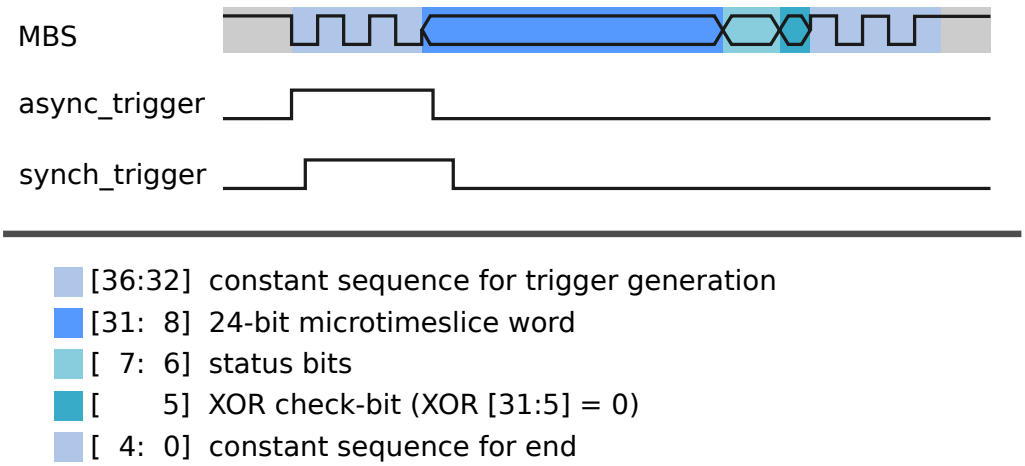

Figure 6.6: MBS style trigger message from DPB to Hub/CTS TRB3sc. A trigger code is transmitted with a 40 MHz clock speed and sampled on the TRB3sc with 200 MHz. Based on the first five bits of the MBS signal, an asynchronous and a synchronous trigger is derived. The synchronous trigger is synced to the 100 MHz system clock of the TRB3sc and is furthermore the input signal for the CTS trigger generation. The microtimeslice number of the mCBM microtimeslice is encoded in bit [36:8] with 2 status bits and a control bit.

inside each endpoint is necessary. It checks the reference time signal length for spike rejection. A typical reference time is 100 ns. If the time is below 60 ns or above 200 ns, the trigger is rejected. Additionally a certain time window for the arrival of the LVL1 trigger message has to be fulfilled. A more detailed description of the exact functionality of the trigger handling can be found in [123]. The generation of the trigger signal is controlled by the CTS. Triggers can be generated internally based on external signals from e.g. sub detectors. The generation of triggers based on internal signals from a random pulser or e.g. a dedicated calibration trigger is provided too. Advanced external trigger sources are supported by the CTS as well. In a standard scenario during beamtimes, an external trigger signal from e.g. a laser can be used to readout detectors for quality assurance. The generation of data for a TDC calibration during spill breaks or during shutdowns is possible by the generation of calibration triggers.

The mRICH in phase-I of the mCBM experiment is based on the previously introduced trigger distribution scheme. A detailed schematic overview on the phase-I readout concept is given in Figure 6.5. In contrast to e.g. HADES, the mRICH trigger is not generated by a sub detector or a pulser. The mRICH detector readout trigger is generated by an external trigger signal from the mRICH DPB, located in the mCBM DAQ container. A separate signal from the mRICH DPB is transmitted as a LVDS signal to an OptoLink board, a special board, that is used to convert the LVDS signal to an optical fiber and reconvert it back to RJ45 at the mRICH detector. A 40 MHz clock and the corresponding data is transmitted on opticals fibers between the DAQ container and the mCBM cave. The optical fibers are identical in length and therefore no additional clock recovery is needed.

Due to the long distance between DAQ container and the mRICH detector the transmission of the external trigger signal from the mRICH DPB requires an OptoLink board. The use of a long copper cable as e.g. an Ethernet cable is critical as the increased capacity and resistance of such a cable disturbs the physical signal and harms the oper-

ation. An optical connection is not sensitive to these influences and allows a reliable transmission over longer distances.

The signal from the DPB is not a simple trigger pulse. The trigger is transmitted as a 37-bit serialised bitstream with a known structure of the Multi Branch System (MBS) developed at GSI. The exact structure of the MBS word (terminology used for the mRICH trigger bit-sequence) is shown in Figure 6.6. Similar to MBS, a 24-bit word is encoded in a serialized bit sequence. The 24-bit word is the corresponding microtimeslice index of the mCBM DAQ for the transmitted trigger.

Each MBS microtimeslice signal, derived from the synchronous mCBM time, is used as the readout trigger of the mRICH detector. The synchronous mCBM time guarantees the synchronous application of the trigger. The MBS word receiver derives an asynchronous and a synchronous trigger from the MBS word as shown in Figure 6.6. The synchronous trigger is in synch with the 100 MHz system clock of the TRB3sc and is the external trigger signal of the CTS. CTS is generating a trigger message based on the synchronous MBS trigger and reads out all TDCs. The readout of the FEE is therefore performed with the microtimeslice frequency and each mRICH event is assigned to a microtimeslice. An own TDC is added to the TRB3sc to perform a measurement of the arrival time of the asynchronous trigger. These TDC measurements are needed to correct for the random uncertainty of 10 ns, introduced by the 100 MHz system clock, between the global mCBM time and the local TDC hit time.

The TDC on the TRB3sc is calibrated by the FPGA based online calibration entity as used in the combiner firmware. A calibration of the TDC with a calibration trigger is executed after each power cycle. The calibrated TDC message is read out together with the FEE data and finally transmitted in an event structure to the mRICH DPB.

The derived microtimeslice start signal should ideally trigger the FEE of the mRICH in the same time, as the global microtimeslice is started. Therefore a measurement of the signal "propagation time" between the DPB MBS-trigger output and the DiRICH reference-time input was performed. The measurement used the identical setup as the final mRICH detector, excluding the optical fiber connection between the DAQ container and the cave. The length of the optical fibre is parametrized as l_{opt} and results in a delay of

$$155.4ns + l_{opt} \cdot 4.972\frac{ns}{m} \tag{6.1}$$

The real optical fibre between DAQ container and mRICH detector is 76 m in length, resulting in a total delay of 533 ns. A total delay of 600 ns is assumed to account for an additional output delay of 50 ns in the firmware of the mRICH DPB and the delay between the DiRICH trigger input and the actual FPGA. Due to a misconfiguration in the mRICH DPB, the offset correction was not used in the mCBM beamtimes and a corresponding correction in the data unpacking process is applied.

An additional small uncertainty source is the walk effect between the mCBM clock and the FEE clock. While the start of a microtimeslice is synchronized by the distributed reference time, the later hit time is measured with the local clock. Each frequency deviation between the clocks leads to an error in the hit time. This error could be corrected by the reference time of the measurement on channel 0 on the TDC. The difference between the reference time in event N and N-1 is a measurement of the microtimeslice period in the local clock, while generated in the mCBM clock. The walk effect could be corrected by this measurement, but it is not foreseen in the current unpacker as the error is only minor (≈1-2 ns @ 1.28 ms μTS) and the correction would

additionally slow down the unpacking procedure. More details on the full mCBM synchronisation and timing is available in the technical note [145].

The readout of the front-end buffers is controlled by the central trigger system in the same manner as the trigger distribution. CTS sends a readout request to all FEEs. The FEEs transmit the data, belonging to the request from CTS. The readout message contains the information on the trigger number and code, as well as informations on the data transport. Different packaging types with different levels of data stripping can be defined. In addition the request contains the information of the event builder, the data is transmitted to. In the mRICH case, the event builder is the DPB. The internal look-up table number of the DPB MAC- and IP-address is transmitted to all FEEs. Based on the packaging code of the CTS readout request, unnecessary overhead data is stripped on the hubs and combined to the readout data stream. The data stream contains the information of the trigger type, the data length and the hub board address. If the information on the event and the data header is transmitted, the FEE data is forwarded by the round-robin principle. More detailed information on the TrbNet readout can be found in [123].

The TrbNet readout stream is further processed for Gigabit Ethernet transmission. The HadesTransportUnitQueue is added to the sub event structure and further transmitted in UDP packages and frames to the DPB by the Gigabit Ethernet wrapper entity of TrbNet.

6.2.2 Data Processing Board (DPB)

The data processing board (DPB) of the mRICH experiment is an **A**MC **F**MC **C**arrier **K**intex (AFCK)[2] that is operated in a MicroTCA crate inside the mCBM DAQ container. The AFCK is equipped with a Xilinx Kintex-7 325T FFG900 FPGA and features a very flexible clock circuit. Figure 3.32 in the introduction to the mCBM DAQ depicts the position of the DPB in the DAQ chain. The DPB aggregates the data from the downlinks and further processes it in terms of e.g. sorting (mSTS) or feature extraction (mTRD). The data stream is packed in microtimeslices and transmitted via a 10 Gbit/s high-speed line per DPB. The length of a microtimeslice is adjustable and is defined before the beamtime (mCBM 2020: 1.28 ms). A bunch of single mode optical fibers connects the DPBs to the FLIB inside the Green IT cube.

A single DPB is used in the mRICH detector DAQ. The Timing Synchronizer (TS) is connected to the AFCK via a custom FPGA Mezzanine Card (FMC) and provides a synchronous 40 MHz clock and a Puls-Per-Second (PPS) Signal ($\approx$0.839 sec) [146]. Based on the 40 MHz clock and the PPS signal, the external trigger for the TRB3sc is generated and equipped with the microtimeslice index.

A single 1000 base-X UDP connection receives the TDC data stream from the TRB3sc in the cave. The Trb event data is parsed from the incoming UDP packets and checked for basic data correctness. The microtimeslice index is extracted from the data and added as meta data to the beginning of the 64-bit AXI stream, that transports the data between entities. The 64-bit data in the AXI stream is processed in a micro-slice generation entity. This entity compares the microtimeslice index of the data with the ex-

[2]Board is available as open hardware project: https://ohwr.org/project/afck/wikis/home

pected index in the DPB. In case the index is not as expected, the Trb data is discarded and an empty microtimeslice is send to the FLIB. Correct data is finally transmitted to the FLIB by a FLIM wrapper entity, that utilises the 10 GBit optical fiber connection to the green IT cube.

The mRICH DPB is prepared to be operated in a standalone mode or in a common mode. Accordingly to the needs, the corresponding firmware has to be written to the FPGA. An own FLIB module is connected to the mRICH PC to allow for a standalone data readout.

6.2.3 mRICH Data Format (mCBM Phase-I)

A schematic overview of the mRICH data format in mCBM phase-I is shown in Figure 6.7. The data format can be separated in two parts: The first two words (32 bit = 1 word) are related to the mRICH DPB and provide a mRICH header as well as mRICH flags and the MBS trigger number. This part is inserted by the DPB and followed by the second part, the original TrbNet event-data structure. The TrbNet data contains a header, a data and a trailer part. This "HADES Transport Unit Queue" is included to the data by the Gigabit Ethernet wrapper and gives informations about the length and decoding of the queue. The trailer of the queue consists of an optional padding word, to get the queue size to a multiple of 8, and a repetition of the first 8 "HADES Transport Unit Queue" words in the end. This repetition serves as a last check for data corruption. The data in the "HADES Transport Unit Queue" is depicted in a schematic view in Figure 6.7. A detailed description of the TRB sub-event, sub-sub event structure and TDC message format is provided in [123] and [147].

The mRICH readout uses a TDC in all DiRICH boards as well as the TRB3sc. The TDC messages are part of the TrbNet data in different sub sections. The Trb sub-event is the basic structure of the board, transmitting the data (the TRB3sc in the mRICH detector). A chain of hub blocks is summing up to the content of the Trb sub-event. The hubs in the mRICH readout are equal to the combiner boards as well as the endpoint data of the TRB3sc. A sub-event consists of several "sub-sub-event" blocks. The sub-sub-event blocks contain the complete data from the connected DiRICH boards. The CTS is a special part of the hub block, as it contains the TDC messages of the TRB3sc TDC as well as the microtimeslice index transmitted by the DPB.

All TDC messages in the data stream follow the same structure. A TDC header word is indicating the start of the TDC data, including an information on the used hardware and an error mask. The end of the TDC part is marked by the trailer word. It includes the trigger type, the random trigger number and an additional error mask. In the beginning of a TDC packet or in case the coarse counter has overflown, an EPOCH message is included into the data. Each rising and each falling edge of a TDC channel is adding an own TDC word to the data. The TDC message itself is constructed by the channel number, the fine time, a flag for the edge type and the coarse time.

All DiRICH boards on a backplane are operated with a 100 MHz clock, that is shared with the combiner board. Therefore each backplane with its DiRICHes has a local time, as the DiRICHes only known their 100 MHz time from the oscillator. The TRB3sc is also operated with an own local 100 MHz oscillator. The local mRICH TDC time of a hit in a DiRICH as well as in the TDC of the TRB3sc is calculated by the epoch value e, the coarse time c and the fine time f of the TDC message:

$$t_{local} = e \cdot 10240ns + c \cdot 5ns - f \cdot 5ps \tag{6.2}$$

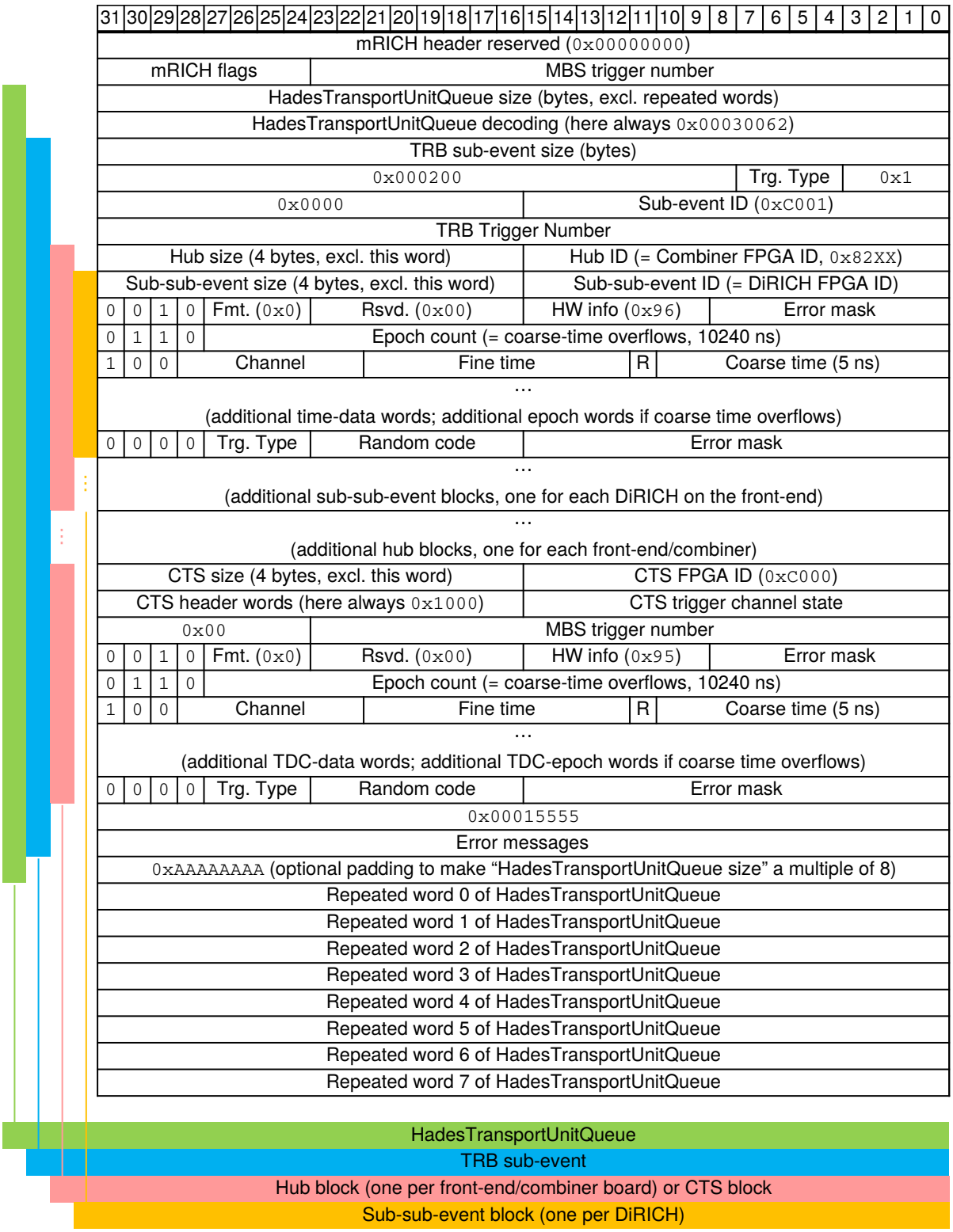

Figure 6.7: Format of the mRICH data in a microtimeslice for mCBM in phase-I. Figure taken from [148].

The local time of a hit in the data stream has to be converted to the global mCBM time of the experiment. All subdetectors in mCBM have to be synchronized to this global clock, that is distributed by the TS (respectively TFC in phase-II). The time difference between the reference time (the local time) on the TRB3sc and the mCBM microtimeslice signal (synchronous to the global mCBM time) is used for the transformation of the clock domain in the unpacker. The reference time is the pseudo trigger signal, that is generated by the CTS and therefore in the local time of the TRB3sc (channel 0 of the TDC). The microtimeslice signal is the MBS signal that is synchronous to the global mCBM time and finally triggers the pseudo trigger generation in the CTS logic.

For each hit in channel c of a DiRICH D in microtimeslice N, the absolute mCBM time can be calculated. The microtimeslice index t_{ms}, the rising edge of the reference time channel 0 of the previous microtimeslice (N-1) of the same channel of the DiRICH and the difference between channel 0 and 2 of the CTS TDC in the microtimeslice (N-1) are used to transform the hit timestamp into the mCBM time [148]:

$$t_{mCBM} = t_{MS} + (t_{D,c,N} - t_{D,0,N-1}) - (t_{CTS,2,N-1} - t_{CTS,0,N-1}) \tag{6.3}$$

Unfortunately this calculation of the timestamp of a hit in the mCBM time domain needs the previous microtimeslice for the calculation and therefore contradicts the required self-consistency of a microtimeslice. Phase-I of mCBM was not using an online reconstruction and therefore this was not an issue for the operation of mCBM. This issue will be fixed in the upcoming mCBM phase-II concept.

6.2.4 Readout Performance

The following considerations on the performance of the mRICH detector and its DAQ are based on six runs during the mCBM beamtime campaign in 2020. Different interaction rates of the ions, measured by the T0 detector, and different thicknesses of the gold target were used. The thin gold target provides a thickness of 250 µm with a 1% interaction probability, whereas the thick target has a total thickness of 2.5 mm (10% interaction probability).

In the following, the mean data rates of DiRICHes as well as channels, including spill breaks of ≈4 s, are discussed. Furthermore data losses and the maximal rate of the DiRICHes is investigated with a look at the data sizes and limits of the mRICH. Finally the timing of the mRICH with respect to the T0 and mTof detector is shown.

The mRICH detector was operated in two different modes, to compare the behaviour of the readout:

- Low Rate (LR) setup for the standard operation. All 59 DiRICH boards, that could be operated in a stable system with an acceptable voltage on the pre-amplification, where operational. The configuration of the TDC ring buffer limit is 9 and the maximum event size per DiRICH is set to 245.

- High Rate (HR) setup for the operation at ion rates above 10^8 per 9 sec spills length. A subset of 24 equally distributed DiRICH boards on 6 backplanes was operated. The configuration of the TDC ring buffer limit is 15 and the maximum event size per DiRICH is set to 499. The event size of 499 words is the maximum that is configurable. A TDC Limit of 15 produces no loss on the data merging in the event buffer.

run	au target	ion rate [1/9s spill]	mean DiRICH rate [Hz]	mean channel rate [Hz]
819	thin	$2{\cdot}10^6$	1749.96	54.69
831	thick	$2{\cdot}10^6$	4696.21	146.76
836	thin	$2{\cdot}10^7$	13852.60	432.89
841	thick	$2{\cdot}10^7$	26096.9	815.53
855*	thin	$1{\cdot}10^8$	49328.8	1541.53
856*	thick	$1{\cdot}10^8$	92300.4	2884.39

Table 6.3: mRICH DAQ performance in different runs during the 2020 mCBM beamtime campaign. Runs with different intensities and target thicknesses are compared. The mean rate in the runs are extracted in the data unpacking per DiRICH and per channel. Run 855 and 856 are in a high rate configuration with a small fraction of the available FEE to enhance the throughput in the combiners respectively the UDP packages.

In both modes, the threshold value of the TDC channels was set to the standard value of 70 mV.

An analysis based on data from the mRICH unpacker is performed in order to validate the functionality of the mRICH readout and to evaluate the expected limitations of the system. The spill breaks are not excluded in the analysis as the detection of spill breaks would require major changes in the structure of the unpacker. A simple calculation of the rates without the spill breaks would ignore the fact, that also in between spills data is recorded by the FEE.

The maximum rate in a DiRICH is of higher interest for the investigation of the limits of the hardware. Therefore a second analysis based on the digis after unpacking was performed (see Table 6.4). This analysis can only investigates the rates on a timeslice basis as, due to technical reasons, the microtimeslice information is not available anymore. A timeslice is the combination of 10 microtimeslices and therefore has a duration of 12.8 ms. The highest amount of digis (raw hits after unpacking) per timeslice in the analysed runs is extracted and converted to Hz. This analysis gives the maximum rate that was achieved by the mRICH detector during the investigated runs. E.g. a maximum of 3407 digis in a timeslice would result in a rate of 3407/(10·1.28 ms) = 266171 Hz. Taking the total number of 1871 active pixels of the mRICH into account, the mean pixel rate in the timeslice with the maximum number of digis is 142 Hz.

The UDP protocol, that is used for the data transport between TRB3sc and DPB, is limited to a theoretical value of 65535 Bytes. This limits the readout capability of the mRICH detector in the mCBM phase-I to an event size of maximum approximately 65 kB. The limit of the TDC ring buffers as well as the DiRICH event size is adjusted to a value, that is slightly lower than the maximal UDP packet size. The unpacked data was analysed in terms of the event size, the DiRICH maximum event size as well as the TDC ring buffer size. The low rate (LR) and the high rate (HR) operation modes were tested in the beamtime to observe the intended increase between LR and HR in DiRICH maximum event sizes, as well as TDC ring buffer size in the disabled trigger window mode.

Based on the leading and falling edges of the raw data from the DiRICH FEE, the number of TDC hits in a microtimeslice could be calculated in the unpacker. During the mCBM 2020 beamtime, a microtimeslices has the length of 1.28 ms. The overall amount of TDC hits from DiRICHes, divided by the number of active DiRICH boards and the total length of the run (number of microtimeslices times 1.28 ms), results in

run	au target	ion rate [1/9s spill]	max. digis in timeslice	mean max. pixel rate [Hz]
819	thin	$2{\cdot}10^6$	3407	142
831	thick	$2{\cdot}10^6$	9421	393
836	thin	$2{\cdot}10^7$	26787	1119
841	thick	$2{\cdot}10^7$	42279	1765
855*	thin	$1{\cdot}10^8$	36940	3758
856*	thick	$1{\cdot}10^8$	40190	4088

Table 6.4: Performance of the mRICH in the peak load. The maximum number of digis in a timeslice in the analysed run is presented. The value is calculated to a mean rate per pixel on the mRICH camera. Individual pixels could see higher peak rates. The shown mean rates are in good agreement to the scalar rate online monitoring during the beamtime.

a mean rate per DiRICH in Hz (Table 6.3, 4th column), including spill breaks of ≈4 s. By dividing the mean rate per DiRICH by 32 TDC channels, the mean rate per channel (Table 6.3, 5th column) is calculated.

The mean rates per DiRICH and per TDC channel were determined in the six listed runs, including spill breaks, with the two mRICH measurement modes in different interaction rates. Table 6.3 summarises the extracted rates in the six different measurements. Run 855 and 856, marked with *, were performed in the HR mode of the mRICH readout.

The ion rate is only an approximation because this value is a rough estimate from the online beam monitoring by the shift leader and has unknown errors.

In the worst case scenario, each TDC hit consists of 3 words. In this case a TDC ring buffer could hold 3 hits per readout request in the LR operation and 5 hits in the HR mode. The mRICH beamtime 2020 was operated with a microtimeslice adjusted for the mTRD needs with a microtimeslice period of 1.28 ms, respectively 781.25 Hz. Taking these numbers into account, a theoretical maximum pixel rate of above 2343 Hz for the LR setup and a pixel rate above 3905 Hz for the HR setup could be achieved with the setup. Higher rates could only be in principle possible if e.g. two hits are detected within one EPOCH time.

An analysis of the maximum number of digis (raw hits in the detector plane without cuts) per timeslice is shown in Table 6.4. This analysis result is only an approximate number, as the digis are distributed over 10 microtimeslices. The values are thus calculated assuming a homogenous distribution of the digis in the 10 microtimeslices of a timeslice. In the LR setup in run 841, a mean hit rate per pixel (Table 6.3) of up to 815.53 Hz could be achieved, including the spill breaks. More important, a mean pixel rate in the timeslice with the highest amount of digis (Table 6.4) of 1765 Hz could be reached.

This mean maximum rate is still below the theoretical limit of the LR setting and in very good agreement with the scalar rate monitoring, that was available during the mCBM beamtime. This measurements indicate, that no severe data loss appeared in the LR configuration.

The HR setup leads to an increase in the possible rate per pixel to 3605 Hz. The increase of interactions in the target between run 855 and 856 is pronounced in the mean rate increase over the full run (Table 6.3), but very limited in the mean maximum rate (Table 6.4). This discrepancy indicates a loss of data due to full buffers on the FEE in

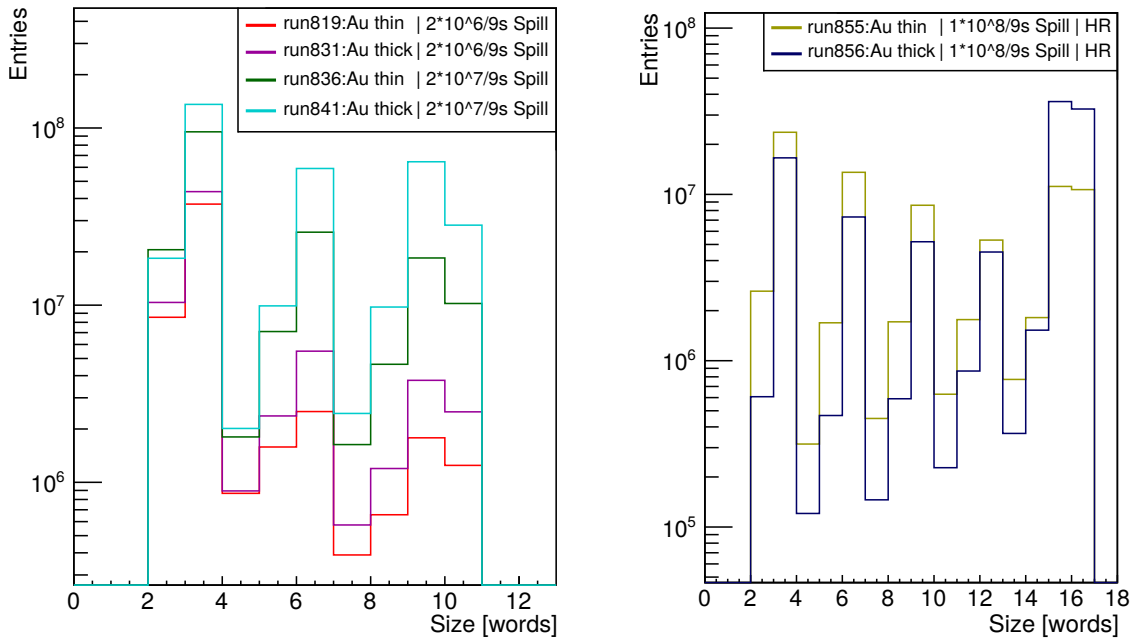

Figure 6.8: **(left)** Size of the TDC data from the DiRICH FEE in words (32-bit). The shown data was taken in the LR setup. **(right)** TDC data size distribution for the two runs in the HR setup with increased ring buffer. The ring buffer size is not a hard cut. Slightly bigger data sizes are possible.

run 856 with the highest interaction rate (theoretically equivalent to an interaction rate of $1.1 \cdot 10^6$ Hz).

Further tests of the unpacker were performed for the listed runs. The LR runs show the expected distribution in the number of words per TDC. The number of words per TDC should in principle be a multiple of 3 due to the nominal data size of three words (EPOCH, rising and falling edge). The LR data shows this expectation (Figure 6.8,left). Hits with less than three words are possible but more seldom and lead to the final structure of the TDC size distribution. The increase in collision rate shows an increase in the total TDC messages, as well as a shift towards larger TDC sizes (see Figure 6.8, left). As there is no clear enhancement just in the last bins, this supports the observation that the limit of the FEE readout is not reached. This was already indicated in the peak rate analysis.

Figure 6.9 supports this observation. The "event size" of a DiRICH is shown for the different runs. In the LR runs, the distribution is limited by the configured value of 245. Many DiRICH boards are not fully occupied and see most of the time just a minor load. Nevertheless, an increase in the load with increasing collision rates is clearly observed. A peak is appearing at the configured limit, showing that some of the DiRICH boards reached the limit even in the LR setup and sometimes even at lowest rates. Figure 6.10 shows the full event size of the mRICH detector with all connected combiner boards with their DiRICH boards and some additional overhead. The event size of the mRICH is increasing with collision rates, as already seen in the previous distributions. This figure shows, that the UDP limit is only reached in run 841 of the LR setup. The reached limit is matching exactly the theoretical value in the case of completely full DiRICH buffers, indicated by a blue vertical line (The line is below the 65 kByte as a

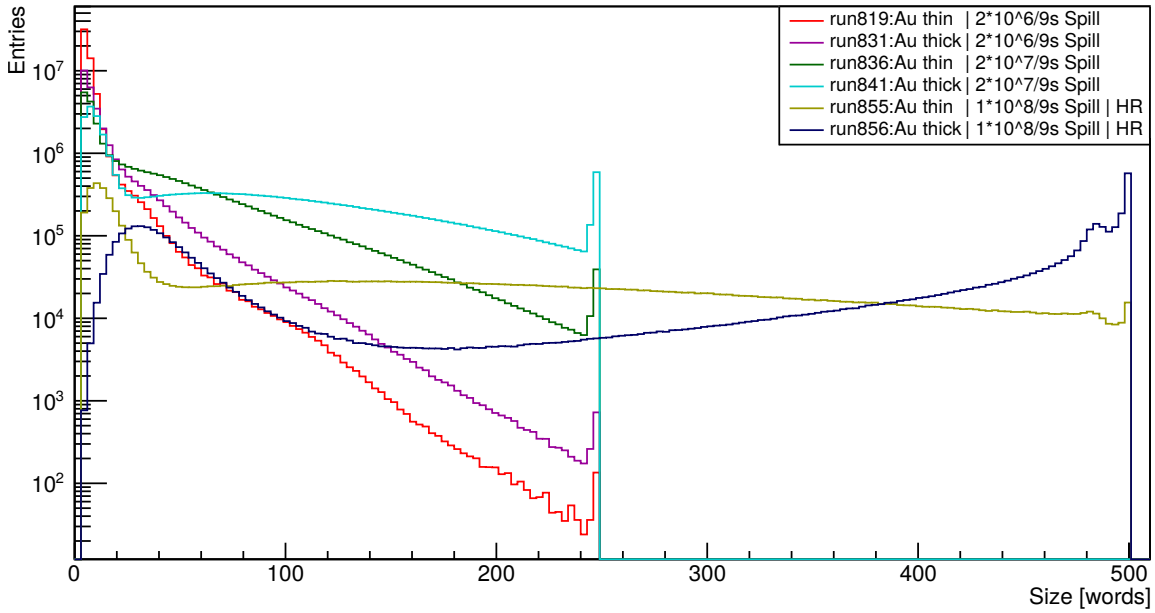

Figure 6.9: Size of the DiRICH data in words. The size is limited by the maximum event size. The LR runs are all limited by 245 words, whereas the HR runs are limited to 499 words.

safety margin for overhead was taken into account, when selecting the FEE buffer limits). The low rate setup of the mRICH increases in the size of the mRICH Events with collision rate and thus matches the expected behaviour. The amount of lost data due to full buffers is on a very low level and primary related to the limit in the mRICH DiRICH buffers (set to 245 words). For collision rates below those of run 841 even a higher size

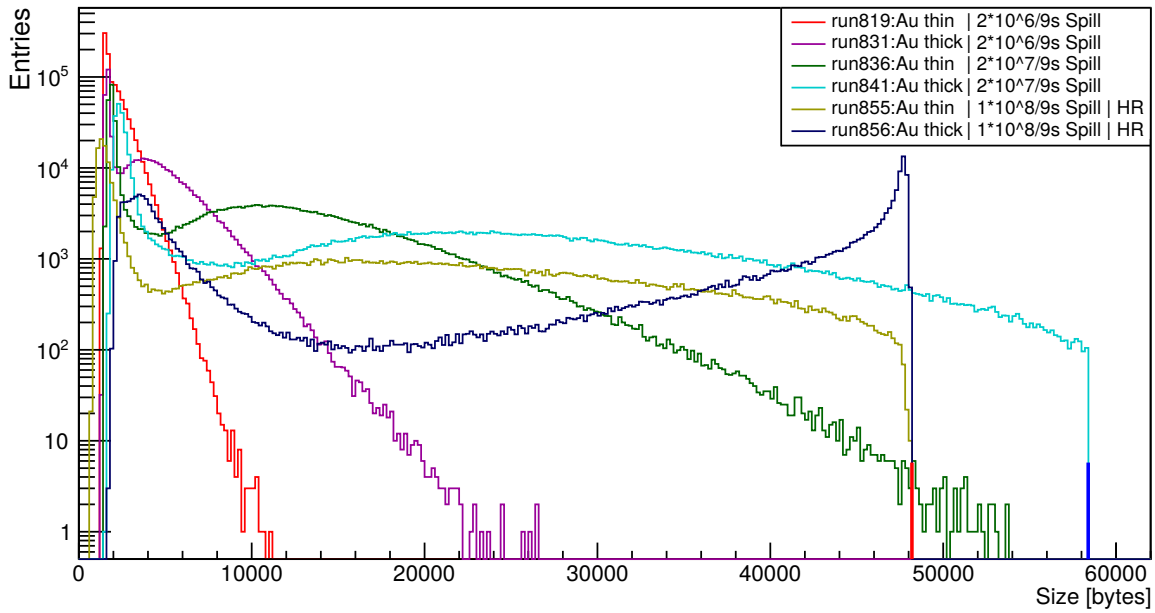

Figure 6.10: Size of the full mRICH Events in different runs. The actual size is limited by the settings of the TDC ring buffer size and the maximal DiRICH event size. The red and the blue vertical lines at 48192 bytes and 58388 bytes indicate the theoretical limit from the applied LR and HR settings.

of words in the DiRICHes could prevent from the seen loss, as the total event size is still not reaching the limitations (see Figure 6.10).

Comparing these observations to the high rate runs, unveils the real limits of the mRICH phase-I setup. The TDC size (Figure 6.8, right) is showing the same structure as in the LR setup. Nevertheless, a clear enhancement in the maximum TDC size is visible and indicates loss of data, due to full TDC ring buffers. The loss of data, primarily seen at the highest rate (run 856), is reflected in the DiRICH size distribution (see Figure 6.9). The enhanced limit of 499, the absolute configurable maximum of a DiRICH, works fine for run 855 with only a small increase of word size at the limit and a smooth distribution over the full size. The more pronounced enhancement at low sizes stems from off-spill measurements. Due to the high rates radiation is increased in the cave. Run 856 shows a clear increase in the word size towards and with a peak at the limit. The small peak in front of the limit is an artefact of the configured TDC and DiRICH settings. This last run completely reaches the limits of the mRICH readout. Figure 6.10 confirms this observation, as the last run peaks at the theoretical limit of the total event size of the HR setup of 48192 bytes (red vertical line). In contrast, run 855 still has a decreasing size towards the limit.

The measurements in the low rate setup show a very nice and predictable behaviour of the phase-I DAQ in low rate conditions. A sufficient performance of the high rate setup could be reached even in run 855, with an approximate interaction rate of $1.1 \cdot 10^5$ Hz. Reaching to higher rates, the phase-I DAQ is very limited and loses data. This limitation was known and accepted in the planning. The future change to phase-II with a CRI system will solve these rate issues, as the UDP packet limit will be obsolete and a readout of the mRICH with a higher frequency than the microtimeslice frequency is aimed for. Finally the same amount of data will be separated in e.g. 10 smaller packages, that are later on merged to a microtimeslice on the CRI board. In addition, a limitation of the DiRICH event size to a value below 499 words is not needed anymore, and thus also the TDC limit can be increased to the HR setup configuration.

As a final remark to the readout behaviour, the time synchronisation in the mCBM experiment was investigated. For the mRICH detector, the T0 and the mTOF detectors are the main reference, as these are also important for the later data and spatial correlation analysis. The time difference between hits in the detectors is presented in Figure 6.11 and Figure 6.12. A clear correlation can be observed in between the mTOF and T0, as well as in between the mRICH and T0 detectors. The correlation to T0 is adjusted by an offset of -310 ns for the mRICH and +30 ns for the mTOF. The applied offset is determined once and used in all runs of the beamtime. The synchronisation between the detectors is very stable and reliable. No change of the peak position is observed at all (see Figure 6.12).

Figure 6.12 shows the correlation for all individual timeslices of run 831. The correlation in time is stable for all timeslices. The regular structure in the timeslice distribution grouping always 4 of them is related to the incoming spills in the mCBM cave and shows the spill breaks.

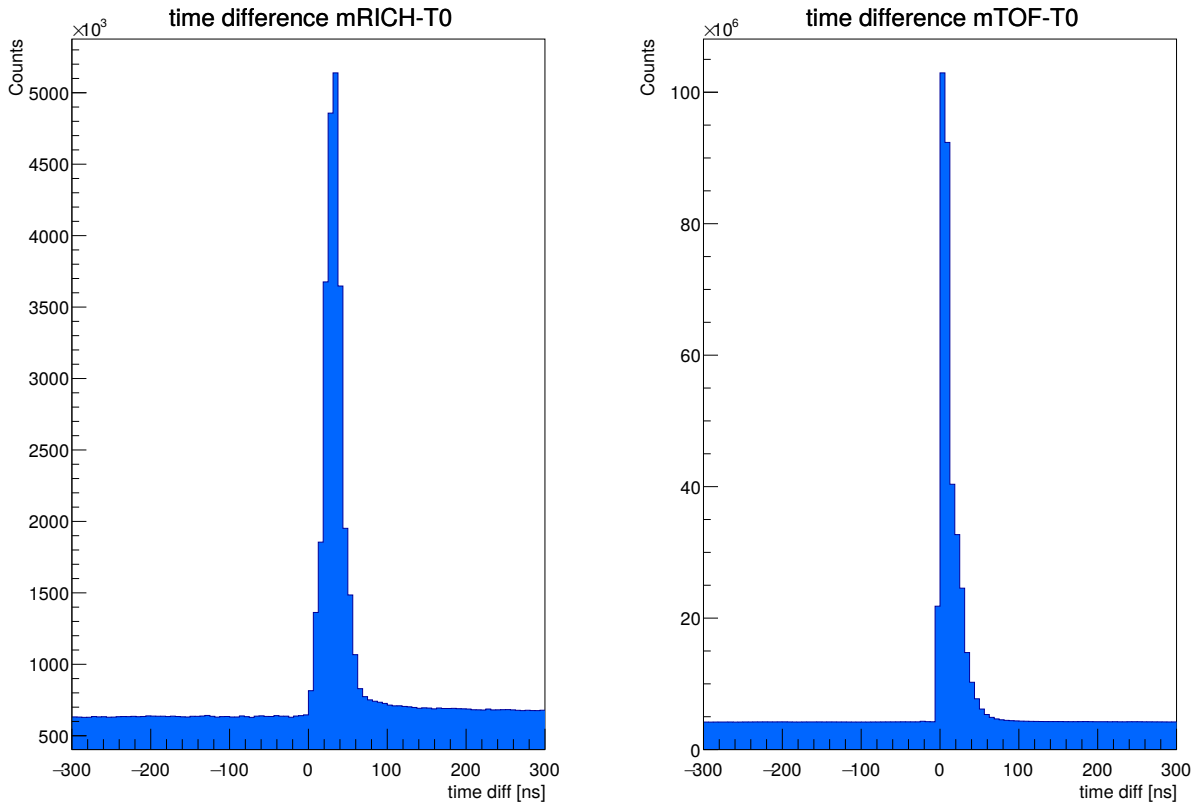

Figure 6.11: **(left)** Time difference between mRICH and T0. **(right)** Time difference between mTOF and T0. mRICH and mTOF are shifted in time with a constant offset with respect to T0. The 30 ns misalignment between mRICH and T0 is on purpose for an improvement in event building procedures.

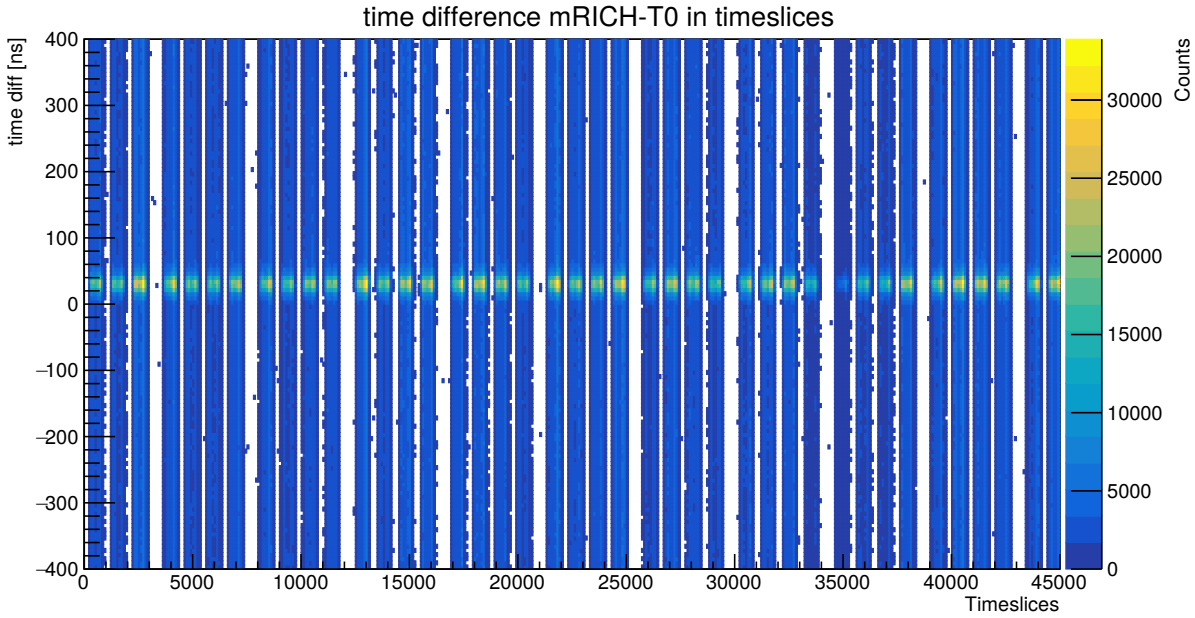

Figure 6.12: Time difference between mRICH and T0 for all timeslices in run 831. The time correlation stays constant over the full analysis and no jumps are observed.

6.3 Monitoring

The mRICH monitoring is a spin-off of the HADES HMON monitoring and called DMON. The DMON monitoring is a flexible and individually adjustable monitoring interface, based on Apache HTTP server, Perl back-end scripts and a HTML/CSS/JavaScript based web front-end. A new graphical layout with influence of the nowadays famous material design is created to bring a modern look to the monitoring interface. The web based monitoring allows the full control and monitoring of the detector in a light-way attempt. The full monitoring is remotely accessible without the need of a VNC connection. Only a simple and secure ssh tunnel connection is needed. First of all, this improves the full operating process from remote as a less powerful and stable network connection is needed. On the other hand, a multi client usage is available and protected by the ssh access.

The back-end is based on Perl scripts, running in the background and generating the input data, based on SNMP, TrbNet or e.g. JSON data. The main page of the web interface is hosting the main control interface as shown in Figure 6.13. The main control interface with its tactical overview summarises the state of the main parameters and observables of the mRICH detector.

TrbNet with the TrbNet daemon access is available. A full overview of the GbE data rate between mRICH detector and the DPB is presented. Additionally the dead time of the detectors' FEE is giving an overview on the detector readout state. An overview on the generated trigger rate on the mRICH CTS with an indication of the applied trigger type is completing the main TrbNet readout overview.

All temperature values and limits are shown in a summary for the FEE as well as for the backplane and the Hub/CTS TRB3sc. The tactical overview serves additionally as a monitoring system for the power. The state of the low voltage power supply, the state of the high voltage, as well as the voltages at the FEE are presented to the operator. The state of the online calibration on the FPGAs is indicated and shows the chosen operation mode. Finally, an overview on the available FPGAs as well as the programmed thresholds on the DiRICH boards is available.

The data of the gas monitoring sensors is shown in the last row of the tactical overview. After flushing the gas volume with N_2 for a few days, the humidity in the detector reached a measured value of 0%. This is the ideal operating and storage condition of the mRICH aerogel radiator.

More detailed overviews on the individual detector parameters are selectable by a header bar. Figure 6.14, left, presents the overview on the programmed DiRICH channel threshold values, that are generated by the baseline finding software. All channels are scanned by the software, as introduced in Chapter 5, and a baseline value is extracted. A threshold of 70 mV above the baseline is written to the threshold FPGAs on the DiRICH boards. The figure is representing the electronics view, the view when standing behind the detector and looking at the FEE in the direction to the aerogel. It is identical to the view in Figure 6.3,right.

The right figure is showing the scalar rates of the individual channels of the FEE during a run in the 2020 mCBM beamtime with 2×10^7 ions per 9s spill and a thick gold target. The overview is updated all 2 sec and gives an important feedback on the current detector functionality and maximum rate on the MAPMTs.

Figure 6.15 is inspired by the HADES RICH web monitoring of the temperature and has the identical features. The temperature distribution of the mRICH shows the influence of the cooling fans, that are mounted on the right side of the detector box. The

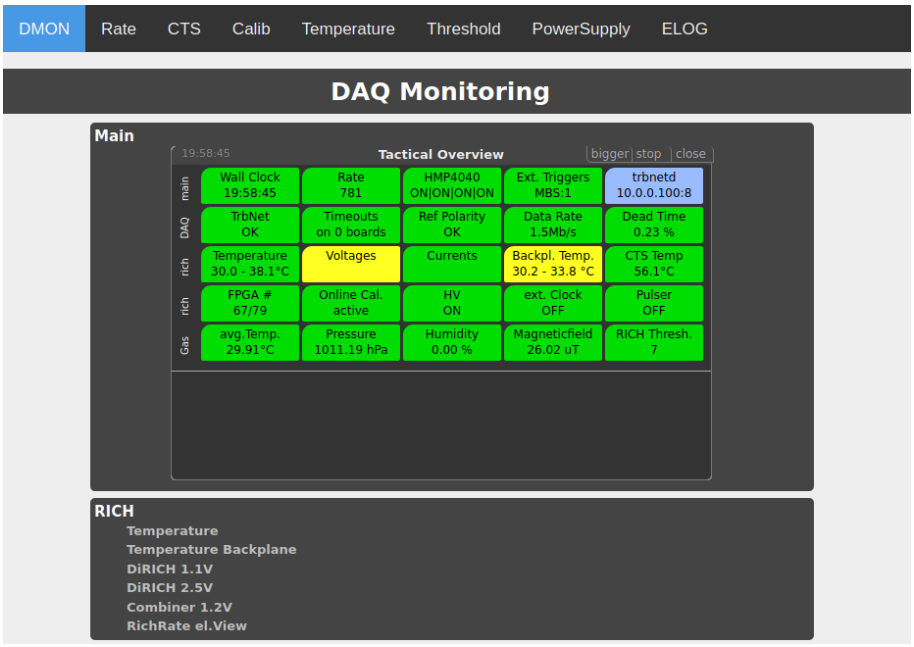

Figure 6.13: The mRICH tactical overview main screen. A summary of the main detector parameters and observables is available. A color code is indicating the individual state of each parameter.

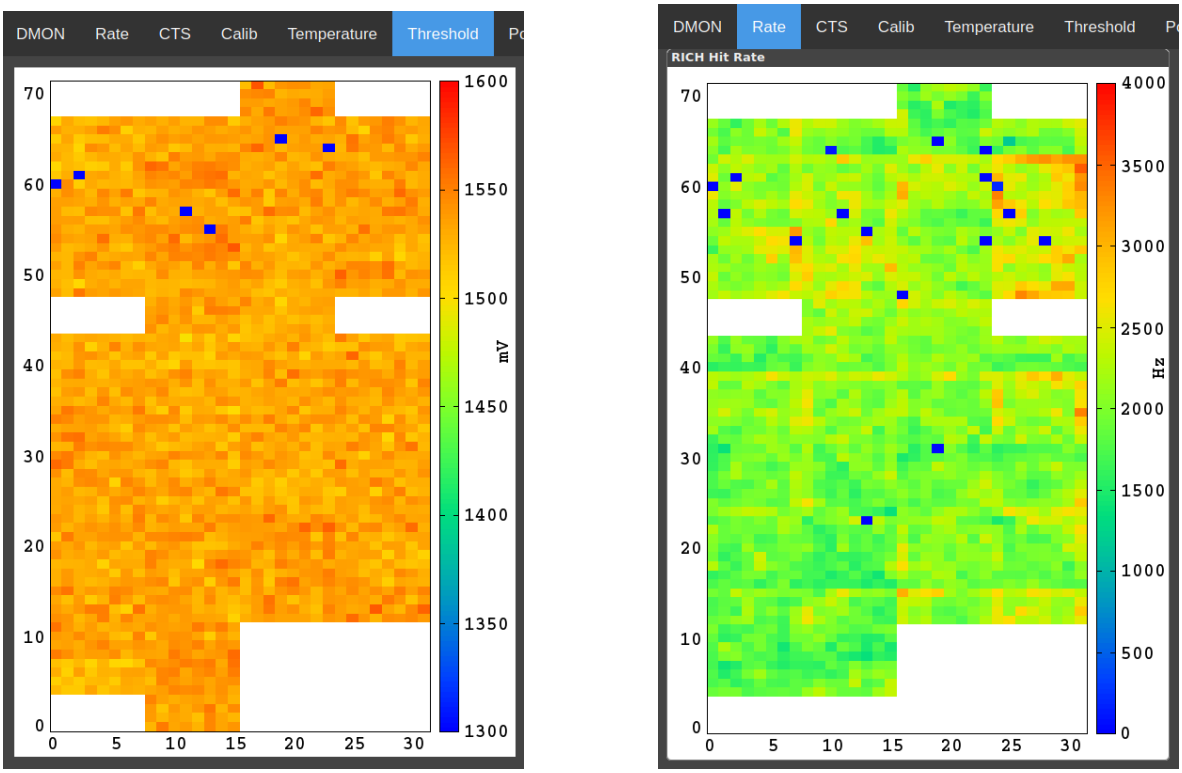

Figure 6.14: **(left)** The individual thresholds of all channels of the mRICH detector in the 2020 mCBM beamtime. **(right)** The scalar rate in Hz of all active FEE channels in a run with $2{\cdot}10^7$ ions/spill (9s) and a thick gold target in electronics view. The rate is determined from the integrated number of hits in 2 sec.

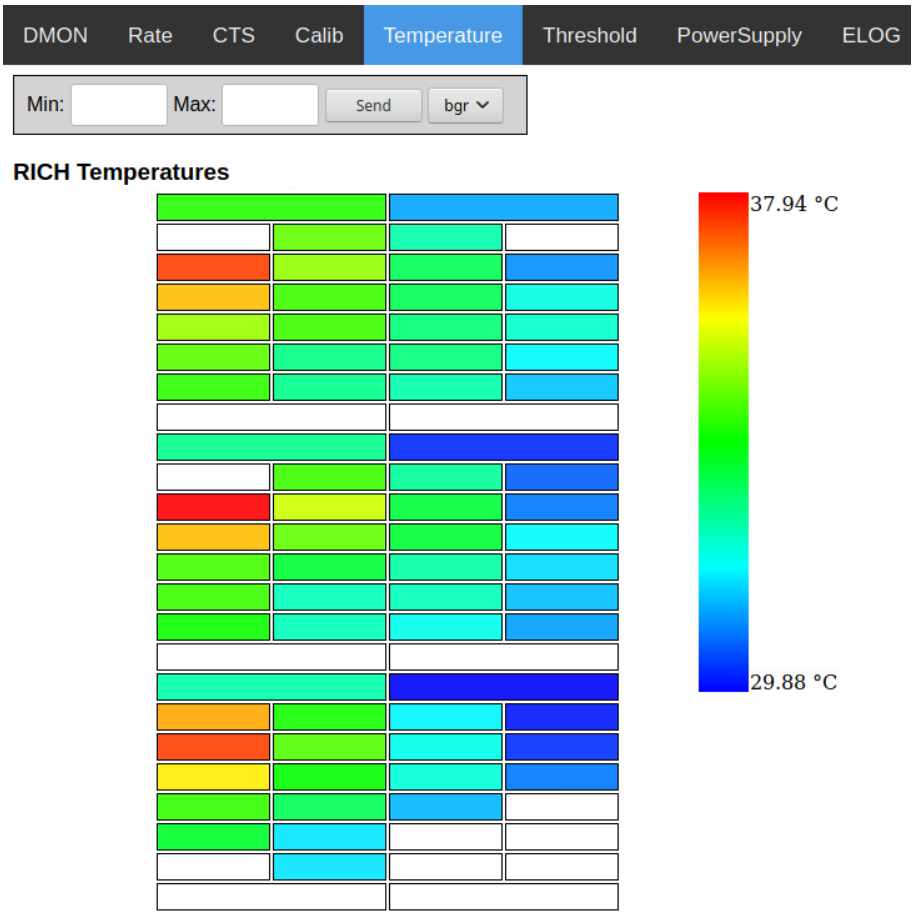

Figure 6.15: Overview of the FEE temperature of the mRICH. The web page monitoring allows the selection of three different color palettes as well as the selection of a value range. A mouse hover on the fields unveils an info box with details, i.e. the FEE address and the measured value.

fans are cooling the FEE to roughly 30°C near the fans. With increasing distance to the fans, the cooling effect is decreasing and the air flow is less guided. Nevertheless a sufficiently low and stable operating temperature could be achieved.

CHAPTER 7

Development of the CBM RICH readout

The previous chapter gave an overview in particular on the readout of the mRICH detector in phase-I of the mCBM experiment. The mCBM experiment is undergoing major changes in the structure of the readout concept towards the first real implementation of the CBM readout in mCBM phase-II, starting in 2021. A new common readout interface (CRI) replaces the phase-I DPB (AFCK) and FLIB boards (see Section 3.4.7.2) and combines their functionality in one new readout board (see Figure 7.1). The new Timing and Fast Control (TFC) system will synchronize all detector components and PCIe connects the CRI directly to the FLES entry node. InfiniBand cables connect the FLES entry node to the Green IT cube, where the data is processed further.

The CRI board of the mCBM is generally known as a FLX-712 respectively BNL-712. It is also the proposed candidate for the CRI of the CBM experiment. The main parameters of the CRI are listed in Table 7.1. The Kintex UltraScale FPGA provides a Gen3 x16 respectively 2x x8 PCIe connection to the FLES entry node, an ASUS ESC8000 G3 server. The entry node server connects to the Green IT cube and serves in parallel as the experiment control system (ECS) connection.

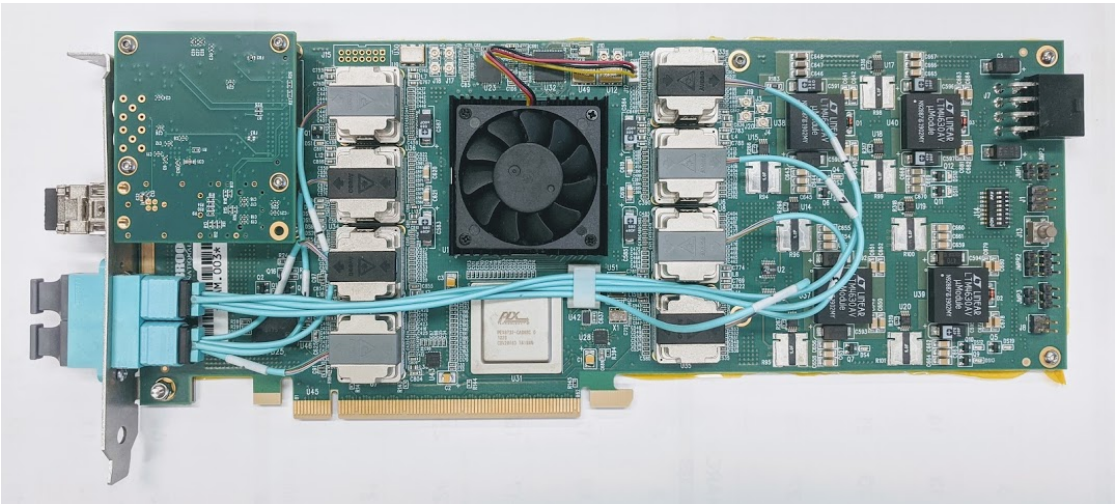

Figure 7.1: Photography of the FLX-712/BNL-712 readout card with timing mezzanine card [94]. It will act as the CRI board in the mCBM experiment and for the RICH also in the CBM experiment.

Part	Description
FPGA	Xilinx Kintex UltraScale XCKU115
	2 Super Logic Regions
	48 GTH transceivers with up to 16.3 Gbps
CRI links	48 bidirectional optical links (4×TX and 4×RX MiniPODs)
optical connection	2× 48-MTP connectors (TX/RX mixed)
PCIe	Gen3 x16 (2x8 with switch)
jitter cleaner	Si5345
TFC	Timing mezzanine card (TMC)

Table 7.1: Overview of the main hardware of the FLX-712/BNL-712 that is used as the CRI board [149, 150].

The mRICH detector is the first application and test bed of the CRI board for the RICH detector itself. The basic readout concept of the mCBM phase-I is upgraded to a CRI based readout concept in phase-II. The basic principle of the future CRI based mRICH readout as well as the first implementations are discussed in this chapter.

The main change from the HADES RICH to the mRICH phase-I readout is manifested in the Hub/CTS TRB3sc, that connects the TrbNet readout to the CBM DAQ, as

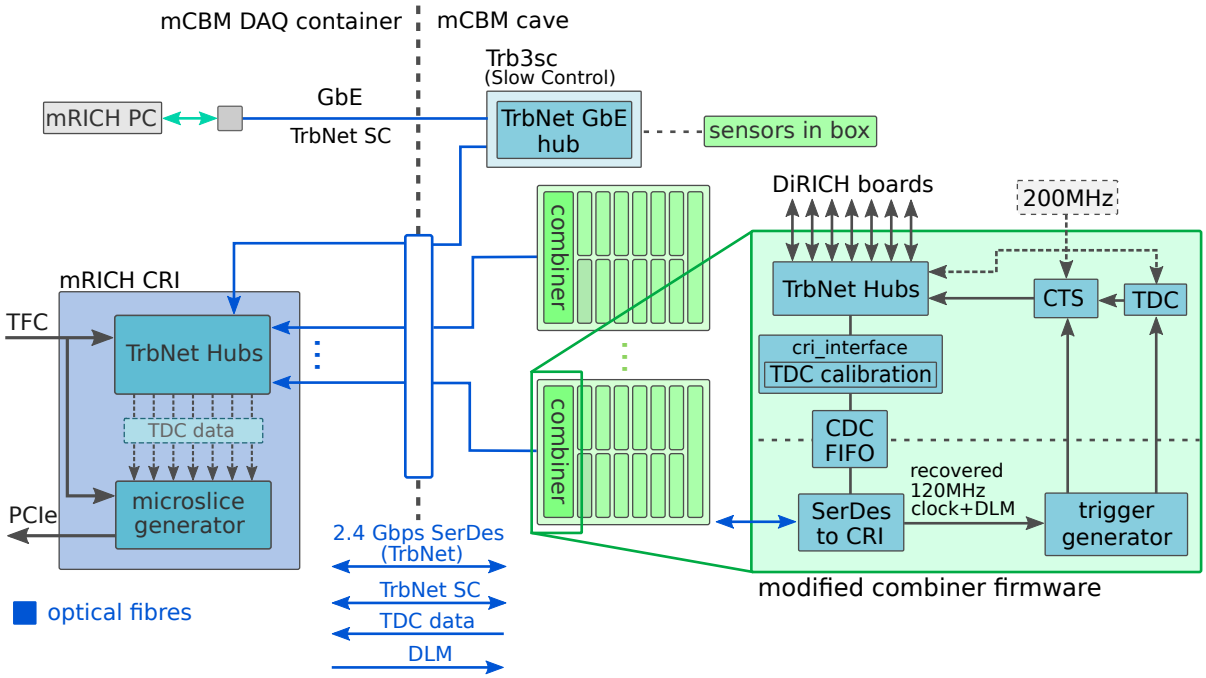

Figure 7.2: Schematic overview of the mRICH readout concept in phase-II and for the CBM RICH. The combiner is a standalone readout board with an own CTS and on board trigger generation. TDC data is calibrated and transmitted on the virtual data channel via TrbNet. A dedicated hub system on the CRI for CBM RICH data is combining the combiner data and handles the slow control connection. Generated microtimeslices are transmitted via PCIe to the FLES entry node. The TRB3sc is the slow control connection to the TrbNet daemon in the beginning of mRICH phase-II. In future this will be included to the experiment Control System (ECS) and realised by a Device Control Agent (DCA) that utilizes the PCIe connection.

well as the trigger generation, based on the microtimeslice intervals. The step from mRICH phase-I to phase-II needs an even deeper change in the data handling and flow.

7.1 Towards a Standalone DiRICH Backplane

The concept of the CBM RICH readout, that is implemented in the mRICH phase-II, foresees a standalone frontend running TrbNet on each backplane that is synchronous to the CBM clock. A schematic overview of the new readout scheme is shown in Figure 7.2.

Each backplane represents the smallest package of an independent RICH readout. The combiner board of a backplane is in future hosting the central trigger system (CTS) and controlling the full readout of the DiRICH boards on the backplane. The DiRICH as well as the combiner logic is connected to the same 200 MHz clock from an oscillator that is additionally the origin of the 100 MHz system clock, that is derived from the 200 MHz via a PLL. Therefore the synchronous operation on a backplane itself is guaranteed. Nevertheless, the backplane has to be synced to the global CBM clock. The future RICH synchronisation principle is identical to the synchronisation in phase-I as it showed a great performance. Still some changes in the final implementation are necessary.

The synchronous 120 MHz clock of the CRI is recovered from the RX link on the combiner board. This 120 MHz is the common mCBM clock and is distributed to the CRIs via the TFC. Due to the recovery of the 120 MHz instead of the standard 100 MHz of TrbNet, the data rate is increased from the standard 2.0 Gbps of TrbNet to 2.4 Gbps. The main data flow is coming from the combiner board and reaches the CRI. Therefore the increase in rate is not harming the operation. Inside the TrbNet deterministic latency messages (DLMs) are implemented and can transport 8-bit of data with a constant time offset between CRI and combiner board. The constant time offset is assured by a word alignment correction as well as the clock recovery. The word alignment of the TrbNet link has to be 0. Unless an alignment of 0 is reached, the link is reset. Measurements of the DLM messages between CRI and combiner in the laboratory confirmed the stability of the clock.

The transmitted DLM messages are replacing the MBS signal transmission via the OptoLink board in mRICH phase-I. The DLM message flag is generating a CTS input trigger, while the 8-bit of data payload are transmitting the microtimeslice index. The DLM flag, transmitted in the CBM time domain, is used as an input for a dedicated TDC on the combiner. The TDC measurement of the DLM is equivalent to the TDC measurement on the Hub/CTS TRB3sc of phase-I and links the local combiner time to the global CBM time. The TDC data from the combiner is included into the general TDC data stream in the TrbNet hub.

The CTS on each combiner board is generating a readout trigger signal based on the DLM messages. While the LVL1 trigger message is transmitted via SerDes on the backplane, the trigger signal is directly distributed to the on-board trigger fan out chip of the power module on a backplane and further on distributed to the DiRICH boards. This scheme comes along without an external trigger connection. Next to the power lines, only an optical fiber is connected to the combiner board. The copper based reference time distribution is no longer necessary. The CTS on the combiner boards has the full flexibility of the standard TrbNet CTS and allows for trigger rate limitations, start

and stop of the trigger distribution, the creation of additional pulser trigger signals, as well as the selection of the trigger type.

The calibration of the DiRICH and combiner TDC can be activated by the CTS. Unfortunately the combiner board has no external 125 MHz clock, that is needed for the generation of an independent 50 MHz clock for the TDC calibration signals. As a solution, the recovered 240 MHz clock is used as a replacement of the external 125 MHz oscillator. The TDC online calibration is positioned directly at the output of the data stream. The final data stream in the data format as explained later is fed in the calibration entity. A state machine decodes the format and controls the calibration of the TDC data from the DiRICH boards as well as the on-board DLM TDC.

7.2 The mRICH Phase-II and CBM RICH Combiner Firmware

The previously introduced changes are necessary to transform the backplanes to standalone readout systems. These changes do give new degrees of freedom to the overall data transport and connection between the CRI and the combiner via TrbNet. The data readout on the combiner firmware is utilising the standard TrbNet entity **trb net16 hub streaming port sctrl cts**. This entity includes the full functionality of the TrbNet hub with CTS handling and a slow control interface. The data from the hub and the connected CTS are prepared for a connection to the standard GbE-wrapper entity of TrbNet.

The connection is separated in a slow control part, a CTS part, where CTS informations are provided and additionally sent back to CTS, as well as an FEE part where data from the FEEs is transmitted. The slow control part allows the communication between higher level readouts like a CRI and the combiner board. The other two parts, CTS and FEE data, are controlling the readout and data transmission process from the TDCs towards the CRI.

The GbE-wrapper data format is reused for the CRI communication interface entity towards the CRI, **trb net16 cri interface**. This entity is shown in a schematic representation in Figure 7.3 and is the key part in the data transfer between the combiner board and the CRI.

The standard TrbNet protocol foresees the concept of up to four virtual channels on the same optical data connection.

- **Channel 0 :** The trigger channel. This channel is used by CTS for the LVL1 communication.
- **Channel 1 :** The data channel. This channel is used for the complete data transfer on TrbNet.
- **Channel 2 :** empty. This channel is always unused in TrbNet and kept as spare.
- **Channel 3 :** The slow control channel. This channel provides the data transport of the slow control.

In case of the CBM RICH, the CTS is moved to the combiner board and the full trigger handling is done autonomously on the backplane. No trigger distribution to

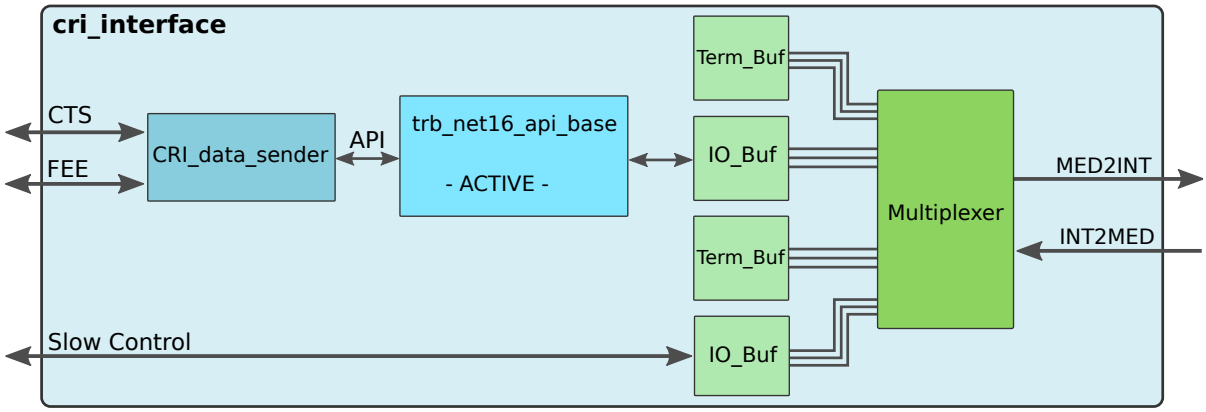

Figure 7.3: Schematic diagram of the cri_interface entity in the combiner board firmware.

respectively from the CRI is foreseen and channel 0 of TrbNet is not used any more. The full data transfer between CRI and combiner is based on the virtual data and slow control channels where the data channel is prioritized with respect the slow control.

The two unused data channels are properly terminated in the cri interface entity. The cri interface connects to the CTS and FEE data from the streaming port scrtl cts entity for the data transmission procedure. The data is prepared for the transmission in a dedicated entity (cri data sender) and finally forwarded in the data structure necessary for the trb_net16_api_base entity. An active API initialises the data transfer towards the CRI board. A layer of IO-buffers connects the data stream from the API and the slow control data from the streaming port sctrl cts entity to the multiplexer. The multiplexer offers the final med2int and int2med data formats for the SerDes based data transfer on a 2.4 Gbps connection.

The entity **cri data sender** is shown in Figure 7.4. It is part of the cri interface entity and prepares the incoming CTS and FEE data for the transmission via TrbNet. A first state machine handles the communication with the hub and CTS for the CTS and

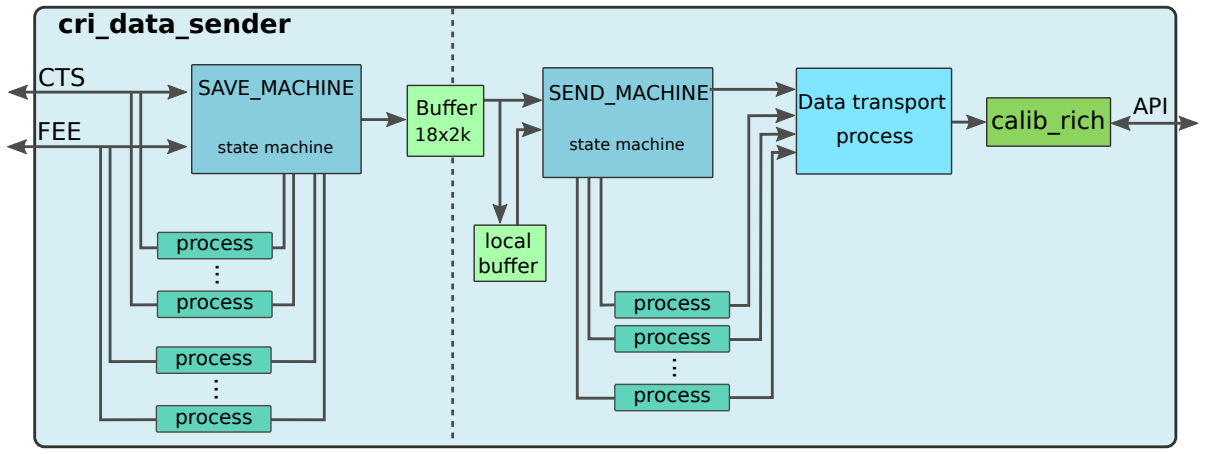

Figure 7.4: Schematic diagram of the TrbNet based data transmission between combiner and CRI. Data from CTS and the hub is formatted according to Figure 7.5 and cached in an 18-bit buffer. The formatted data is separated into TrbNet API packages and later on calibrated.

FEE data with additional processes and prepares the data format of the TrbNet data transmission between the combiner and CRI board (see Figure 7.5). The TDC messages from the DiRICH boards as well as the on-board TDC data of the combiner and the microtimeslice index is received and placed in the formatted data.

The data is cached in an 18 bit wide FIFO with a small local buffer connected. The local buffer is used in edge cases where the timing of the FIFO readout and the second state machine, the send machine, could lead to small delays. The 18-bit FIFO with a depth of 2k is buffering the data, but does not necessarily store a complete event.

The send machine reads out the FIFO and in combination with the data transport process, processes the formatted data into TrbNet API packages. The fully prepared API package data, including the FEE TDC and combiner TDC messages, is further calibrated in the **calib rich** entity. The API data is checked for the data format and the found TDC messages of the individual boards and channels are calibrated as described earlier. The calibrated data is finally forwarded to the active API (see Figure 7.3).

The format of the data transmitted between the combiner and CRI board is shown in Figure 7.5. The TrbNet data is transmitted in separate packages. A data transfer in the TrbNet is initialised by the transmission of a header packet. Following to the header package, the data payload is transmitted in the data packages. The completion of the TrbNet data transfer and the end of the data payload is implemented in the transmission of a finalizing trailer package. In case all the data, the header and the trailer packages are transmitted, the data transport waits for a reply from the receiver side of the TrbNet (here: the CRI). The reply is implemented by a short transfer message and finishes the transmission process. The reception of the reply message brings the state machine back into an IDLE mode and the next event can be transmitted.

The transmitted TrbNet packages are 80-bit in size and consist of five 16-bit words: 1 header and 4 data words (`c_F0` to `c_F3`). In case the sum of all messages from FEE and CTS are not matching the 4 word size of the last package, an additional padding of hexadecimal `0xA` is included in the data payload of the final data package to fill up the 4-word package structure.

The header package of TrbNet consists of general informations concerning the data transmission. These informations are relevant in some applications, however the RICH readout is only utilising a subset of these. The initial word of the header package contains the sender address of the combiner (e.g. `0x8200`, see Figure 7.5), followed by the target address. The target address is set to `0xFFFF`, the broadcast address to all TrbNet boards. The introduced data transfer is designed for a connection from a combiner board to only one CRI and therefore the broadcast address is used as the target address. The last words are giving the length of the transmission and the sequence number of the TrbNet transmission. The length is for now unused and hardcoded to 0. The usage of the length information is not foreseen in the current concept and therefore hardcoded to 0.

The TrbNet data package payloads are similar to the basic TrbNet data structure known from the mRICH phase-I concept. In the beginning of the data segment, the trigger type as well as the trigger code are transmitted, followed by the trigger number. These numbers are important for the possible selection of data by its trigger type and a possible cross check of the data consistency by the trigger number. The last two words of the first data package give the length of the following data as well as the address of the combiner board that is sending the data. The normal data structure of the TDC

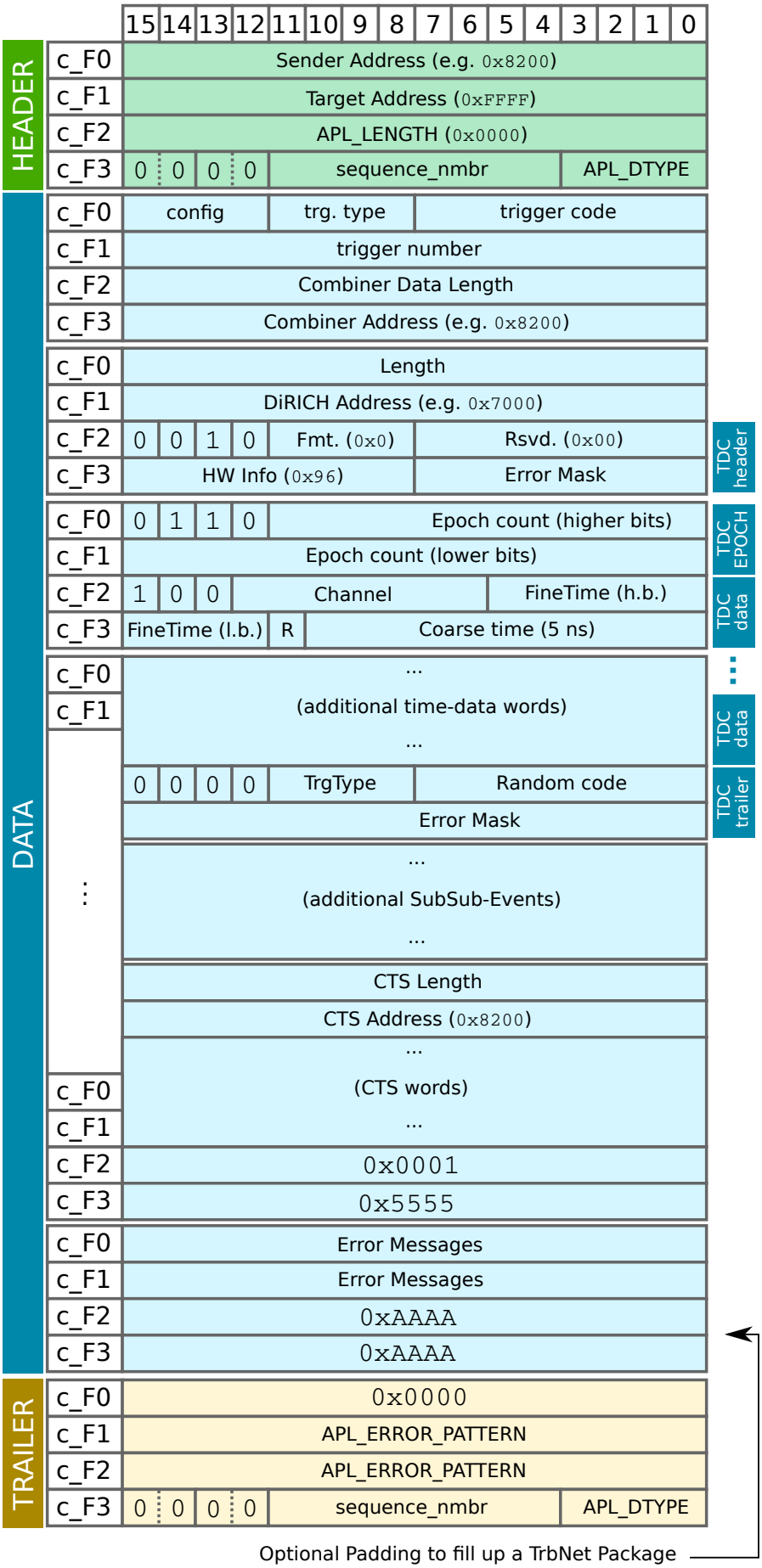

Figure 7.5: TrbNet data format for the transmission between combiner and CRI.

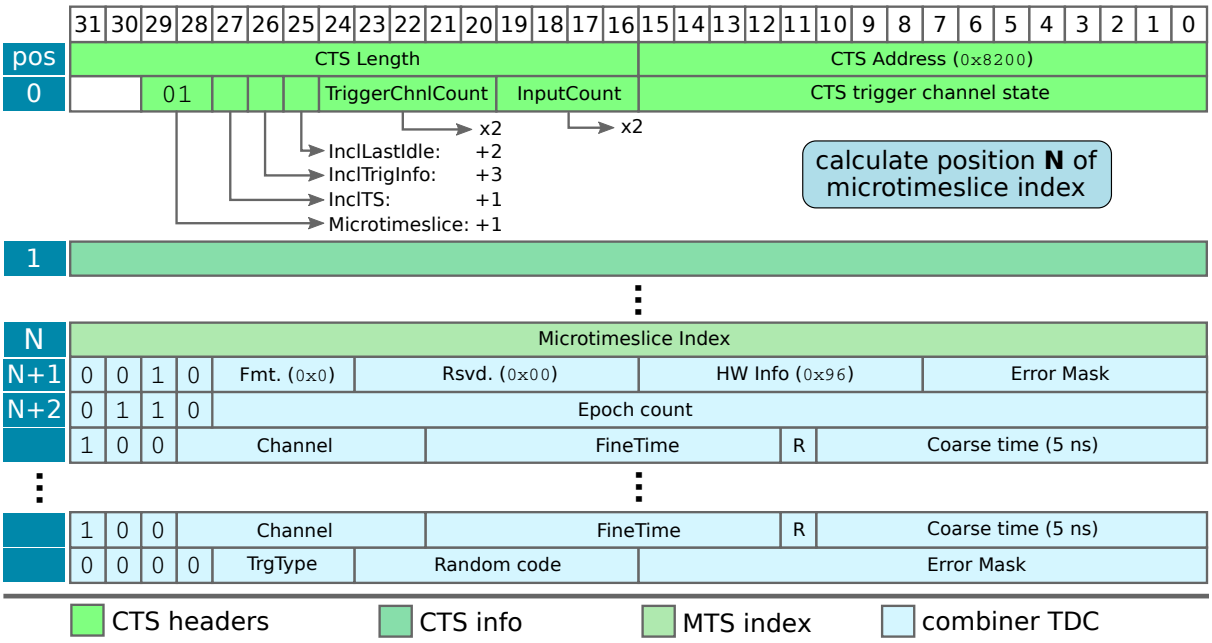

Figure 7.6: CTS message data format in transmission between CRI and combiner. The second word decodes the length of the information and finally the microtimeslice index position in the CTS data. Following to the index, the combiner TDC messages are positioned in the data.

words is 32 bit in width. The 32 bit words are split in two 16 bit words. Consequently the given length is referring to the 32-bit format and has to be taken into account if any calculations on the discussed packages are processed.

The initial data package is followed by data blocks from the connected DiRICH FEE boards (subsub-events). Each of the DiRICH boards sends the length of its following data payload, followed by the DiRICH address and further the TDC messages (header, epoch, data and trailer). Each DiRICH board transmits its full payload, before the data of the next DiRICH board is transmitted. After the transmission of the TDC data from all connected DiRICH boards, the CTS data payload is transmitted. The CTS address is defined to be identical to the combiner address. The CTS data could contain several different data types, including the microtimeslice index and the combiner TDC messages (see Figure 7.6). Based on the third and fourth 16-bit word of the CTS block, the position of the microtimeslice index in the CTS data can be calculated. The TDC messages of the combiner TDC follow after the microtimeslice index position. The TDC data length can be calculated from the microtimeslice index position and the CTS data block length.

A subsub-event with the length of 1 and the address `0x5555` terminates the subsub-event blocks. The data block of the TrbNet packages is finalised by 32-bit of error messages and the potential padding sequence.

The final trailer package of TrbNet contains an additional error pattern and repeats the sequence number as well as the APL data type from the header package.

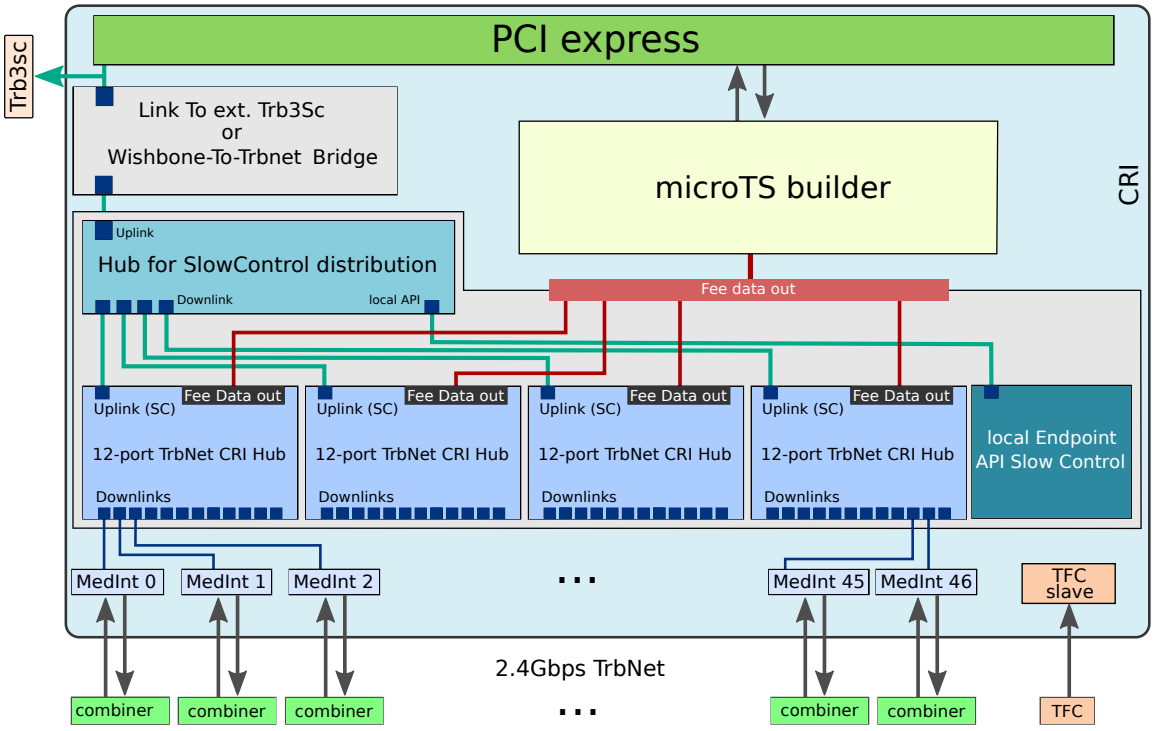

Figure 7.7: Schematic diagram of the basic CRI logic for slow control access and data extraction. Up to four sub-hubs are controlled by a control hub. Each sub-hub connects to up to 12 combiner boards on an optical downlink. The extracted data from all connected FEE boards is combined to microtimeslices in the microTS builder. The microtimeslices and later on the slow control are transmitted via PCIe to the FLES entry node. At the start of mRICH phase-II, one optical link is connected to a TRB3sc that serves as TrbNet slow control input node.

7.3 The CRI Firmware Concept

Figure 7.7 shows a schematic representation of the basic CRI firmware. The CRI firmware includes the counter part of the CRI sender and finally generates microtimeslices out of the received data from the connected combiner boards. The CRI board provides up to 48 optical links, including one link for the TFC system. Consequently up to 47 downlinks are available to connect combiner boards to the CRI. The TrbNet data from the connected downlinks is fed into a staged hub. A standard TrbNet hub is operated with up to 12 downlinks. An increase to more downlinks is possible, but unfortunately has drawbacks in terms of data processing time. The well known standard TrbNet hub was taken as a basis and changed in several points. Four individual hubs with up to 12 downlink ports each could be included into the firmware. Nevertheless, the number of downlinks is scalable. E.g. if 15 downlinks are needed, one hub with 12 and one additional hub with 3 downlinks will be generated in the firmware, based on the generic configuration.

A fifth hub, the control hub, is combining the uplinks of the four sub-hubs and distributes primary the slow control to all FEEs. The control hub is additionally connected to the local endpoint and gives access to the CRI registers via TrbNet slow control. Additionally this local endpoint provides the UID of the CRI, that is extracted from the Xilinx FPGAs XDNA. All five hubs will show up in the TrbNet with the same UID, but

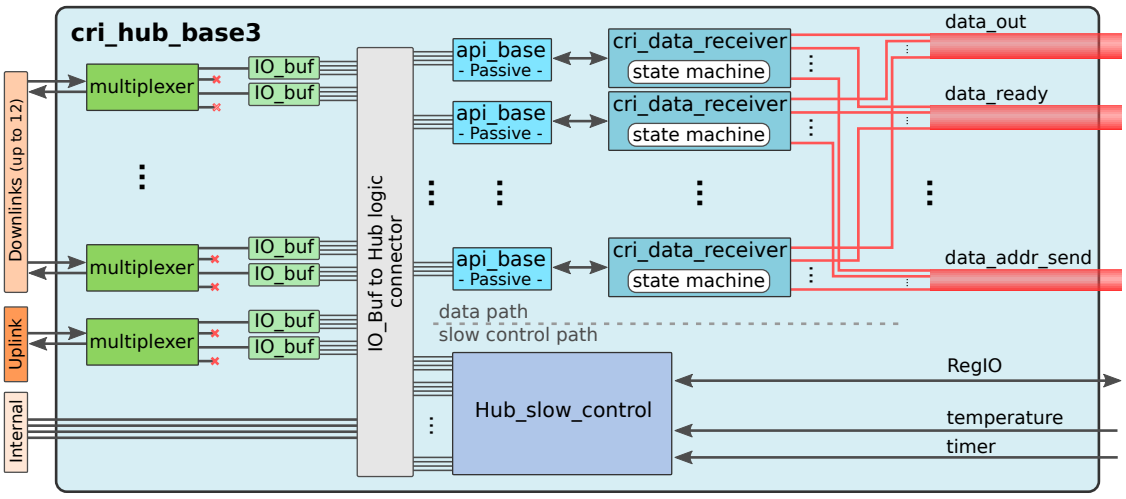

Figure 7.8: Schematic diagram of a sub-hub of the CRI. Each sub-hub can connect to up to 12 combiner boards and extracts the FEE data as well as it distributes the slow control messages. The downlink connects to the combiner boards, whereas the uplink is connected to the primary hub, that distributes the slow control messages to up to four sub-hubs (see Figure 7.7). The extracted FEE data from all downlinks is available in an up to 13·32 bit wide data vector with additional control and parameter signals.

different Endpoint IDs. Therefore each Hub in a CRI has the same unique ID but is uniquely identified.

The combined data from the connected FEE boards of a hub are passed on to the microTS builder that generates self-contained microtimeslices out of the FEE and combiner data. The control hub provides the slow control connection to the FEE and the access to the configuration of the hubs as well as the local endpoint. At the start of mRICH phase-II, a dedicated TRB3sc board, that also connects to the gas and backplane temperature sensors, is providing the slow control connection to the CRI. The well known control from phase-I is continued to be used. One of the 48 optical fiber connections is connected to the TRB3sc and serves as the uplink for the control hub.

In future beamtimes of mRICH phase-II and in CBM RICH, a bridge between the TrbNet slow control and the wishbone based CBM control interface will be available and provide a direct access to the RICH firmware from the common control system.

Signal	sub-hub width	CRI hub width	description
`data_out`	`[(N·32-1):0]`	`[(M·32-1):0]`	received TrbNet data.
`data_active`	`[(N-1):0]`	`[(M-1):0]`	active TrbNet transmission.
`data_ready`	`[(N-1):0]`	`[(M-1):0]`	data_out is valid and ready for read out.
`data_address_sender`	`[(N·16-1):0]`	`[(M·16-1):0]`	Sender Address from TrbNet.
`data_seqnmbr`	`[(N·8-1):0]`	`[(M·8-1):0]`	Sequence number of TrbNet transmission.
`data_length`	`[(N·16-1):0]`	`[(M·16-1):0]`	Length of data (here always 0).

Table 7.2: Summary table of the FEE and combiner data output structure at the sub-hub and CRI hub. N: sum of up- and downlinks of a sub-hub. M: Number of downlinks of full CRI hub.

The up to four sub-hubs of the CRI are different to the standard hubs of TrbNet as no trigger data will arrive at the hubs and no further transfer of the TDC data to the control hub layer is needed. A schematic diagram of the implementation of the sub-hub (**cri hub base3**) is depicted in Figure 7.8. The up to 12 downlinks of the hub and the uplink to the control hub are connected to a multiplexer each. The multiplexer separates the virtual channels from the incoming TrbNet data. The unused channels are terminated and the used channels are connected to the slow control part of the hub and the data part of the hub by IO-buffers and a connection logic. The slow control hub part of the sub-hubs is extracted from the standard hub implementation and provides access to the temperature, a timer as well as a possible connection to a RegIO logic. Furthermore the slow control hub is distributing the slow control commands to the connected downlinks and finally to the attached combiner boards.

The data path of the sub-hub receives the virtual data channel paths from all links with passive APIs. A CRI data receiver entity for each of the links takes the API data as input, extracts the formatted and calibrated TrbNet data from the API packets (see Figure 7.5) and controls the reply to the combiner board by a short transfer message as demanded by the CRI sender entity. The extracted data of each downlink (and theoretically the uplink) is available in the data structure as shown in Table 7.2. The data connections from all N up- and downlinks of a sub-hub is combined to e.g. a `data_out` signal with a width of N·32 bits. The data output of the CRI hub scales in width with the number of connected CRI downlinks M, as the uplink channels are already stripped off. The final data structure to the microTS builder has a width of M·32 bits.

The implementation of the microTS builder is inspired by the microtimeslice building of mRICH phase-I. Nevertheless some major improvements and a more advanced logic are needed for the phase-II and CBM RICH implementation. The presented CRI readout concept is implemented in this basic version. The final microTS building and therefore the final data format in the microtimeslice data is under developing.

The full DAQ will be improved and further developed in the next years, especially based on the input from upcoming mCBM beamtime experiences.

7.4 Phase-II Readout in Beamtime June 2021

In June 2021 a first full standalone readout of phase-II of mRICH with the CRI at a beamtime with O^{8+}-ions at 2 GeV beam energy was achieved. With a fixed 4 mm nickel target, an interaction rate of up to 1 MHz was reached. Data from the FEE was transmitted to the CRI, combined and packed into microtimeslices with a beta-version of the microTS builder. Furthermore the mRICH data was transported to FlesNet in standalone mode via the DMA FLIM connection and stored as `.tsa` files.

First Time over Threshold spectra of the DiRICH boards were inspected in the online monitoring during the beamtime and they showed the expected shape of the detector signals under realistic conditions.

Figure 7.9, left, shows the ToT-spectrum of channel 6 of DiRICH `0x7001` of the mRICH detector with different threshold settings. The spectrum is chosen as one example out of many to show the functionality of the first phase-II standalone data transport chain as it is generated from the finally stored `.tsa` files. The expected influence of different threshold values in mV above the baseline of the channel is shown. The decrease of the

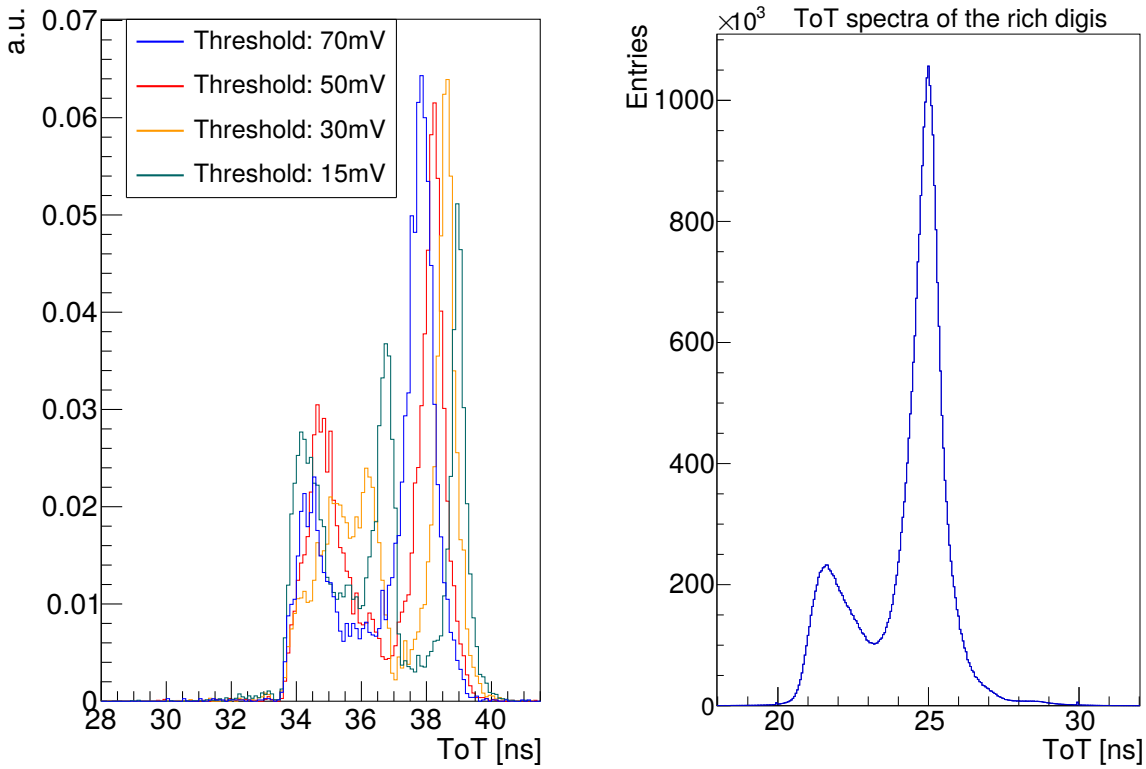

Figure 7.9: **(left)** Time over Threshold of channel 6 of DiRICH 0x7001 for different threshold settings with phase-II readout. The blue line shows the nominal threshold setting of 70 mV as also used in chapter 8. The decrease in threshold shifts the distributions to higher values and increases the contribution from the small noise peak on the left side of the spectrum. **(right)** Combined ToT spectra of digis from all active channels after the application of an offset correction. The shown combined data is from run 1588 with the full phase-II readout chain and a threshold setting of 70 mV.

threshold from its nominal value of 70 mV shifts the ToT distribution to higher values, as it is expected. Furthermore the decrease in threshold results in an increase of the small (noise) peak. Even small threshold values lead to a good separation between the two peaks and prove the low noise level in the detector. Figure 7.9, right, shows the combined ToT spectra of digis from all active channels in run 1588. The application of an offset correction shifts the main peak to a value of 25 ns and results in an ideal ToT distribution. More details on the ToT distributions and corrections, based on the phase-I readout, will be given in section 8.1.

After the successful standalone measurements, a common data taking later in the same beamtime period was performed. Finally, all mCBM subsystems participated with a synchronized CRI based readout. All of them were synchronized by a TFC master and showed a high stability during the measurements. Figure 7.10, left, shows the first measured time correlation between the mTOF and the mRICH with the CRI based readout scheme in run 1588. The mRICH time is corrected by the duration of one microtimeslice (in run 1588: 256000 ns) and additionally -1200 ns. The mTOF time is corrected by -1220 ns. Time correlations are found with respect to all subsystems and prove the full functionality of the synchronisation between the CRIs as well as the functionality of the developed mRICH readout scheme. Figure 7.10, right, shows a single

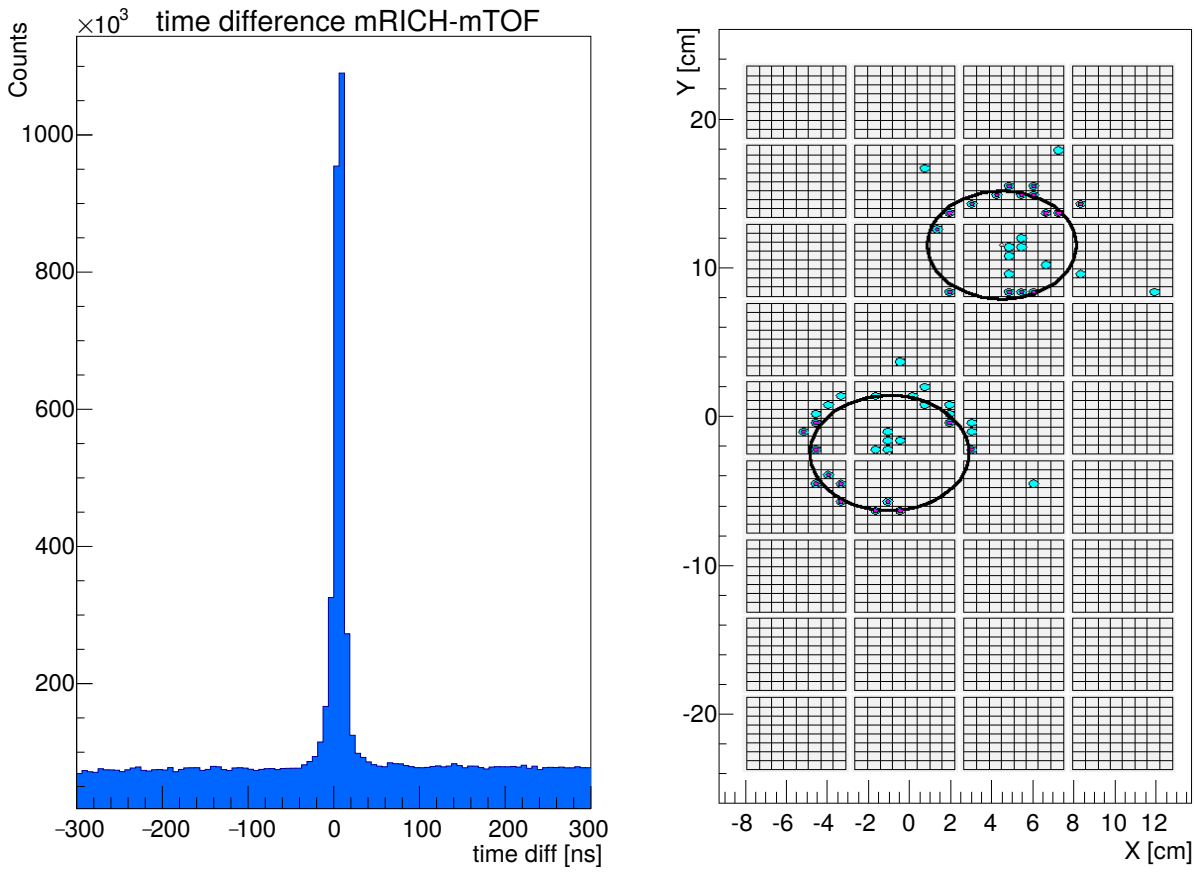

Figure 7.10: **(left)** Time correlation between mRICH and mTOF in run 1588 with the (TFC master) synchronized CRI readout from phase-II. **(right)** Single event display with two reconstructed Cherenkov rings from run 1588.

event display with reconstructed Cherenkov rings from the common run 1588. Next to the time over threshold distributions and the synchronisation between subsystems, the data from different combiner boards is correctly combined on the CRI to the microtimeslices and results in good reconstructed rings.

All in all the new phase-II readout of the mRICH detector as well as of the full mCBM experiment was established and shows a good performance. The new mRICH data transport, trigger generation, trigger distribution as well as synchronisation worked out very well and results in a very stable behaviour over the full beamtime.

The RICH CRI firmware implementation is available at :
`https://git.cbm.gsi.de/daq/fpga-firmware/cri/rich-firmware/cri-rich`

The RICH combiner firmware with included CTS and CRI connection is available in the DiRICH submodule as "combiner_cts" at:
`https://git.cbm.gsi.de/rich/rich_trb`

CHAPTER 8

Analysis of the mRICH Detector Performance and Track Reconstruction with mTOF

The mRICH detectors hard- and firmware development as well as results on the performance are introduced in Chapter 6. The synchronisation to other mCBM sub detectors as e.g. the mTOF and the T0 detector are shown and are giving a first prove of the functionality of the readout concept of the mRICH detector.

The complete analysis of this chapter is referring to run 831 of the mCBM beamtime in 2020. This run is chosen as the reference run for all sub-detectors of mCBM as it provides high statistics of 48786 timeslices and no corrupted data from any of the sub-detectors. The cbmroot version of the following analysis is completely available at `https://git.cbm.gsi.de/a.weber/cbmroot/-/tree/phD_Thesis_analysis` and referring to commit 9cfbe08a.

The data of the mRICH detector is analysed in terms of standalone mRICH data as well as in combination with the mTOF and T0 detectors. The mTOF detector is the reference detector of the mCBM experiment and is the neighbouring detector to the mRICH. The mTOF in combination with the T0 detector serves as additional trigger input for the offline event reconstruction in the free streaming data as well as tracking detector in the mCBM beamtime in phase-I.

8.1 Time over Threshold

The data from all sub detectors is saved on the lustre file system at GSI as `.tsa` files and available for the analysis. As first step of the analysis, the raw data has to be unpacked for all individual detectors. The raw data from the mRICH detector is stored in the format equivalent to Figure 6.7. In the unpacking process the raw detector response information, consisting of an address, the leading edge time information as well as the Time over Threshold (ToT), calculated from the measured rising and falling edge of the MAPMT signal in the mRICH TDCs, is stored as a so called digi. The ToT gives a correlation to the signal amplitude and helps to separate noise (small peak) from photon signal. The resulting ToT distribution with both characteristic peaks is shown in Figure 8.2.

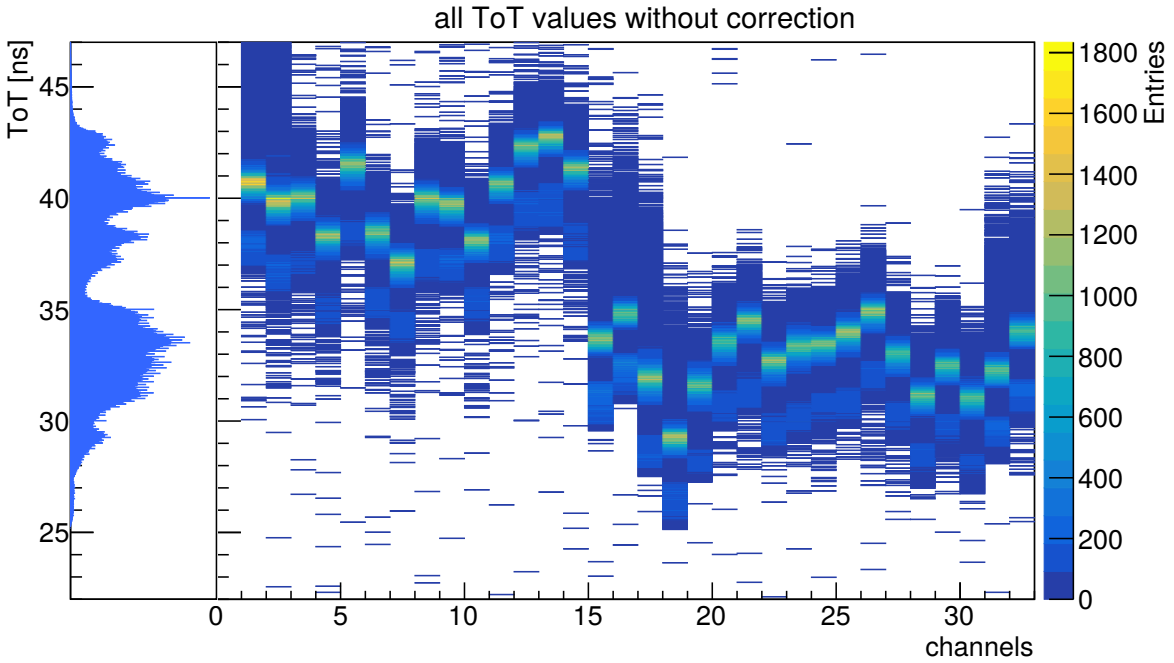

Figure 8.1: Distribution of the uncorrected time over threshold of all 32 channels of DiRICH 0x7261 of mRICH with a projection of all these channels on the left side.

The ToT value of each individual channel is differing. Among others the ToT value is influenced by the threshold value, as well as the signal stretcher in the FPGA logic. Therefore the rough ToT position of e.g. channel 14 is similar on all DiRICH boards, but nevertheless in detail slightly differing from DiRICH to DiRICH. The uncorrected ToT distribution of all channels of one DiRICH board is shown in Figure 8.1. The left side of

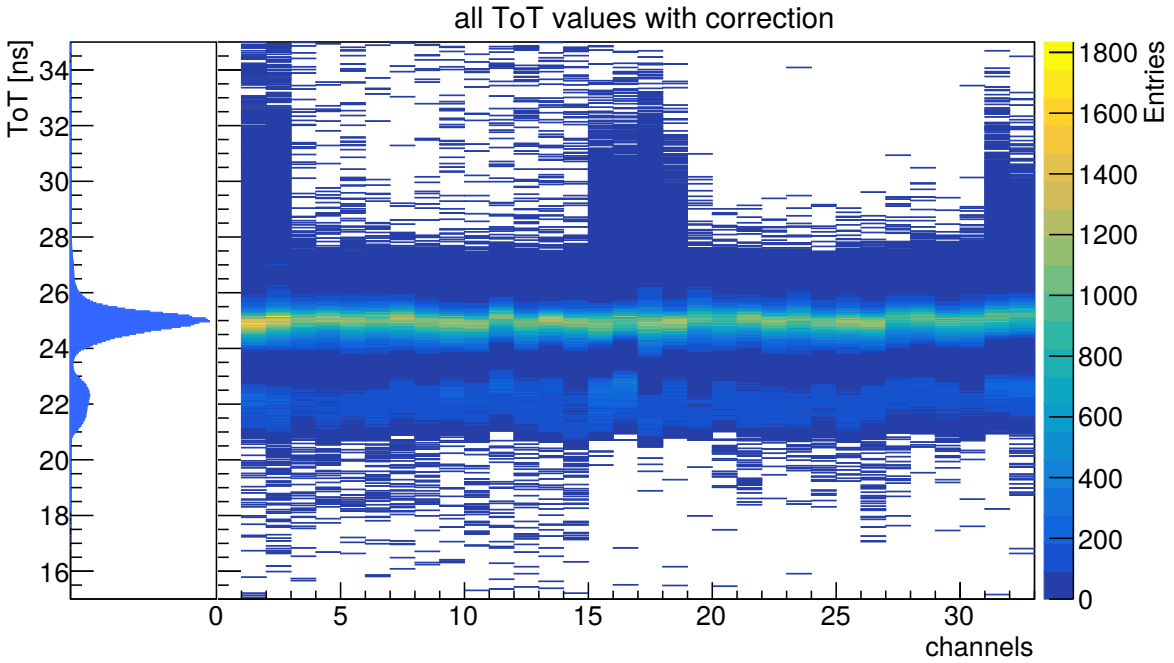

Figure 8.2: Distribution of the corrected time over threshold of all 32 channels of DiRICH 0x7261 of mRICH with a projection of all these channels on the left side.

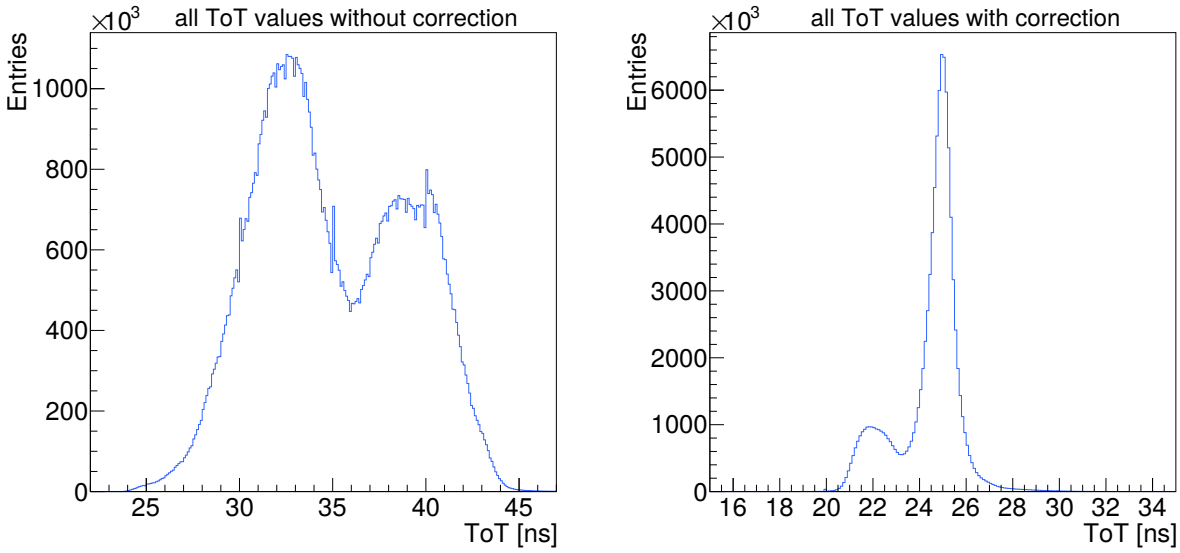

Figure 8.3: Additive representation of the ToT distributions of all channels in the mRICH detector of run 831 with a threshold value of 70 mV. **(left)** The uncorrected ToT spectra with two similarly pronounced peaks due to the FPGA channel implementation. **(right)** The corrected spectra show a perfect shape with a small peak and a large peak with a peak to peak difference of roughly 3 ns.

the figure shows a projection of all 32 channels. The individual ToT values of the channels vary in a range of ≈10 ns. An application of a single cut on the ToT for the reduction of background and secondary hits in the MAPMTs is not reasonable at this stage. The ToT has a standard structure of two peaks. One small peak and a pronounced peak. The small peak is appearing at smaller ToT values than the pronounced peak. This double peak structure is already visible in the individual channels of Figure 8.1. For all channels of the mRICH detector, the position of the pronounced peak is extracted and all spectra are shifted such that the means are positioned at the arbitrarily chosen value of 25 ns.

The corrected ToT structure of DiRICH `0x7261` is shown in Figure 8.2. The channels main peak is now shifted to 25 ns. The projection of all channels on the left side unveils the clean double peak structure of the ToT values in DiRICH boards for a threshold setting of 70 mV. Additionally, the additive picture of the ToT distributions of all channels of the mRICH detector is shown in Figure 8.3. A broad double peak structure with spikes is visible in the left figure for uncorrected ToT values. Figure 8.1 already showed, that this double peak is related to a different general ToT position between the first 14 and the last channels. This difference is directly related to the positioning of the individual channel and its stretchers on the FPGA and therefore generally speaking constant for all DiRICH boards.

The application of the ToT correction shifts all the individual channels providing as result the excellent ToT spectra shown in Figure 8.3, right. The produced offset correction is usable for all runs with the same threshold setting with a reasonable good correction.

The correction on the position of the right peak has the advantage that in case of a misidentification of the left peak instead of the right peak as the main peak, the right peak would still be showing up on the right side of the ToT distribution. In this case, a sufficiently high cut on the end of the accepted ToT window would still include the

correct peak, unfortunately in combination with the peak that had to be cut away. The shape of the corrected ToT distribution in Figure 8.3 (right) confirms the very good functionality of the correction algorithm, as only a very small amount of data is showing up in the tail above the main peak. All the shown corrections are extracted from a run prior to run 831 and demonstrate the reliability of the correction between different runs.

8.2 Inner Channel Delay Correction

In the mRICH detector, the reference time signal is distributed from the TRB3sc below the mRICH box via a distribution board to the six backplanes. On each backplane the trigger is routed from the combiner board to a fanout chip on the power module and further on to the twelve DiRICH boards, where the reference time is internally distributed to channel 0. All the individual connections of cables and PCB traces sum up to a slight delay in the readout and finally variation of the time information of the channels. The delay between the individual channels is well known and called **I**nner **C**hannel **D**elay (ICD). The ICD can be calculated by different methods. An iterative procedure showed in previous test beamtimes of RICH detector prototypes good results and was adopted to the mRICH detector. The iterative procedure is based on ring

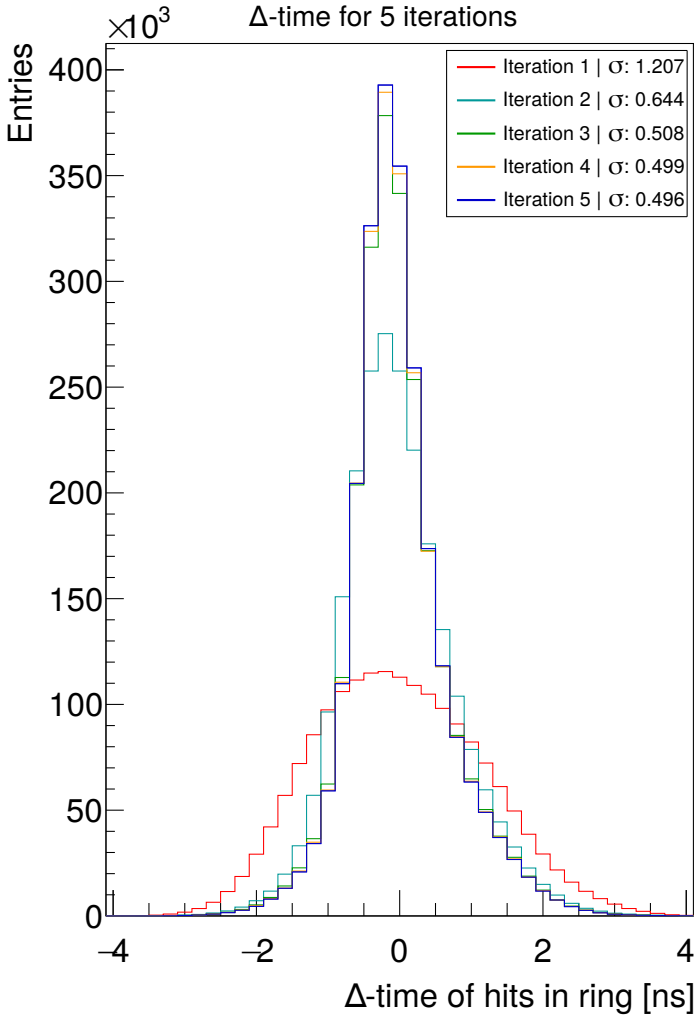

Figure 8.4: Difference of hits of a ring to the mean time of the corresponding ring. The decrease of the width of the distribution is shown for the five iterations on the first 20.000 TS of run 836. The sigma of the five distributions is extracted by a Gaussian fit. After five iterations only a small improvement on a picoseconds level is visible. The ICD correction improves the overall hit timing in the mRICH. Nevertheless the correction is limited by the ring finder performance. The improvements of the hit timing are giving only minor improvements on the full presented analysis.

finding. A physical Cherenkov ring is identified by several hits on the MAPMT plane. Per definition the time information of hits of a true Cherenkov ring has to be the same, as all hits by principle are produced and detected at the same point in time.

Hits from reconstructed rings from the first 20000 TS in the mRICH in run 836 have been used to generate an ICD correction. The time difference of all hits of a ring to the mean time of the ring (Δ-time) has been calculated for all available channels. The mean values of all calculated differences of a channel are finally generated and stored.

These generated corrections are applied in a next iteration again. The ring finder is processing the corrected data, finds rings and a new correction of the ICD is calculated for each channel. In total five iterations are applied on the data of run 836 and a final ICD correction file is produced.

Figure 8.4 shows the improvement of the Δ-time, the difference between a hit and the mean time of the corresponding ring. After five iterations the results improve only minor and no more iterations are processed. The ICD correction gives a good improvement of the timing of the rings. The application of the ring finder after each iteration results in slightly different found rings and hits attached to a ring. Therefore the Δ-time is partially calculated with different hits in a ring. Overall this method leads to a good result, as e.g. double rings could be more precisely separated in time. Never-

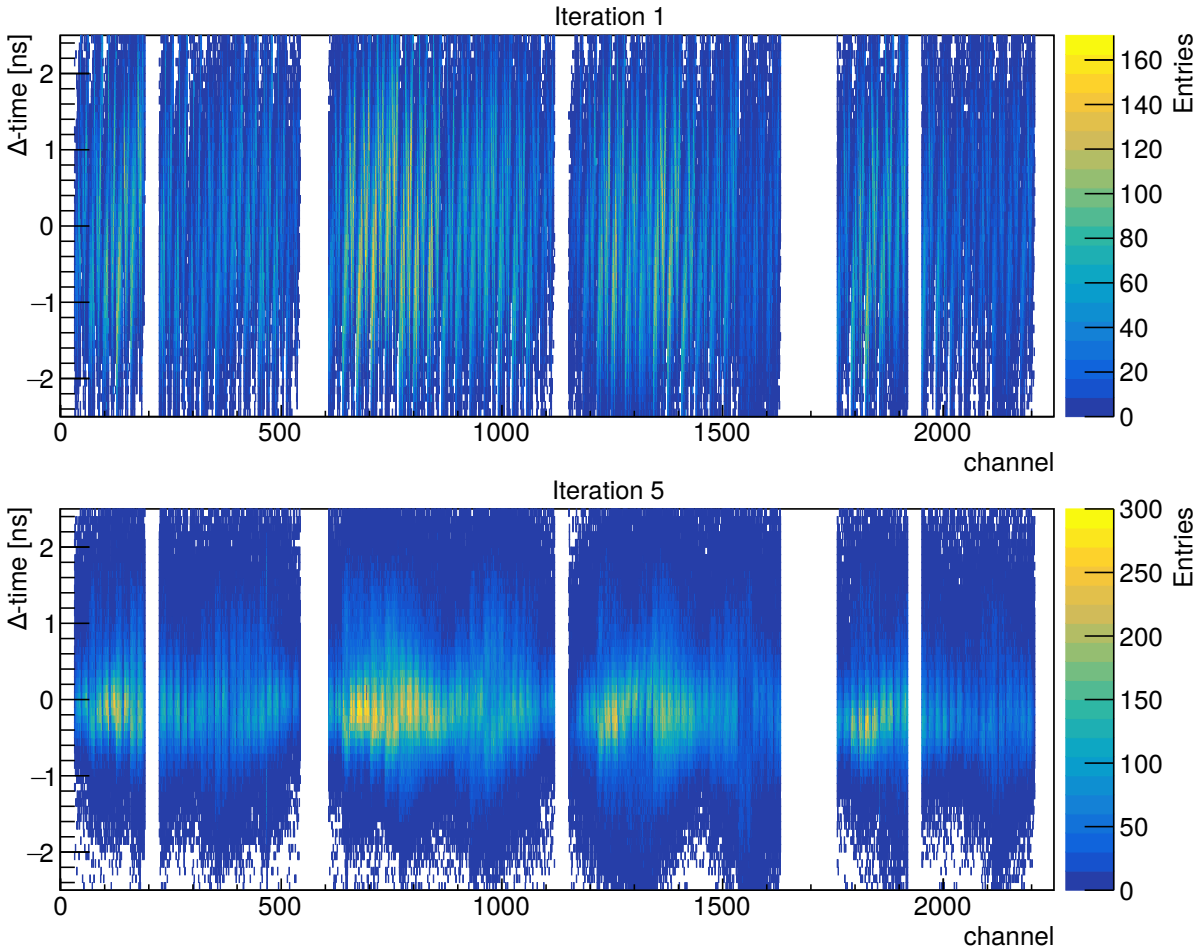

Figure 8.5: Δ-time distributions for all available channels in the mRICH detector. **(top)** Resulting distribution generated during iteration 1. **(bottom)** Resulting distribution generated during iteration 5.

theless the final analysis in this chapter is only improved slightly, as the inner channel delay is only of minor influence for the shown results.

Figure 8.5, top, shows the Δ-time distributions of the first iteration for all available channels of the mRICH. In comparison, the bottom of Figure 8.5 shows the same distribution after the last iteration. A clear improvement on each channel is visible in the comparison of both histograms.

8.3 Geometry and Mapping

The mRICH geometry is implemented in cbmroot to match the reality as well as possible. A positioning with the center of the MAPMT plane on the 25° line of the mCBM experiment is chosen and corrected by 2.5 cm towards the actual main beamline, based on the data analysis. The full analysis is based on the geometry version rich_v20d_mcbm. This geometry is fully corrected, but has no MAPMT window activated as this is harming simulations and has no influence on the data analysis. The mTOF detectors utilise the tof_v20f_mcbm geometry version in the analysis. The complete setup with the correct geometry of all detectors is given by the setup_mcbm_beam_2020_03 macro.

The mRICH detector is centered behind the mTOF detector's triple stack. The triple stack is a combination of three mTOF M4 modules that are stacked next to each other. The stack is centered around the 25° line with respect to the beam and offers the possibility to form triple hit tracklets.

The mapping of the DiRICH front-end channels to the corresponding MAPMT pixels is provided on two ways. First a simple mapping ASCII file is provided with all necessary informations. This file was used for the hit production process (conversion of digis to hits) and in the online rate monitoring.

The second implementation of the mapping is the prioritised method in the analysis with cbmroot. The mapping is directly implemented in the geometry file. Each node of the MAPMT pixels in the geometry file has the correct DiRICH channel address decoded. In the hit production, the geometry file is loaded and the correct address for each pixel with the correct spatial position from the geometry file is extracted and the corresponding position information is added to the digi data.

This procedure has several advantages. First, the full mapping is included in one file, that is already existing. Second, the correct mapping is already part of the geometry and no mismatch between a geometry and a mapping is possible. The implemented mapping was tested in several beamtime runs with different DiRICH boards active and no miss-mapping was found.

The mCBM representation based on the geometry file was already shown in Figure 3.29. A photography of the real mCBM experiment with the main beamline and all sub detectors, lined up on the 25° line with respect to the beam, is given in Figure 3.30.

8.4 Analysis Settings for Beamtime 2020

The free streaming data from the mCBM experiment is used as an input for the following analysis. The collision of an ion with the gold target reflects an event in the reconstruction. Therefore the free streaming, untriggered data has to be separated into events in time. An event reconstruction algorithm is used to detect digis of the

parameter	value
analysed beamtime run	run 831
target of mCBM	0.25 µm thin fixed Au target
beam	^{208}Pb @ 1.06 AGeV
Detectors for event building	mRICH, mTOF and mT0
Trigger Window mRICH	-50 ns to 50 ns
Trigger Window mTOF	-150 ns to +10 ns
Trigger Window T0	-1 ns to +10 ns
Minimum Digis mRICH	5
Minimum Digis mTOF	10
Minimum Digis T0	1
mRICH ToT-cut	23.7 ns < ToT < 30.0 ns
mRICH ICD reference run	run 386
mCBM geometry setup	mcbm_beam_2020_03.geo.root
ToF cluster calibration	831.100.4.0_set010020500_93_1_noWalk
Track calibration parameters	831.100.4.0

Table 8.1: Overview of all important settings of the mRICH analysis of mCBM run 831.

sub detectors in a defined trigger window in time with respect to the reference detector. The reconstructed events are further selected by the application of a multiplicity trigger on different sub detectors. In case of the mRICH detector a minimum of 5 digis is required to use the reconstructed event for the further analysis. In addition, the analysis algorithm requires a minimum of 5 mRICH hits in the event. This trigger can be changed to a different value, but this work on the data analysis showed a good and reliable behaviour with this trigger condition and thus this condition was kept.

The additional cut on hits is required, as RICH hits are a subgroup of digis: RICH digis are called hit, if they are accepted in the event building, i.e. are mainly accepted concerning their timing, are mapped to a position in the MAPMT plane and lie within the chosen ToT window. So it is possible, that e.g. only 2 hits out of originally 9 digis are left after the event building and ToT cut application.

In addition more than 10 digis (but not a minimum of 10 hits) in the mTOF detector are required with a minimum of 1 digi in the T0 detector. This trigger selection of the mTOF is chosen following recommendations from the TOF experts. The selection of one digi in the T0 is related to the high performance of the T0 detector and the detection of each primary beam particle, passing the detector.

The (FPGA based) TDC time calibrated mRICH data and the ToT offset correction are used. The data are further cleaned by the application of a time over threshold cut. Digis with a ToT value between 23.7 ns and 30 ns are labelled valid hits, if they are part of the reconstructed events. The ToT cut is selected based on the ToT distribution of the digis as shown in Figure 8.3, right. The application of the cut is possible due to the clean separation between the main single photon peak and the smaller ToT peak, related to e.g. capacitive crosstalk.

In addition to the ToT cut, the ICD correction from section 8.2 is applied on the data. No further correction of the measured data is necessary. The complete mRICH data used for further analysis is based on the introduced settings and corrections.

The mTOF detector with the reconstructed tracklets is the reference detector for the

spatial correlation analysis of the mRICH detector. To achieve the best performance of the mTOF, a calibration of the TOF clusters and the tracks (tracklets) is necessary. All applied corrections, calibrations, cuts and selections as well as the basic collision conditions of run 831 are summarised in Table 8.1.

8.5 mRICH Detector Analysis

The detected digis of the mRICH are further converted to hits with the application of the event building, mapping and time over threshold cuts. Based on the resulting hits, a ring finder is applied and the reconstructed rings are stored. The analysis of the mRICH behaviour is mainly concentrating on the influence of the event building on the resulting hits and their ToT distributions as well as the influence of the settings on the found rings in an event.

Figure 8.6 shows the ToT spectra with different event selections. The left side shows the raw digi ToT distribution of all channels except two masked bad channels. The digi distribution is of course the same for all event selections. The right side shows the ToT distributions of hits in different settings. A RICH trigger window of $\pm$500 ns in combination with a trigger condition of minimum 1 hit in the mRICH and no condition on

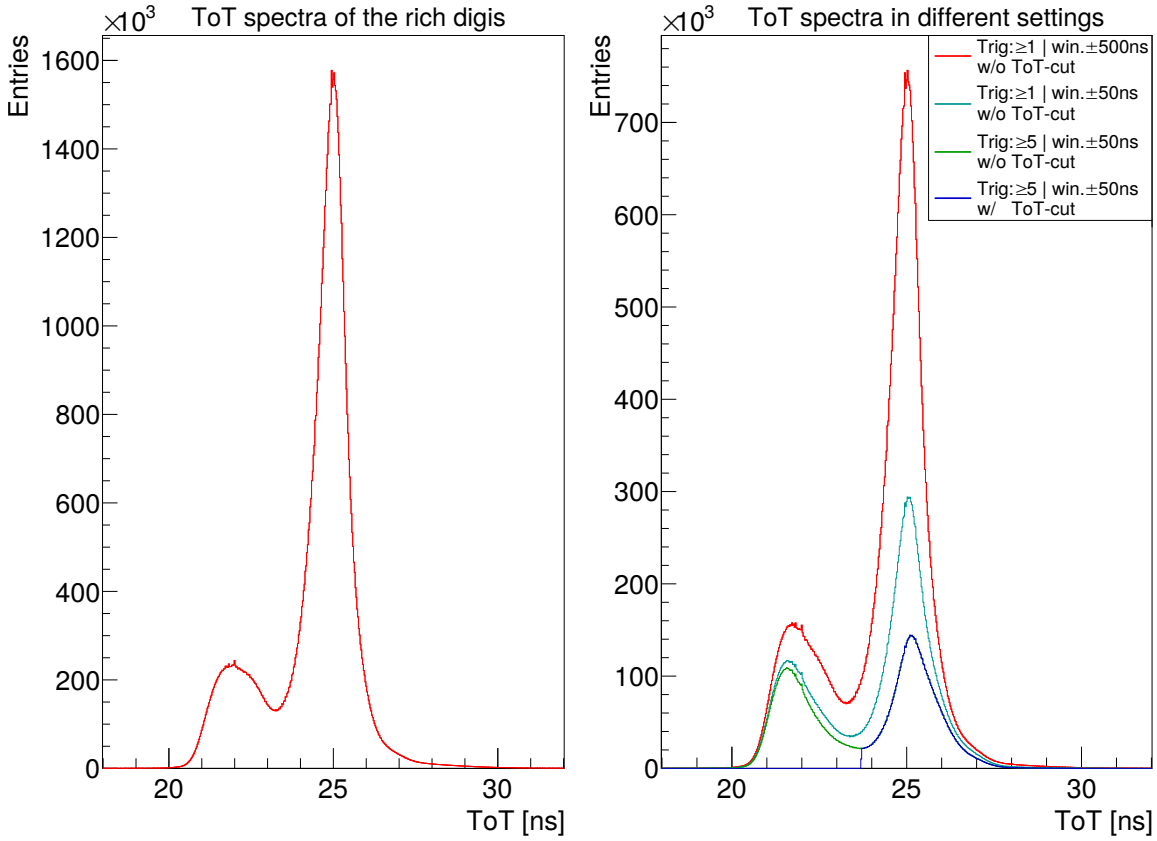

Figure 8.6: ToT spectra in different event building settings. **(left)** The offset corrected ToT spectrum of the raw digis. It is the same for all settings. **(right)** ToT spectra for different event builder settings. The variation of the settings unveils the influence of background photons on the main peak, as well as the correlation of the small peak to reconstructed events and moreover to events with many hits.

the other detectors in the event builder process results in a ToT spectrum with roughly the same shape as in the digis. Only the cross-talk peak[1] is more enhanced than on the left side. This shows, that the main peak, the single-photon peak, is mostly influenced by random background hits in the detector.

Changing of the trigger window size to the standard setting of ± 50 ns the cyan line is achieved. The main peak is decreasing clearly whereas the crosstalk peak is decreasing less. This behaviour underlines the correlation of the random hits to the signal hits. A further sharpening of the trigger condition to a minimum of 5 hits in the mRICH reduces the remaining contribution of random events with only a few hits. The cross-talk peak remains nearly untouched, whereas the main peak is still decreasing further. Obviously, crosstalk is strongly correlated to events with a certain hit activity in the mRICH. An application of a trigger condition on the T0 and mTOF, as done in the later analysis, shows no further influence on the distribution. This validates the chosen settings as they correlate with the trigger of the reference detectors. The main and the crosstalk peak are nearly of the same height (green/blue). The application of the ToT-cut from Table 8.1 results in the blue distribution. The complete crosstalk peak is removed by the application of the cut.

[1] This name is used for the small left peak in the ToT spectrum. It is a name summarizing effects like capacitive crosstalk, charge sharing and other effects.

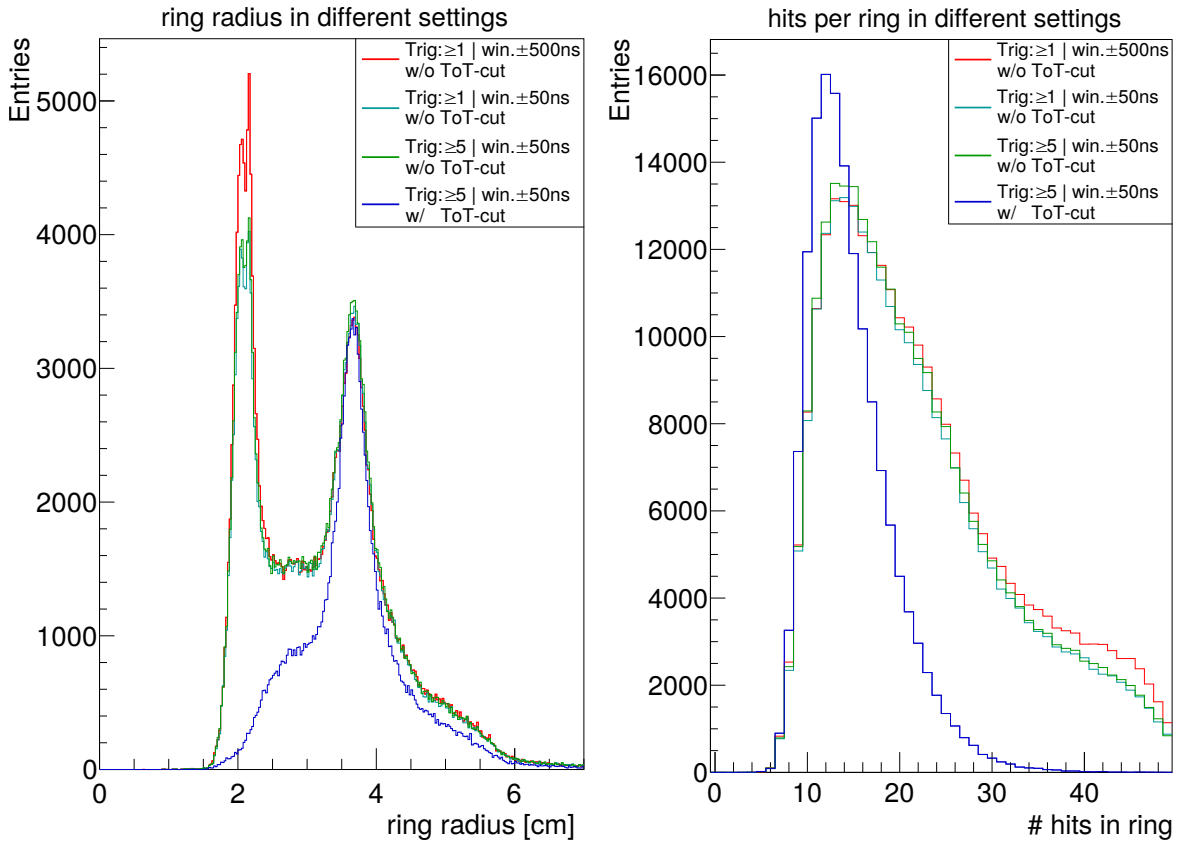

Figure 8.7: **(left)** The radius of reconstructed rings in an event. A second unexpected peak is visible at small radii vanishing with the application of the ToT-cut (blue). **(right)** Number of hits per found ring in an event. All settings except the one with ToT cut show the same distribution. Only the ToT-cut has an influence on the distribution and leads to a clean peak at around 12 hits per ring with a strongly reduced tail.

The application of the ToT-cut to reject the crosstalk is verified by the investigation of its influence on the reconstructed rings, checked also by single event displays. Figure 8.7, left, depicts the radius distribution of the reconstructed rings in the mRICH in run 831. A double peak structure with a strong peak at around 2 cm radius and a second peak at ≈3.6 cm radius is visible. For all settings, except the application of the ToT window, the distribution remains rather unchanged. The application of the ToT cut rejects nearly all small rings and leaves the peak at around 3.6 cm including tails.

The event selection has a strong influence on the main ToT-peak in Figure 8.6, but only influences the small ring radii in Figure 8.7. In addition the right side of Figure 8.7 shows the influence of the changes in the settings on the number of hits that are assigned to a reconstructed ring. Nearly all the hits, that are rejected by the application of the smaller trigger window and the increase in the trigger condition on the mRICH in the main peak are not related to reconstructed rings and are therefore considered as background.

The application of the ToT cut between 23.7 and 30.0 ns shows a pronounced effect in both figures. On the left side, the the strong peak at small radii is rejected. This is in agreement with the expectation from simulations that did not expect the existence of the peak on the left. The peak at a radius of around 3.6 cm stays nearly untouched. Even the contribution of very large rings is decreasing due to the cut. The ToT-cut leads in parallel to a decrease of the number of hits per reconstructed ring. Contributions from rings with many hits are reduced while the peak of the distribution nearly stays unchanged.

Figure 8.8 shows the rings radius vs. their number of hits for a selection with minimum multiplicity of 5 and without a ToT-cut (left) as well as with a ToT-cut (right). The use of a cut in time over threshold enhances the rings with a larger radius and a smaller number of hits in comparison to the analysis without a ToT-cut. The separated structure of low radii rings with large number of hits in the left plot is related to MAPMTs showing signals in many pixels. The structure becomes visible from around 20 hits per ring on and rises towards above 50, as expected from Figure 8.7. This structure is

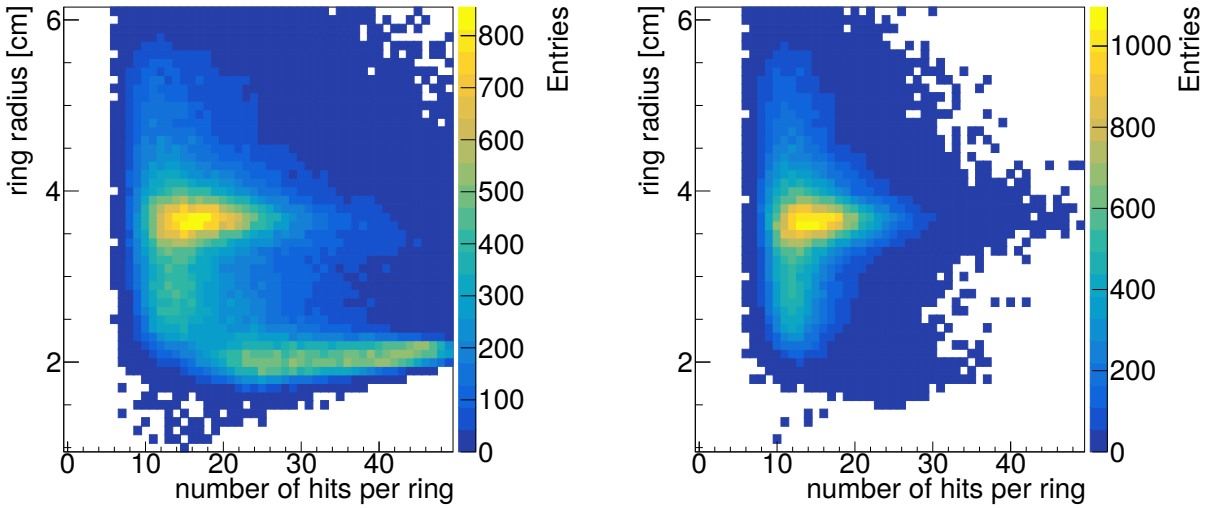

Figure 8.8: Ring radius vs. number of hits on the corresponding ring for run 831 with full statistics. **(left)** Minimum 5 hits in the mRICH and no ToT-cut. **(right)** Minimum 5 hits in the mRICH and the application of the ToT-cut.

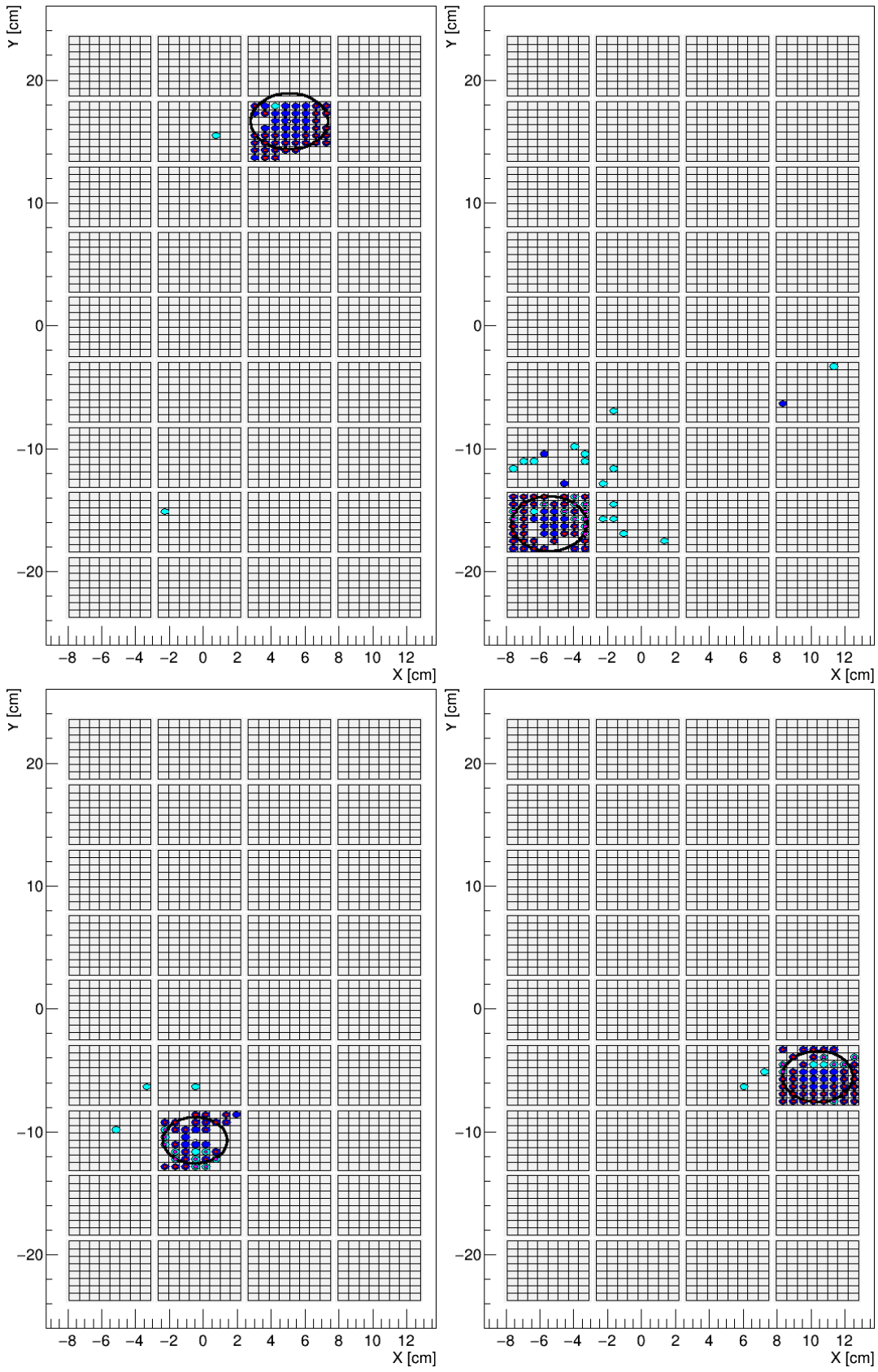

Figure 8.9: Single event displays of found rings with a radius below 2.5 cm and without a ToT-cut applied. In most cases, nearly a full MAPMT is illuminated. Most of the illuminating pixels are correlated to hits with a ToT outside of the chosen ToT window (blue). All cyan colored circles are hits with a ToT in the chosen ToT-window and the red dots show the hits assigned to the ring. The black ring shows the position of the reconstructed ring. The leading edge of all the hits on a MAPMT is very close in time. No difference in time between hits in- and outside the ToT-cut is visible.

clearly separated from rings, that behave as expected, i.e. as simulated. The figures show again the very reliable reduction of those rings by the use of a ToT-cut.

The previous observations suggest a very high hit density for small rings. As the size of the MAPMT is approx. 5×5 cm^2 rings of radius 2 cm would well fit within one MAPMT. Figure 8.9 shows four single event displays of run 831 with a trigger window of ±50 ns and a multiplicity trigger of minimum 5 hits in the mRICH without a cut in ToT and a radius of the reconstructed ring below 2.5 cm. The single event displays clearly show the reason for the peak at 2 cm in the radius distribution, as well as for the pronounced crosstalk peak in the ToT distribution and the high number of hits per ring.

In those events nearly all pixels of a MAPMT are firing and produce a hit. Most of those hits have a low ToT value and are treated as crosstalk. If no ToT-cut is applied, the ring finder reconstructs a ring with the hits of one MAPMT, leading to a radius below 2.5 cm.

The reason for the response of a full MAPMT could be related to the arrangement in the mCBM experiment. Differently to HADES RICH and the future CBM RICH detector, the mRICH is located in the acceptance of the experiment and suffers from charged particles passing through the detection plane. The charged particles can create a signal in the cathode, anode or dynode structure itself and can lead to scintillation light in the MAPMT entrance window. All those effects can lead to strong crosstalk and thus many hits in the MAPMT.

In general this is an effect seen also in rings with larger radii. The charged particles that corresponds to the reconstructed ring passes through the MAPMTs and produces hits in their pixels by the mechanism previously introduced. In case of a straight track between the mRICH radiator and the MAPMT, what is the main case, the track pro-

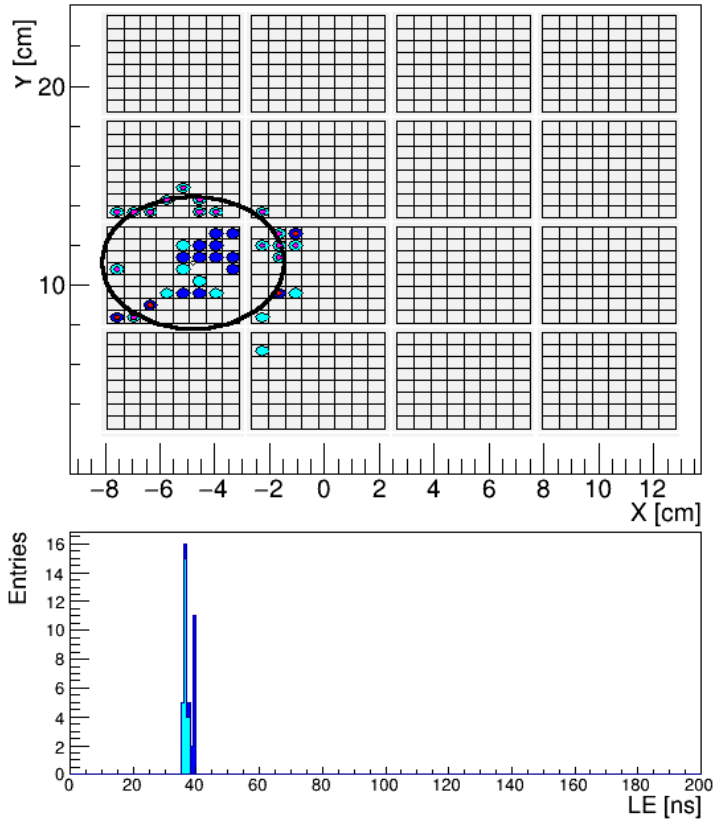

Figure 8.10: Cutout of a single event display with a well reconstructed ring. The center of the ring is dominated by an additional hit structure that is reduced by the use of the ToT-cut (blue circles). The hits of the ring itself are primarily untouched by the ToT-cut. The hits of the ring form a sharp peak in the leading edge time (LE) distribution. The hits outside of the ToT-cut are slightly shifted to higher LE times.

duces hits in the center of the ring. The additional center hits in the ring are a challenge for the CBM ring finder and lead to some problems as discussed later in this chapter. An improved version of the ring finder for the mRICH detector is under development.

The application of the ToT cut helps to reduce the center hits in a ring and therefore improves the ring finding procedure even with the current ring finder. Figure 8.10 shows one example of a reconstructed ring with a ring radius of 3.4 cm and hits in the center. The enlarged single event display shows that the application of the ToT-cut reduces the number of hits in the ring center without a major reduction of hits on the ring itself. In addition, the leading edge distribution of the rings is showing a peak in time with a slight shift towards later LE times for hits with a ToT outside the cut range.

All in all, the shown mRICH detector performance in terms of ring finding and the hit distributions by applying different event selections is very promising. The usage of a ToT-cut helps to improve the overall ring finding performance and validates the basic functionality of the mRICH detector.

8.6 mRICH Functionality and Spatial Correlations to mTOF

Based on the previous analysis of the to be chosen parameters for the mRICH data itself, a full analysis of the mRICH in combination with the mTOF as reference detector is performed. A deeper look into the actual ring finding performance and the spatial correlations to the mTOF is taken.

The mRICH detector is operated in mCBM beamtimes with the mTOF as a reference detector. Figure 8.11 shows the time dependence of the number of digis for both detectors in parallel. In addition, the corresponding number of reconstructed rings is shown.

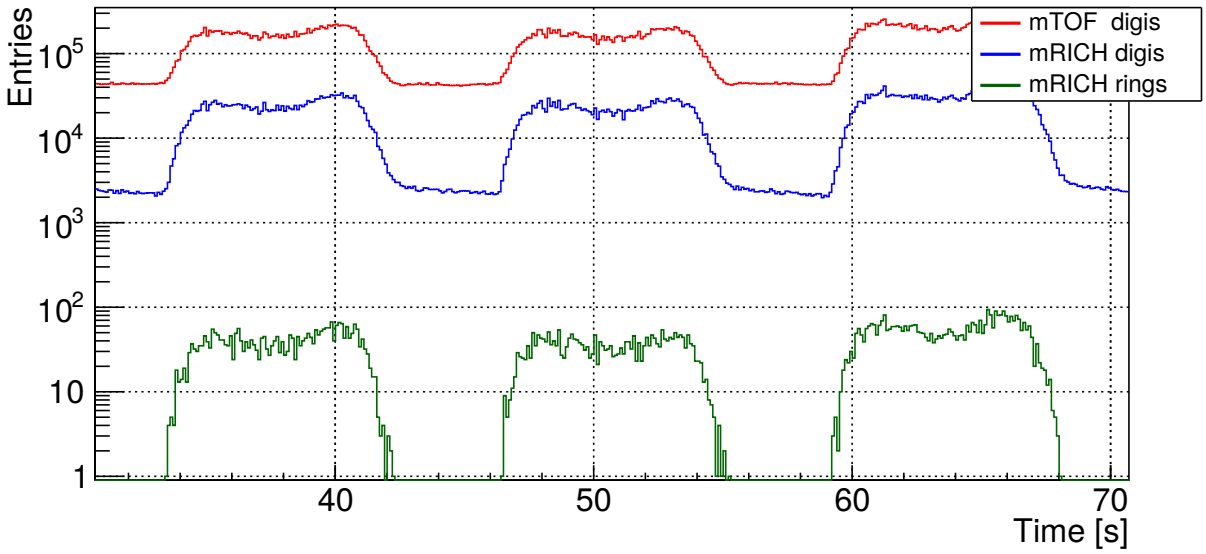

Figure 8.11: Evolution of number of mTOF and mRICH digis as well as rings over time. All three observables reflect the shape of the spills in the mCBM experiment.

The shape of the time distribution reflects perfectly the spill structure of the beam in the mCBM cave. The spill length is approximately 8.5 s with 4 s break in between. The number of reconstructed rings in the corresponding time slot is reflecting the same shape as well. In between spills the number of reconstructed rings decreases to zero as expected. The mRICH sees no fake rings in between the spills.

Figure 8.12 shows the number of digis respectively hits in a timeslice (12.8 ms). A minimum of about 200 digis is existing in a timeslice with an increase towards 300. The timeslices with more than 400 digis are suppressed by more than an order of magnitude, but the overall contribution of timeslices with more than 400 digis is relatively constant. The right side of Figure 8.12 shows the number of hits in a timeslice. The power of the event building and the application of the ToT-cut in rejecting uncorrelated hits are reflected in a shift of the minimum to fully empty timeslices, compared to the digis. The peak of the distribution itself is constant at around 300 hits per timeslice, as seen in the digi distribution. The long range tail to high number of hits per timeslice is vanishing and drops out at around 1000 hits per timeslice. This reflects the previous observation of the reduction of background hits due to the event building and ToT-cut resulting in the clean up of the fully responding MAPMTs with a high number of hits.

Figure 8.13, left, shows the distribution of the reconstructed hits in an event in the mRICH acceptance. The mRICH is operated with some DiRICH boards deactivated in order to improve stability. The deactivated boards lead to missing MAPMT parts in the hit distribution. The pixel rate is separated in a relatively homogenous illumination on the top and on the bottom part of the detectors. Both parts see an overall different illumination as both are correlated to the two aerogel radiator blocks. The upper aerogel radiator block was installed recently before the beamtime, whereas the lower aerogel is installed one year longer and was already used in previous mCBM beamtimes. The transmittance of the lower aerogel seems to be deteriorated in comparison to the

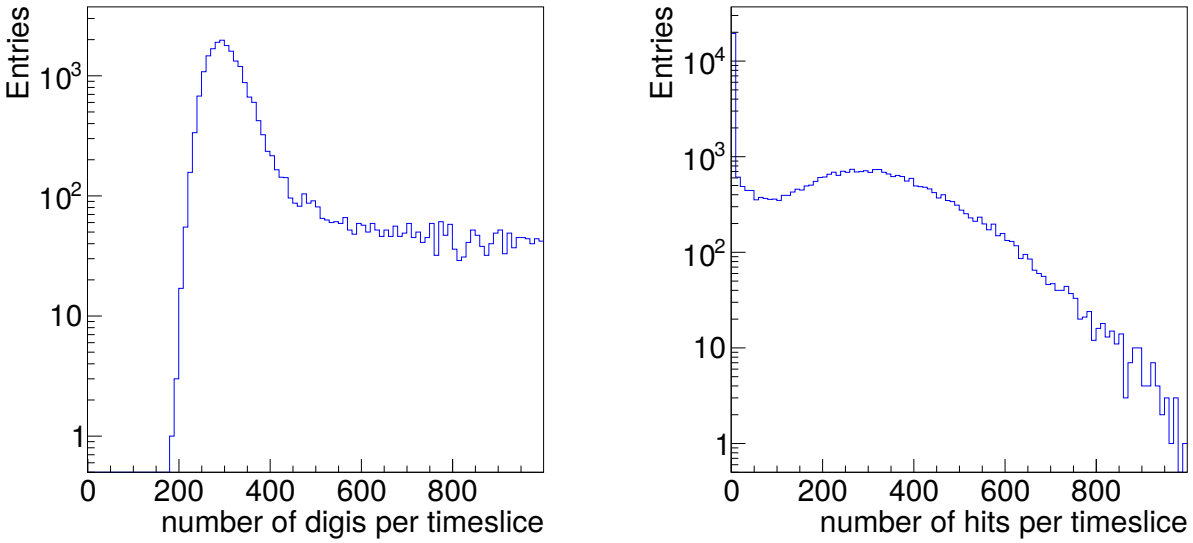

Figure 8.12: **(left)** Number of digis in a timeslice. **(right)** Number of reconstructed hits in a timeslice. The influence of the event building as well as the ToT-cut are reflected in these distributions.

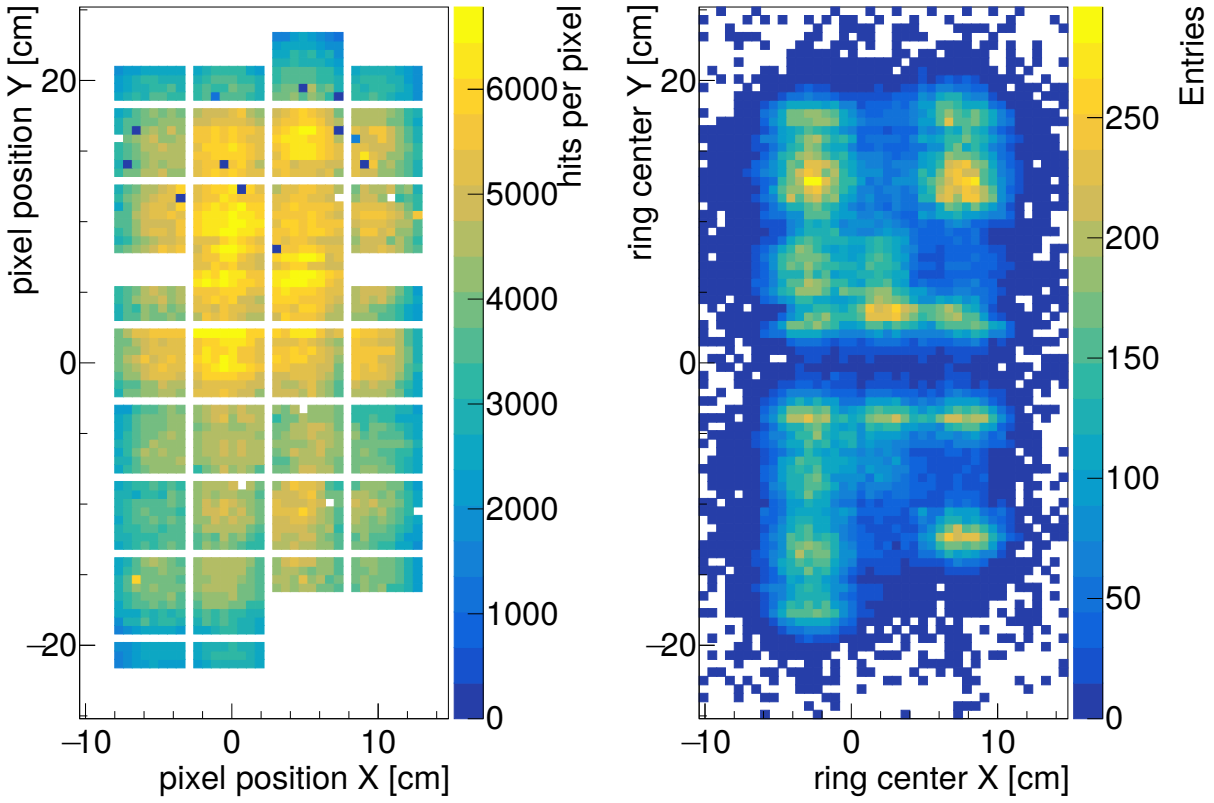

Figure 8.13: **(left)** Position dependant distribution of hits on the mRICH in a reconstructed event. The upper half of the mRICH sees a higher rate per pixel than the lower half, most probably related to the transmittance of the aerogel block. The lower aerogel radiator block is one year longer mounted in the detector and seems to suffer from ageing. **(right)** Positions of the center of reconstructed mRICH rings on the detection plane. The ring finder tends to find rings with the center in between MAPMTs. The positioning of both plots is given in the global mCBM geometry with its center at the 25° line.

newer one, due to ageing throughout the year.

The outer part of the mRICH detector sees the lowest amount of hits per pixel. In this area, the aerogel blocks geometrical acceptance is reached. The shown position of the mRICH pixels is given in the global mCBM geometry with its center on the 25° line with respect to the beam axis including the previously introduced additional shift of the mRICH.

The right side of Figure 8.13 shows the distribution of the center of reconstructed rings in the mRICH detection plane. The reconstructed ring centers are clustering in positions in between MAPMTs, resulting in a 3 row structure.

Also besides this inhomogeneity the distribution of the rings is not homogenous over the upper respectively the lower half. Areas with many hits per pixel sometimes have a low number of reconstructed rings and vice versa. The gap in between the two aerogel blocks, that are separated by a thin and non-transparent plastic layer, is clearly visible in the ring center distribution by a lack of rings.

The inhomogenous distribution of the rings unveils a imperfection of the RICH ring finder in the mCBM experiment. The currently used ring finder is the standard ring finder of the CBM RICH. It is not designed for the reconstruction of rings with addi-

tional hits in the center and therefore shows problems in the reconstruction. Regarding the parameters of the reconstructed rings, e.g. the radius or the number of hits, the ring finder is giving reasonable results as shown in the previous mRICH standalone analysis.

Figure 8.14 shows four single event displays (SEDs) of the mRICH detector in combination with tracks extrapolated using mTOF. The first SED shows a well reconstructed ring with a few hits in the center of the ring. The cyan colored points represent the hits in the detection plane whereas the red points indicate the hits, that are assigned to the ring. In addition, a green point is visible near the center of the reconstructed ring. This point represents an extrapolated track, detected by the mTOF detector. The track is matching the ring center quite well and confirms the principal functionality of the ring finding procedure. The second and third SED show similar reconstructed rings with hits in the center. More over, the third SED shows already first problems of the ring finder as not all hits, that are matched to the ring, are assigned to it. The last SED is an example of the main problem of the ring finder. A nice ring with hits in the center is visible by eye. Even a TOF tack is detected relatively nearby to the ring. Nevertheless, the ring finder misinterprets the center hits and fits them to the ring, leading to a wrong set of parameters of the reconstructed ring.

The misidentification of rings with hits in the center is a general problem of the ring finder and will be solved in the future by the development of a dedicated ring finder for the mCBM experiment.

The rings of the mRICH and the inner hits of the rings are further investigated in terms of timing within the ring as well as timing relative to the start time of the reconstructed event. An analysis of the hits on a reconstructed ring is shown in Figure 8.15. The top left figure shows the difference of the hit time to the mean time of the reconstructed ring (Δ-time). The time of all hits is corrected by the use of the ICD correction created on run 836. The resulting distribution shows mainly a Gaussian shape with a tail towards positive Δ-times (Peak: -0.144 ns, width of Gaussian: 0.390 ns). This measurement results in a overall time resolution of the mRICH of 390 ps. First of all the correction with the ICD, that is created with uncorrelated data, works well and verifies the overall principle. Nevertheless, the reconstructed rings are not perfect as shown before and therefore a certain contamination of correlated hits slightly later in time (tail appears toward positive Δ-times) are assigned to the rings (e.g. from a ring center). This gives an additional uncertainty in the distribution and finally leads to an additional tail in the distribution.

The structure of the ToT values of the hits (top,right) is reflecting the distribution of all hits and shows no significant difference (Mean: 25.3 ns, width of 0.638 ns). The third figure (bottom, left) shows the time difference of the hits in a ring to the start time of the reconstructed event. Most of the hits are reconstructed in a 30 ns window, starting 15 ns after the start of the event. This somehow confirms the chosen trigger window as the distribution fits the settings. Nevertheless, one expects a sharp peak for this distribution. The width of the distribution can be explained by the origin of the start time of the event. In case of noise in different detectors, the start of an event could be earlier in time than e.g. the correct T0 start time. In addition to all rings (blue), distributions for different ring selections in combination with mTOF are shown. The red curve represents rings in an event, where no close track is found. The purple distribution shows rings with a close track in a distance above 10 cm to the ring center and the green distribution shows good rings. Good rings are rings with a radius between 2.0 cm and

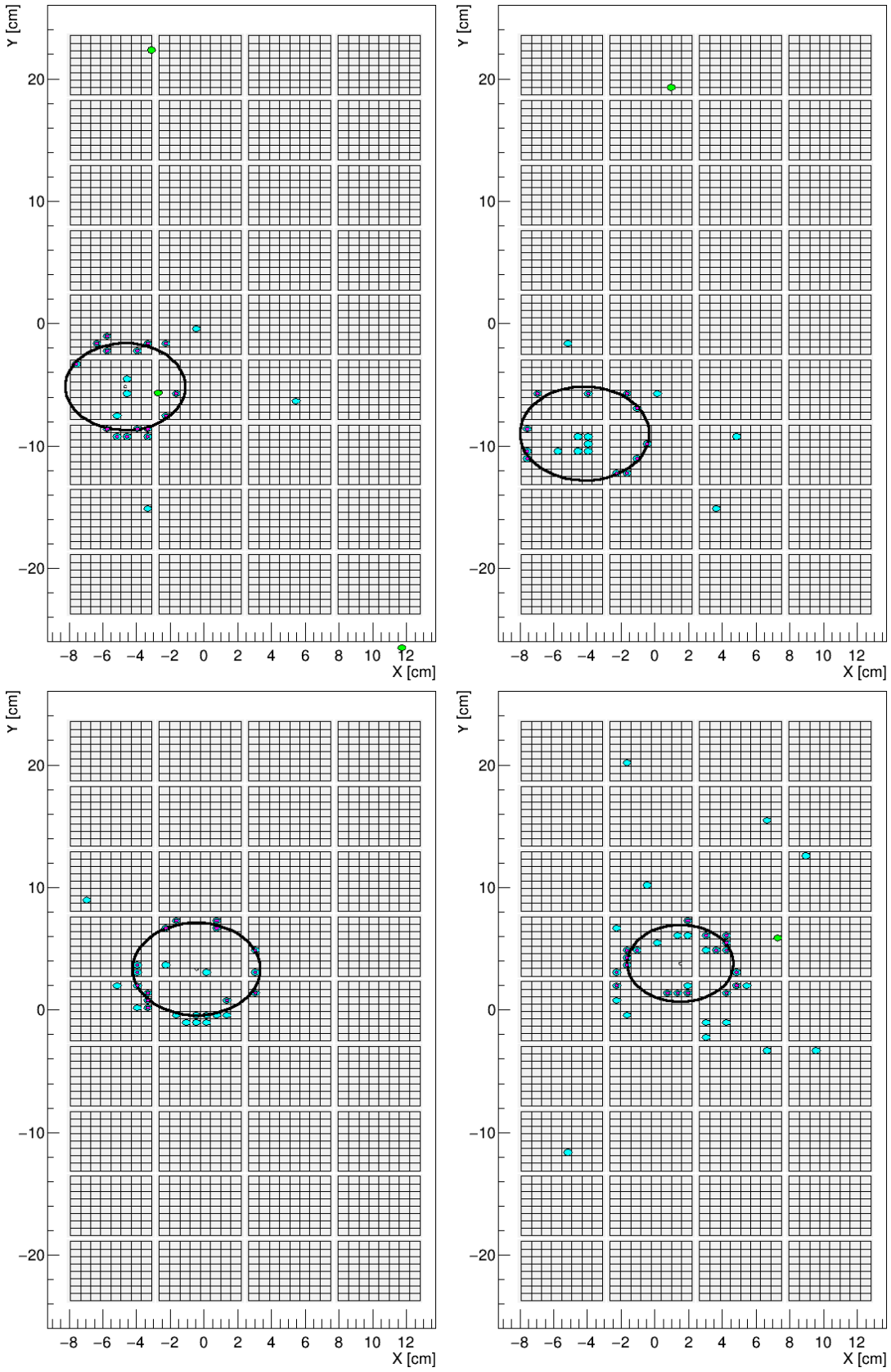

Figure 8.14: Single event displays (SED) of reconstructed rings and extrapolated mTOF tracks. Cyan: hits on the mRICH after ToT-cut. Red: hits assigned to a ring. Green: extrapolated mTOF track in the mRICH detector plane. The first three single event displays represent well reconstructed rings with a certain amount of hits in the center. The first SED also shows a perfect match to an extrapolated mTOF track. The last SED is an example for a misbehaviour of the ring finder with hits in the ring center.

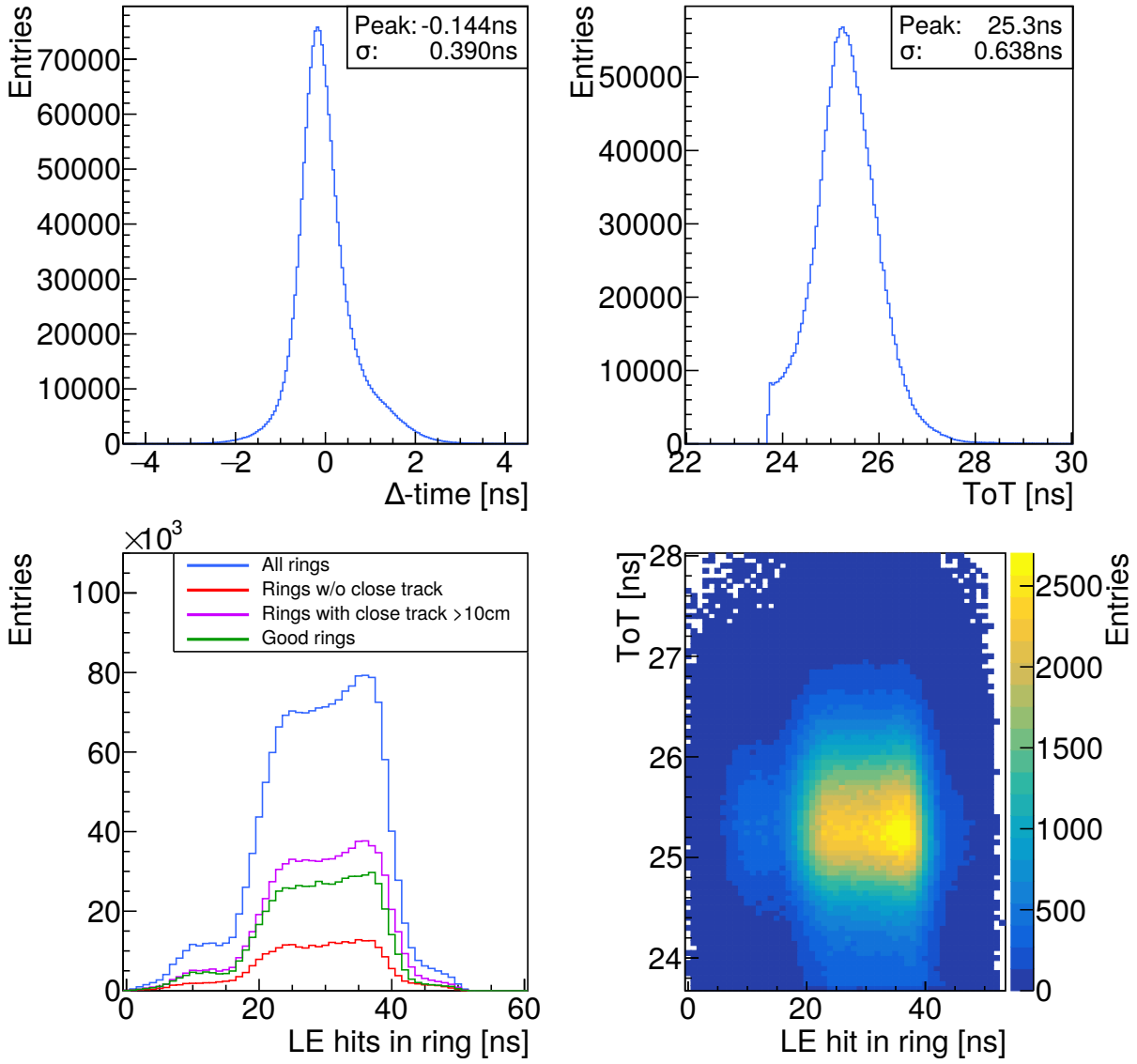

Figure 8.15: Analysis of parameters of hits assigned to a ring. **(top left)** Time difference between hit and mean time of ring. **(top right)** ToT spectra of the hits on a ring. **(bottom left)** Difference of hit time to the start of an event for four different ring-track conditions. **(bottom right)** ToT vs. hit to start time difference. No unexpected structure is visible.

4.2 cm and a track closer than 10 cm. The different categories unveil the existence of a certain amount of rings without any reconstructed track as well as a non neglectable contribution of rings with tracks that are not close to the ring. Nevertheless a huge amount of rings with a track closer than 10 cm are reconstructed.

The two dimensional representation of the time over threshold versus the time difference of a hit to the start of the event is presented in the bottom right figure. No hidden structure is unveiled and a clear correlation between the ToT peak and the start time offset is visible.

Figure 8.16 shows the same distributions, except the last figure, for the inner hits of a ring. Inner hits of a ring are defined in a distance to the ring center of 80% of the ring radius. The Δ-time distribution of the inner hits of a ring shows a clear distri-

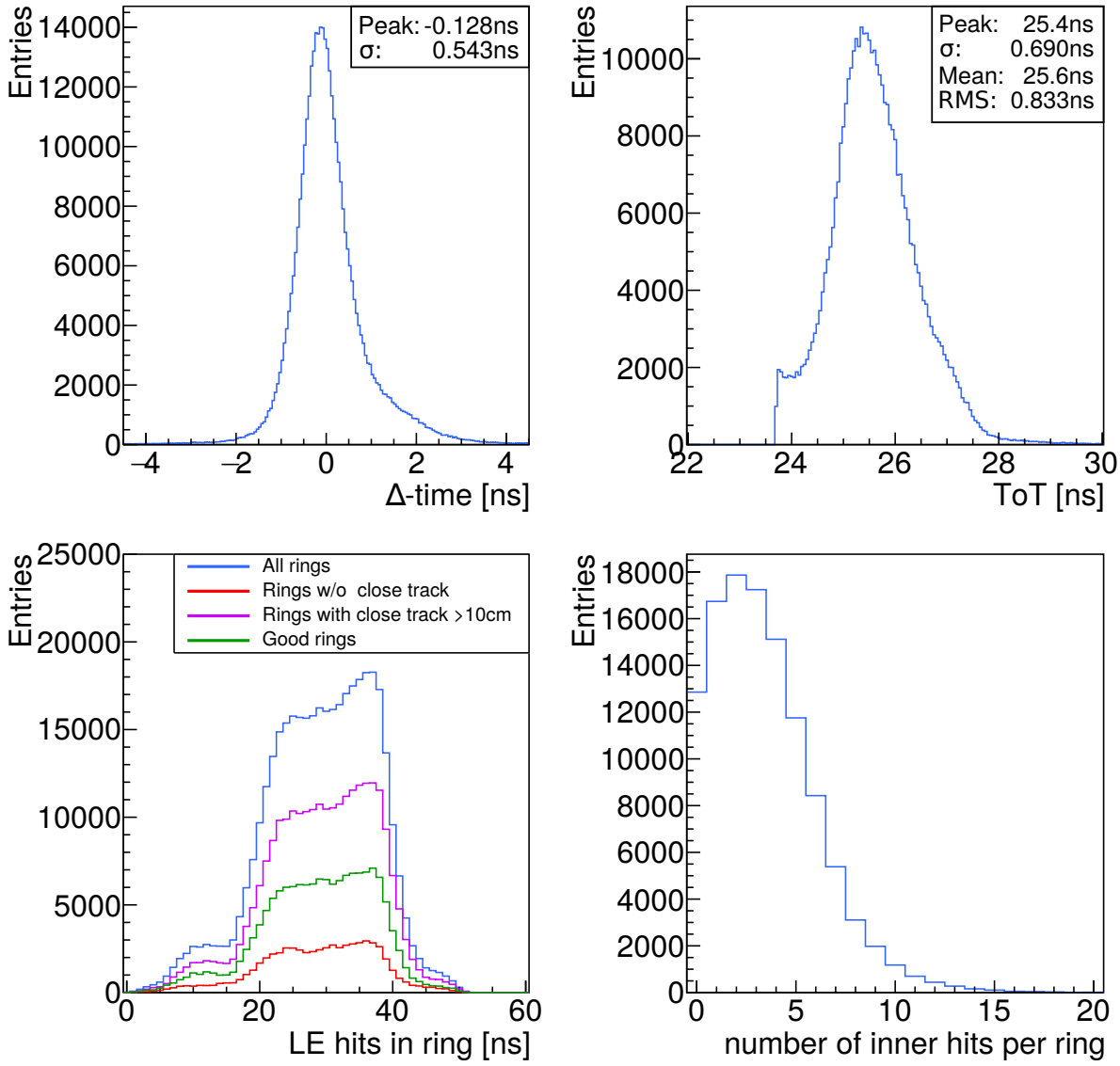

Figure 8.16: Analysis of parameters of hits in the inner 80% of a ring. **(top left)** Time difference between inner hit and mean time of the ring. **(top right)** ToT spectra of the hits in the ring. **(bottom left)** Difference of hit time to the start of an event for four different ring-track conditions. **(bottom right)** number of hits in the inner 80% of a ring.

bution around the mean time of the ring. The shift of the distribution is comparable to the Δ-times of the rings itself. This indicates, that the inner rings are correlated to the ring and are not random hits in the detector. Nevertheless the distribution is wider (σ=0.543 ns) than the Δ-time on a ring (σ=0.390 ns) (Figure 8.15) and has a more pronounced tail towards positive Δ-times. A higher contribution of hits, later in time is found in the inner of the ring and indicates a slight contamination with correlated hits, respectively some kind of induced hits (e.g. crosstalk hits that survives the ToT-cut). This is even reflected in the ToT distribution as this shows a broader distribution as in the case of hits on a ring. A fit of the ToT-distribution with a Gaussian is only possible near the peak. This results in a peak position of 25.4 ns and a width of σ=0.690 ns, comparable to Figure 8.15. In contrast to latter figure, the overall distribution deviates

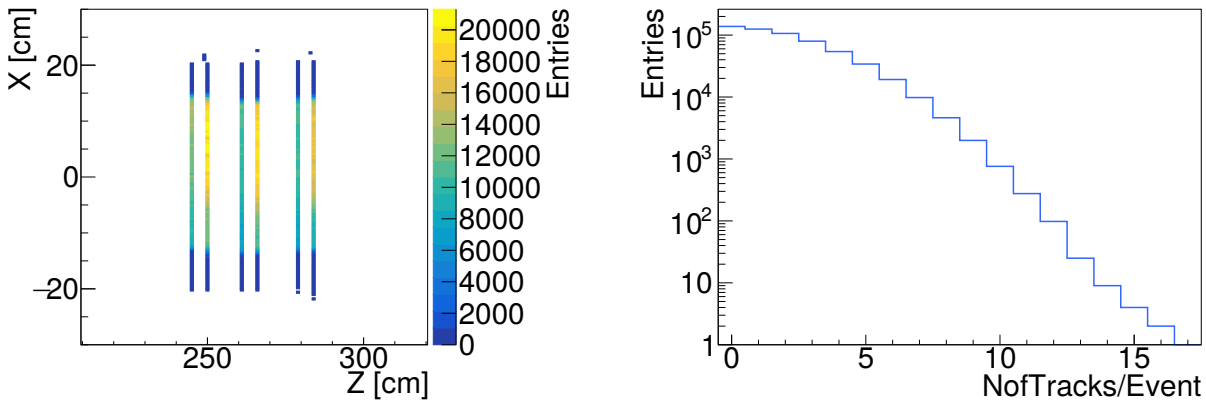

Figure 8.17: **(left)** Hits in the sensitive areas of the mTOF detector in the global mCBM X and Z position. **(right)** Distribution of the number of reconstructed mTOF tracks per Event in run 831.

from a Gaussian. The mean of the distribution is 25.59 ns with a width of 0.833 ns. The different width of the ToT can be explained by the origin of the inner hits. On the one hand Cherenkov light can be produced in the entrance window of the MAPMT and the light can hit several pixels. On the other hand, the charged particles can pass the dynode structure of the MAPMTs and produce a signal in it. Depending on which dynode is hit (or even several are hit), a different signal amplitude can be reached and therefore a different ToT is measured. This gives a higher variation in the measured width. Badly corrected ToT values from certain channels could also lead to cross talk hits even after the ToT cut. These hits are, as shown previously, related to rings and show up more prominently in the inner part of the ring as also visible in Figure 8.10.

The third figure (bottom, left) of Figure 8.16 shows overall the same shape as the corresponding figure for hits on a ring. The fraction of rings with a closest track in a distance larger than 10 cm is enhanced compared to Figure 8.15. This shows that the existence of inner hits in a ring is related to a reconstructed track in the TOF detector. The existence of rings without a track could be reduced by the application of a cut on the hits in the mTOF, but as this contribution does not change the overall analysis, but would reduce statistics, the cut was not used.

The last figure shows the number of hits in the inner part of a ring. A clear peak around 3 hits is visible with a long but suppressed tail to 15 hits. The distribution additionally shows that a non neglectable number of rings exists with no hits in the center at all, as it would be the case in the future CBM RICH detector.

Despite some imperfections, the analysis of results of the ring finder and the hits attached to and within a ring in combination with the mTOF detector shows still a good performance. Improvements of the ring finder which are currently underway will certainly increase the efficiency and performance. Nevertheless, the prove of principle of the read out and operations with a free streaming DAQ has been successfully done.

The previous analysis already used reconstructed mTOF tracks and their extrapolation to the mRICH detection plane. The mTOF detector geometry of run 831 is only made of the triple stack. The double stack is not in use. Figure 8.17, left, shows hits in the sensitive areas of the three mTOF stacks with the two modules per stack. The positioning of the modules in the X-Z plane in the global mCBM geometry is visible. The right side of the figure depicts the number of reconstructed mTOF tracks in a CBM

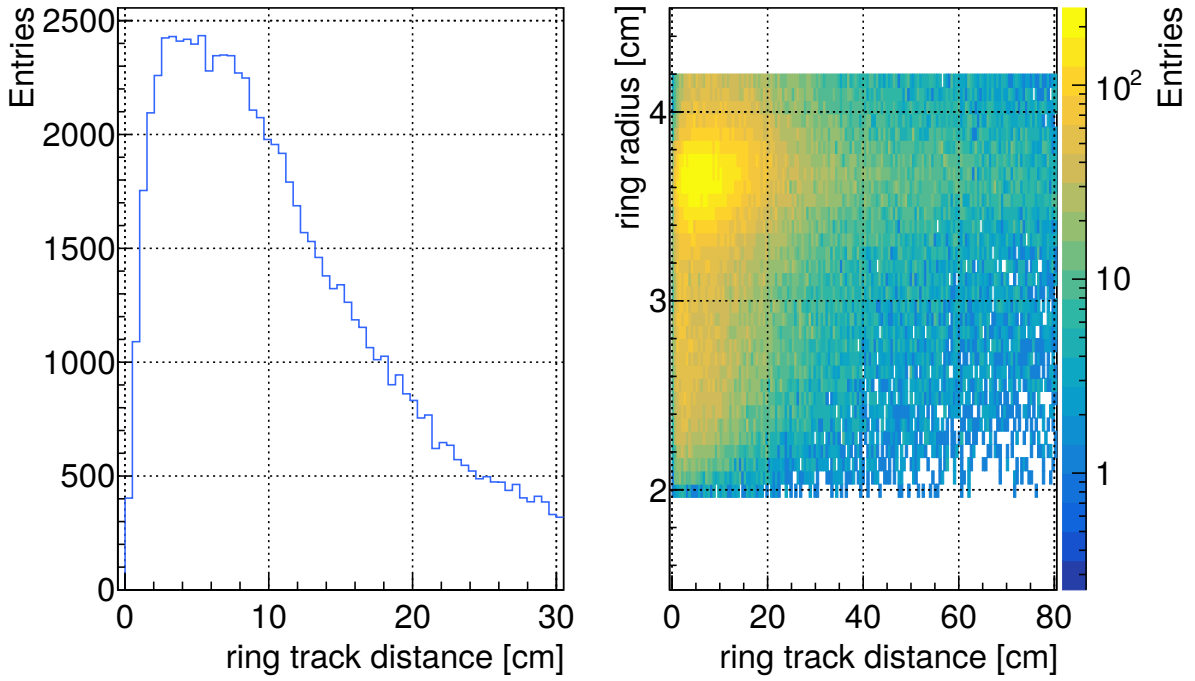

Figure 8.18: **(left)** Ring track distance for run 831 with all available calibrations. The distribution peaks at a distance of around 5 cm and shows a fast decrease with higher distances. **(right)** Ring track distance versus ring radius. A very clean correlation between the radius and the distance is observed. A tail towards lower radii at small ring track distances can be seen.

event. Up to 16 tracks could be reconstructed in a single event without a cut on the number of hits in the mTOF. The use of a cut on minimum 10 mTOF hits would reduce the contribution of events with only up to 2 tracks.

The left of Figure 8.18 shows a distribution of distances between a ring and the extrapolated track. The landau shaped distribution of the ring-track distances has a peak of a ring track distance (see Figure 8.18, left) around 4 to 6 cm. Simulations of the mRICH ring-track distance result in a peak around 1.5 cm (see Figure 8.32 in section 8.7). This difference in the ring track distance between data and simulation could be explained by the influence of the ring finder deficits (see Figure 8.13, right). The favoured ring center in between MAPMTs artificially increase the ring track distance. Still the reconstruction is good enough to match ring-track pairs.

Figure 8.18, right, presents the ring track distance in combination with the ring radius of the reconstructed rings. The distribution shows a peak at a radius of around 3.6 cm and a ring track distance of 4-6 cm. A tail towards lower radii at small ring track distances can be seen. This contribution is expected to be related to pions, whereas the main peak around a radius of 3.6 cm is expected to be related to electrons.

The extrapolated tracks from the mTOF are further used searching for a spatial correlation between the mRICH and the mTOF detector. Figure 8.19 shows the first correlation between the mTOF tracks and the mRICH detector. The left figure depicts the X-Y position of mTOF tracks at the Z-position of the mRICH detector plane. The distribution of the tracks shows a clear correlation to the actual position of the mRICH

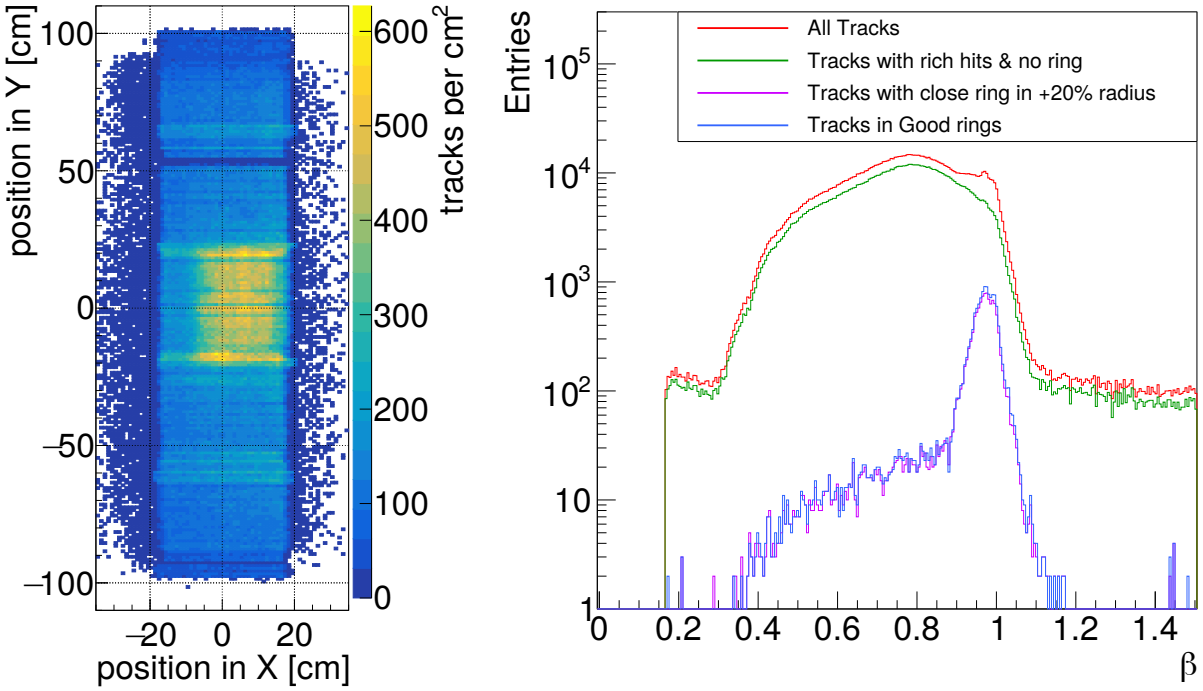

Figure 8.19: **(left)** X-Y position of mTOF tracks in the mRICH detection plane. A correlation of the track position with the mRICH detector position is visible. No further cuts as the standard event building and a minimum of 10 hits in the mRICH detector are resulting in the correlation (yellow enhancement). **(right)** Beta spectrum of mTOF tracks. Different distributions with and without rings in the near range of a track are shown. The detection of a mRICH ring near a mTOF track or vice versa results in an enhancement in the beta distribution around β=1.

detector. The correlation is achieved by the use of the standard event building and the multiplicity trigger of 10 hits in the mRICH detector. Without any ring track matching the enhancement of tracks at the position of the mRICH detector becomes visible (yellow blob). A deeper look on the blob even shows the missing DiRICH boards at the borders of the mRICH. The increase in the number of track of tracks above and below the mRICH is related to the overlap of two mTOF modules.

Figure 8.19, right, shows the measured relativistic velocity (β) spectrum of the mTOF tracks for different conditions. The red distribution shows the β spectrum of all measured tracks in the mTOF. It shows an additional enhancement around a β value of 1. The green distribution shows the beta spectrum for all tracks in events with hits in the mRICH detector but no reconstructed ring. The shape of the distribution follows the shape of the distribution of all tracks, except the enhancement at β=1. The purple distribution shows the beta spectrum for tracks with a close by ring. The track has to be located within the radius of the ring with an additional margin of 20%. The blue distribution shows the same distribution for rings with a radius between 2.0 cm and 4.2 cm and a close track within the radius with additional margin of 20%. The use of both distributions is a cross check of the analysis and shows differences in cases, where e.g. a ring could be assigned as a close ring to 2 different tracks.

Good ring-track combinations result in a prominent peak in the beta spectrum at β=1. The enhancement is primary caused by electrons. Figure 8.20 shows the ring-radius versus β of the good rings. The peak at β=1 is a composition of rings with a

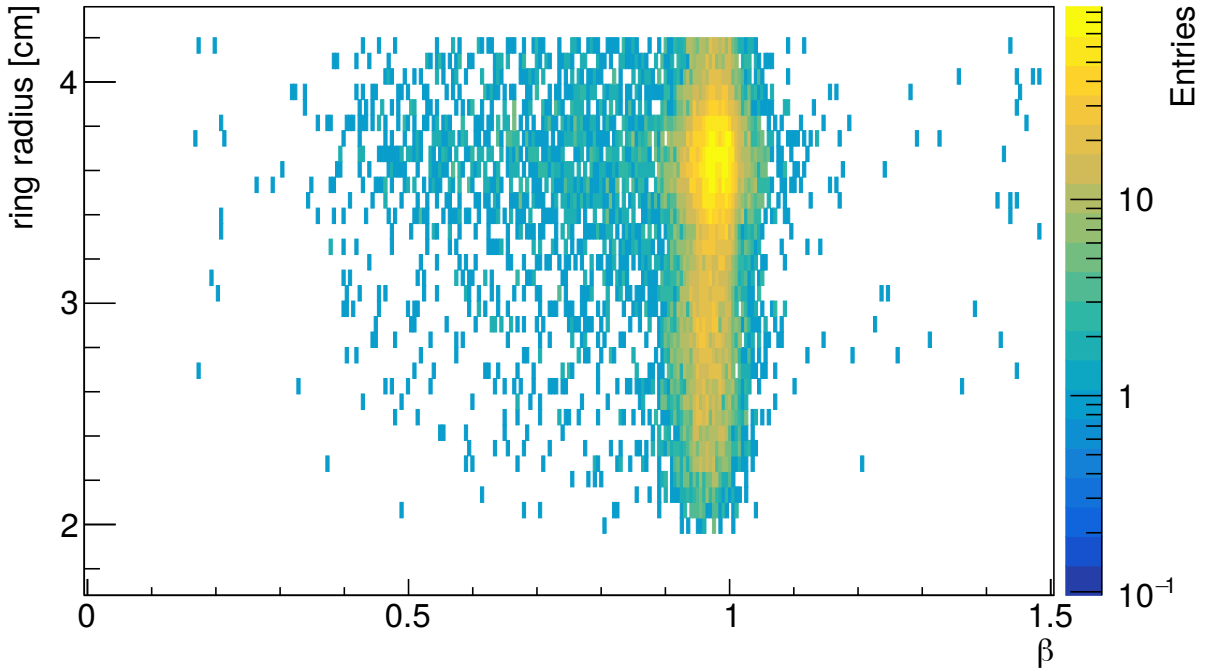

Figure 8.20: Ring-radius versus β of good RICH rings. Most of the tracks matched to a nearby ring have a measured β of roughly 1. The mTOF β measurement in combination with the ring radius information from mRICH gives the possibility of particle identification.

large radius as well as a small radius. Only pions are able to produce small rings in the mRICH with β=1, whereas electrons are detected with a radii of approx. 3.6 cm. The combination of the ring radius information of the mRICH and the β-information from the mTOF tracks can be used as a tool for particle identification. Furthermore this gives physics potential for future mCBM runs.

The strong enhancement of the beta distribution around β=1 for good ring-track matches allows a more detailed analysis of spatial correlations. Before these correlations of tracks and rings are further discussed, more basic correlations between mTOF hits and mRICH hits are presented, which, historically, were the first prove of a successful mCBM event reconstruction with the free-streaming readout concept.

Figure 8.21 shows the correlation in spatial coordinates between mTOF hits and mRICH hits. The correlation between both detectors is visible in horizontal (X) and vertical (Y) direction. In case of the horizontal correlation, an additional increase of hits in the background towards the beamline (increasing values of X) is visible. Due to a visible offset in the X-direction of the mRICH and mTOF correlation, the mRICH detector was shifted in spatial coordinated by 2.5 cm to improve the alignment of the detectors. The shown figures of this thesis all include the correction in X direction.

In Y-direction, a clear correlation is visible. In addition, there are lines seen at a constant Y-value in mTOF. These periodical enhancements in the hits of the mTOF are originating from the overlap regions between two detector modules inside an mTOF stack and are therefore expected.

The large background in the X-direction is overlaying the main correlation. In order to improve the situation, the shown diagram is separated into all three stacks as

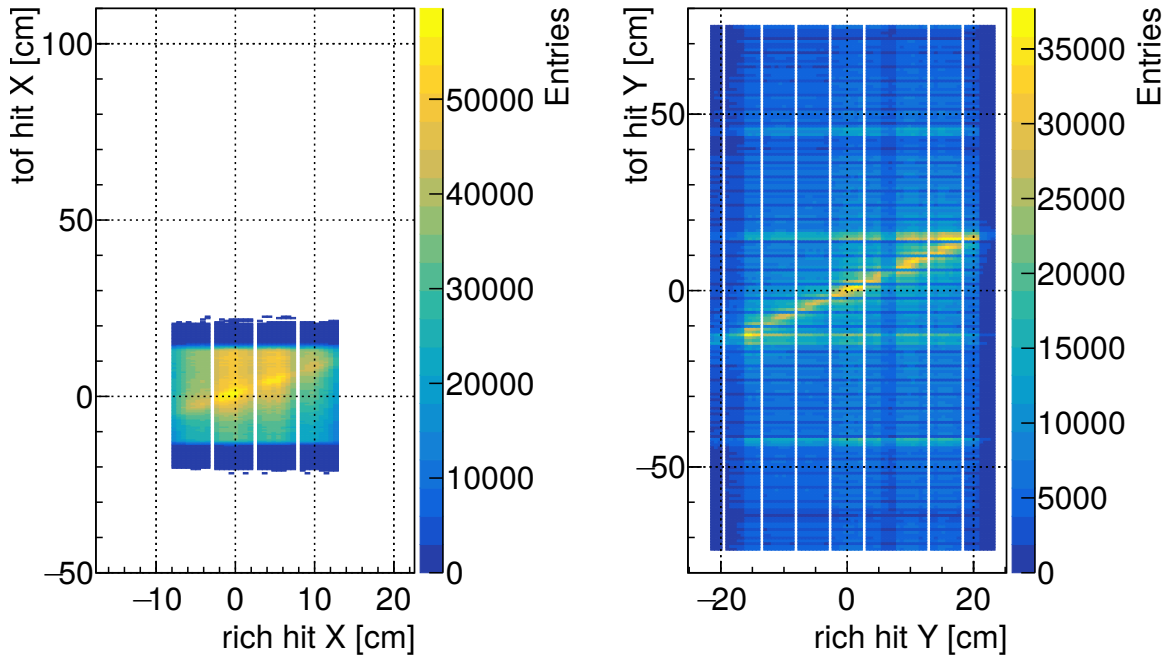

Figure 8.21: Correlation between spatial coordinates of mTOF hits and mRICH hits in **(left)** X- and **(right)** Y-direction. Both diagrams show a correlation between hits in the mTOF and the mRICH detectors. The correlations are matching (0,0) of the global mCBM geometry in the order of the available geometrical alignment.

shown in Figure 8.22. The separation into the three stacks shows an decreasing influence of the background with increasing distance to the target and therefore also to the beamline (25° alignment of detectors to beamline). The correlation itself is nearly constant for all three stacks. Only a minor decrease towards the last stack is visible. In the case of the first mTOF stack, a slight shift from a correlation through (0,0) is visible. The other two are matching this origin perfectly.

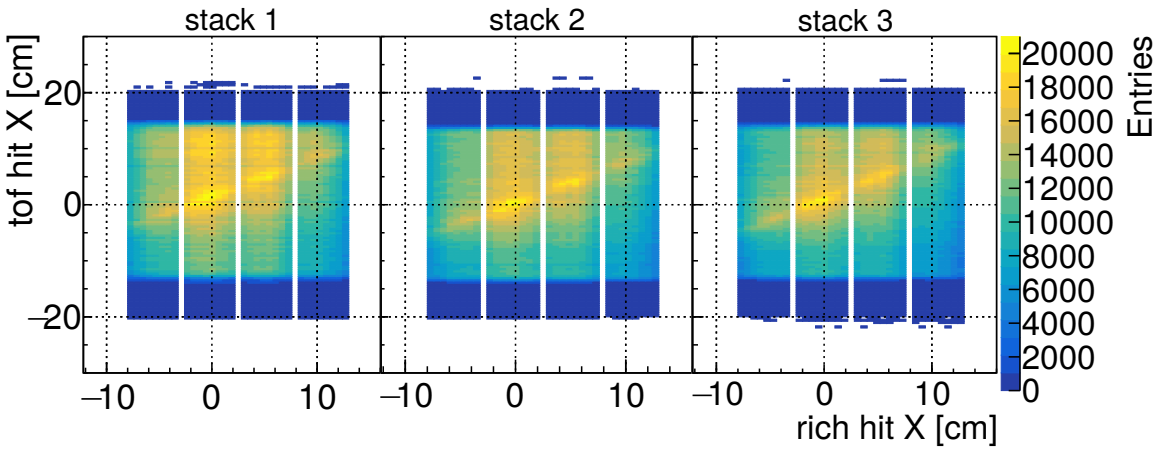

Figure 8.22: Spatial correlation in X direction in all three stacks of the mTOF detector. All three correlation diagrams show the correlation between both detectors. The alignment of the stacks to (0,0) of the geometry is showing a good quality for all three with a slight shift for stack 1.

In order to improve the correlations and as a final confirmation of the functionality of the mRICH and the mTOF as well as the free-streaming readout, a higher level of abstraction, namely tracks for the mTOF and rings for the mRICH are taken into account. Figure 8.23 shows the correlation between tracks in the mTOF detector and hits in the mRICH. A minimum of 3 hits per track is required to accept the track for the analysis. The step from hits to tracks smears the distribution in Y and reduces the influence of the overlapping regions in the mTOF. However, the correlation in X is still weak and the background contribution is still visible. In order to reduce the effect of uncorrelated background, the β-spectrum from Figure 8.19, right, is taken into account. A correlation in case of a match between tracks and nearby rings is investigated in a range of $0.9<\beta<1.1$ (Figure 8.24). The application of this beta cut on reconstructed tracks can reduce the influence of uncorrelated tracks even without using parameters of the reconstructed rings. Despite that the existence of minimum one reconstructed ring is required for this check.

The use of the beta cut cleans up the spectrum and enhances the correlations in X and in Y. In both cases the background is strongly suppressed with little change in the signal. The main correlation in X becomes more clean without the additional background towards the beamline of mCBM. The reduced amount of hits in the lower half ($Y<0$) of the mRICH is visible, but the correlation is clearly seen against the background.

As a cross check of the power of the beta cut, the same spectrum with tracks outside the chosen beta region is produced (see Figure 8.25). The resulting spectrum shows only a minor correlation in Y and none in X. The increased amount of tracks towards the beamline (correlation in X) as well as the overlap region between the mTOF mod-

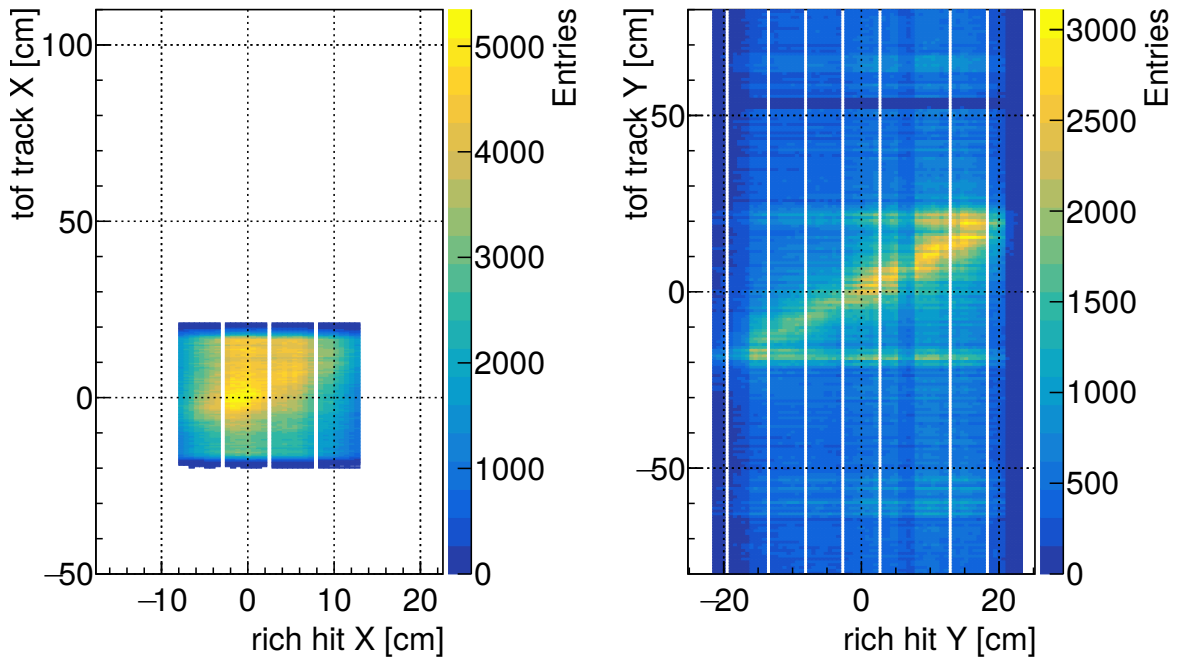

Figure 8.23: Spatial correlation between mTOF tracks and mRICH hits without cuts. The distributions are similar to the hit distribution in Figure 8.21 with a smoothening of the structures in Y. The increased hit rate in the upper mRICH half is now clearly visible.

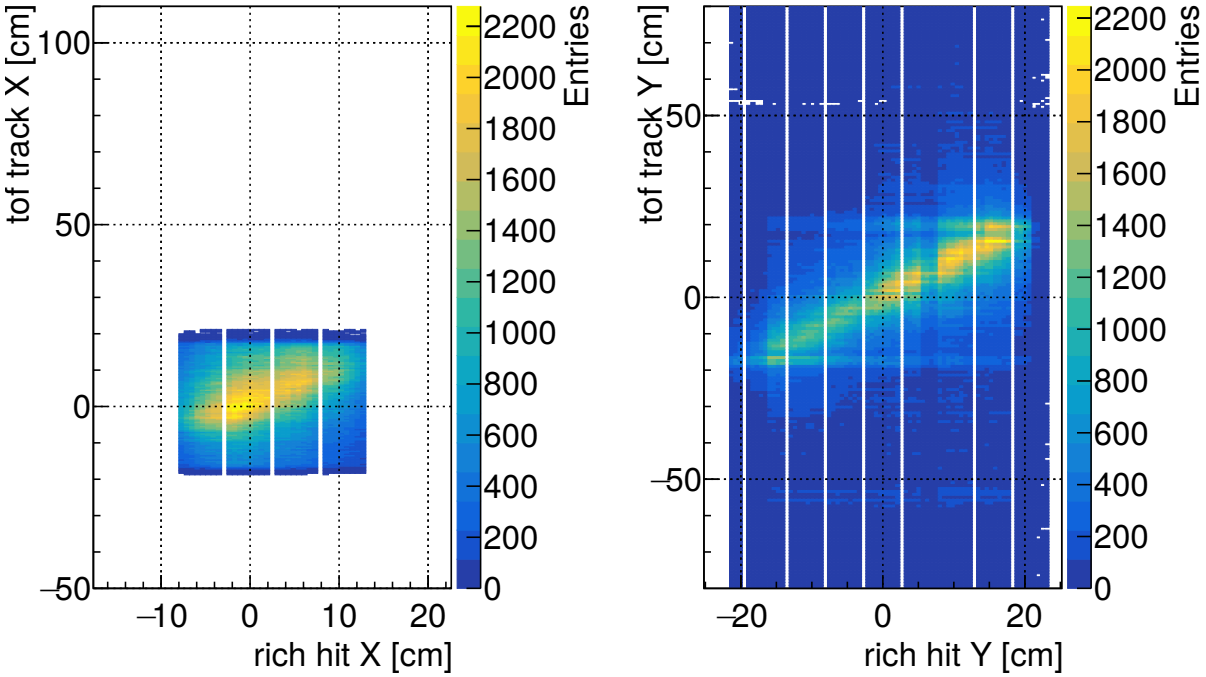

Figure 8.24: Spatial correlation between mTOF tracks and mRICH hits. A cut on the reconstructed relativistic velocity of the tracks of $0.9<\beta<1.1$ is applied. The beta cut reduces the background and strengthens the correlations.

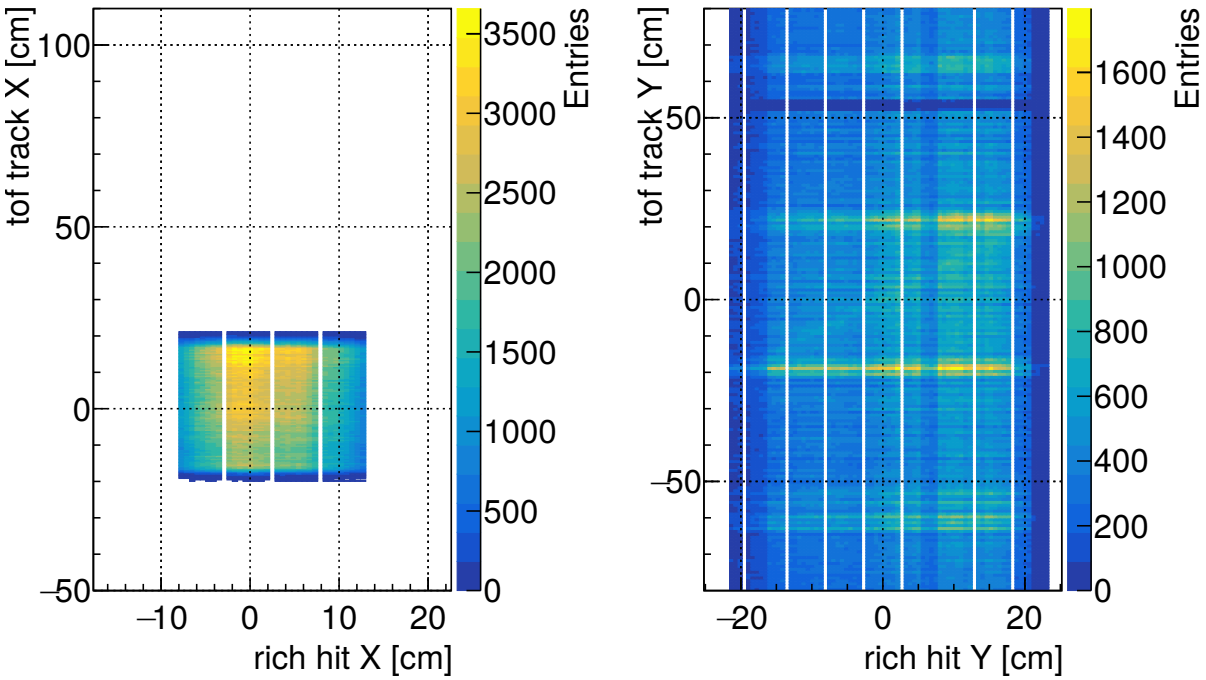

Figure 8.25: Spatial correlation between mTOF tracks and mRICH hits. A cut on the reconstructed relativistic velocity of the tracks of $\beta<0.9$ and $\beta>1.1$ is applied. The resulting distributions show only a very minor correlation in the Y-direction. The use of a cut in the β-spectrum is a powerful tool to remove background from uncorrelated tracks and rings.

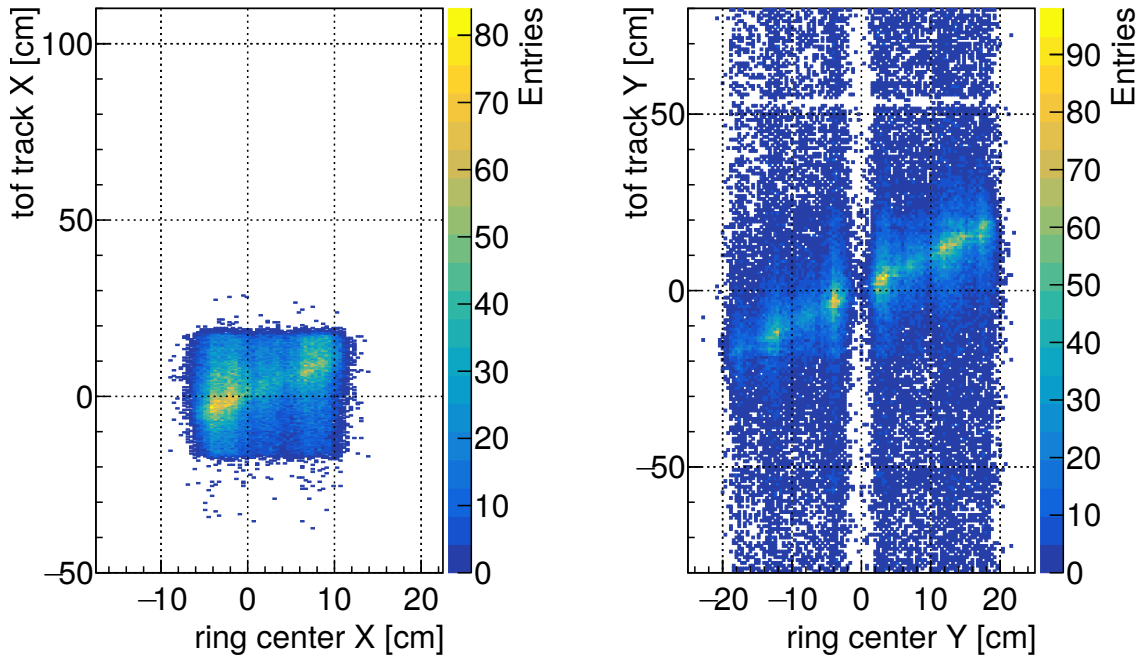

Figure 8.26: Spatial correlation between mTOF tracks and mRICH ring centers. Only tracks with $0.9<\beta<1.1$ and 3 or 4 hits assigned to them, in an event with a reconstructed ring are shown. In addition, a ring radius between 2.0 cm and 4.2 cm is required. A clean correlation between tracks and rings is seen, with enhancements in the region of preferred ring centers.

ules (correlation in Y) is visible. The enhancement of tracks towards the beamline, excluded by the beta cut, suggests an increasing amount of hadrons with a decreasing distance towards the beamline.

Finally, Figure 8.26 shows the correlation between a reconstructed track and the center of a reconstructed ring. Only rings with a radius R of 2.0 cm<R<4.2 cm and a track in the same event are accepted to create the presented figures. The tracks in the distributions require a relativistic velocity of $0.9<\beta<1.1$ and 3 or 4 hits assigned to them. The resulting distribution shows a spatial correlation between the selected tracks and rings. The correlation is clean without a contribution of overlapping mTOF modules respectively hadrons near the beampipe. The correlation is not homogeneous due to the preference of the ring finder towards center positions in between MAPMTs. Nevertheless the overall correlation is perfectly visible and confirms the overall functionality of the mRICH ring finding and the mTOF tracking, i.e. event building with the new, free-streaming readout.

The previously shown correlations between hits, tracks and ring centers show remarkable good spatial correlations in all cases. The use of the beta distribution of tracks as well as the ring radii or assigned hits to tracks can improve the correlations and clean up the background contributions. The analysis of the mRICH detector itself, its timing and spatial correlations with the mTOF and T0 detector show a great performance of the prototype detector as well as the developed readout and DAQ in a free-streaming environment as the mCBM experiment is.

8.7 Timebased Simulations of the mRICH

The previously shown results from the 2020 beamtime campaign of mRICH have been compared to timebased simulations. The simulation is setup with the identical geometry as the previous data analysis and analysed with the same code base. As the statistics for the Pb+Au@1.06 AGeV collision system, as used in run 831, is quite small, an analysis with Ag+Au@1.58 AGeV minimum bias was chosen (setup of march 2019). Next to the increase in statistics, most of the shown distributions are not influenced by the chosen system. An overview of the simulation setup is shown in Table 8.2. The shown simulation results give a classification of the data analysis results and will show the functionality of the timebased simulations with different settings.

All following histograms with a comparison between real data from section 8.4 and simulations are normalised. The shown real data in the histograms is taken from section 8.4.

Figure 8.27 shows the simulated ring radius distribution for different collection efficiencies in a geometry with an MAPMT entrance window (left) and without an entrance window (right). Different collection efficiencies are chosen to find the best agreement between the simulation and real data. The change of the collection efficiency has no significant impact on the position of the ring radius peak in the simulation. The shown measured distribution (red) shows a slightly different peak position of 3.6 cm instead of 3.8 cm for the simulation. The difference in the peak position can be explained by small differences in the distance between the MAPMT windows and the aerogel in the simulation and the real detector. In addition, the difference in the ring radius is smaller than the pixel granularity of the mRICH. The tail towards smaller ring radii is slightly visible in the simulations, but much more pronounced in the real data. A relation between the small radii and the problematic behaviour of the ring finder on data with center hits could not be excluded.

Figure 8.28 shows the number of hits per ring for the same simulation settings as in the previous figure. The change of the collection efficiency shows its full potential: While a collection efficiency of 100% results in a broad distribution with up to 40 hits

parameter	value
kind of simulation	timebased
simulation package	UrQMD
simulated events	100.000
target of mCBM	0.25 µm thin fixed Au target
beam	Ag @ 1.58 AGeV (minimum bias)
Detectors for event building	mRICH, mTOF and mT0
Trigger Window mRICH	-50 ns to 50 ns
Trigger Window mTOF	-150 ns to +10 ns
Trigger Window T0	-1 ns to +10 ns
Minimum Digis mRICH	5
Minimum Digis mTOF	10
Minimum Digis T0	1
mCBM geometry setup	mcbm_beam_2020_03.geo.root

Table 8.2: Overview of settings for the analysis with timebased mCBM simulations.

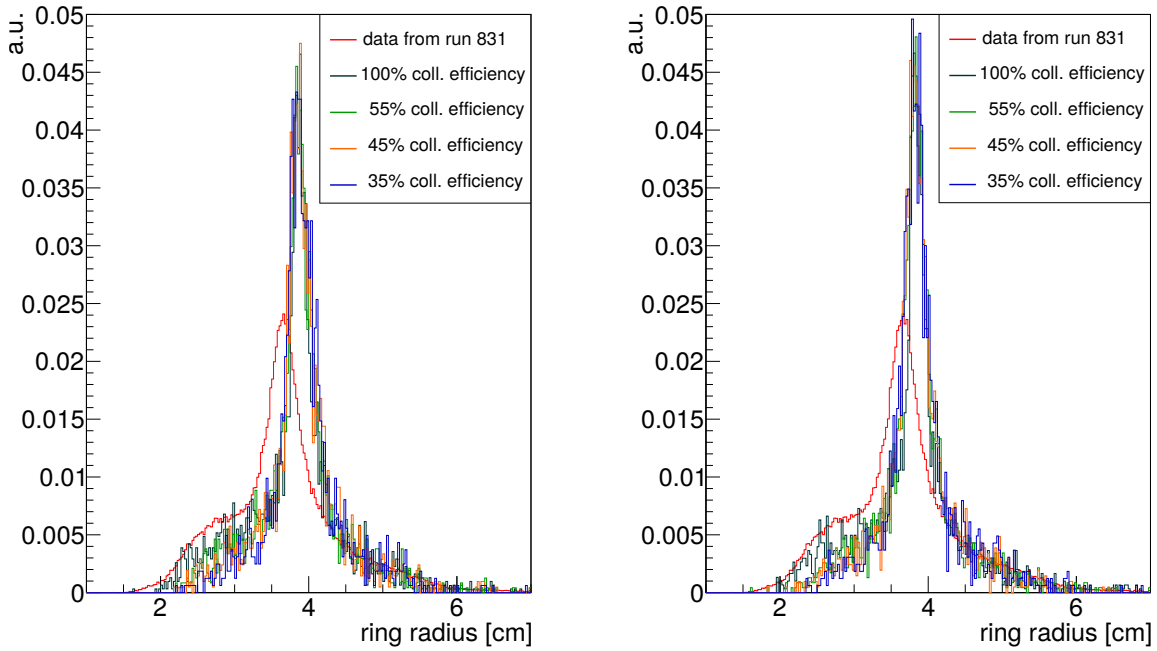

Figure 8.27: Ring radius distribution in simulations with different collection efficiencies as well as with **(left)** and without **(right)** MAPMT entrance window. The red distribution shows the measured ring radius distribution from run 831 (Figure 8.7, left).

per ring, the decrease in the collection efficiency leads to a change in the shape towards a more narrow peak. An efficiency of 45% reproduces the measured data from run 831 very well and seems to be the correct setting for a realistic simulation. The distribution ends at a number of hit per ring of about 30 with a peak at 12. The re-

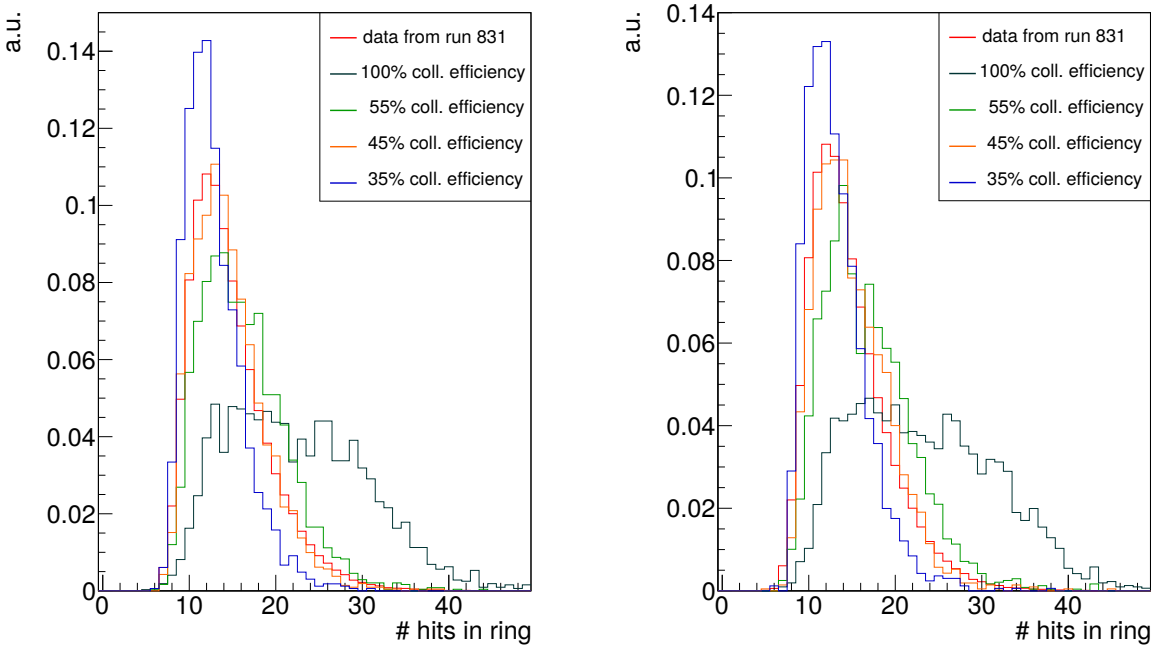

Figure 8.28: Number of hits per ring in simulations with different collection efficiencies as well as with **(left)** and without **(right)** MAPMT entrance window. The red distribution shows the measured amount of hits per ring from run 831 (Figure 8.7, right).

duction of the collection efficiency to 45% is needed, as the exact parameters as e.g. the transmittance of the aerogel in the mRICH are unknown. This differences of the real aerogel parameters to the aerogel used in simulations are reflected in the adjusted collection efficiency. The previous observations are similar for simulations with (Figure 8.28, left) and without (Figure 8.28, right) entrance window of the MAPMT. The influence of the entrance window in the simulations of the ring radius as well as the number of hits per ring is only minor.

In the following, only simulations with a collection efficiency of 45% are shown, as these reproduce the measurements of mRICH with a good agreement.

Figure 8.29, left, shows the position dependant distribution of mRICH hits in simulations with an entrance window. The figure is in good agreement with the measured data (Figure 8.13). The seen reduction of number of hits towards outer pixels of the detector is identical for both, simulated and measured data. Nevertheless the reduction of hits in the lower half of the detector is not seen in the simulation. This confirms the statement, that the reduction is related to ageing of the aerogel.

Figure 8.29, right, shows the position dependant distribution of centers of reconstructed rings. The centers are homogeneously distributed in the lower and the upper half with a gap in between the two halfes. This splitting in two halfes is seen in the real data too and is expected due to the ABS spacer in between the two aerogel blocks.

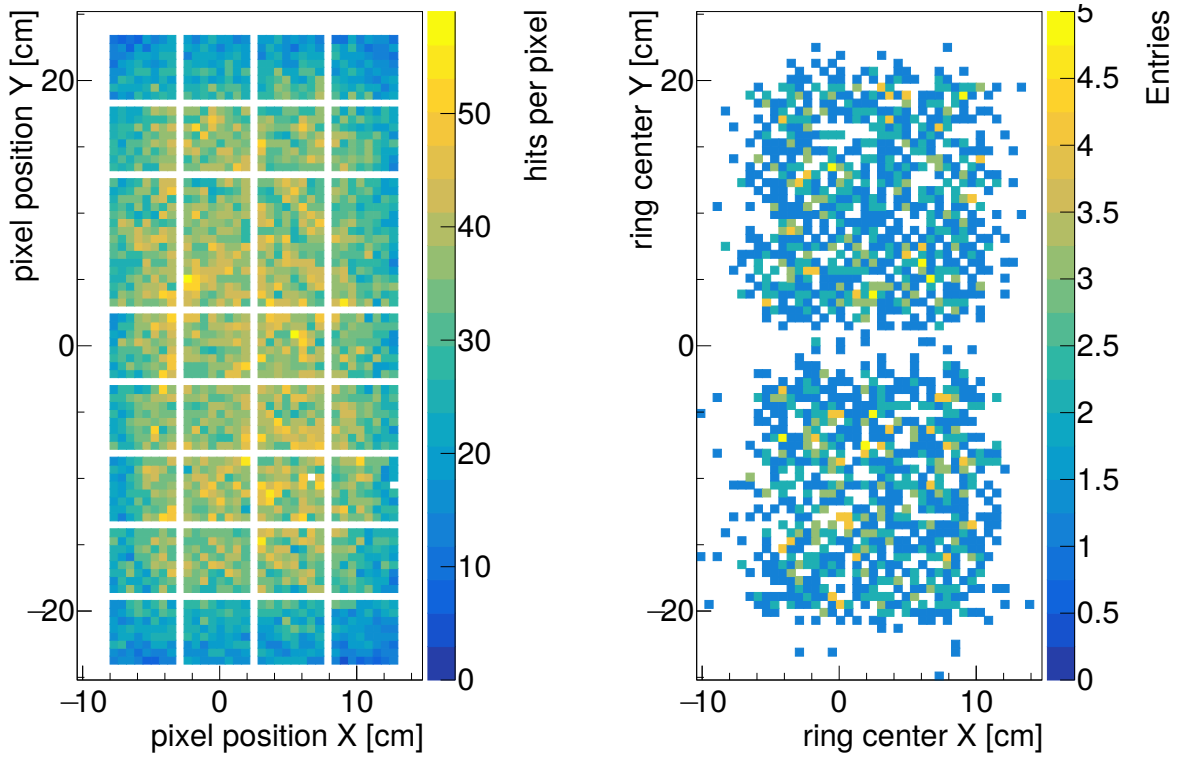

Figure 8.29: **(left)** Position dependant distribution of hits on the mRICH in timebased simulation with 45% collection efficiency and with a MAPMT entrance window. **(right)** Positions of the center of reconstructed rings from simulation. No preference towards positions in between MAPMTs as in the real data is seen.

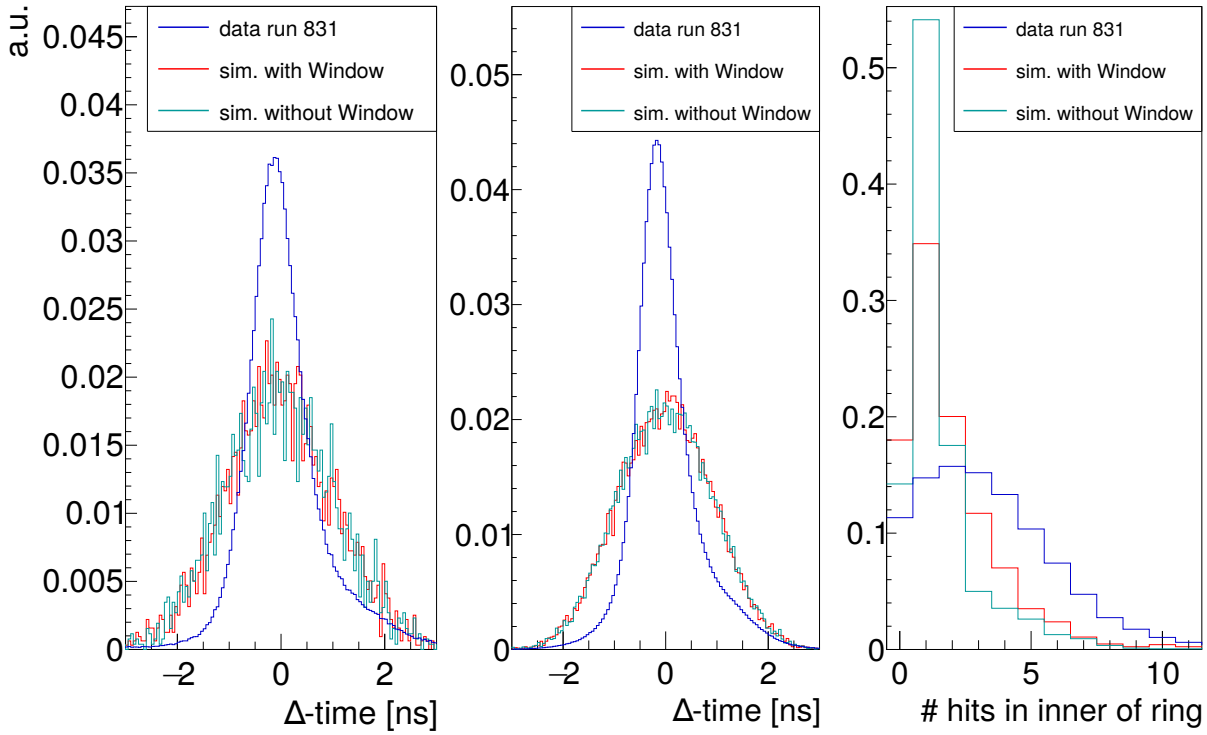

Figure 8.30: All histograms show data from simulations with (red) and without (cyan) an entrance window of the MAPMT as well as for measured data (blue) from run 831. **(left)** Δ-time distribution of hits inside a reconstructed ring. **(middle)** Δ-time distribution of hits matched to a reconstructed ring. **(right)** Number of hits inside a reconstructed ring.

Nevertheless, the simulation does not reproduce the problematic behaviour of the ring finder. No preference of positions of the ring centers in between MAPMTs is seen. This is the main difference of simulated results in comparison to the real data. Figure 8.30, right, shows the number of hits in the inner 80% of the radius of a reconstructed ring. A clear difference between the amount of hits inside real rings and simulated rings is visible and could explain the difference in the ring center distribution. In measured data the distribution peaks at 2-3 hits inside a ring with a tail up to 11 hits. Simulations peak at 1 hit in the center with a smaller tail up to 8 hits. The simulated distributions with and without an entrance window are significantly tighter than the measured data. The simulation with an entrance window shows an improvement towards the results from measurements. Unfortunately the discrepancy is still large. A possible explanation of this could be the dynode structure of the MAPMT as this is not implemented in detail in the simulation. As the dynode structure is just an active pad in the simulation, also the influence of hits to neighbouring pixels is not simulated properly. So many effects on the MAPMT itself from particles passing it and depositioning energy in it, are not well covered and could explain the higher amount of inner hits in the measured data.

Figure 8.30, left, shows the Δ-time distribution of the inner hits of a ring. As the simulated data does not suffer from timing imperfections between channels and backplanes, in contrast to the measured data, no ICD correction was applied to the data. The simulated distributions (red and cyan) have an increased width (σ=1.0 ns) compared to the measured data (σ=0.54 ns). Both simulated distributions have a mean value of -0.04 ns. The simulated data does not show the tail towards positive Δ-times that are ex-

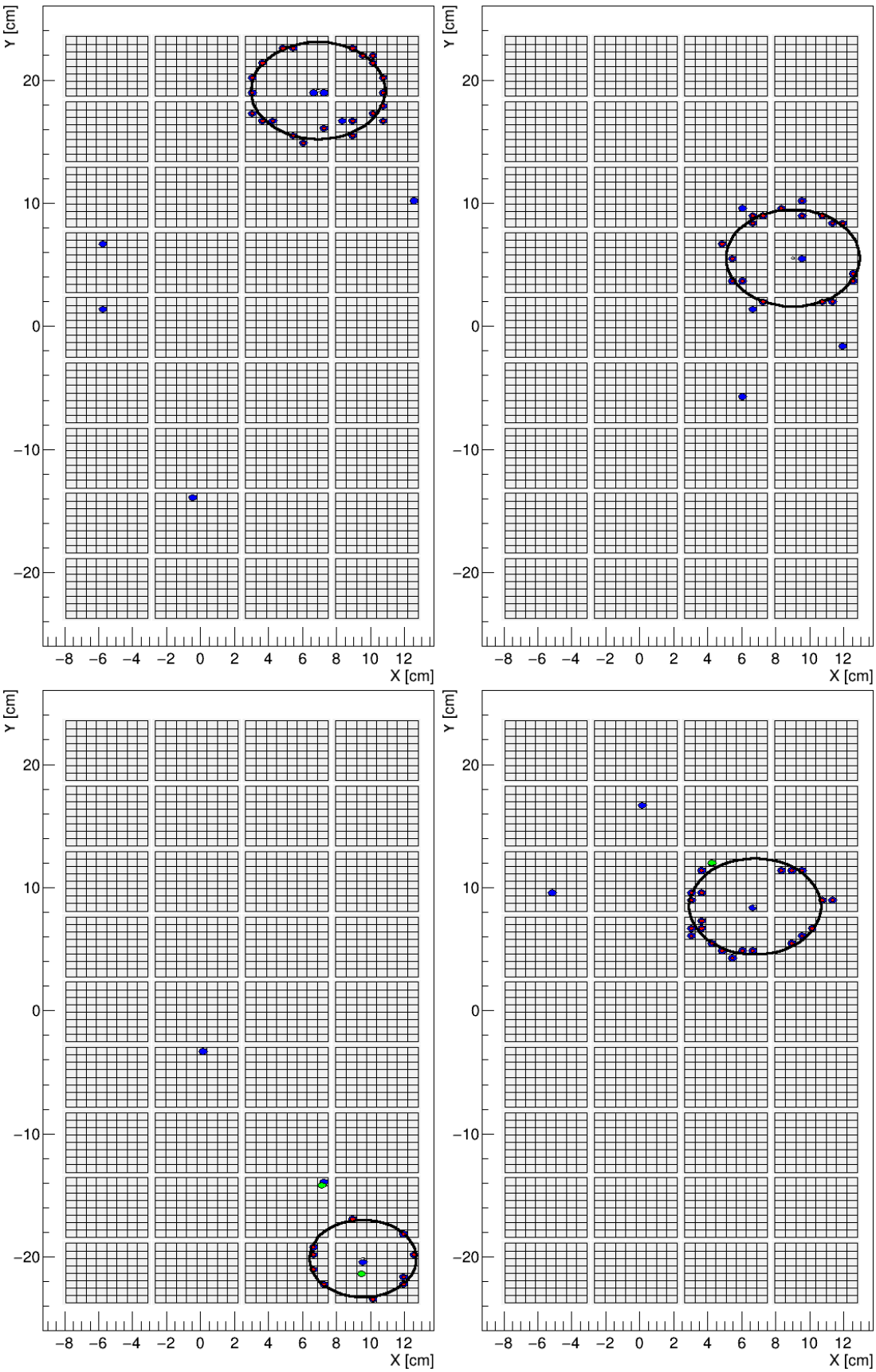

Figure 8.31: Simulated single event displays. **(top)** 45% collection efficiency without an entrance window. **(bottom)** 45% collection efficiency with an entrance window. The entrance window increases the center hits slightly.

pected to come from correlated effects as crosstalk. As the simulation does not cover crosstalk effects and the bad ring finding behaviour, the result matches the expectations. The middle of Figure 8.30 shows the same distribution for hits matched to a ring. The distribution shows the same behaviour as for inner hits. The mean is located at 0 and the simulated width is σ=0.9 ns compared to σ=0.39 ns in the measured data. This confirms the seen effect of an increase in width between hits matched to the ring itself and the inner hits of a ring. The overall larger width of the simulation results in a better time resolution of the real data, compared to the simulation.

Figure 8.31 shows single event displays for simulations with a collection efficiency of 45%. The top row shows simulations without an entrance window, whereas the bottom row shows results with an entrance window. No big difference between both cases is visible. Only a slight increase in the number of inner hits is visible. Furthermore the SED shows, that some of the rings have no track matched. Only the lower SEDs have a track (green point) near the ring. This is not related to the entrance window and just a coincidence of the shown SEDs. The lower left figure shows a ring with a track near its center. An additional track next to the ring matches a single hit in the mRICH and shows the passing of a particle in the detection plane, that did not create Cherenkov light in the aerogel. In the lower right SED the distance of the track to the ring center is in the order of the ring radius and not aligned with the ring center. Multiple scattering of the particles could play a role and lead to increased ring track distances, as seen in the measured data (Figure 8.18).

Figure 8.32 shows the simulated ring track distance. The ring track distance peaks at about 1 cm. The tail of the distribution goes up to above 30 cm but is very small. The right figure shows in addition the radius of the matched rings. The distribution shows

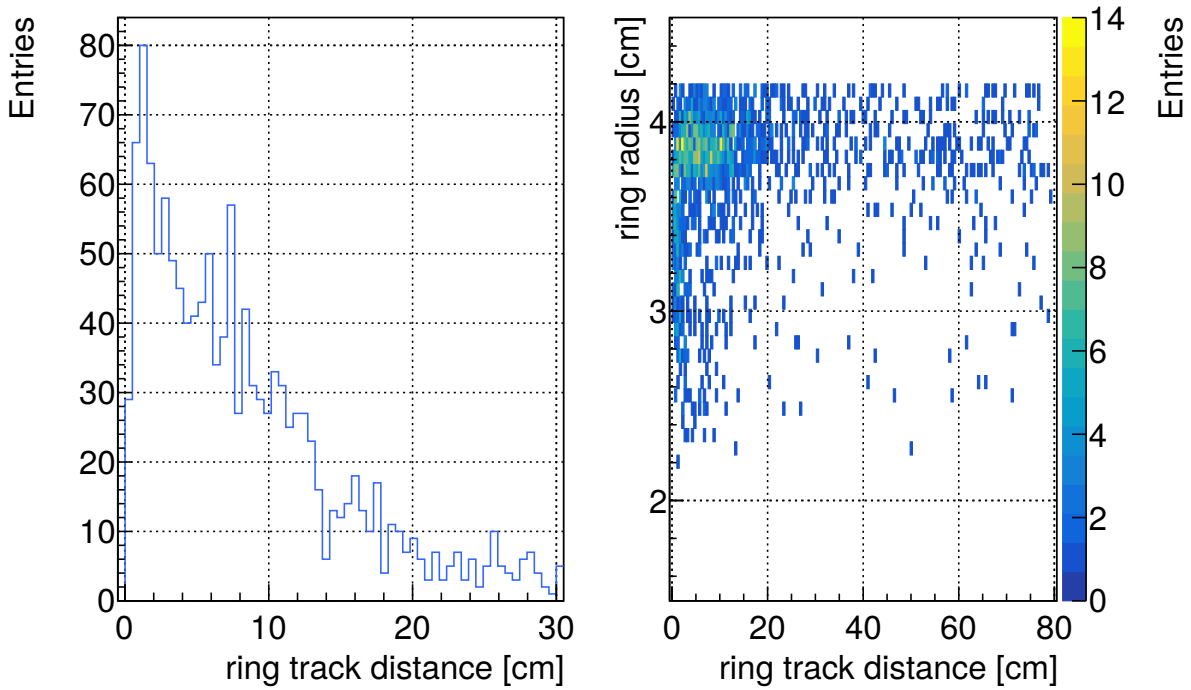

Figure 8.32: **(left)** Ring-track distance in simulation. A peak at a ring-track distance of 1 cm is seen. **(right)** Ring-track distance versus ring radius in simulation. A correlation between the radius and the distance is observed.

an enhancement at low distances and a radius of approx. 3.8 cm. The simulated track-ring distance is smaller than the measured. This difference could be well explained by the misbehaviour of the ring finder with an artificial positioning of ring centers in between MAPMTs that is not seen in the simulation.

Figure 8.33, left, shows the mTOF track distribution in the detection plane of the mRICH. The same selection criteria, the standard event building with 10 mRICH hits in addition, as in section 8.6 result in the shown distribution. A clear correlation in the position of the mRICH detector is visible and reproduces the results from the measurements.

The right figure shows the simulated distribution of the β values of the reconstructed mTOF tracks under different scenarios. The red line shows all tracks. An increase towards approx. β=0.9 with a following dip and a final peak at β=1 is seen. The same behaviour with overall less entries is seen for tracks with hits in the mRICH but without a found ring (green). The peak at β=1 is further reduced compared to the rest of the distribution. The blue and the purple distributions show tracks with a ring track distance of less than 120% of the ring radius and a ring radius between 2.0 cm and 4.2 cm. A clear peak near β=1 is visible. The start of the beta peak matches the expected β_{thr} = 0.95. The beta distributions reproduce the measured result with some limitations. The measured data from run 831 shows a more pronounced tail at lower β values. In addition, the peak at β for good rings is extended towards smaller β values, even below the threshold value. Therefore the measured data and primary the mTOF tracks from Figure 8.19 are not reproducing the simulation in all details. An uncertainty for tracks in the region of low β is probable, but also the difference in the collision system

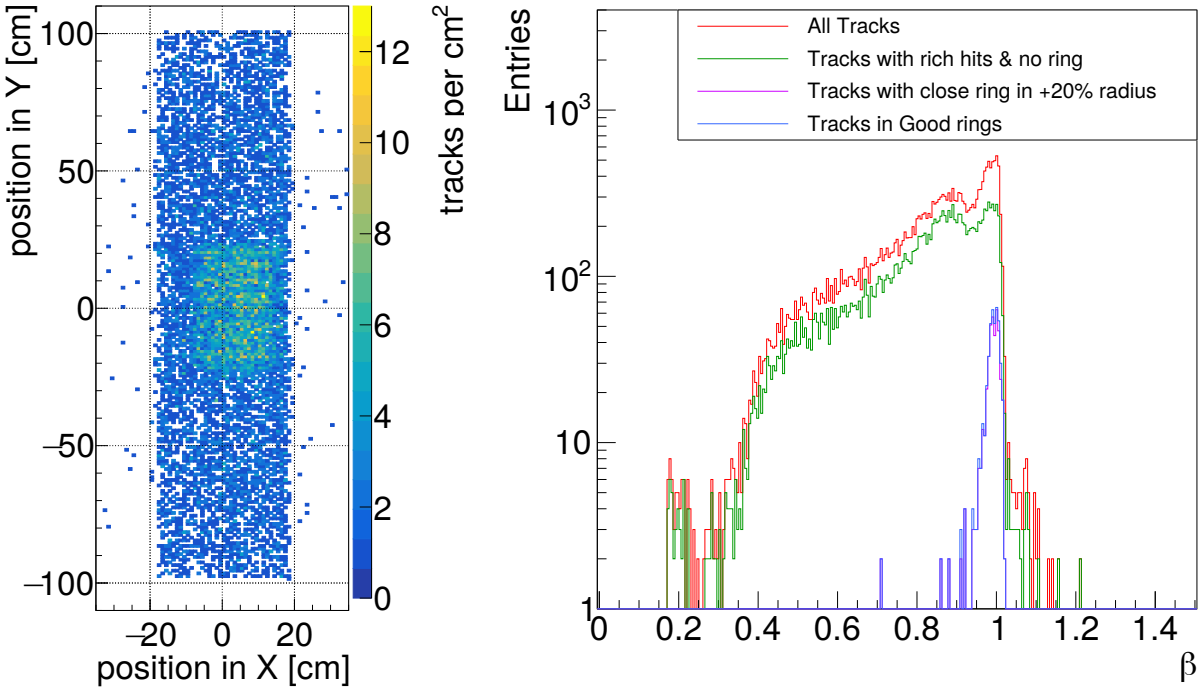

Figure 8.33: **(left)** Simulated mTOF tracks extrapolated to the mRICH position in Z. No further cuts than the standard event building and a requirement of minimum 10 hits in the mRICH result in a correlation (yellowish area) **(right)** Simulated β-distribution of mTOF tracks under different scenarios. The detection of a mRICH ring near a mTOF track or vice versa results in an enhancement in the beta distribution around β=1.

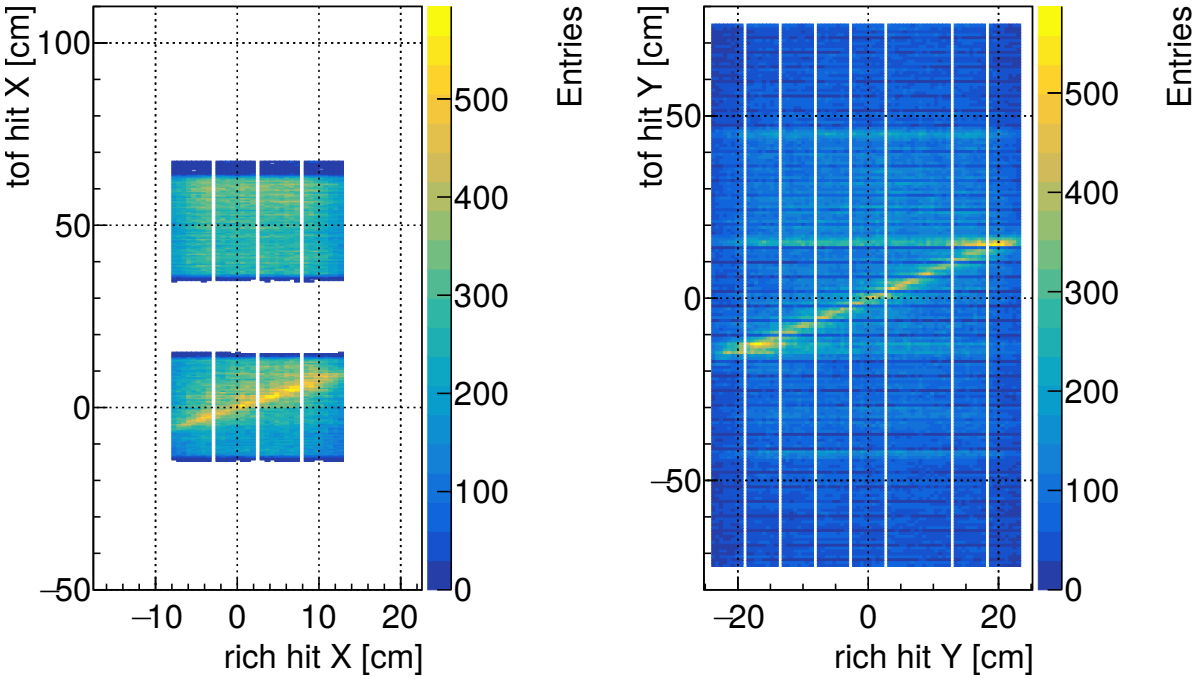

Figure 8.34: Spatial correlation in X **(left)** and Y **(right)** direction between mTOF hits and mRICH hits. Both correlations are very clean without a major background contamination.

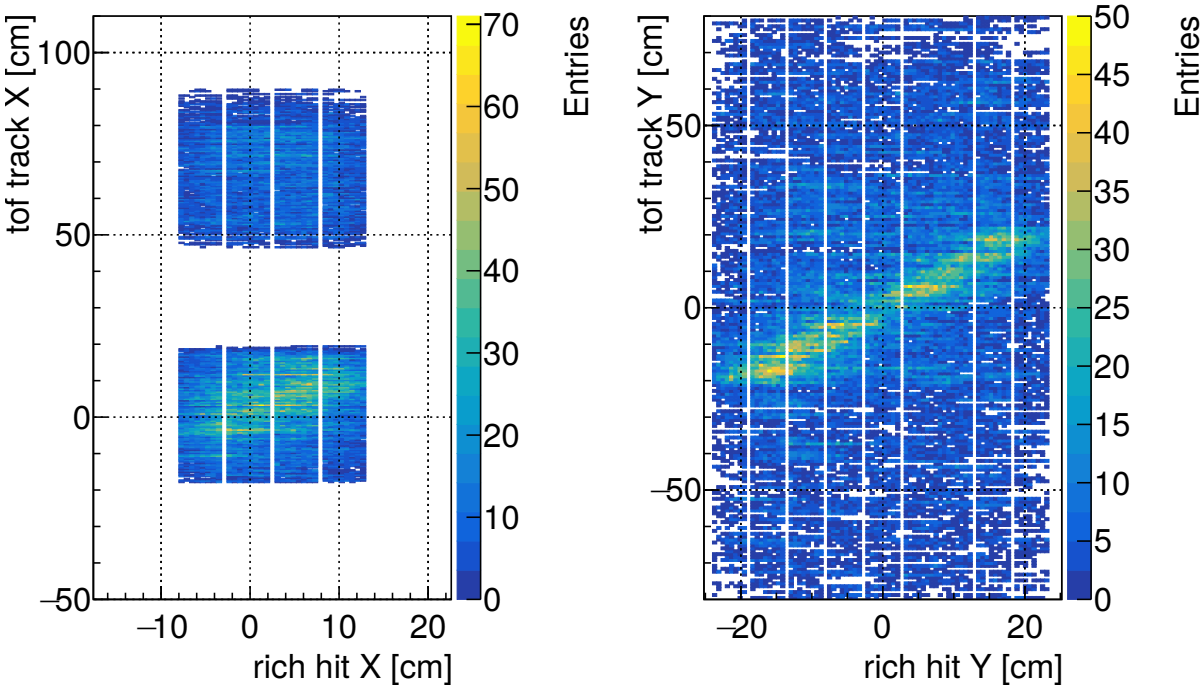

Figure 8.35: Spatial correlation in X **(left)** and Y **(right)** direction between mTOF tracks and mRICH hits after a cut of $0.9<\beta<1.1$. The width of the correlations is comparable to the measured data.

between simulation and measured data has to be taken into account. Nevertheless the agreement between simulation and reality at β=1 is promising. The matching between tracks and rings clearly selects tracks with β=1 and could be well used for PID and further physics analysis.

Figure 8.34 shows the simulated correlations between the mRICH hits and the mTOF hits in the same conditions as Figure 8.21. The simulated correlation shows less background contamination in X and contains the double stack, that was not used in the measurement of run 831. In Y direction, also the simulation shows the effect of overlapping modules in the mTOF with a clean correlation between both detectors.

The additional application of a cut on the beta value of the reconstructed tracks in the range of $0.9<\beta<1.1$ for the measured data cleaned the distribution from uncorrelated background (Figure 8.24). The same distribution for the simulation is shown in Figure 8.35. The correlations in X and Y are smoothed. The overlapping regions between two TOF modules in Y are not visible anymore. Due to statistical limitations, the correlation in X looks less clear, but is still visible. The application of the beta cut and the use of mTOF tracks broadens the distributions similar to the measured data. The correlations from the simulations are in very good agreement with the measurements in run 831.

All in all, the simulations of the mRICH and the mTOF could reproduce the measured data. Many of the investigated distributions, taken the difference in the collision system into account, match the measurements very well. Nevertheless, the behaviour of the ring finding differs between simulation and reality. A difference in the amount of hits in the inner of a ring is seen and could be the reason for the different behaviour. A new ring finder for the mRICH detector is currently under development and will hopefully solve the discrepancy.

CHAPTER 9

Summary and Outlook

This work focusses on the development of the front-end electronics and readout system for the Ring Imaging Cherenkov (RICH) detector of the upcoming CBM experiment with prior tests in the mCBM setup, and the upgrade of the HADES RICH. The FEE of both RICH detector systems in combination with the use of the same MAPMTs for the identification of single photons is the same, however with different requirements on the data acquisition. This allowed for a great synergy in the development of the RICH readout for both experiments.

The HADES RICH upgrade was based on a complete redesign of the photon detection camera as the previous photon detector was replaced by MAPMTs. The newly developed DiRICH board, based on the FPGA based time-to-digital converter (TDC) technology of the TRB collaboration of GSI, is the center readout piece of this upgraded RICH detector. Twelve DiRICH boards in combination with a combiner and power module are forming one of 74 backplanes of the new photo detection plane, each backplane hosting 6 MAPMTs. The plane is separated in two planes in beam direction. Additional sensors in the photo detection plane for temperature monitoring of the MAPMTs as well as special magnetic field sensors for a measurement of the influence of the HADES magnet on the MAPMTs are developed and integrated into the RICH control. Next to the integration of the FEE into the triggered HADES DAQ, a new powering scheme of pre-regulated voltages for the FEE and a single channel floating ground high voltage system is integrated to the HADES RICH detector.

Based on all the work for the upgrade of the RICH, a new RICH monitoring and control is developed and successfully used in the HADES 2019 Ag+Ag beamtime at 1.58 AGeV. The upgraded FEE shows a reliable and excellent performance in the beamtime and paves the way for a fruitful future of the HADES RICH as a key detector in the di-electron reconstruction at low energies, even still at the upcoming SIS100 facility.

The TrbNet based DiRICH backplane is the smallest unit of readout boards in the HADES RICH experiment and is equal to the readout electronics and smallest unit in the CBM RICH experiment. The knowledge and synergies from developing and running the triggered HADES RICH detector, so to say a large scale prototype for the CBM RICH, is integrated into the development of the free-streaming readout for CBM. Prior to CBM, the free-streaming readout is developed and tested in a small scale CBM setup at SIS18, mCBM. The mRICH detector is part of the mCBM experiment and thus serves as test facility under realistic conditions for the development of the free-streaming, TrbNet based CBM RICH readout. A first functional, free-streaming and synchronously operating readout based on the DiRICH-FEE is successfully implemented and integrated into the mCBM DAQ in phase-I with an AFCK board as the data processing board.

In order to safe space, the mRICH has been designed as a proximity focussing detector with 2×3 fully equipped backplanes and two aerogel blocks as radiator material. The successful development of the readout and the necessary upgrades in the FEE lead to the participation in several beamtimes of mCBM showing an excellent performance of the readout concept for phase-I.

The knowledge gained in phase-I is the starting point of the development of the phase-II readout of the mRICH detector, that is based on the future CBM readout concept and utilises the common readout board (CRI), based on an FLX-712/BNL-712 card. The first synchronisation between the CRI and the mRICH, based on the concept of phase-I has been implemented. Learning from phase-I and benefiting from the new CRI card, many items were improved as e.g. now the microtimeslice index distribution utilises special DLM messages instead of an external board. Further, a newly developed data transport concept between a combiner board as the smallest self running detector unit and the CRI has been implemented. The knowledge from the HADES RICH and the mRICH phase-I leads to new developments, solutions and ideas for the future CBM RICH readout with e.g. improvements in the temperature and magnetic field monitoring in the detector as well as improvements in the data generation on the FEE and CRI boards. The development of the CRI and CTS based combiner firmware are ongoing and improving towards a final reliable and stable readout in the free-streaming high rate concept of CBM. A mCBM beamtime in June/July 2021 with the CRI based phase-II readout proved the functionality of the new data transport concept of the mRICH detector.

The participation of the mRICH detector in beamtimes with the other mCBM subdetectors allows for correlation measurements between mCBM detectors in time and space as well as an analysis of the mRICH standalone performance. The results from the 2020 beamtime with a ^{208}Pb beam at 1.06 AGeV and a thin fixed Au target are confirming the full synchronisation between the mRICH as well as the T0 detector. The analysis of the spatial correlations results in excellent correlations between the mTOF and mRICH detector in all abstractions of the measured data. The analysis of the mRICH readout and beamtime performance confirms the expected functionality of the developed free-streaming readout system, even in conditions that are not ideal for the RICH detector.

Nevertheless the beamtimes revealed limitations of the mRICH system in terms of the ring finder due to additional hits in the center of a ring. An upgrade of the ring finder is underway and will further improve the performance of the mRICH detector. The change of the mRICH readout towards the mCBM phase-II concept with the CRI board as the key component is ongoing and will improve the rate capability. Major tests as well as more features and improvements are planed in upcoming testbeams. Moreover, the integration of the first concept of the mRICH phase-II into the full (m)CBM control interface and the upscaling towards the full CBM RICH will open new challenges and will demand for advanced solutions.

APPENDIX A

DCDC Converter and Noise Measurement

The DiRICH FEE is powered by one power module per backplane. The power module can be operated in two modes: The 4 voltages needed by the FEE are generated on the power module by DCDC converters or pre-regulated voltages are inserted in the board by a Weidmüller connector.

The use of DCDC converters has the advantage of a very light cabling and a clean detector with the best access to the FEE. Nevertheless, DCDC converters produce noise by its internal switching. The power modules with the DCDC converters are close to the FEE and therefore the radiated noise from the power module is visible in the TDC channels of the DiRICH boards. In order to improve the situation, a new external DCDC converter was developed. Different positions relative to the existing power module as well as the DiRICH boards have been measured.

A.1 New External DCDC Converter Board

Based on the DCDC converters of the existing power module, a new external DCDC converter board with several improvements for flexible use has been developed. The final DCDC board is shown in Figure A.1. The board utilises four different ViCor PI33**-**-LGIZ ICs as DCDC converters with additional Murata BNX027H01L filters. A DC voltage with 8 V to 36 V and a maximum of 8 A (fuse) can be connected as input. The input voltage is filtered and deployed to the four DCDC ICs. The voltage and current at the input of the board are monitored by dedicated ICs. An Atmega32U4 microcontroller is used for the readout of the power monitoring, as well as for the selection of the output voltages of the DCDC converters. The microcontroller is connected to four 8-bit open drain shift registers. They control the resistance at the feedback of the DCDC converters and therefore control the final output voltage. The shift register are relatively simple circuits and minimize the risk of problems on the output voltage in radiation environments.

The Atmega32U4 is a microcontroller, that is well known in the TrbNet related electronics. It provides a USB connection, can be operated at 3.3 V with 8 MHz and has a variety of general purpose input-output (GPIO) pins. The microcontroller communicates via UART to other boards. A chaining of several DCDC converter boards via pin headers is foreseen and up to 16 DCDC boards can be controlled with one connection. The first DCDC board of such a chain is connected to a dedicated board, that provides the interface to networks or computers. The last board in a chain closes the loop with

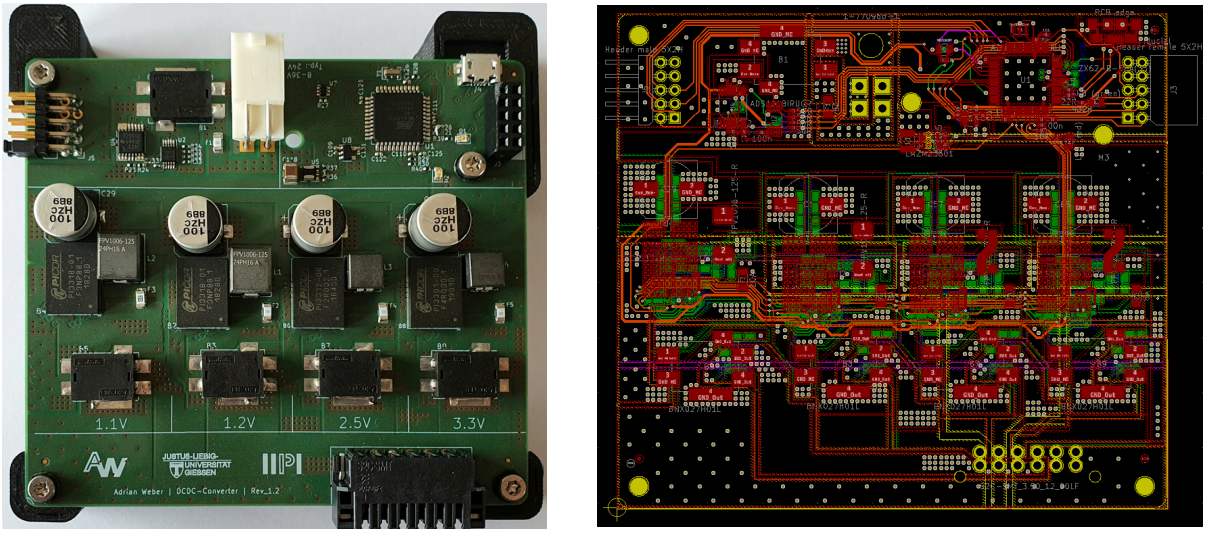

Figure A.1: **(left)** Photography of the DCDC converter board as it is mounted in mCBM in phase-II. **(right)** Layers of the DCDC converter board in KiCAD.

a jumper on the pin header. An incoming command from the communication board is transmitted to the first board in the chain. This board checks whether the command is addressed to it or not. In case it is not addressed, the command is forwarded to the next board. In case the board matches the address from the command, the command is executed and an answer is transmitted through the chain back to the communication board.

The communication boards pin header is compatible to the FTDI board of the TrbNet group, as well as a dedicated Ethernet or Wifi board, based on an ESP32. Both communication boards are powered via the DCDC converter board and allow for a very flexible usage in different environments.

A.1.1 Protocol Definition

The communication is based on a defined protocol that was later also adapted for the use with the HADES MDC power modules. The data format is given by `XuuGcRvvvv` (see Table A.1). The data format has to end with "\n".

All in all 10 characters are combined to form a valid command. E.g. the command "RF2012FE51\n" would be valid.

Value	Description
X	command (write: W, read: R, answer: A etc.)
uu	controller number (Hex value)
G	group number (to talk to all channels, that belong together)
c	channel number in the group (Hex value)
R	register (Hex value)
vvvv	16 bit value

Table A.1: Definition of the protocol for a chained DCDC converter operation.

A.1.2 Register Definition

The DCDC board has 7 registers that are accessed via the previously defined protocol. Next to the setting of the voltage of each channel, the input voltage and current are accessible. The temperature of the board, the firmware version as well as a LED and a switch for a loop back are available. Finally, an offset for the correction of the measured current is available.

Value	Description
0	DCDC on/off $\rightarrow$ not available
1	DCDC set voltage adjustment resistors
2	input voltage V
3	input current C
4	temperature
5	[15:4] firmware; [3:2] reserved; [1] switch; [0] LED
6	current offset

Table A.2: Definition of all seven registers of the new DCDC converter board.

A.2 Schematics

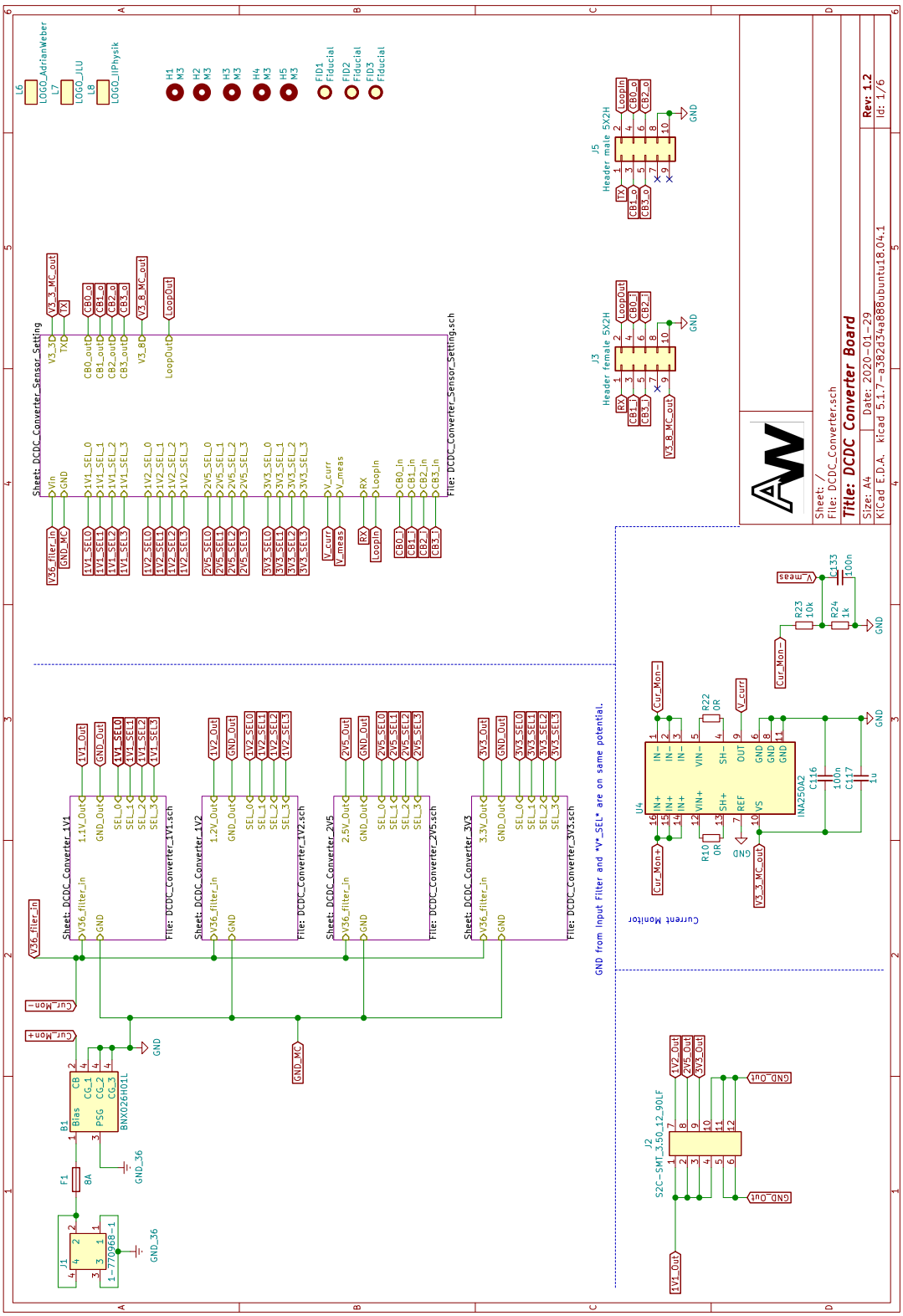

Figure A.2: Main page of hierarchical schematic of DCDC converter board.

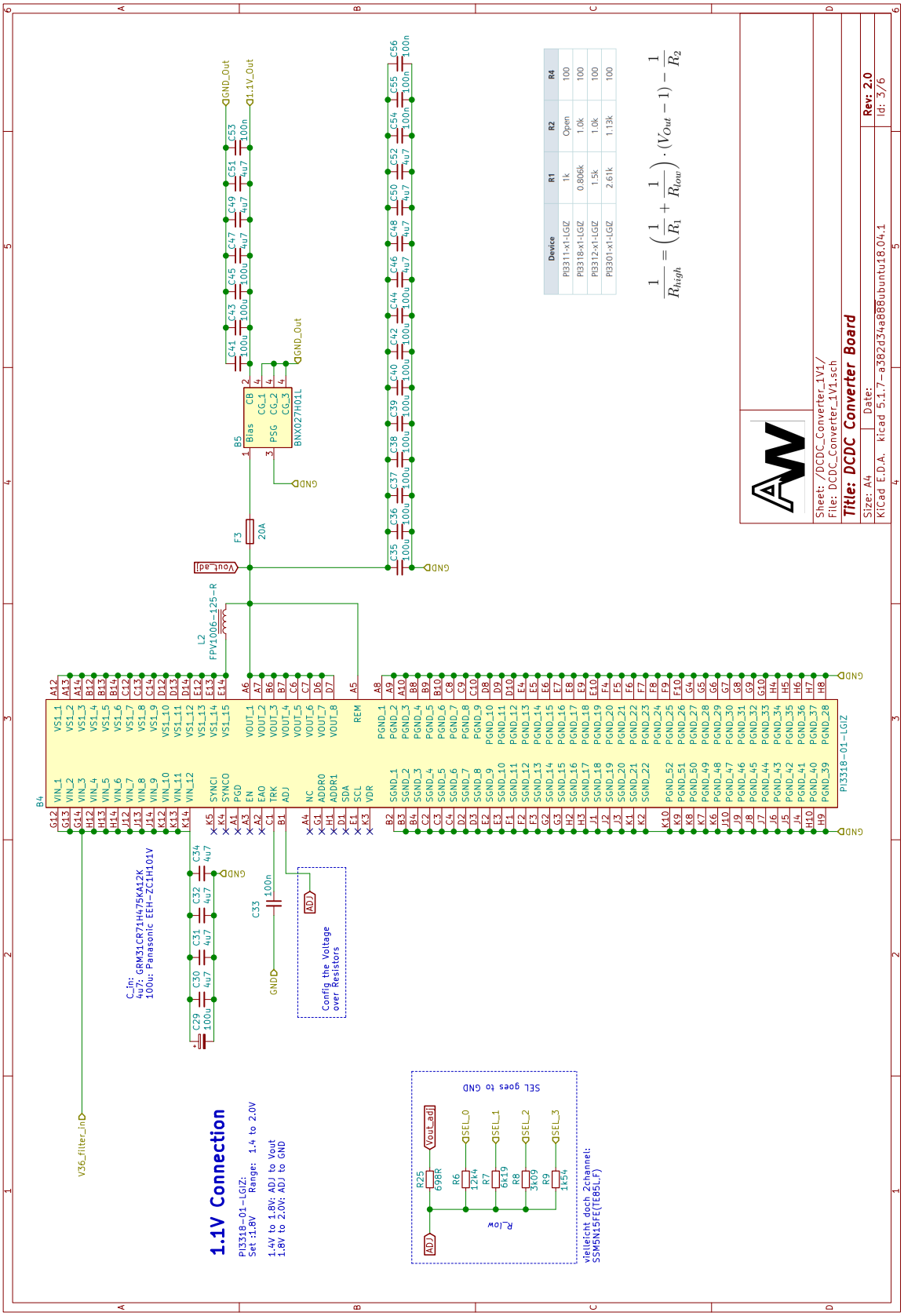

Figure A.3: 1.1 V conversion in hierarchical schematic of DCDC converter board.

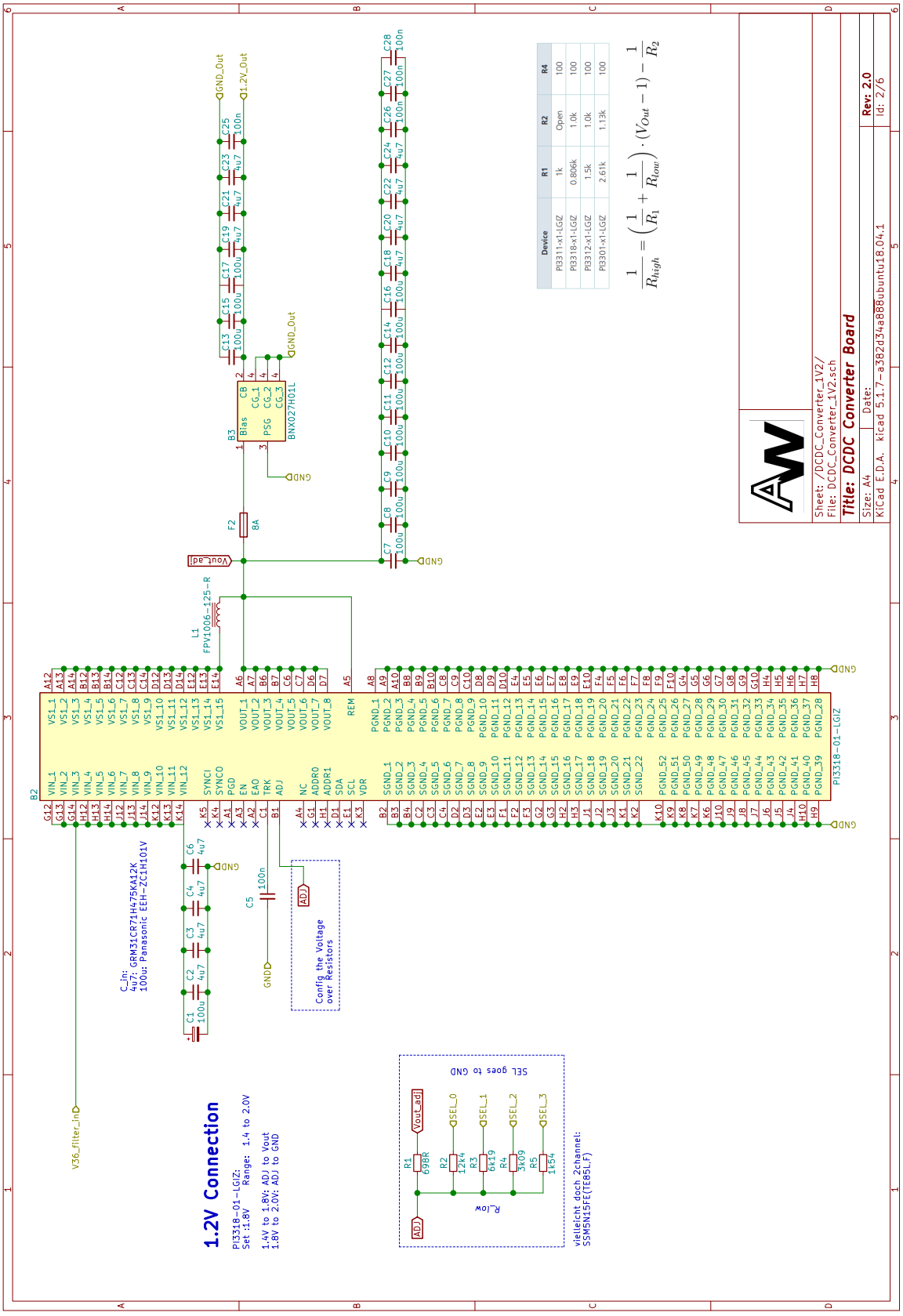

Figure A.4: 1.2 V conversion in hierarchical schematic of DCDC converter board.

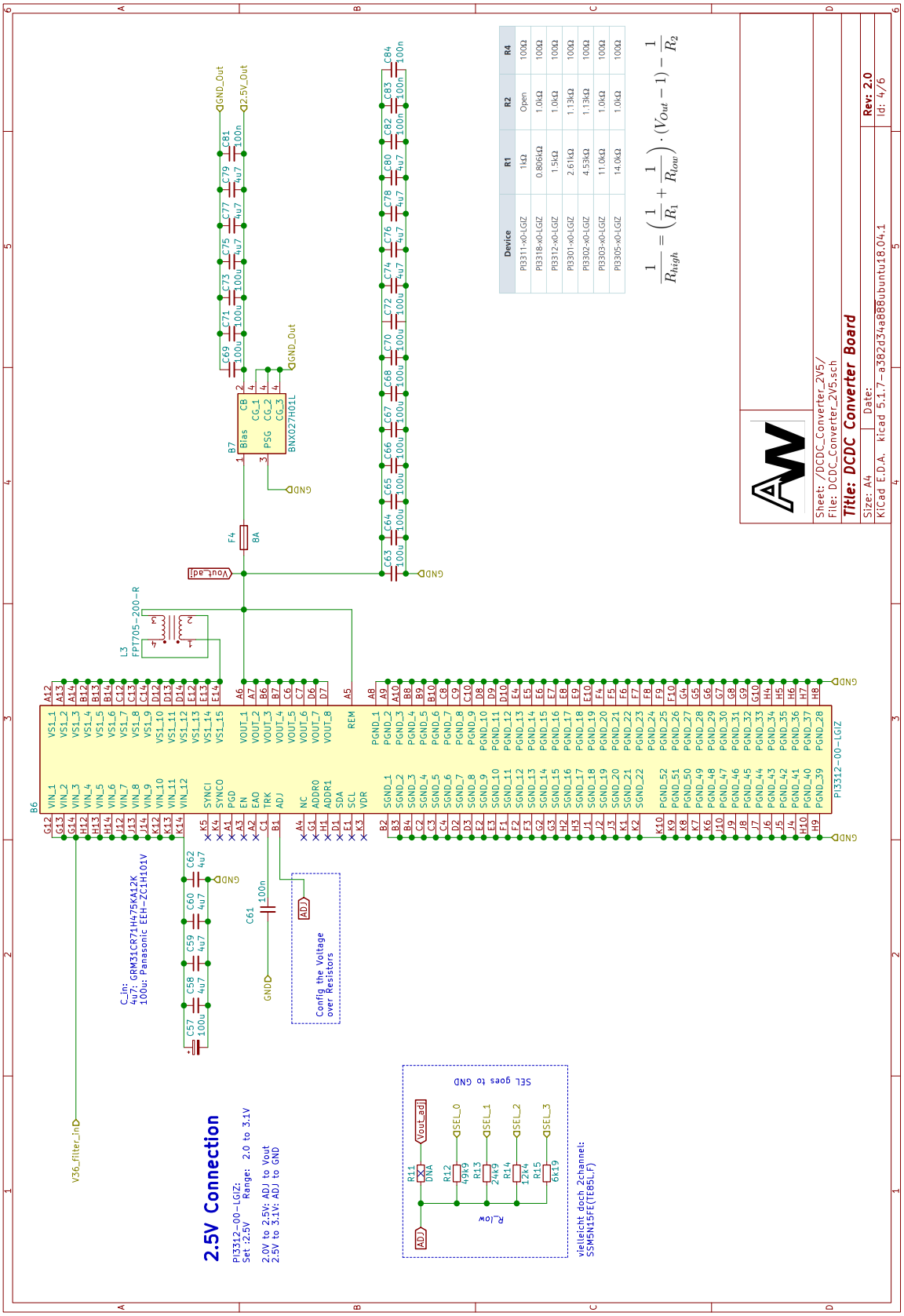

Device	R1	R2	R4
PI3311-x0-LGIZ	1kΩ	Open	100Ω
PI3318-x0-LGIZ	0.806kΩ	1.0kΩ	100Ω
PI3312-x0-LGIZ	1.5kΩ	1.0kΩ	100Ω
PI3301-x0-LGIZ	2.61kΩ	1.13kΩ	100Ω
PI3302-x0-LGIZ	4.53kΩ	1.13kΩ	100Ω
PI3303-x0-LGIZ	11.0kΩ	1.0kΩ	100Ω
PI3305-x0-LGIZ	14.0kΩ	1.0kΩ	100Ω

Figure A.5: 2.5 V conversion in hierarchical schematic of DCDC converter board.

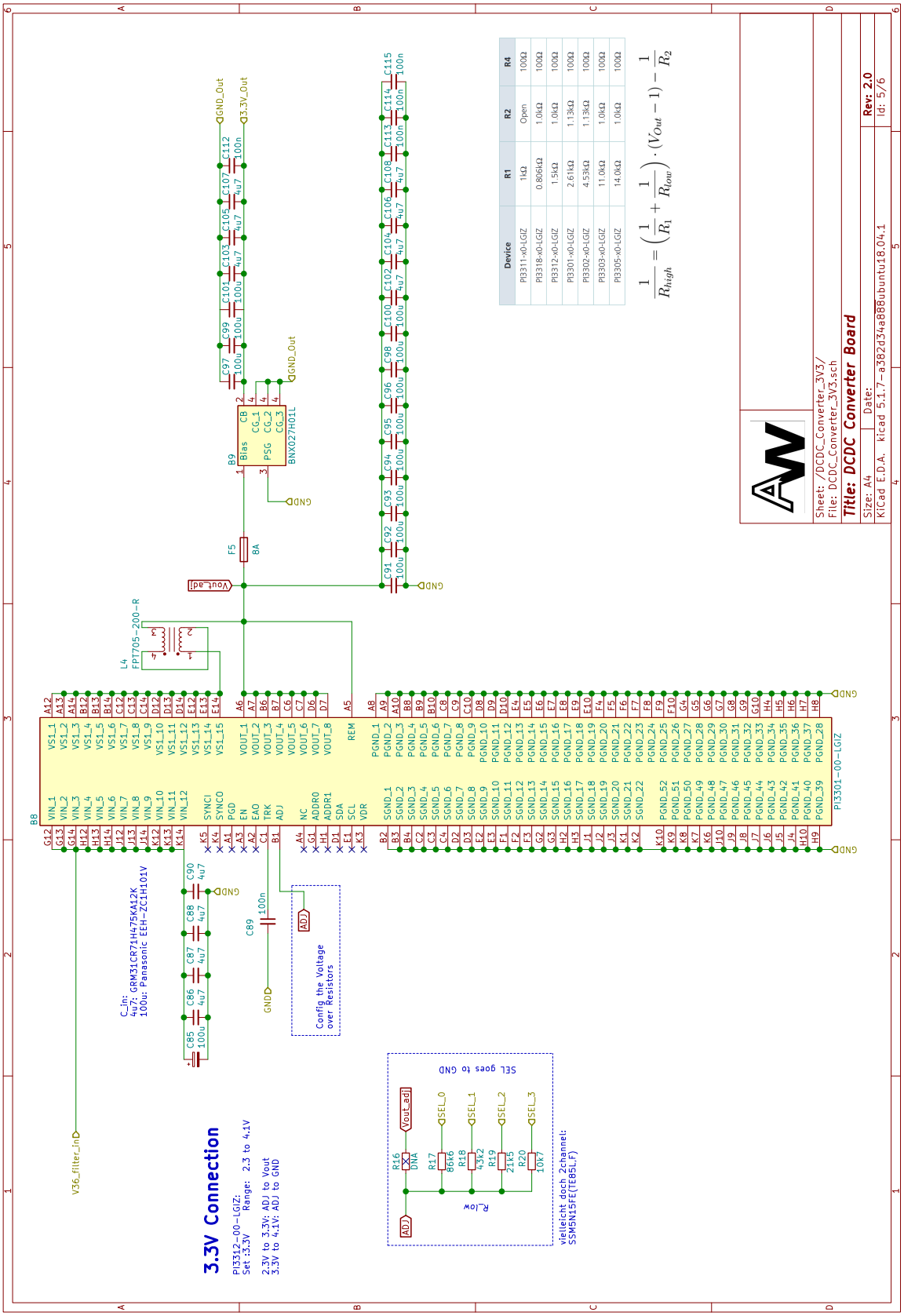

Figure A.6: 3.3 V conversion in hierarchical schematic of DCDC converter board.

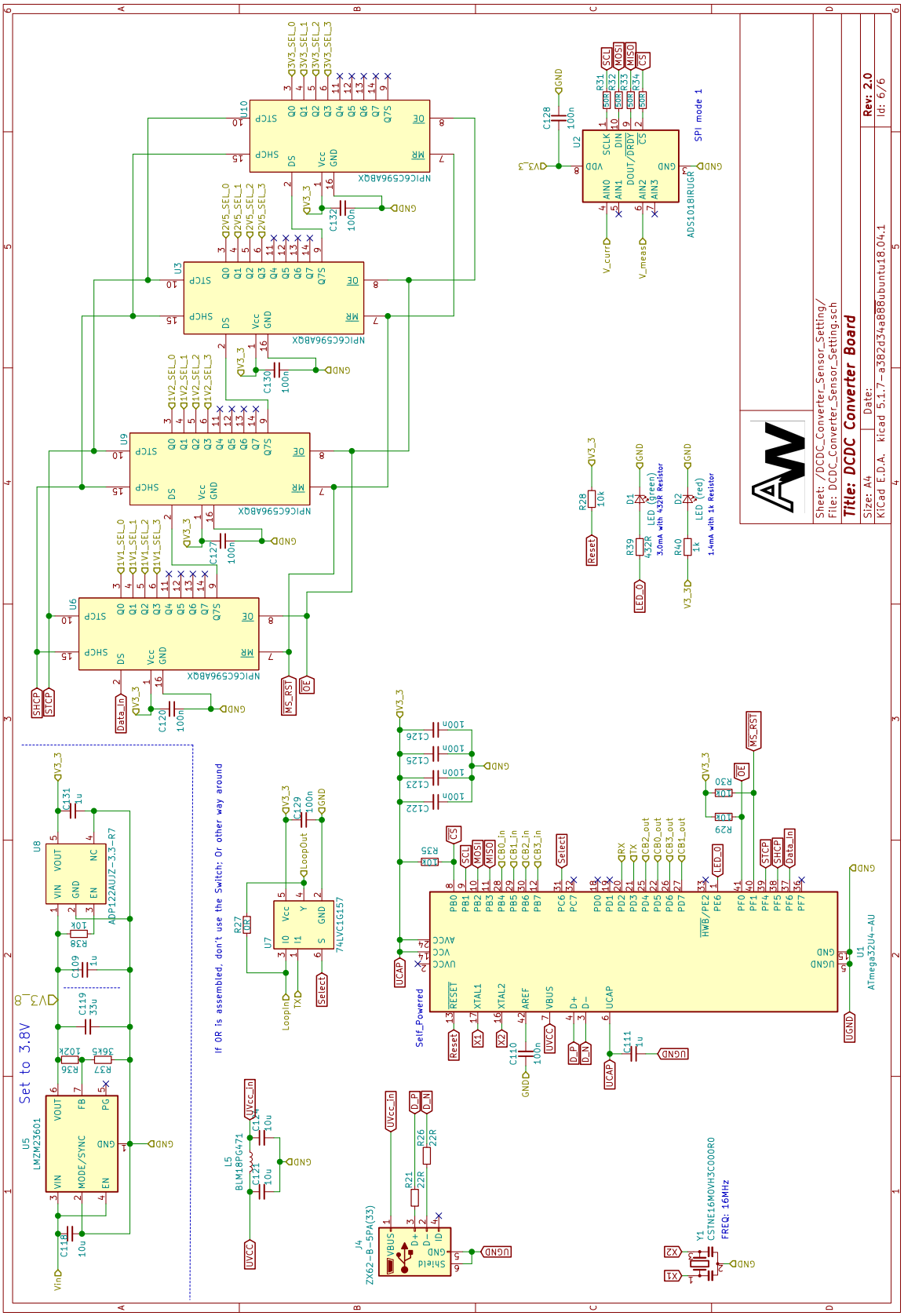

Figure A.7: Microcontroller and monitoring in hierarchical schematic of DCDC converter board.

A.3 Measurements of the Noise Band Width with Different Setups

The new DCDC converter board can be used to supply the existing power module with pre-regulated voltages. A test setup with a few DiRICH boards on a backplane with an old power module and the new DCDC converter board was installed and measurements were done. The DiRICH boards have small differences in the capacitance of the inputs as indicated in the legend of Figure A.8. Different lengths of the cable between the power module and the DCDC converter board as well as different positions and distances of the DCDC converter board to the power module were measured. In addition, the orientation of the DCDC ICs were changed and measured. The noise on the DiRICH modules was measured with a baseline scan. The average noise band width at the half of the distribution (half noise band width) is analysed and presented in Figure A.8 as an indicator for the noise.

First of all the measurements confirm the expectation, that the noise is mostly radiated via air, as longer cables are showing just a small influence, but different positioning relative to the DiRICH board shows a clear improvement. The abscissa of Figure A.8 represents different settings of e.g. distances of power module to external DCDC converters. The measurements show a clear improvement if the DCDC converters are more far away from the backplane. Especially an enhancement of the distance in Z-direction out of the DiRICH plane shows promising results. In addition, an increase of the supply voltage has only a minor effect in the noise behaviour of the power module.

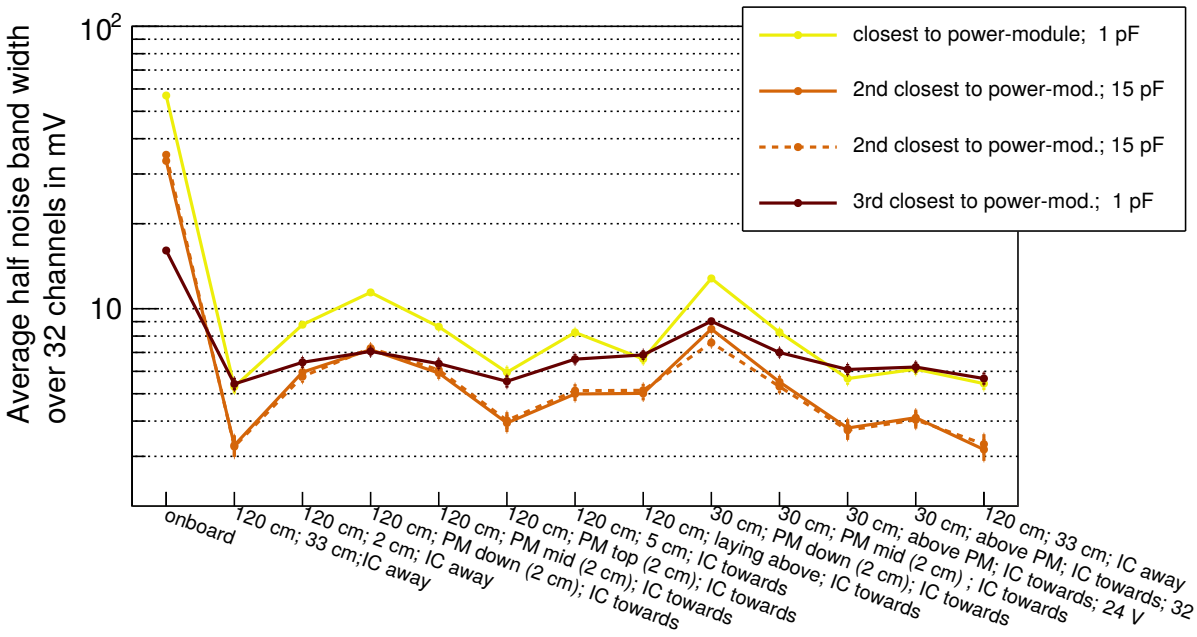

Figure A.8: Average half noise band width over all 32 channels of a DiRICH in different measurement setups. Measurements with different cable length of 120 cm and 30 cm, supply voltage setting of 24 V and 32 V and positioning relative to the power module (distances of 2 cm or 5 cm; same high as power module; mid of power module; above power module) were performed. The pointing of the ICs was changed between pointing away and towards the power module.

Based on these measurement and the steadily improvements on the available DCDC converter ICs, a new generation of power modules is under development. A first version of a new power module was tested in the June 2021 beamtime of mCBM and shows a very low noise level, comparable to the external DCDC converters (Figure 7.9 shows the ToT of a channel of a DiRICH, powered by a new power module).

APPENDIX B

Study of the Magnetic Field Sensor Board

A custom sensor board for the mount on the inner HADES RICH spokes was developed for the measurement of the magnetic field near the MAPMTs. In preparation of the mounting inside the RICH detector, the different boards have been measured in the laboratory with the controlled magnetic field of a Helmholtz coil. The measurements were performed in a climate chamber under controlled temperature to study the influence of a temperature change on the magnetic field sensors as well as to test their internal correction.

Figure B.1: Photography of the magnetic field sensor board with labels of the main ICs: red labels the Melexis MLX90393 magentic field sensor and the cyan label is the ATmega168PA microcontroller.

The PCB is shown in Figure B.1. It is equipped with Melexis MLX90393 3-axis magnetic field sensors and transmits the measured fields and temperatures via UART. For more details on the protocol see [130].

All measurements of the sensor boards were performed with additional holding structures to fix the PCBs in the middle of the Helmholtz coil. The structures allow for rotations and the change of the angle to the coil by 90°. Figure B.2 shows the PCB with its readout cabling in the coil inside the climate chamber. The temperature was increased in steps of 5°C from 10°C to 40°C with currents of the Helmholtz coil between 0.5 A and 5 A (see Figure B.3 to Figure B.6). In addition, measurements of all PCBs were performed with currents of the coils of 1 A, 2 A and 4 A, resulting in a calculated magnetic field of 739.05 µT, 1478.1 µT respectively 2956.2 µT (see Figure B.7 as an example).

Figure B.3 to Figure B.5 show the behaviour of the X-, Y- and Z-axis of the magnetic field sensors at 1 A, 2 A and 4 A coil current and a change in temperature. A grey band is drawn to show a ±7% error region around the calculated magnetic field at the coil current. The sensors `0xC` and `0xD`, the closest to the pin header connection, are configured with an internal temperature compensation. The sensors `0xE` and `0xF` (the numbers are the I2C addresses of the sensors) are configured without the compensation of temperature effects. The measured data shows a good performance of the internal temperature compensation. Without compensation, a linear dependency between the temperature and the measured field is seen. The compensation flattens the curve.

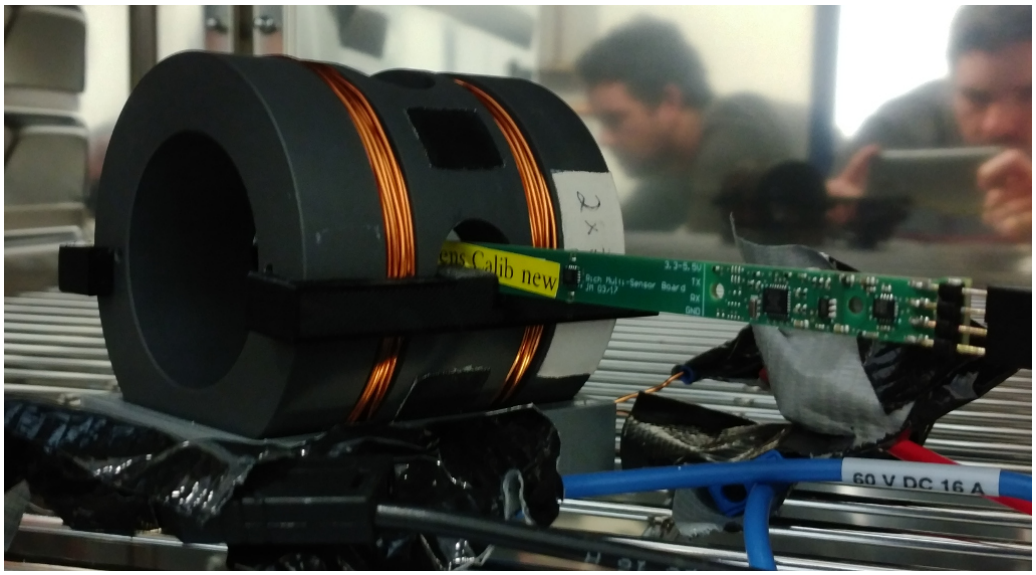

Figure B.2: Photography of the Helmholtz coil with a sensor board in measurement position inside the climate chamber.

Nevertheless a slight overcorrection is seen, as the magnetic field shows a very slight negative slope. The behaviour of the compensation is similar for all three axis of the sensors.

In addition to the temperature dependence, the linearity of the measured magnetic field was investigated. Figure B.6 shows the measured magnetic field in Y-direction of a

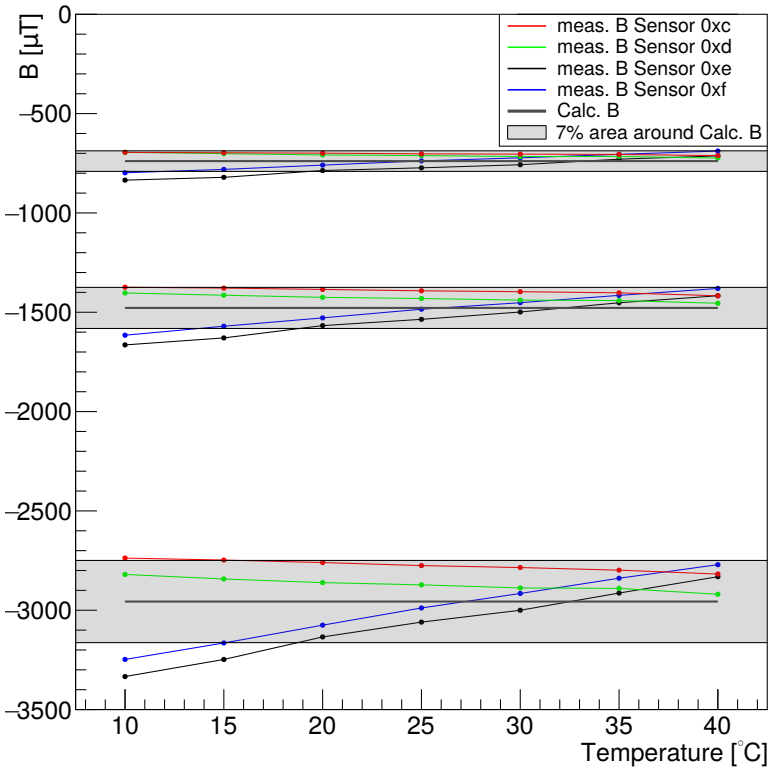

Figure B.3: Temperature dependency of the measured magnetic field in the X-axis with (0xC,0xD) and without (0xE,0xF) temperature effect compensation.

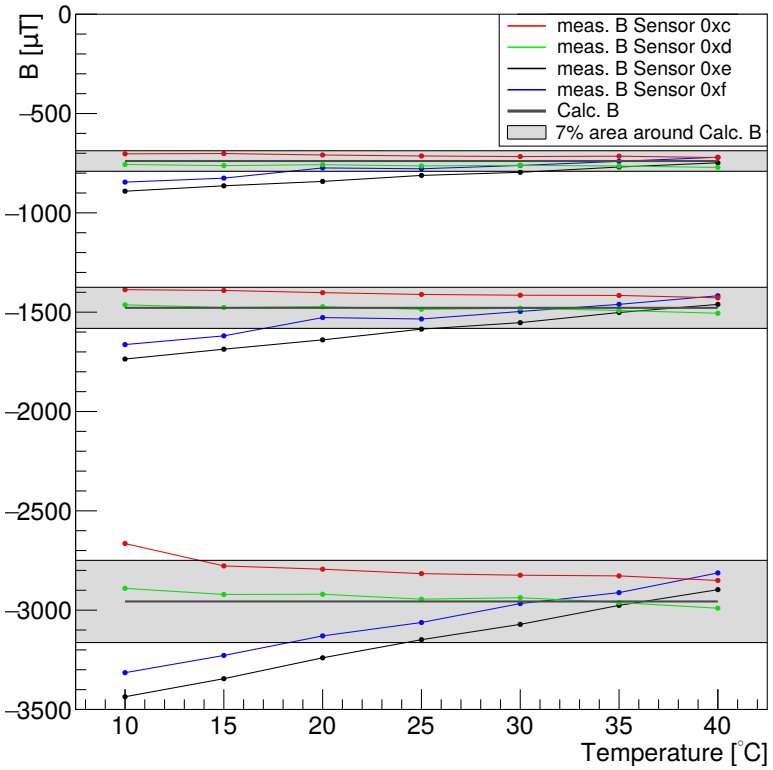

Figure B.4: Temperature dependency of the measured magnetic field in the Y-axis with (0xC,0xD) and without (0xE,0xF) temperature effect compensation.

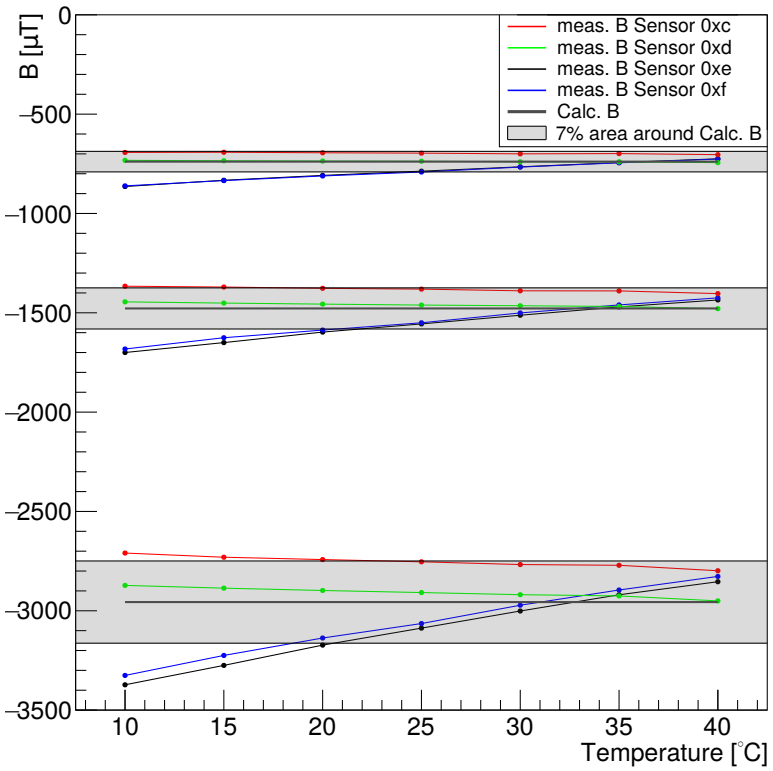

Figure B.5: Temperature dependency of the measured magnetic field in the Z-axis with (0xC,0xD) and without (0xE,0xF) temperature effect compensation.

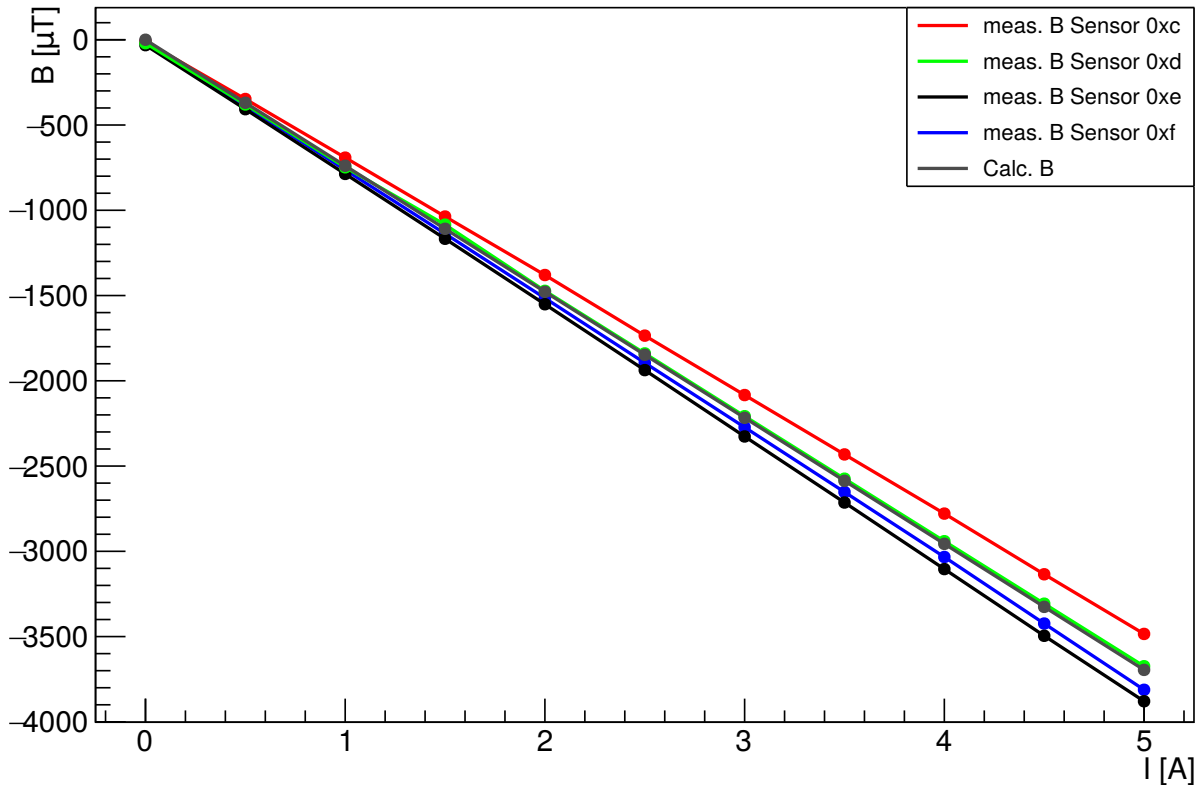

Figure B.6: Magnetic field measurement in steps of 500 mA coil current in Y-direction of Sensor 00 with a constant temperature of 26°C. The sensors show a linear increase of the field with increased currents. Nevertheless the different sensors on a PCB show slightly different results.

sensor at a constant temperature of 26°C. This temperature is very close to the radiator gas temperature of the RICH detector and is therefore a good measurement point for a check of the behaviour in the detector. The linearity of the measured magnetic field is in agreement with the calculated field of the coil. The four sensors mounted on the PCB are fluctuating around the calculated value.

Last but not least, the measured magnetic field of all 3-axis of the sensors of PCB 01 are shown in Figure B.7. The figure shows the difference of the values with and without a correction of the magnetic field of the earth. The magnetic field of the earth was measured without the field of the Helmholtz coil and later it is subtracted from all 3 axis of the measured values with the Helmholtz coil.

In case the magnetic field of the earth is taken into account and the measured values are corrected for it, the data improves and the values are matching the calculated values in the ±7% error bar. The corrected values are aligning with a trend towards lower values than the calculated field. This could be explained by a systematic uncertainty of the calculated field due to uncertainties of the measured coil radius as well as the number of windings of the coil, that are needed for the calculation of the magnetic field of the Helmholtz coil.

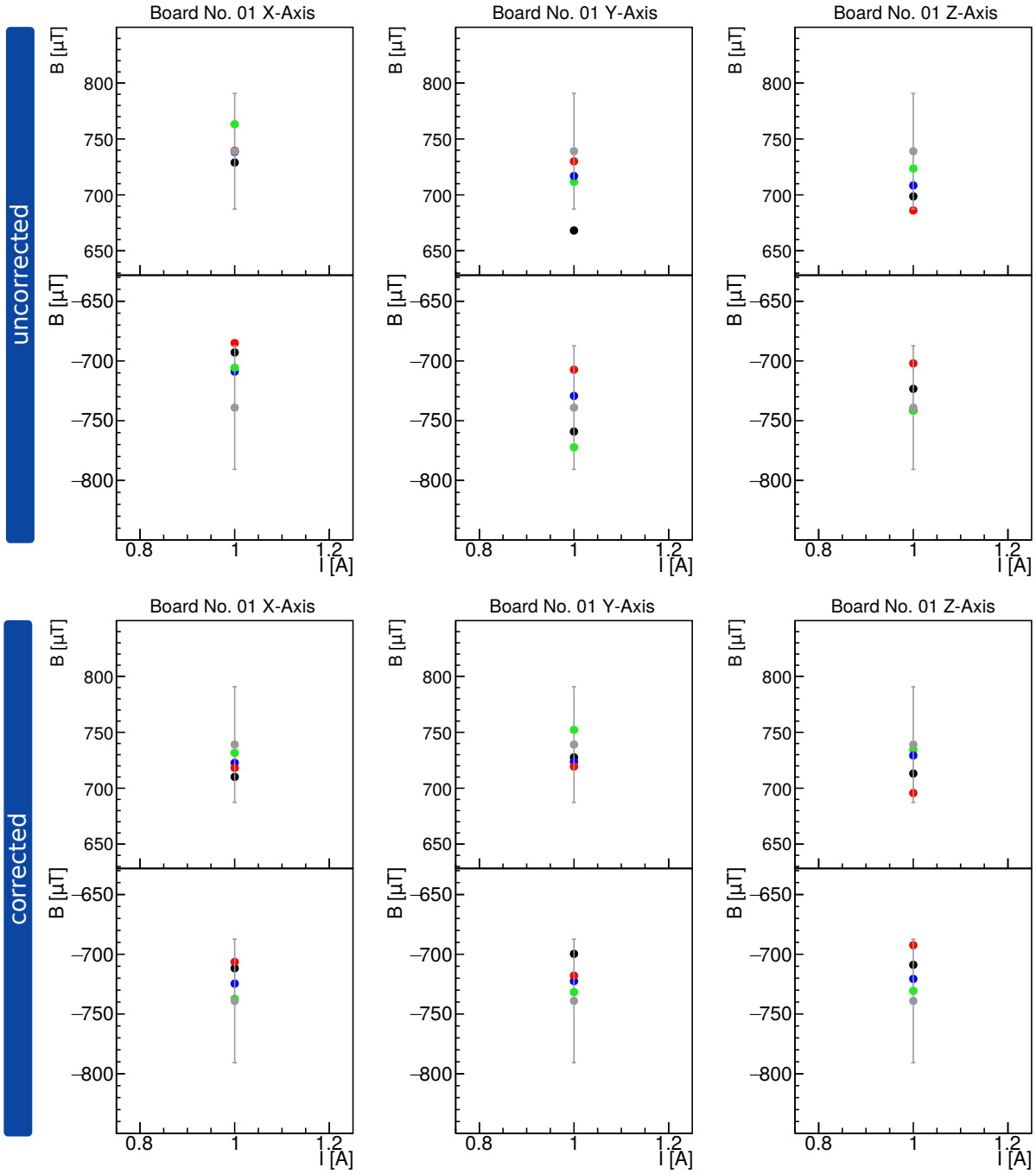

Figure B.7: Measured magnetic field of PCB 01 at 1 A coil current in all 3-axis with and without correction of the magnetic field of the earth.

APPENDIX C

Interlock PCB

The HADES RICH detector is equipped with a very simple interlock board. It is used to switch two relays that are connected in series to trigger the internal interlock of the 3.3 V low voltage power supply. The PCB uses a NUD3105 to control the relays as it already provides the free wheeling diode needed for a secure relay operation and has an included MOSFET for the control. This allows the control of the relays with the 2.5 V from the FPGA output pin. Two relays are used for the case of a stuck relay. In this case, the second can still control the full interlock.

Version 1 of the interlock board is shown in Figure C.1. A 2.5 V signal line from the interlock logic inside the sensor FPGA directly controls the NUD3105 and furthermore the relays. A combination of a resistor and a capacitor is used to prevent for an accidental trigger of the interlock while a reboot of the FPGA. The schematic of version 1 of the interlock board, as it is installed in HADES, is shown in Figure C.3.

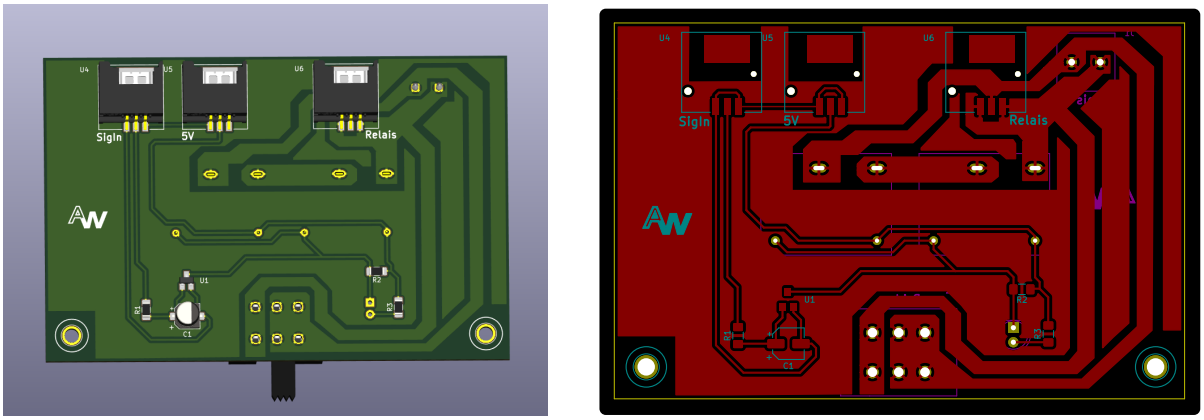

Figure C.1: **(left)** 3D rendering of the interlock board version 1 as it is installed in HADES. **(right)** Layers of the interlock board in KiCAD.

Version 2 of the interlock is an improvement for possible FPGA problems by a watchdog feature. The FPGA sends a sequence of high and low on the signal line to keep the interlock inactive. In case the FPGA is not generating rising edges anymore for a time of ≈1.1 sec, a retriggered NE555 switches its output into a low state. The control of the relays itself is similar to version 1. A resistor-capacitor combination delays the activation of the interlock, too. In addition to the watchdog feature, the switch for a manual deactivation of the board was changed. With version 2, the switch is changed to a barrel jack connector. The expert who wants to deactivate the board, needs a separate plug and the risk of a deactivation by an accidentally moved switch is reduced. The schematic of version 2 of the interlock board is shown in Figure C.4.

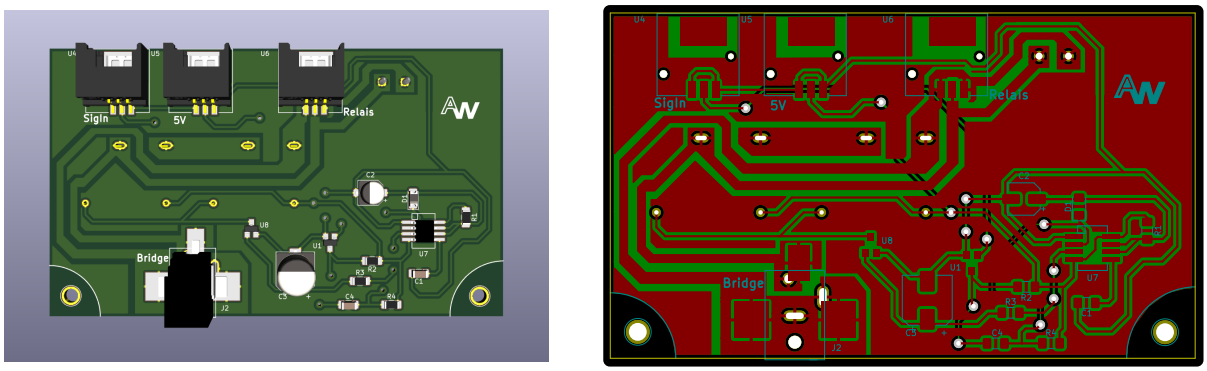

Figure C.2: **(left)** 3D rendering of the interlock board version 2. **(right)** Layers of the interlock board in KiCAD.

C.1 Schematic Version 1

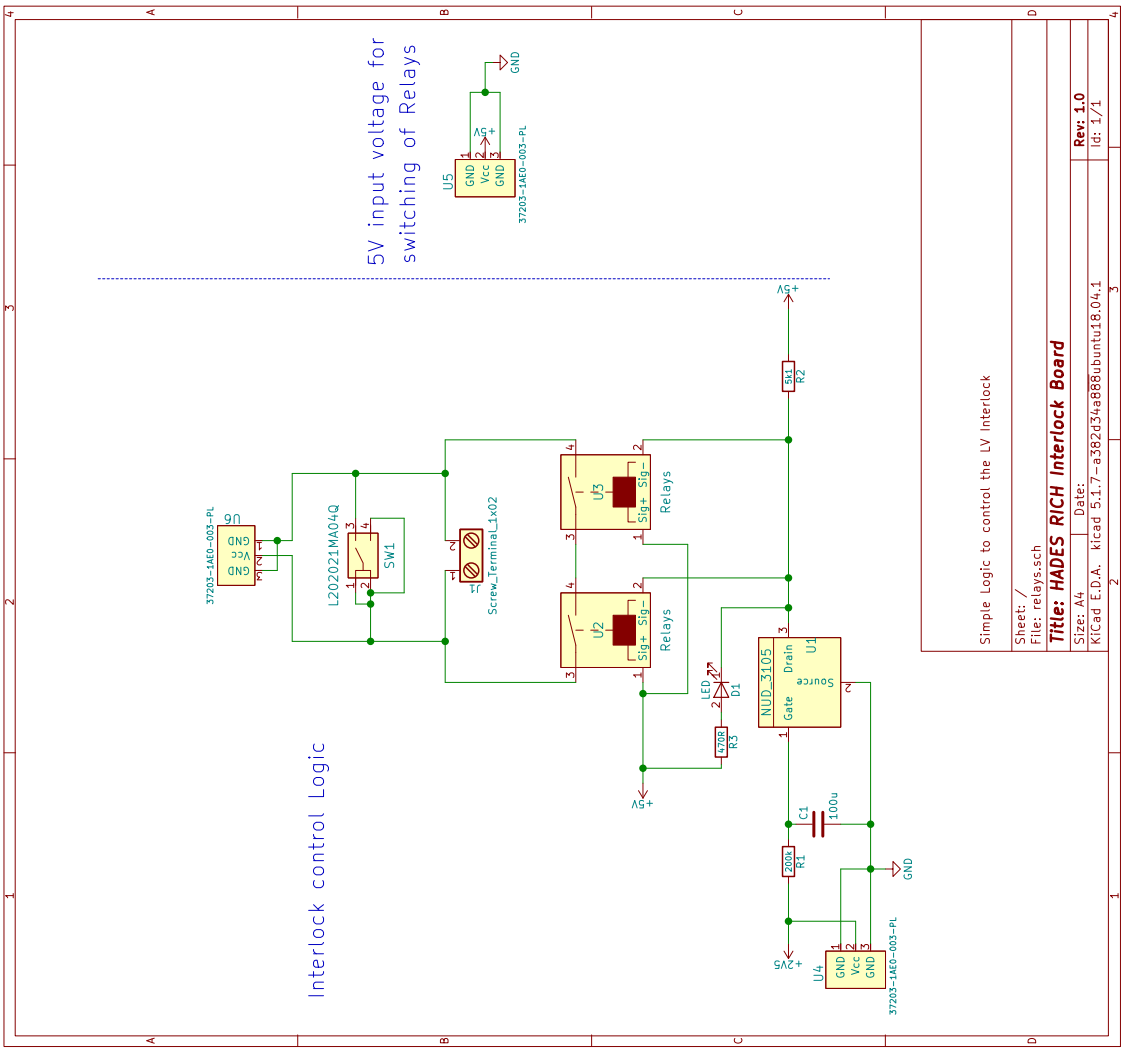

Figure C.3: Schematic of version 1 of the interlock board.

C.2 Schematic Version 2

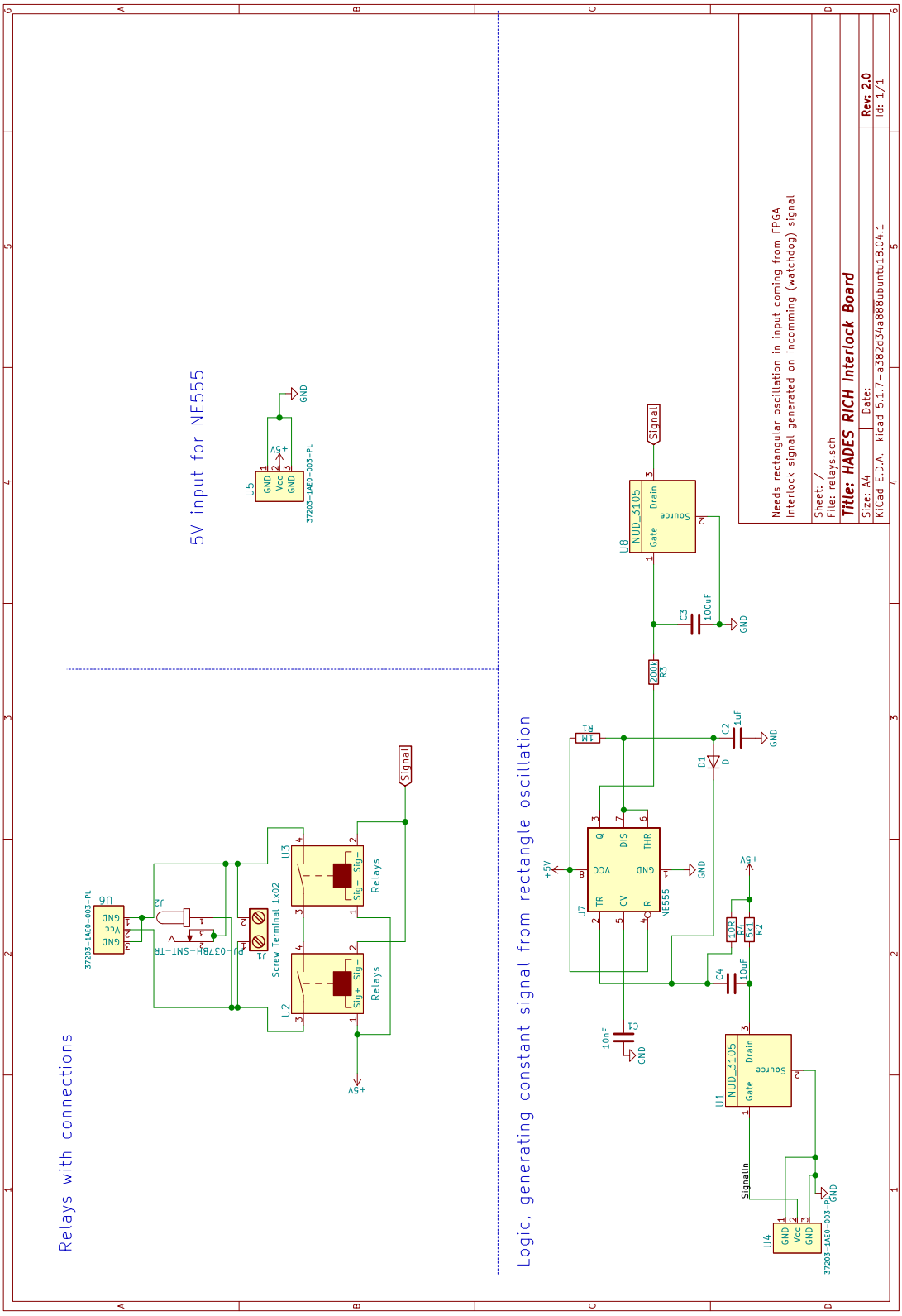

Figure C.4: Schematic of version 2 of the interlock board.

APPENDIX D

HADES RICH HV Mapping

HV module	channel	cable mark	back-plane	channel	cable mark	back-plane	HV module
0	0	1	17	0	49	87	3
0	1	2	27	1	50	97	3
0	2	3	56	2	51	88	3
0	3	4	92	3	52	67	3
0	4	5	54	4	53	66	3
0	5	6	63	5	54	N.C.	3
0	6	7	60	6	55	89	3
0	7	8	62	7	56	68	3
0	8	9	40	8	57	25	3
0	9	10	22	9	58	24	3
0	10	11	82	10	59	13	3
0	11	12	83	11	60	26	3
0	12	13	81	12	61	14	3
0	13	14	61	13	62	15	3
0	14	15	64	14	63	45	3
0	15	16	52	15	64	58	3
1	0	17	41	0	65	06	4
1	1	18	42	1	66	16	4
1	2	19	12	2	67	04	4
1	3	20	44	3	68	5A	4
1	4	21	43	4	69	79	4
1	5	22	A4	5	70	50	4
1	6	23	95	6	71	91	4
1	7	24	65	7	72	A5	4
1	8	25	51	8	73	98	4
1	9	26	96	9	74	18	4
1	10	27	A6	10	75	05	4
1	11	28	94	11	76	11	4
1	12	29	93	12	77	N.C.	4
1	13	30	84	13	78	N.C.	4
1	14	31	85	14	79	N.C.	4
1	15	32	86	15	80	N.C.	4

HV module	channel	cable mark	back-plane	channel	cable mark	back-plane	HV module
2	0	33	28	0	81	N.C.	5
2	1	34	29	1	82	N.C.	5
2	2	35	39	2	83	N.C.	5
2	3	36	71	3	84	N.C.	5
2	4	37	48	4	85	N.C.	5
2	5	38	46	5	86	N.C.	5
2	6	39	47	6	87	N.C.	5
2	7	40	59	7	88	N.C.	5
2	8	41	6A	8	89	N.C.	5
2	9	42	N.C.	9	90	N.C.	5
2	10	43	69	10	91	N.C.	5
2	11	44	4A	11	92	N.C.	5
2	12	45	49	12	93	N.C.	5
2	13	46	23	13	94	N.C.	5
2	14	47	21	14	95	N.C.	5
2	15	48	31	15	96	N.C.	5

Table D.1: Mapping between HV module channels, cable marks and backplane numbers.

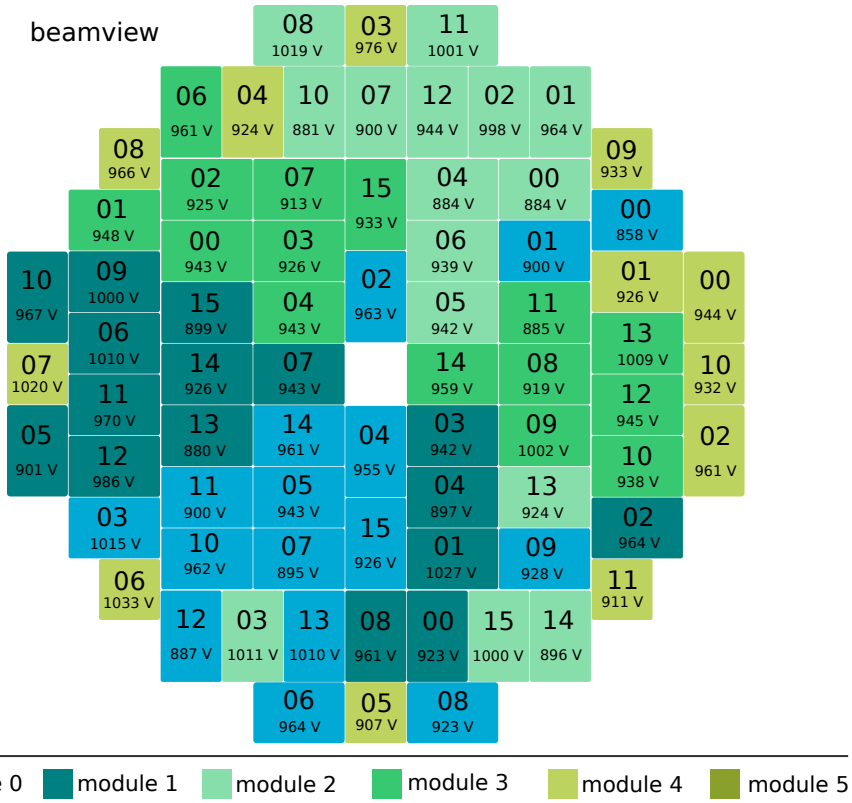

Figure D.1: Graphical representation of channels of the HV modules on backplanes. The standard voltage values during the March 2019 beamtime are shown.

APPENDIX E

Schematics DCDC Converter Board of mRICH Phase-I

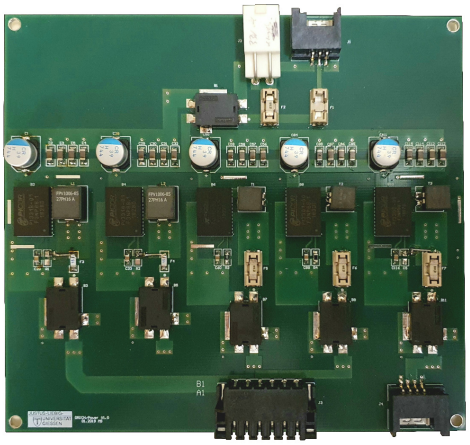

Figure E.1: Photography of the mRICH DCDC PCB in the first version fully assembled. The five dedicated DCDC ICs with the filters and the input as well as output connectors are visible.

In mCBM phase-I all combiner boards were connected to the first version of the DCDC converter board. It is based on the power module design of the DiRICH FEE and converts an input voltage between 8 V and 36 V to the four input voltages, required by the DiRICH setup. In addition, a fifth DCDC converter is added to give the possibility to have easy access to 3.6 V respectively 5.5 V. These voltages are needed to power e.g. the TRB3sc of mRICH or to power the optoLink board. The DCDC converter board is fixed to defined voltages. A change of the voltage in the ranges defined by the ICs is possible by the exchange of the soldered resistors.

The chosen configuration of the voltages to counteract the voltage drop on the power lines from the DCDC converter boards to the combiner boards are shown in Table E.1.

PowerLine	Resistors		calc. voltage
1.1 V	R1: DNA	R6: 10k	1.75 V
1.2 V	R2: DNA	R7: 3k3	1.65 V
2.5 V	R3: 5k76	R8: DNA	2.77 V
3.3 V	R4: 9k76	R9: DNA	3.57 V

Table E.1: Chosen resistors and resulting voltages of the DCDC converter board of mCBM phase-I.

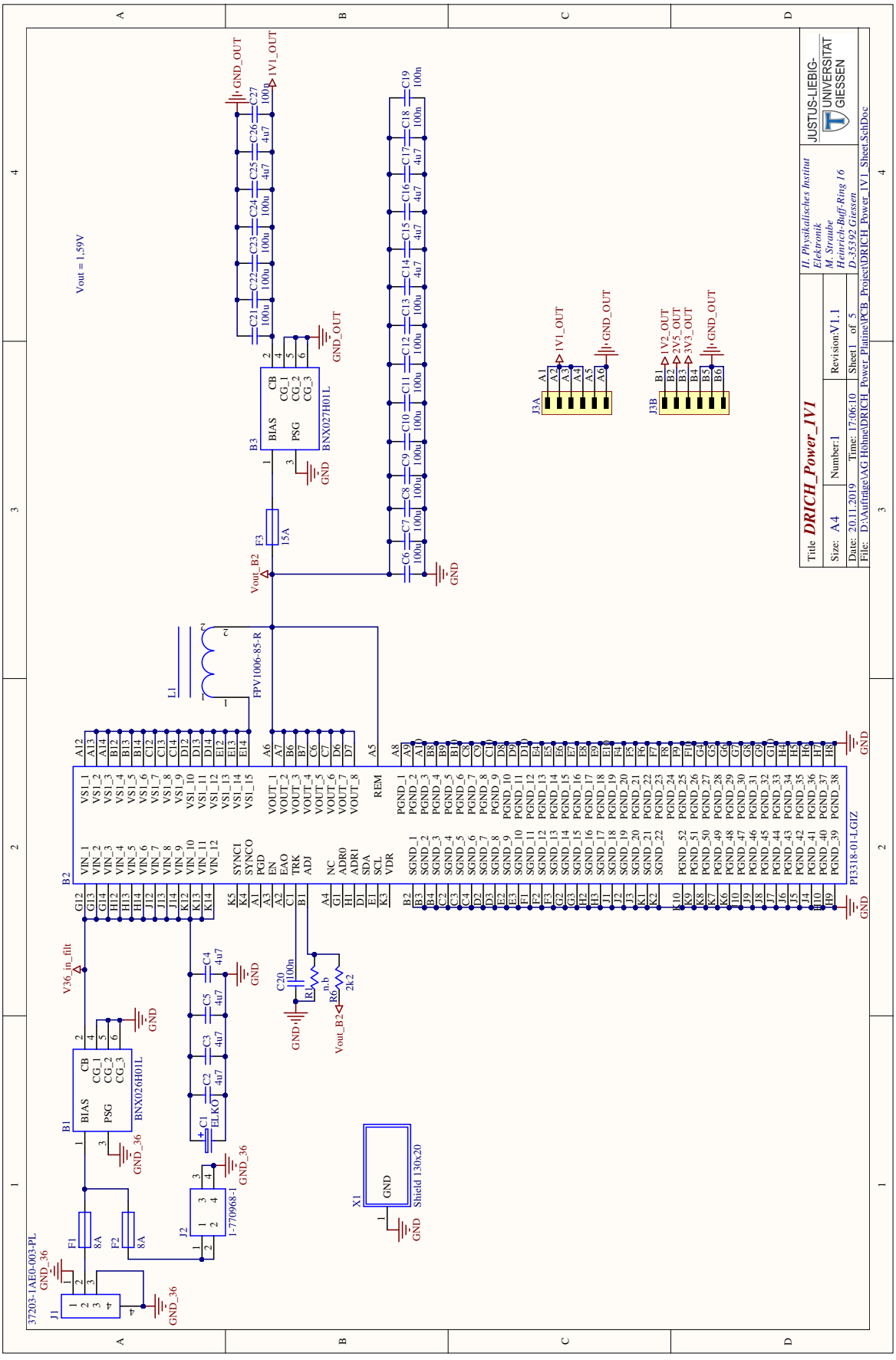

Figure E.2: 1.1V conversion of DCDC converter board of mRICH phase-I.

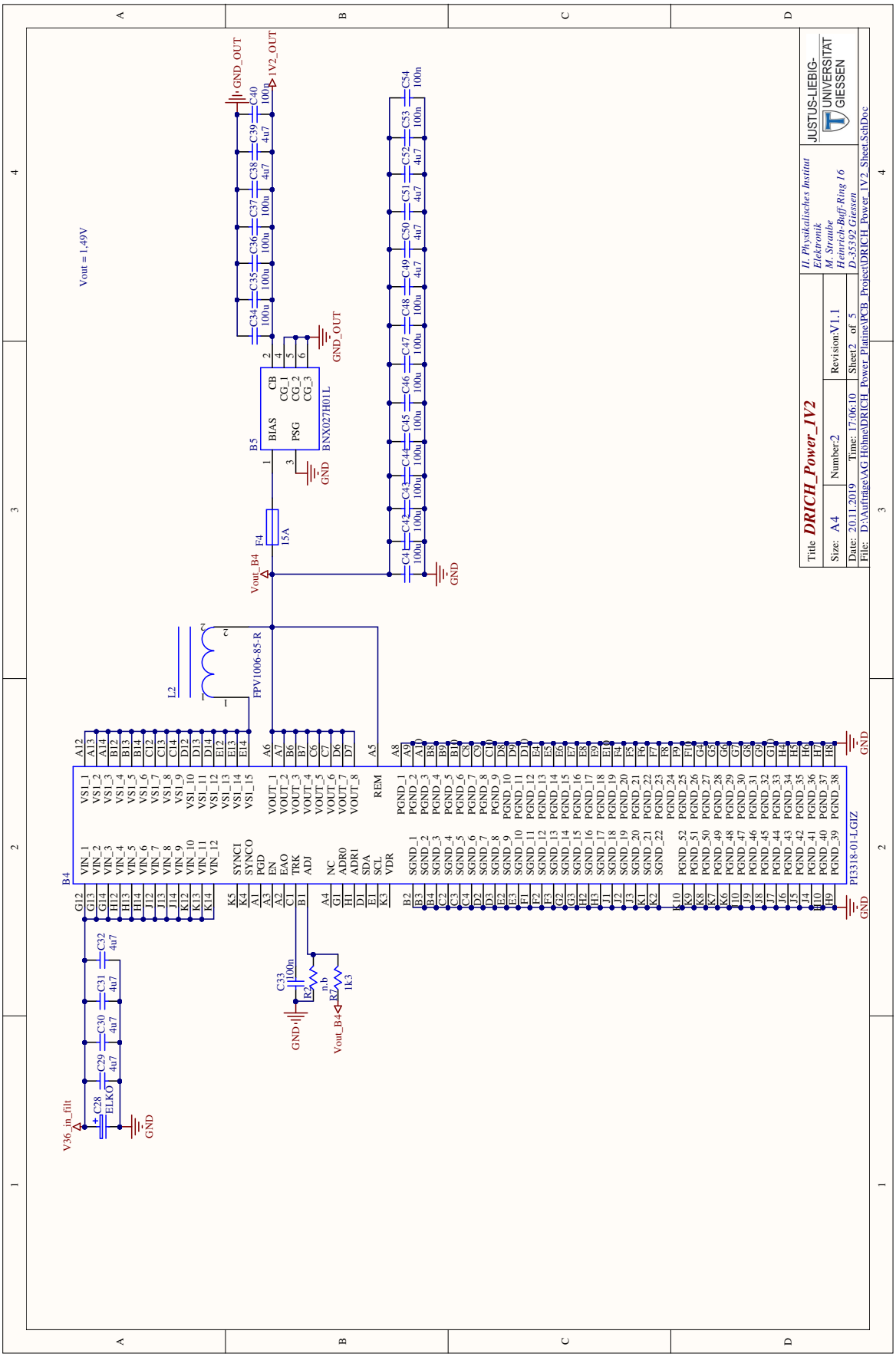

Figure E.3: 1.2V conversion of DCDC converter board of mRICH phase-I.

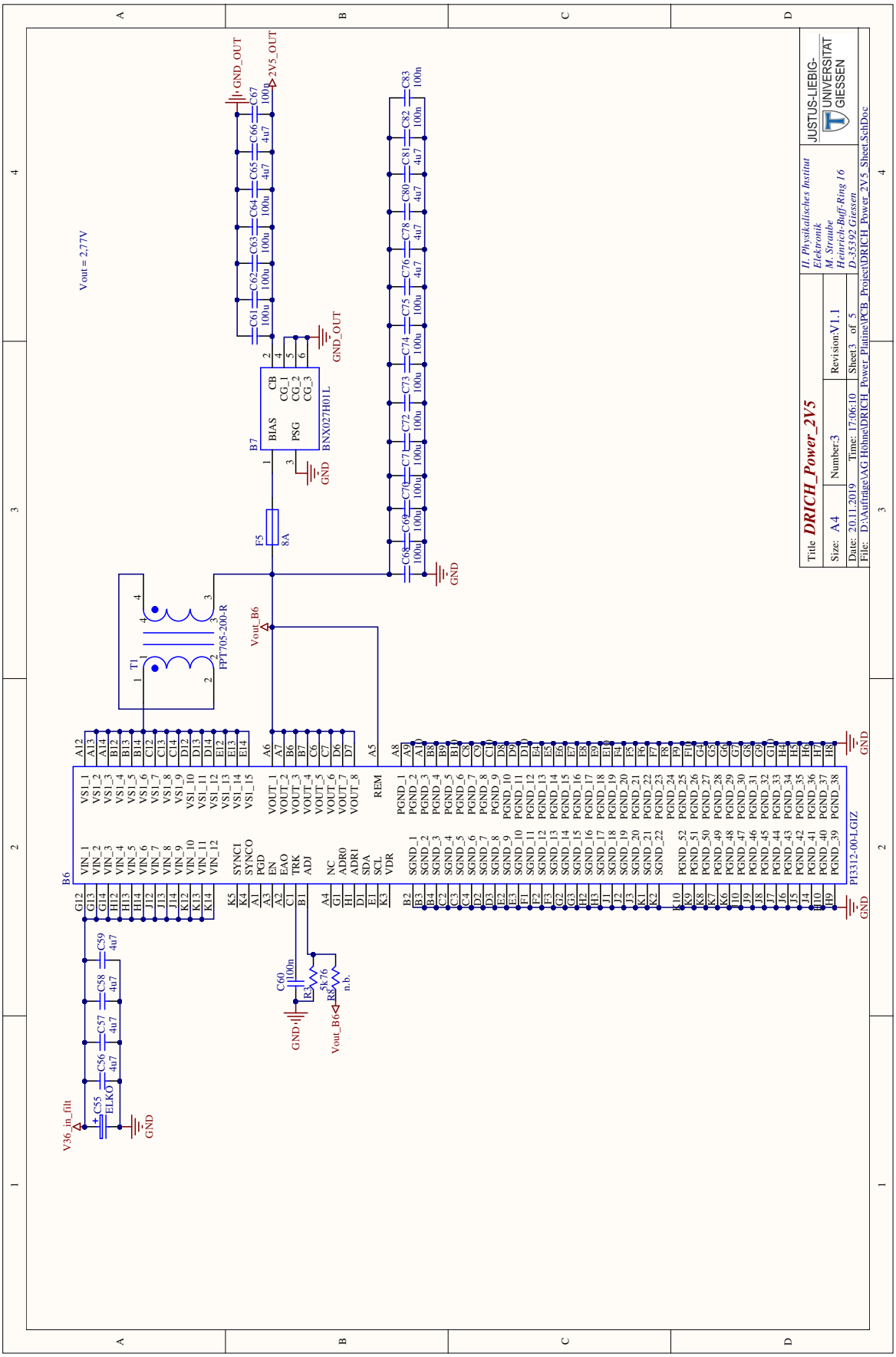

Figure E.4: 2.5V conversion of DCDC converter board of mRICH phase-I.

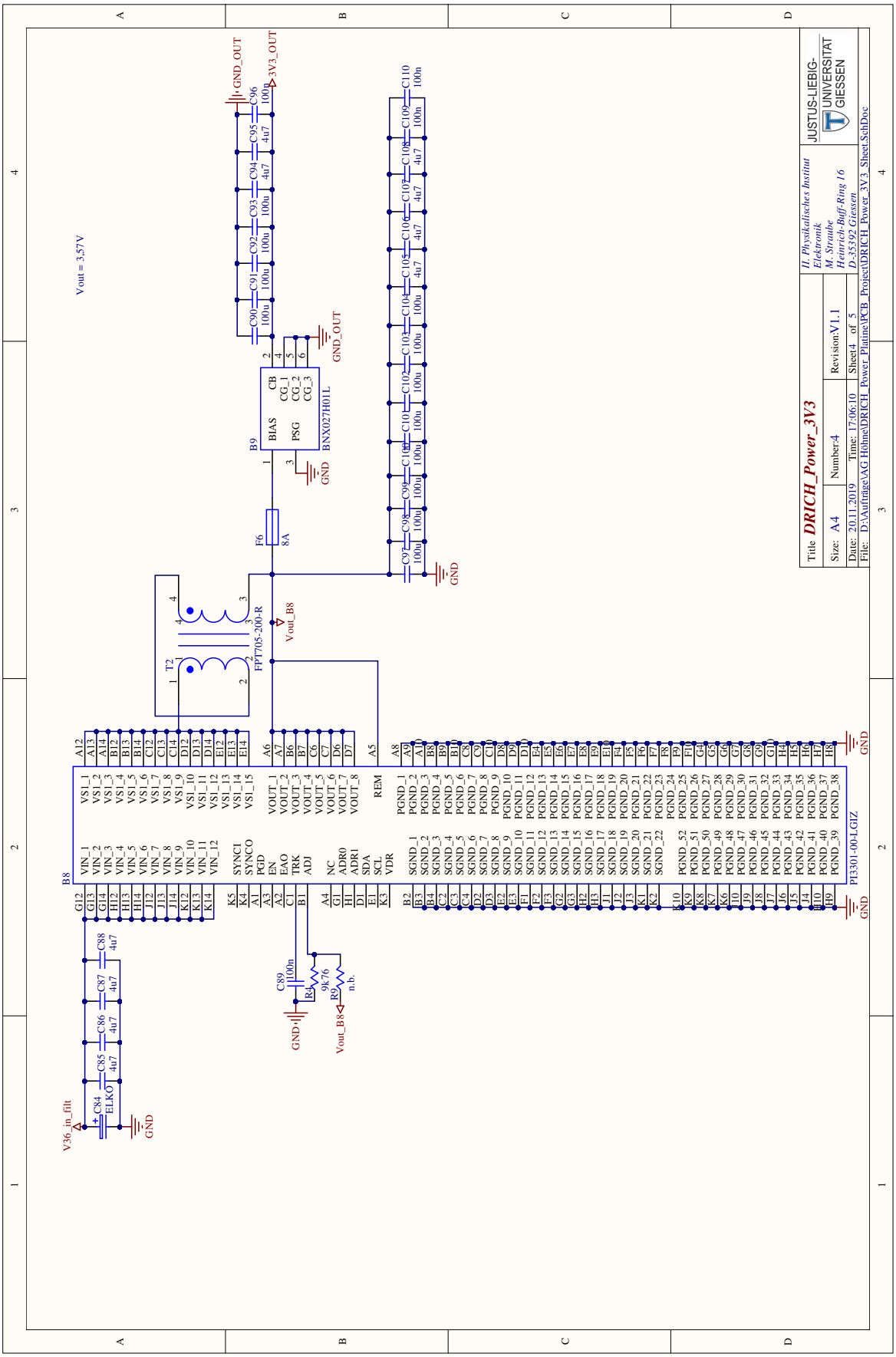

Figure E.5: 3.3V conversion of DCDC converter board of mRICH phase-I.

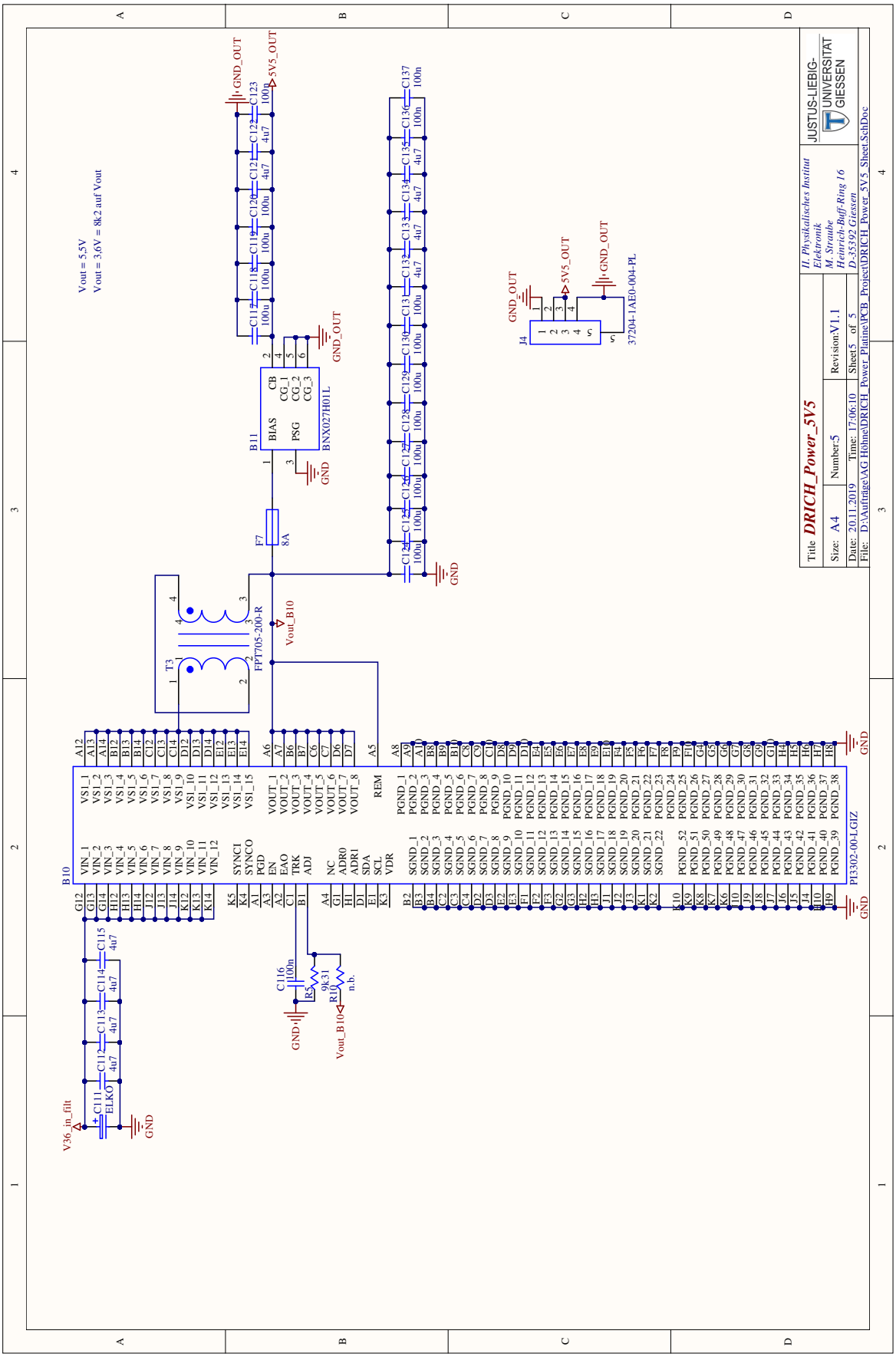

Figure E.6: 5.5V conversion of DCDC converter board of mRICH phase-I.

APPENDIX F

Overview of the mRICH FEE Boards, MAPMTs and High Voltage

The mRICH detector is fully equipped since the march 2020 beamtime. The FEE is equipped with standard combiner boards as well as power modules without onboard DCDC converters. In mRICH phase-II newly developed power modules with low noise onboard DCDC converters are used on 5 backplanes. Power module 5 is equipped with the old module and the external DCDC board form A.1. The DiRICH boards on the six backplanes are of revision 3. Figure F.2 gives an overview of the serial numbers of the DiRICH boards, the combiner and power modules at the corresponding position in the mRICH. The positions are given in the electronics view.

After the first beamtimes of mRICH, the old H8500 MAPMTs were exchanged. Since December 2019 the full mRICH backplane is equipped with H12700 MAPMTs. An overview of the serial numbers of the MAPMTs with their positions is given in Figure F.3. The positions are shown in the beam view.

The standard high voltage settings of the six backplanes of the mRICH detector are shown in Figure F.1. The shown values are calculated for a gain of $2.5{\cdot}10^6$. In addition, the connections between the power modules on the mRICH and the high voltage module in the crate in the DAQ container are listed.

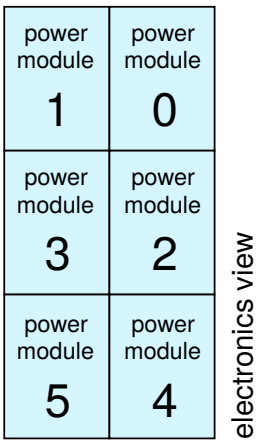

Power Module	HV module	voltage
0	channel 0	1014.74 V
1	channel 1	985.21 V
2	channel 2	976.36 V
3	channel 4	978.01 V
4	channel 5	982.04 V
5	channel 6	972.20 V

Figure F.1: **(left)** Schematic overview of the location of the power modules in electronics view. **(right)** Tabular overview of the high voltage connections between mRICH and HV module in the DAQ container. The voltage values are selected based on a MAPMT gain of $2.5{\cdot}10^6$.

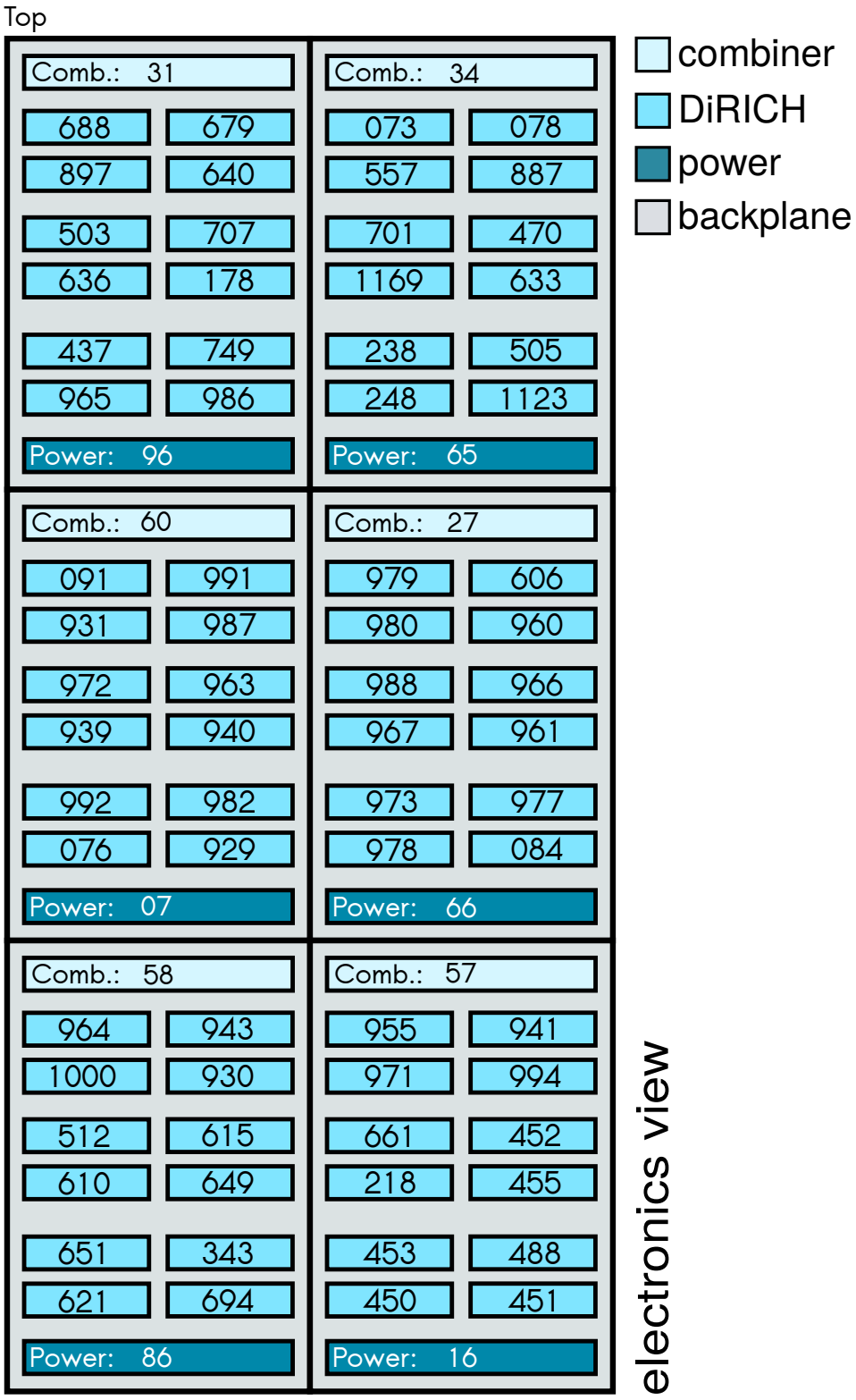

Figure F.2: Schematic overview of the DiRICH, combiner and power module serial numbers as they are mounted in the mRICH detector. The figure shows the view on the FEE from behind the mRICH detector.

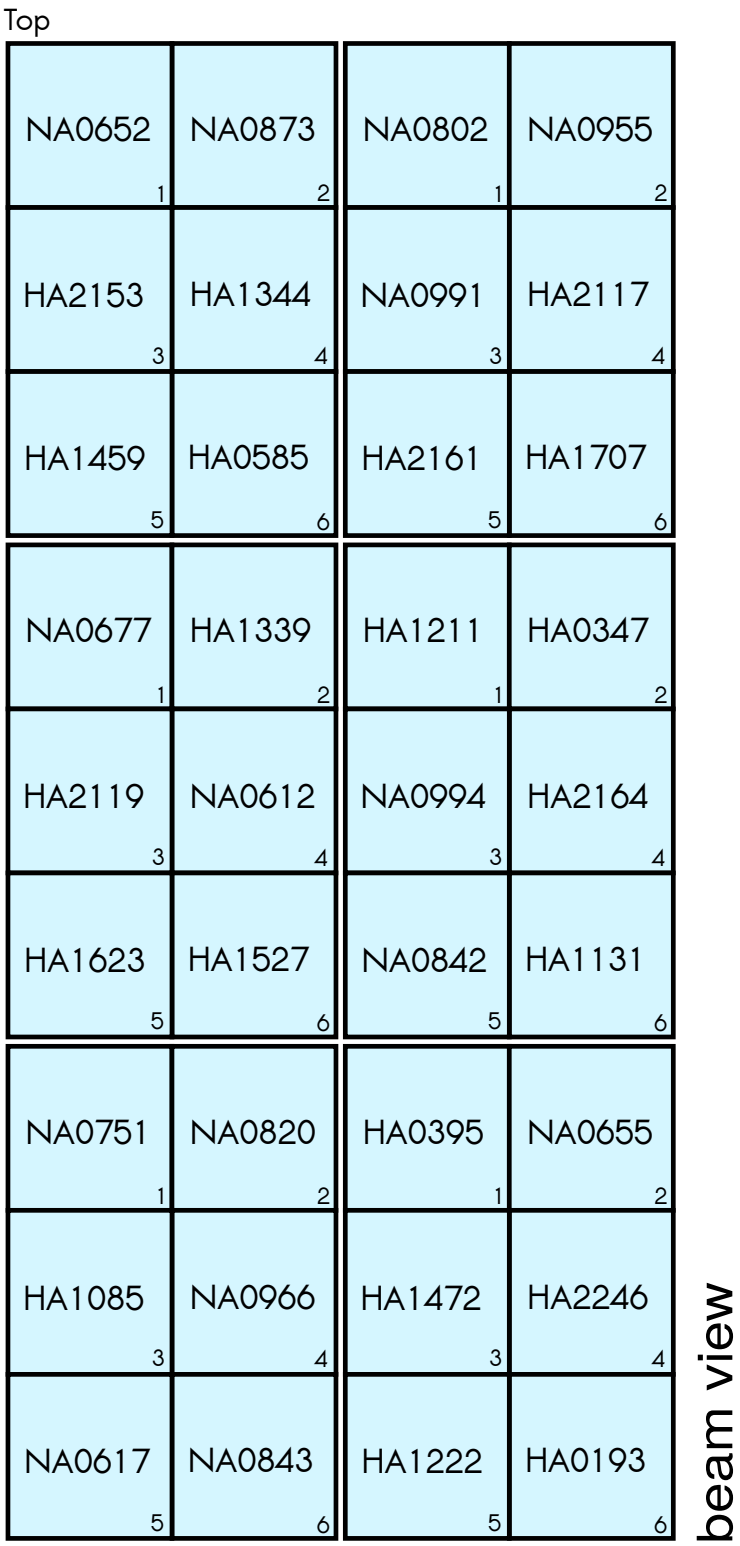

Figure F.3: Schematic overview of the MAPMT serial numbers as mounted in the mRICH detector. The figure shows the positions in the beamview.

ACRONYMS

A

ADC Analog to **D**igital **C**onverter
AFCK **A**MC **F**MC **C**arrier **K**intex
ALEPH Apparatus for **LEP** **PH**ysics
ALICE **A** **L**arge **I**on **C**ollider **E**xperiment
AMC **A**dvanced **M**ezzanine **C**ard
API **A**pplication **P**rogramming **I**nterface
APL **A**pplication **P**rogramming **L**ogic
APPA **A**tomic **P**hysics, **P**lasma and **A**pplied science.
ASCII **A**merican **S**tandard **C**ode for **I**nformation **I**nterchange
ASIC **A**pplication-**S**pecific **I**ntegrated **C**ircuit
ATLAS **A** **T**oroidal **L**HC **A**pparatu**S**
AWG **A**merican **W**ire **G**auge
AXI **A**dvanced e**X**tensible **I**nterface

B

BES **BE**ijing **S**pectrometer
BNL **B**rookhaven **N**ational **L**aboratory

C

CAD **C**omputer-**A**ided **D**esign
CBM **C**ompressed **B**aryonic **M**atter
CERN **C**onseil **E**uropéen pour la **R**echerche **N**ucléaire
CKM **C**abibbo-**K**obayashi-**M**askawa
CLAM **C**ontinuous **L**ine **A**lignment **M**onitoring
CLAS12 **C**EBAF **L**arge **A**cceptance **S**pectrometer for operation at **12** GeV beam energy
CMOS **C**omplementary **M**etal-**O**xide-**S**emiconductor
COSY **CO**oler **SY**nchrotron
CRC **C**yclic **R**edundancy **C**heck
CRI **C**ommon **R**eadout **I**nterface
CROB **C**ommon **R**ead**O**ut **B**oard

CSS **C**ontrol **S**ystem **S**tudio
CTS **C**entral **T**rigger **S**ystem

D

DABC **D**ata **A**cquistion **B**ackbone **C**ore
DAQ **D**ata **A**c**Q**uistion
DCA **D**evice **C**ontrol **A**gent
DHCP **D**ynamic **H**ost **C**onfiguration **P**rotocol
DiRICH **Di**rc-**RICH**
DLM **D**eterministic **L**atency **M**essage
DMA **D**irect **M**emory **A**ccess
DMON **D**ata **MON**itor
DPB **D**ata **P**rocessing **B**oard

E

ECAL **E**lectromagnetic **CAL**orimeter
ECS **E**xperiment **C**ontrol **S**ystem

F

FAIR **F**acility for **A**nti Proton and **I**on **R**esearch
FEB **F**ront **E**nd **B**oard
FEE **F**ront **E**nd **E**lectronics
FELIX **F**ront-**E**nd **LI**nk e**X**change
FFC **F**lat **F**lex **C**able
FLES **F**irst-**L**evel **E**vent **S**elector
FLIB **FLES** **I**nterface **B**oard
FLIM **FLES** **I**nterface **M**odul
FMC **F**PGA **M**ezzanine **C**ard
FPGA **F**ield **P**rogrammable **G**ate **A**rray
FRS **FR**agment **S**eparator

G

GEM **G**as **E**lectron **M**ultiplier
GSI **G**esellschaft für **S**chwer**I**onenforschung
GUI **G**raphical **U**ser **I**nterface

H

HADES **H**igh **A**cceptance **Di**-**E**lectron **S**pectrometer
HIC **H**eavy **I**on **C**ollision
HMON **HADES** **MON**itoring
HTML **H**yper**T**ext **M**arkup **L**anguage
HTTP **H**yper**T**ext **T**ransfer **P**rotocol
HV **H**igh **V**oltage

I

IC **I**ntegrated **C**ircuit
ICD **I**nter **C**hannel **D**elay

IOC **I**nput / **O**utput **C**ontroller
IP **I**nternet **P**rotocol or
IP-Core **I**ntellectual **P**roperty Core

K

KIT **K**arlsruher **I**nstitut für **T**echnologie

L

LAN **L**ocal **A**rea **N**etwork
LC **L**ucent **C**onnector
LHC **L**arge **H**adron **C**ollide
LVDS **L**ow **V**oltage **D**ifferential **S**ignaling

M

MAC **M**edia-**A**ccess-**C**ontrol
MAPMT **M**ulti-**A**node **P**hoton-**M**ultiplier **T**ube
MBS **M**ulti **B**ranch **S**ystem
MDC **M**ini **D**rift **C**hamber
microTCA micro **T**elecommunications **C**omputing **A**rchitecture
miniPOD mini **P**arallel **O**ptical **D**evice
MRPC **M**ulti-Gap **R**esistive-**P**late **C**hambers
MTP **M**ulti-fiber **T**ermination **P**ush-on connector
MUCH **Mu**on **Ch**ambers
MVD **M**icro **V**ertex **D**etector
MWPC **M**ulti-**W**ire **P**roportional **C**hambers

N

NUSTAR **Nu**clear **ST**ructure, **A**strophysics and **R**eactions

O

OPAL **O**mni **P**urpose **A**pparatus at **L**EP

P

PANDA Anti**P**roton **AN**nihilation in **DA**rmstadt
PCB **P**rinted **C**ircuit **B**oard
pcCVD **p**oly**c**rystalline **C**hemical **V**apor **D**eposition
PCIe **P**eripheral **C**omponent **I**nterconnect **e**xpress
PEXOR **P**CI-**EX**press **O**ptical **R**eceiver]
PHENIX **P**ioneering **H**igh **E**nergy **N**uclear **I**nteraction e**X**periment
PLC **P**rogrammable **L**ogic **C**ontroller
PLL **P**hase-**L**ocked **L**oop
PMT **P**hoto**M**ultiplier **T**ube
PSD **P**rojectile **S**pectator **D**etector

Q

QCD **Q**uanten**C**hromo**D**ynamik
QE **Q**uantum **E**fficiency

QED Quantum ElectroDynamics
QGP Quark–Gluon Plasma

R

RHIC Relativistic Heavy Ion Collider
RICH Ring Imaging CHerenkov detector
RPC Resistive Plate Chamber

S

scCVD single crystal Chemical Vapor Deposition
SerDes Serializer/Deserializer
SFP Small Form-factor Pluggable
SHV Safe High Voltage
SIS SchwerIonenSynchrotron
SNMP Simple Network Management Protocol
SPADIC Self-triggered Pulse Amplification and Digitization asIC
SPI Serial Peripheral Interface
SPS Super Proton Synchrotron
STAR Solenoidal Tracker At RHIC
STS Silicon Tracking System

T

TDC Time to Digital Converter
TFC Timing and Fast Control
TMC Timing Mezzanine Card
TOF Time Of Flight
TRB Trigger and Readout Boards
TRD Transition Radiation Detector

U

UART Universal Asynchronous Receiver-Transmitter
UDP User Datagram Protocol
UNILAC UNIversal Linear ACcelerator

V

VHDL Very High Speed Integrated Circuit Hardware Description Language
VNC Virtual Network Computing

W

WLS WaveLengthShifter

Bibliography

[1] M. Tanabashi et al. “Review of Particle Physics”. In: Phys. Rev. D 98 (3 Aug. 2018), p. 030001. DOI: 10.1103/PhysRevD.98.030001. URL: https://link.aps.org/doi/10.1103/PhysRevD.98.030001.

[2] Owe Philipsen. “Quantenfeldtheorie und das Standardmodell der Teilchenphysik - Eine Einführung”. Berlin Heidelberg New York: Springer-Verlag, 2018. ISBN: 978-3-662-57820-9.

[3] Nicola Cabibbo. “Unitary Symmetry and Leptonic Decays”. In: Phys. Rev. Lett. 10 (12 June 1963), pp. 531–533. DOI: 10.1103/PhysRevLett.10.531. URL: https://link.aps.org/doi/10.1103/PhysRevLett.10.531.

[4] Makoto Kobayashi and Toshihide Maskawa. “CP-Violation in the Renormalizable Theory of Weak Interaction”. In: Progress of Theoretical Physics 49.2 (Feb. 1973), pp. 652–657. ISSN: 0033-068X. DOI: 10.1143/PTP.49.652. eprint: https://academic.oup.com/ptp/article-pdf/49/2/652/5257692/49-2-652.pdf. URL: https://doi.org/10.1143/PTP.49.652.

[5] Bogdan Povh et al. “Teilchen und Kerne - Eine Einführung in die physikalischen Konzepte”. Berlin Heidelberg New York: Springer-Verlag, 2013. ISBN: 978-3-642-37822-5.

[6] Donald H. Perkins. “Introduction to High Energy Physics”. 4th ed. Cambridge University Press, 2000. DOI: 10.1017/CBO9780511809040.

[7] Sheldon L. Glashow. “The renormalizability of vector meson interactions”. In: Nuclear Physics 10 (1959), pp. 107–117. ISSN: 0029-5582. DOI: https://doi.org/10.1016/0029-5582(59)90196-8. URL: http://www.sciencedirect.com/science/article/pii/0029558259901968.

[8] Abdus Salam and John Clive Ward. “Weak and electromagnetic interactions”. In: Nuovo Cim. 11 (1959), pp. 568–577. DOI: 10.1007/BF02726525.

[9] Steven Weinberg. “A Model of Leptons”. In: Phys. Rev. Lett. 19 (21 Nov. 1967), pp. 1264–1266. DOI: 10.1103/PhysRevLett.19.1264. URL: https://link.aps.org/doi/10.1103/PhysRevLett.19.1264.

[10] LHCb collaboration et al. “Observation of structure in the J/Ψ-pair mass spectrum”. 2020. arXiv: 2006.16957 [hep-ex].

[11] Wolfram Weise. “The QCD vacuum and its hadronic excitations”. 2005. arXiv: nucl-th/0504087 [nucl-th].

[12] K. Ackerstaff et al. “Measurement of the strong coupling constant α_s and the vector and axial-vector spectral functions in hadronic tau decays”. In: The European Physical Journal C 7.4 (Mar. 1999), pp. 571–593. ISSN: 1434-6052. DOI: 10.1007/s100529901061. URL: http://dx.doi.org/10.1007/s100529901061.

[13] Volker Koch. “Aspects of Chiral Symmetry”. In: International Journal of Modern Physics E 06.02 (June 1997), pp. 203–249. ISSN: 1793-6608. DOI: 10.1142/s0218301397000147. URL: http://dx.doi.org/10.1142/S0218301397000147.

[14] Murray Gell-Mann, R. J. Oakes, and B. Renner. "Behavior of Current Divergences under $SU_3 \times SU_3$". In: Phys. Rev. 175 (5 Nov. 1968), pp. 2195–2199. DOI: 10.1103/PhysRev.175.2195. URL: https://link.aps.org/doi/10.1103/PhysRev.175.2195.

[15] Martin Kotulla, Volker Metag, and Ulrich Mosel. "Hadronen im Medium". In: Physik J. 8N3 (2009), pp. 41–46.

[16] S. Klimt, M. Lutz, and W. Weise. "Chiral phase transition in the SU(3) Nambu and Jona-Lasinio model". In: Physics Letters B 249.3 (1990), pp. 386–390. ISSN: 0370-2693. DOI: https://doi.org/10.1016/0370-2693(90)91003-T. URL: http://www.sciencedirect.com/science/article/pii/037026939091003T.

[17] ALEPH Collaboration: R. Barate - et al. "Measurement of the axial-vector τ spectral functions and determination of $\alpha_s(M_\tau^2)$ from hadronic τ decays". In: Eur. Phys. J. C 4.3 (1998), pp. 409–431. DOI: 10.1007/s100520050217. URL: https://doi.org/10.1007/s100520050217.

[18] Bengt Friman et al. "The CBM Physics Book - Compressed Baryonic Matter in Laboratory Experiments". Berlin Heidelberg: Springer Science & Business Media, 2011. ISBN: 978-3-642-13292-6.

[19] R. Arnaldi et al. "First Measurement of the ρ Spectral Function in High-Energy Nuclear Collisions". In: Physical Review Letters 96.16 (Apr. 2006). ISSN: 1079-7114. DOI: 10.1103/physrevlett.96.162302. URL: http://dx.doi.org/10.1103/PhysRevLett.96.162302.

[20] D. Adamová et al. "Modification of the ρ meson detected by low-mass electron-positron pairs in central Pb-Au collisions at 158 A GeV/c". In: Physics Letters B 666.5 (Sept. 2008), pp. 425–429. ISSN: 0370-2693. DOI: 10.1016/j.physletb.2008.07.104. URL: http://dx.doi.org/10.1016/j.physletb.2008.07.104.

[21] Tapan K. Nayak. "Heavy Ions: Results from the Large Hadron Collider". In: Pramana 79 (2012). Ed. by Rohin Godbole and Naba K. Mondal, pp. 719–735. DOI: 10.1007/s12043-012-0373-7. arXiv: 1201.4264 [nucl-ex].

[22] Michael Annan Lisa. "Size Matters: Spacetime geometry in subatomic collisions". 2004. URL: https://www.asc.ohio-state.edu/lisa.1/SizeMattersSambamurti2004.pdf.

[23] Wit Busza et al. "Heavy Ion Collisions: The Big Picture and the Big Questions". In: Annual Review of Nuclear and Particle Science 68.1 (Nov. 2018), pp. 339–376. ISSN: 1545-4134. DOI: 10.1146/annurev-nucl-101917-020852. URL: http://dx.doi.org/10.1146/annurev-nucl-101917-020852.

[24] Kenji Fukushima and Tetsuo Hatsuda. "The phase diagram of dense QCD". In: Reports on Progress in Physics 74.1 (Dec. 2010), p. 014001. ISSN: 1361-6633. DOI: 10.1088/0034-4885/74/1/014001. URL: http://dx.doi.org/10.1088/0034-4885/74/1/014001.

[25] Z Fodor and S.D Katz. "Critical point of QCD at finite T and , lattice results for physical quark masses". In: Journal of High Energy Physics 2004.04 (Apr. 2004), pp. 050–050. ISSN: 1029-8479. DOI: 10.1088/1126-6708/2004/04/050. URL: http://dx.doi.org/10.1088/1126-6708/2004/04/050.

[26] Y. Aoki et al. “The order of the quantum chromodynamics transition predicted by the standard model of particle physics”. In: Nature 443.7112 (Nov. 2006), pp. 675–678. ISSN: 1476-4687. DOI: 10.1038/nature05120. URL: http://dx.doi.org/10.1038/nature05120.

[27] B.-J. Schaefer, J. M. Pawlowski, and J. Wambach. “Phase structure of the Polyakov-quark-meson model”. In: Physical Review D 76.7 (Nov. 2007). ISSN: 1550-2368. DOI: 10.1103/physrevd.76.074023. URL: http://dx.doi.org/10.1103/PhysRevD.76.074023.

[28] Larry McLerran. “Quarkyonic Matter and the Phase Diagram of QCD”. In: Continuous Advances in QCD 2008 (Dec. 2008). DOI: 10.1142/9789812838667_0011. URL: http://dx.doi.org/10.1142/9789812838667_0011.

[29] Ph. Chomaz. “The nuclear liquid gas phase transition and phase coexistence: A review”. 2004. arXiv: nucl-ex/0410024 [nucl-ex].

[30] Patrick Steinbrecher. “The QCD crossover at zero and non-zero baryon densities from Lattice QCD”. In: Nuclear Physics A 982 (Feb. 2019), pp. 847–850. ISSN: 0375-9474. DOI: 10.1016/j.nuclphysa.2018.08.025. URL: http://dx.doi.org/10.1016/j.nuclphysa.2018.08.025.

[31] Francesco Becattini et al. “Hadron Formation in Relativistic Nuclear Collisions and the QCD Phase Diagram”. In: Phys. Rev. Lett. 111 (8 Aug. 2013), p. 082302. DOI: 10.1103/PhysRevLett.111.082302. URL: https://link.aps.org/doi/10.1103/PhysRevLett.111.082302.

[32] J Stachel et al. “Confronting LHC data with the statistical hadronization model”. In: Journal of Physics: Conference Series 509 (Feb. 2014), p. 012019. ISSN: 1742-6596. DOI: 10.1088/1742-6596/509/1/012019. URL: http://dx.doi.org/10.1088/1742-6596/509/1/012019.

[33] Grazyna Odyniec. “Beam Energy Scan Program at RHIC (BES I and BES II) – Probing QCD Phase Diagram with Heavy-Ion Collisions”. In: PoS CORFU2018 (2019). Ed. by Konstantinos Anagnostopoulos et al., p. 151. DOI: 10.22323/1.347.0151.

[34] R. Averbeck. “Heavy-flavor production in heavy-ion collisions and implications for the properties of hot QCD matter”. In: Progress in Particle and Nuclear Physics 70 (May 2013), pp. 159–209. ISSN: 0146-6410. DOI: 10.1016/j.ppnp.2013.01.001. URL: http://dx.doi.org/10.1016/j.ppnp.2013.01.001.

[35] T. Matsui and H. Satz. “J/ψ Suppression by Quark-Gluon Plasma Formation”. In: Phys. Lett. B 178 (1986), pp. 416–422. DOI: 10.1016/0370-2693(86)91404-8.

[36] T. Ablyazimov et al. “Challenges in QCD matter physics –The scientific programme of the Compressed Baryonic Matter experiment at FAIR”. In: The European Physical Journal A 53.3 (Mar. 2017). ISSN: 1434-601X. DOI: 10.1140/epja/i2017-12248-y. URL: http://dx.doi.org/10.1140/epja/i2017-12248-y.

[37] A. Adare et al. “J/ψ Production versus Centrality, Transverse Momentum, andRapidity in $\mathrm{Au}+\mathrm{Au}$ Collisions at $\sqrt{s_{NN}} = 200$ GeV”. In: Phys. Rev. Lett. 98 (23 June 2007), p. 232301. DOI: 10.1103/PhysRevLett.98.232301. URL: https://link.aps.org/doi/10.1103/PhysRevLett.98.232301.

[38] B. Abelev et al. “J/psi Suppression at Forward Rapidity in Pb-Pb Collisions at $\sqrt{s_{NN}}$=2.76TeV”. In: Physical Review Letters 109.7 (Aug. 2012). ISSN: 1079-7114. DOI: 10.1103/physrevlett.109.072301. URL: http://dx.doi.org/10.1103/PhysRevLett.109.072301.

[39] A. M. Poskanzer and S. A. Voloshin. “Methods for analyzing anisotropic flow in relativistic nuclear collisions”. In: Physical Review C 58.3 (Nov. 1998), pp. 1671–1678. ISSN: 1089-490X. DOI: 10.1103/physrevc.58.1671. URL: http://dx.doi.org/10.1103/PhysRevC.58.1671.

[40] Raimond Snellings. “Elliptic flow: a brief review”. In: New Journal of Physics 13.5 (May 2011), p. 055008. ISSN: 1367-2630. DOI: 10.1088/1367-2630/13/5/055008. URL: http://dx.doi.org/10.1088/1367-2630/13/5/055008.

[41] Yasushi Nara et al. “Enhancement of elliptic flow can signal a first-order phase transition in high-energy heavy-ion collisions”. In: The European Physical Journal A 54.2 (Feb. 2018). ISSN: 1434-601X. DOI: 10.1140/epja/i2018-12413-x. URL: http://dx.doi.org/10.1140/epja/i2018-12413-x.

[42] A. Adare et al. “Scaling Properties of Azimuthal Anisotropy in $\mathrm{Au}+\mathrm{Au}$ and $\mathrm{Cu}+\mathrm{Cu}$ Collisions at $\sqrt{s_{\mathrm{NN}}}=200\ \mathrm{GeV}$”. In: Phys. Rev. Lett. 98 (16 Apr. 2007), p. 162301. DOI: 10.1103/PhysRevLett.98.162301. URL: https://link.aps.org/doi/10.1103/PhysRevLett.98.162301.

[43] Jean-Yves Ollitrault. “Anisotropy as a signature of transverse collective flow”. In: Phys. Rev. D 46 (1992), pp. 229–245. DOI: 10.1103/PhysRevD.46.229.

[44] Volker Koch. “Hadronic Fluctuations and Correlations”. 2008. arXiv: 0810.2520 [nucl-th].

[45] Masayuki Asakawa and Masakiyo Kitazawa. “Fluctuations of conserved charges in relativistic heavy ion collisions: An introduction”. In: Progress in Particle and Nuclear Physics 90 (Sept. 2016), pp. 299–342. ISSN: 0146-6410. DOI: 10.1016/j.ppnp.2016.04.002. URL: http://dx.doi.org/10.1016/j.ppnp.2016.04.002.

[46] Shu He and Xiaofeng Luo. “Event-by-event efficiency fluctuations and efficiency correction for cumulants of superposed multiplicity distributions in relativistic heavy-ion collision experiments”. In: Chinese Physics C 42.10 (Sept. 2018), p. 104001. ISSN: 1674-1137. DOI: 10.1088/1674-1137/42/10/104001. URL: http://dx.doi.org/10.1088/1674-1137/42/10/104001.

[47] Xiaofeng Luo. “Exploring the QCD Phase Structure with Beam Energy Scan in Heavy-ion Collisions”. In: Nuclear Physics A 956 (Dec. 2016), pp. 75–82. ISSN: 0375-9474. DOI: 10.1016/j.nuclphysa.2016.03.025. URL: http://dx.doi.org/10.1016/j.nuclphysa.2016.03.025.

[48] A. Andronic et al. “Production of light nuclei, hypernuclei and their antiparticles in relativistic nuclear collisions”. In: Physics Letters B 697.3 (Mar. 2011), pp. 203–207. ISSN: 0370-2693. DOI: 10.1016/j.physletb.2011.01.053. URL: http://dx.doi.org/10.1016/j.physletb.2011.01.053.

[49] B.I. Abelev et al. “Observation of an Antimatter Hypernucleus”. In: Science 328 (2010), pp. 58–62. DOI: 10.1126/science.1183980. arXiv: 1003.2030 [nucl-ex].

[50] Heidi Schuldes, Timo Scheib, and Manuel Lorenz. “Nucleus and Hypernucleus Measurements with HADES”. In: PoS Bormio2013 (2013), p. 026. DOI: 10.22323/1.184.0026.

[51] Johann Rafelski and Berndt Müller. “Strangeness Production in the Quark-Gluon Plasma”. In: Phys. Rev. Lett. 48 (16 Apr. 1982), pp. 1066–1069. DOI: 10.1103/PhysRevLett.48.1066. URL: https://link.aps.org/doi/10.1103/PhysRevLett.48.1066.

[52] C. Blume and C. Markert. “Strange hadron production in heavy ion collisions from SPS to RHIC”. In: Progress in Particle and Nuclear Physics (May 2011). ISSN: 0146-6410. DOI: 10.1016/j.ppnp.2011.05.001. URL: http://dx.doi.org/10.1016/j.ppnp.2011.05.001.

[53] NA57 Collaboration et al. “Enhancement of hyperon production at central rapidity in 158AGeV/cPb–Pb collisions”. In: Journal of Physics G: Nuclear and Particle Physics 32.4 (Feb. 2006), pp. 427–441. ISSN: 1361-6471. DOI: 10.1088/0954-3899/32/4/003. URL: http://dx.doi.org/10.1088/0954-3899/32/4/003.

[54] A. Andronic, P. Braun-Munzinger, and J. Stachel. “Hadron production in central nucleus-nucleus collisions at chemical freeze-out”. In: Nucl. Phys. A 772 (2006), pp. 167–199. DOI: 10.1016/j.nuclphysa.2006.03.012. arXiv: nucl-th/0511071.

[55] P. Braun-Munzinger, J. Stachel, and Christof Wetterich. “Chemical freeze-out and the QCD phase transition temperature”. In: Physics Letters B 596.1 (2004), pp. 61–69. ISSN: 0370-2693. DOI: https://doi.org/10.1016/j.physletb.2004.05.081. URL: http://www.sciencedirect.com/science/article/pii/S0370269304008822.

[56] G. Agakishiev and ohers. “Statistical model analysis of hadron yields in proton-nucleus and heavy-ion collisions at SIS 18 energies”. 2015. arXiv: 1512.07070 [nucl-ex].

[57] J. Adamczewski-Musch et al. “Deep sub-threshold ϕ production and implications for the K^+/K^- freeze-out in Au+Au collisions”. 2017. arXiv: 1703.08418 [nucl-ex].

[58] Christoph Blume. “Open Questions in the Understanding of Strangeness Production in HIC – Experiment Perspective”. In: EPJ Web of Conferences 171 (2018). Ed. by A. Mischke and P.Editors Kuijer, p. 03001. ISSN: 2100-014X. DOI: 10.1051/epjconf/201817103001. URL: http://dx.doi.org/10.1051/epjconf/201817103001.

[59] Tetyana Galatyuk et al. “Thermal Dileptons from Coarse-Grained Transport as Fireball Probes at SIS Energies”. In: Eur. Phys. J. A 52.5 (2016), p. 131. DOI: 10.1140/epja/i2016-16131-1. arXiv: 1512.08688 [nucl-th].

[60] Sukanya Mitra et al. “Thermal radiation from an expanding viscous medium”. 2011. arXiv: 1107.2500 [nucl-th].

[61] Itzhak Tserruya. “Electromagnetic Probes”. In: Relativistic Heavy Ion Physics. Ed. by R. Stock. Vol. 23. 2010, p. 176. DOI: 10.1007/978-3-642-01539-7_7. arXiv: 0903.0415 [nucl-ex].

[62] P. Spiller et al. “The FAIR Heavy Ion Synchrotron SIS100”. In: Journal of Instrumentation 15.12 (Dec. 2020), T12013–T12013. DOI: 10.1088/1748-0221/15/12/t12013. URL: https://doi.org/10.1088/1748-0221/15/12/t12013.

[63] “FAIR Baseline Technical Report (Volume 2)”. In: (Mar. 2006).

[64] H. Stoecker and C. Sturm. “The FAIR start”. In: Nuclear Physics A 855.1 (2011). Proceedings of the 4th International Conference on Hard and Electromagnetic Probes of High-Energy Nuclear Collisions – HP2010, pp. 506–509. ISSN: 0375-9474. DOI: https://doi.org/10.1016/j.nuclphysa.2011.02.117. URL: http://www.sciencedirect.com/science/article/pii/S0375947411002041.

[65] M Bai et al. “CHALLENGES OF FAIR PHASE 0 *”. In: June 2019, p. 3. DOI: 10.18429/JACoW-IPAC2018-THYGBF3.

[66] David Ondreka et al. “Recommissioning of SIS18 After FAIR Upgrades”. In: 10th International Particle Accelerator Conference. 2019, MOPTS035. DOI: 10.18429/JACoW-IPAC2019-MOPTS035.

[67] Dr. Daniel Severin. “Beam time schedule 2019 v7”. URL: https://www.gsi.de/fileadmin/beamtime/2019/2019-02_BTS2019v7.pdf (visited on 01/25/2021).

[68] HADES collaboration. “HADES: FAIR Phase 0 Experiment”. URL: http://web-docs.gsi.de/~webhades/onlineMon/mar19/hades-online.html (visited on 01/25/2021).

[69] Thomas Nilsson. “The NUSTAR project at FAIR”. In: Physica Scripta T166 (Nov. 2015), p. 014070. DOI: 10.1088/0031-8949/2015/T166/014070.

[70] Herlert, Alexander. “The NUSTAR program at FAIR - Overview and present status of the project”. In: EPJ Web of Conferences 71 (2014), p. 00064. DOI: 10.1051/epjconf/20147100064. URL: https://doi.org/10.1051/epjconf/20147100064.

[71] Th. Stöhlker et al. “APPA at FAIR: From fundamental to applied research”. In: Nuclear Instruments and Methods in Physics Research Section B: Beam Interactions with Materials and Atoms 365 (2015). Swift Heavy Ions in Matter, 18 – 21 May, 2015, Darmstadt, Germany, pp. 680–685. ISSN: 0168-583X. DOI: https://doi.org/10.1016/j.nimb.2015.07.077. URL: http://www.sciencedirect.com/science/article/pii/S0168583X15006552.

[72] C. Sturm, B. Sharkov, and H. Stöcker. “1, 2, 3 ... FAIR !” In: Nuclear Physics A 834.1 (2010). The 10th International Conference on Nucleus-Nucleus Collisions (NN2009), pp. 682c–687c. ISSN: 0375-9474. DOI: https://doi.org/10.1016/j.nuclphysa.2010.01.124. URL: http://www.sciencedirect.com/science/article/pii/S0375947410001259.

[73] Gianluigi Boca. “The experiment PANDA: physics with antiprotons at FAIR”. In: EPJ Web of Conferences 95 (Jan. 2015), p. 01001. DOI: 10.1051/epjconf/20149501001.

[74] Peter Senger. “Exploring Cosmic Matter in the Laboratory—The Compressed Baryonic Matter Experiment at FAIR”. In: Particles 2.4 (2019), pp. 499–510. DOI: 10.3390/particles2040031.

[75] CBM/FAIR. The CBM Webpage. URL: https://fair-center.eu/user/experiments/nuclear-matter-physics/cbm.html (visited on 10/15/2020).

[76] Ievgeniia Momot. “Characterization and radiation hardness studies of the silicon microstrip sensors for the CBM experiment”. PhD thesis. Goethe U., Frankfurt (main), 2019.

[77] Alexander Malakhov and Alexey Shabunov, eds. “Technical Design Report for the CBM Superconducting Dipole Magnet”. Darmstadt: GSI, 2013, 80 S. URL: https://repository.gsi.de/record/109025.

[78] N. Mezentsev et al. “The Report on development of the Superconducting Dipole Magnet for the CBM detector”. Dec. 2019. URL: https://fair-center.eu/fileadmin/fair/experiments/CBM/Reports/CBM_magnet_-_PDR_report__December_2019.pdf.

[79] M. Deveaux et al. “Observations on MIMOSIS-0, the first dedicated CPS prototype for the CBM MVD”. In: Nuclear Instruments and Methods in Physics Research Section A: Accelerators, Spectrometers, Detectors and Associated Equipment 958 (Apr. 2020), p. 162653. ISSN: 0168-9002. DOI: 10.1016/j.nima.2019.162653. URL: http://dx.doi.org/10.1016/j.nima.2019.162653.

[80] Johann Heuser et al., eds. “[GSI Report 2013-4] Technical Design Report for the CBM Silicon Tracking System (STS)”. Darmstadt: GSI, 2013, 167 p. URL: https://repository.gsi.de/record/54798.

[81] Maksym Teklishyn. “The Silicon Tracking System of the CBM experiment at FAIR”. In: EPJ Web of Conferences 171 (Jan. 2018), p. 21003. DOI: 10.1051/epjconf/201817121003.

[82] Norbert Herrmann, ed. “Technical Design Report for the CBM Time-of-Flight System (TOF)”. Darmstadt: GSI, 2014, 182 S. URL: https://repository.gsi.de/record/109024.

[83] “Technical Design Report for the CBM Ring Imaging Cherenkov Detector”. Tech. rep. 2013, 215 p. URL: https://repository.gsi.de/record/65526.

[84] Ilya Selyuzhenkov and Alberica Toia, eds. “CBM Progress Report 2016”. Literaturangaben. Darmstadt: GSI, 2017, 223 Seiten : Illustrationen, grafische Darstellungen. ISBN: 978-3-9815227-4-7. URL: https://repository.gsi.de/record/201318.

[85] Subhasis Chattopadhyay et al., eds. "Technical Design Report for the CBM : Muon Chambers (MuCh)". Darmstadt: GSI, 2015, 190 S. URL: https://repository.gsi.de/record/161297.

[86] Alberica Toia and Ilya Selyuzhenkov, eds. “CBM Progress Report 2017”. Darmstadt: GSI Helmholtzzentrum für Schwerionenforschung, 2018, V, 214 Seiten : Illustrationen, grafische Darstellungen. ISBN: 978-3-9815227-5-4. DOI: 10.15120/GSI-2018-00485. URL: https://repository.gsi.de/record/209729.

[87] Rajesh Ganai. “Feasibility Study of Using RPCs in CBM Muon Chamber”. In: Dec. 2016.

[88] Christoph Blume, C. Bergmann, and D. Emschermann, eds. “The Transition Radiation Detector of the CBM Experiment at FAIR : Technical Design Report for the CBM Transition Radiation Detector (TRD)”. CBM Technical Design Report FAIR Technical Design Report. Darmstadt: Facility for Antiproton and Ion Research in Europe GmbH, 2018, 165 p. DOI: 10.15120/GSI-2018-01091. URL: https://repository.gsi.de/record/217478.

[89] I.E. Korolko, M.S. Prokudin, and Yu M. Zaitsev. “The CBM ECAL”. In: J. Phys. Conf. Ser. 798.1 (2017). Ed. by Arkady Galper et al., p. 012164. DOI: 10.1088/1742-6596/798/1/012164.

[90] Fedor Guber and Ilya Selyuzhenkov, eds. “Technical Design Report for the CBM Projectile Spectator Detector (PSD)”. Darmstadt: GSI, 2015, 75 S. URL: https://repository.gsi.de/record/109059.

[91] Peter Senger. “Status of the Compressed Baryonic Matter experiment at FAIR”. In: International Journal of Modern Physics E 29.02 (Feb. 2020), p. 2030001. ISSN: 1793-6608. DOI: 10.1142/s0218301320300015. URL: http://dx.doi.org/10.1142/S0218301320300015.

[92] David Emschermann and Joerg Lehnert. “CBM Data Acquisition (DAQ)”. URL: https://fair-center.eu/en/for-users/experiments/nuclear-matter-physics/cbm/projects/daq.html (visited on 09/04/2020).

[93] Wojciech Zabolotny et al. “Selection of hardware platform for CBM Common Readout Interface”. In: Aug. 2017, p. 1044549. DOI: 10.1117/12.2280938.

[94] CBM collaboration. “mCBM@SIS18 (June 2020)”. URL: https://indico.gsi.de/event/10698/contributions/44803/attachments/31410/39875/20200610-mCBM-proposal-21-22-fullVersion.pdf (visited on 10/15/2020).

[95] W. Wu. “FELIX: the New Detector Interface for the ATLAS Experiment”. In: IEEE Transactions on Nuclear Science 66.7 (July 2019), pp. 986–992. ISSN: 1558-1578. DOI: 10.1109/tns.2019.2913617. URL: http://dx.doi.org/10.1109/TNS.2019.2913617.

[96] “CBM Progress Report 2018”. Tech. rep. CBM Progress Report 2018. Darmstadt, 2019, 220 p. DOI: 10.15120/GSI-2019-01018. URL: https://repository.gsi.de/record/220128.

[97] Dirk Hutter and Jan de Cuveland. “The FLES Detector Input Interface”. URL: https://raw.githubusercontent.com/wiki/cbm-fles/flesnet/files/fles_input_interface.pdf (visited on 02/03/2016).

[98] “CBM Progress Report 2019”. Tech. rep. CBM-PR-2019. Additional grant : EU-Horizon2020 "STRONG"; NOCHKG STRONG-2020 824093. Darmstadt, 2020, 216 p. DOI: 10.15120/GSI-2020-00904. URL: https://repository.gsi.de/record/228172.

[99] P. A. Čerenkov. “Visible Radiation Produced by Electrons Moving in a Medium with Velocities Exceeding that of Light”. In: Phys. Rev. 52 (4 Aug. 1937), pp. 378–379. DOI: 10.1103/PhysRev.52.378. URL: https://link.aps.org/doi/10.1103/PhysRev.52.378.

[100] “Theory of ring imaging Cherenkov counters”. In: Nuclear Instruments and Methods in Physics Research Section A: Accelerators, Spectrometers, Detectors and Associated Equipment 343.1 (1994), pp. 30–51. ISSN: 0168-9002. DOI: https://doi.org/10.1016/0168-9002(94)90532-0. URL: http://www.sciencedirect.com/science/article/pii/0168900294905320.

[101] Hermann Kolanoski and Norbert Wermes. “Teilchendetektoren - Grundlagen und Anwendungen”. Berlin Heidelberg New York: Springer-Verlag, 2016. ISBN: 978-3-662-45350-6.

[102] Claudia Höhne. Private Communication/"RICH CDR Mechanics". Gießen, Germany, 2020.

[103] Claudia Höhne. Private Communication/"RICH CDR Camera". Gießen, Germany, 2020.

[104] Jordan Bendarouach. “Conception and design of a mirror alignment and control system for the Ring Imaging Cherenkov detector of the CBM experiment”. eng. PhD thesis. Otto-Behaghel-Str. 8, 35394 Giessen: Justus-Liebig-Universität, 2019. URL: http://geb.uni-giessen.de/geb/volltexte/2019/14748.

[105] Hamamatsu Photonics K. K. “PHOTOMULTIPLIER TUBES - Basics and Applications (3rd Edition)”. URL: https://www.hamamatsu.com/resources/pdf/etd/PMT_handbook_v3aE.pdf (visited on 09/25/2020).

[106] Volker Friese and Christian Sturm, eds. “CBM Progress Report 2014”. Darmstadt: GSI, 2015, 159 S. ISBN: 978-3-9815227-1-6. URL: https://repository.gsi.de/record/97909.

[107] Volker Friese, Christian Sturm, and Alberica Toia, eds. “CBM Progress Report 2015”. Literaturang. Darmstadt: GSI, 2016, 155 S. : Ill., graf. Darst. ISBN: 978-3-9815227-3-0. URL: https://repository.gsi.de/record/186952.

[108] Hamamatsu Photonics K. K. “FLAT PANEL TYPE MULTIANODE PMT ASSEMBLY - H12700 SERIES/H14220 SERIES”. URL: https://www.hamamatsu.com/resources/pdf/etd/H12700_H14220_TPMH1379E.pdf (visited on 09/25/2020).

[109] Jörg Förtsch. “Upgrade of the HADES RICH photon detector and first performance analyses”. eng. PhD thesis. Bergische Universität Wuppertal, 2021.

[110] Jörg Förtsch. Private Communication. Wuppertal, Germany, 2020.

[111] “Proposals for experiments at SIS18 during FAIR Phase-0”. Tech. rep. HADES. Darmstadt, 2017, 102 p. DOI: 10.15120/GSI-2019-00976. URL: https://repository.gsi.de/record/220071.

[112] Tetyana Galatyuk. “HADES overview”. In: Nuclear Physics A 931 (2014). QUARK MATTER 2014, pp. 41–51. ISSN: 0375-9474. DOI: https://doi.org/10.1016/j.nuclphysa.2014.10.044. URL: http://www.sciencedirect.com/science/article/pii/S0375947414005399.

[113] G. Agakichiev et al. “The high-acceptance dielectron spectrometer HADES”. In: The European Physical Journal A 41.2 (July 2009), pp. 243–277. ISSN: 1434-601X. DOI: 10.1140/epja/i2009-10807-5. URL: http://dx.doi.org/10.1140/epja/i2009-10807-5.

[114] Adrian Rost et al. “Beam Quality Monitoring System in the HADES Experiment at GSI Using CVD Diamond Material”. In: 7th International Beam Instrumentation Conference. 2019, TUPC03. DOI: 10.18429/JACoW-IBIC2018-TUPC03.

[115] K. Zeitelhack et al. “The HADES RICH detector”. In: Nuclear Instruments and Methods in Physics Research Section A: Accelerators, Spectrometers, Detectors and Associated Equipment 433.1 (1999), pp. 201–206. ISSN: 0168-9002. DOI: https://doi.org/10.1016/S0168-9002(99)00371-X. URL: http://www.sciencedirect.com/science/article/pii/S016890029900371X.

[116] C. Müntz et al. “The HADES tracking system”. In: Nuclear Instruments and Methods in Physics Research Section A: Accelerators, Spectrometers, Detectors and Associated Equipment 535.1-2 (Dec. 2004), pp. 242–246. ISSN: 0168-9002. DOI: 10.1016/j.nima.2004.07.232. URL: http://dx.doi.org/10.1016/j.nima.2004.07.232.

[117] Georgy Kornakov et al. “Development of diamond detectors for HADES”. URL: http://www-adamas.gsi.de/ADAMAS06/talks/Kornakov_2017.pdf (visited on 10/12/2020).

[118] C. Agodi et al. “The HADES time-of-flight wall”. In: Nuclear Instruments and Methods in Physics Research Section A: Accelerators, Spectrometers, Detectors and Associated Equipment 492.1 (2002), pp. 14–25. ISSN: 0168-9002. DOI: https://doi.org/10.1016/S0168-9002(02)01004-5. URL: http://www.sciencedirect.com/science/article/pii/S0168900202010045.

[119] Georgy Kornakov. “NEW ADVANCES AND DEVELOPMENTS ON THE RPC TOF WALL OF THE HADES EXPERIMENT AT GSI”. eng. PhD thesis. Santiago de Compostela: Universidad de Santiago de Compostela Facultad de Física, Sept. 2012. URL: https://hades.gsi.de/sites/default/files/web/media/documents/thesis/PhD/Phd_G_Kornakov_New_advances_and_developments_on_the_RPC_tof_wall_of_the_HADES_experiment_at_GSI.pdf.

[120] D. Belver et al. “The HADES RPC inner TOF wall”. In: Nuclear Instruments and Methods in Physics Research Section A: Accelerators, Spectrometers, Detectors and Associated Equipment 602.3 (2009). Proceedings of the 9th International Workshop on Resistive Plate Chambers and Related Detectors, pp. 687–690. ISSN: 0168-9002. DOI: https://doi.org/10.1016/j.nima.2008.12.090. URL: http://www.sciencedirect.com/science/article/pii/S0168900208019633.

[121] O. Svoboda et al. “Electromagnetic calorimeter for the HADES@FAIR experiment”. In: JINST 9 (2014). Ed. by Pietro Govoni et al., p. C05002. DOI: 10.1088/1748-0221/9/05/C05002.

[122] J Michel et al. “The upgraded HADES trigger and data acquisition system”. In: Journal of Instrumentation 6.12 (Dec. 2011), pp. C12056–C12056. DOI: 10.1088/1748-0221/6/12/c12056. URL: https://doi.org/10.1088%2F1748-0221%2F6%2F12%2Fc12056.

[123] Jan Michel. “Development and implementation of a new Trigger and data Acquisition system for the HADES detector”. PhD thesis. Johann Wolfgang Goethe-Universität Frankfurt, 2012.

[124] Sergey Linev and Jörn Adamczewski-Musch. “Das Data Acquistion Backbone Core (DABC) Framework”. URL: https://www.gsi.de/work/forschung/experimentelektronik/datenverarbeitung/datenerfassung/dabc.htm?m=1 (visited on 10/14/2020).

[125] Sönke Schröder. “Entwicklung und Aufbau eines Systems zur Effizienzkalibration des HADES-RICH”. URL: https://hades.gsi.de/sites/default/files/web/media/documents/thesis/Diploma/SoenkeSchroeder_diploma_Soenke_Schroeder_2005-Sep.pdf (visited on 10/26/2020).

[126] K. Zeitelhack et al. “The HADES RICH detector”. In: Nucl. Instrum. Meth. A 433 (1999). Ed. by A. Breskin, R. Chechik, and T. Ypsilantis, pp. 201–206. DOI: 10.1016/S0168-9002(99)00371-X.

[127] Tobias Kunz. “Sigma0-Produktion in p+Nb-Reaktionen bei E = 3,5 GeV”. Dissertation. München: Technische Universität München, 2017.

[128] C. Pauly et al. “Upgrade of the HADES RICH photon detector with H12700 MAPMTs”. In: Nuclear Instruments and Methods in Physics Research Section A: Accelerators, Spectrometers, Detectors and Associated Equipment 876 (2017). The 9th international workshop on Ring Imaging Cherenkov Detectors (RICH2016), pp. 164–167. ISSN: 0168-9002. DOI: https://doi.org/10.1016/j.nima.2017.02.067. URL: http://www.sciencedirect.com/science/article/pii/S0168900217302632.

[129] J. Adamczewski-Musch et al. “Efficiency and temporal response of p-terphenyl based wavelength shifting films on H12700 multi anode photomultipliers”. In: Nuclear Instruments and Methods in Physics Research Section A: Accelerators, Spectrometers, Detectors and Associated Equipment 952 (2020). 10th International Workshop on Ring Imaging Cherenkov Detectors (RICH 2018), p. 161867. ISSN: 0168-9002. DOI: https://doi.org/10.1016/j.nima.2019.01.093. URL: http://www.sciencedirect.com/science/article/pii/S0168900219301652.

[130] Adrian Amatus Weber. “Entwicklung von FPGA basierter Ausleseelektronik für den HADES RICH upgrade und CBM RICH Detektor”. Master’s thesis. Giessen: Justus-Liebig Universität, 2017.

[131] Jörg Förtsch. Private Communication. Wuppertal, Germany, 2019.

[132] Jan Michel. “Development of a Realtime Network Protocol for HADES and FAIR Experiments”. Diploma. Frankfurt: Goethe Universität Frankfurt, 2008.

[133] V.B. Mikhailik et al. “Scintillation properties of pure CaF2”. In: Nuclear Instruments and Methods in Physics Research Section A: Accelerators, Spectrometers, Detectors and Associated Equipment 566.2 (2006), pp. 522–525. ISSN: 0168-9002. DOI: https://doi.org/10.1016/j.nima.2006.06.063. URL: http://www.sciencedirect.com/science/article/pii/S0168900206012034.

[134] V. B. Mikhailik and H. Kraus. “Performance of scintillation materials at cryogenic temperatures”. In: physica status solidi (b) 247.7 (Mar. 2010), pp. 1583–1599. ISSN: 0370-1972. DOI: 10.1002/pssb.200945500. URL: http://dx.doi.org/10.1002/pssb.200945500.

[135] Jürgen Friese. “RICH Round Trips I -III”. URL: https://indico.gsi.de/event/7689/contributions/34114/attachments/24709/30902/RICH_Roundtrip.pdf (visited on 11/09/2020).

[136] Christian Pauly. “HADES RICH – towards first data online performance”. URL: https://indico.gsi.de/event/7689/contributions/34113/attachments/24723/30917/talk_CP_final.pdf (visited on 11/09/2020).

[137] K. Schmidt-Sommerfeld, J. Friese, and T. Kunz. “Feasibility study for a MAPMT readout of the HADES RICH”. In: Scientific Report 2014. Vol. 2015-1. GSI Report. BMBF 05P12WOGHH, GSI TMLFRG1316 532 HADES. Darmstadt: GSI Helmholtzzentrum für Schwerionenforschung, 2015, 33 p. DOI: 10.15120/GR-2015-1-MU-NQM-HADES-29. URL: https://repository.gsi.de/record/183805.

[138] Sergey Linev and Jörn Adamczewski-Musch. “DABC: FPGA TDC calibration”. URL: https://web-docs.gsi.de/~dabc/doc/dabc2/hadaq_tdc_calibr.html (visited on 04/30/2021).

[139] Jörg Förtsch. “Status dirich Wuppertal – Thresholdscan”. URL: https://wiki.gsi.de/pub/EE/EEMeetVortragArch/170623_Status_dirich_Wuppertal_Threshold_Scan.pdf (visited on 11/11/2020).

[140] Volker Friese and Christian Sturm, eds. “CBM Progress Report 2010”. Darmstadt: GSI, 2011, 97p. ISBN: 978-3-9811298-8-5. URL: https://repository.gsi.de/record/54079.

[141] Volker Friese and Christian Sturm, eds. “CBM Progress Report 2011”. Darmstadt: GSI, 2012, 101p. ISBN: 978-3-9811298-9-2. URL: https://repository.gsi.de/record/54080.

[142] Volker Friese and Christian Sturm, eds. “CBM Progress Report 2012”. Darmstadt: GSI, 2013, 120p. ISBN: 978-3-9815227-0-9. URL: https://repository.gsi.de/record/54078.

[143] “CBM Progress Report 2013”. Tech. rep. CBM Progress Report. Darmstadt, 2014, 133 p. URL: https://repository.gsi.de/record/64893.

[144] M. Contalbrigo et al. “Aerogel mass production for the CLAS12 RICH: Novel characterization methods and optical performance”. In: Nuclear Instruments and Methods in Physics Research Section A: Accelerators, Spectrometers, Detectors and Associated Equipment 876 (2017). The 9th international workshop on Ring Imaging Cherenkov Detectors (RICH2016), pp. 168–172. ISSN: 0168-9002. DOI: https://doi.org/10.1016/j.nima.2017.02.068. URL: http://www.sciencedirect.com/science/article/pii/S0168900217302644.

[145] mCBM collaboration. “mCBM timing synchronization 2018-2019”. URL: https://git.cbm.gsi.de/notes/computing/mcbm-timing-synchronization-2018-2019 (visited on 11/17/2020).

[146] Lukas Dominik Meder. “Timing Synchronization and Fast-Control for FPGA-based large-scale Readout and Processing Systems”. German. PhD thesis. Karlsruher Institut für Technologie (KIT), 2017. 255 pp. DOI: 10.5445/IR/1000071051.

[147] TRB collaboration. “Trb3 manual”. URL: http://jspc29.x-matter.uni-frankfurt.de/docu/trb3docu.pdf (visited on 11/18/2020).

[148] mCBM collaboration. “mCBM Raw Data Format 2020”. URL: https://git.cbm.gsi.de/notes/computing/mcbm-raw-data-format-2020 (visited on 11/17/2020).

[149] Weihao Wu. “FELIX: the New Detector Interface for the ATLAS Experiment”. URL: https://cds.cern.ch/record/2624258/files/ATL-DAQ-SLIDE-2018-375.pdf (visited on 11/24/2020).

[150] Xilinx Inc. “UltraScale Architecture andProduct Data Sheet: Overview”. URL: https://www.xilinx.com/support/documentation/data_sheets/ds890-ultrascale-overview.pdf (visited on 11/24/2020).

Danksagung

An dieser Stelle möchte ich mich bei allen Personen bedanken, die mich auf meinem bisherigen Weg unterstützt haben und mir die Chance eröffnet haben, diese Dissertation zu schreiben.
Zu aller erst möchte ich mich bei meiner Betreuerin Prof. Dr. Claudia Höhne bedanken. Ohne dein Fachwissen, dein offenes Ohr und die Geduld all meine Fragen zu beantworten und aufkommende Probleme zu lösen, wäre ich nie so weit gekommen. Danke für die intensiven Besprechungen und neuen Denkanstöße die ich über all die Jahre erhalten habe.

Des weiteren möchte ich mich bei apl. Prof. Dr. Sören Lange für seine Unterstützung während meiner Promotion, aber auch schon für die Ansteckende Begeisterung auf den Weg dorthin während des Studiums bedanken.

Ein besonderer Dank geht an alle Mitglieder der Arbeitsgruppe Höhne und Kühn für die tolle und abwechslungsreiche Zeit. Danke für das Ertragen des öfters erklingenden Mahlgeräusch der Kaffeemaschine und der Ablenkung von der Arbeit, ohne die ich es nicht bis zu diesem Punkt geschafft hätte. Dabei geht ein großer Dank an Jordan und Cornelius für die tolle Atmosphäre in unserem Büro und den Spaß, den die Arbeit gebracht hat. Danke an Marten, dass wir uns gegenseitig unsere Probleme an den Kopf werfen konnten und gemeinsame Lösungen erarbeitet haben. Es war ein großer Spaß! Genauso geht ein Dank an Jan für die schöne Zeit im Büro, aber auch auf den zahlreichen Reisen in so viele Länder.

Danke Evi und Anita für die Abarbeitung der ganzen Papiere und Bestellungen. Ohne euch würde nichts gehen. Ihr haltet uns den Rücken Frei. Ein großer Dank geht an Marcel für die Hilfe in Elektronik Fragen, tollen Gesprächen und das geduldige Bestücken meiner PCBs.

Danke Klemens, Leo, Katharina, Egor und Thomas K. für die Gespräche, Hilfen und Ablenkungen in all den Jahren. Ein ganz besonderer Dank geht an Thomas G. für die tolle Zusammenarbeit über viel Jahre, das Teilen deines Wissensschatzes und all den Spaß den wir in der Zeit hatten. Es war mir eine Ehre den Weg mit dir zu beschreiten.

Diese Arbeit ist ein Gemeinschaftsprojekte von vielen Menschen und wäre niemals alleine möglich gewesen wäre.

Ein besonders großer Dank geht an Jan für die großartige Zusammenarbeit, den gemeinsamen Spaß im Labor, auf Strahlzeiten aber auch außerhalb der Arbeit. Danke für das Teilen deines unermesslichen Fachwissens, die immer andauernde Geduld und den ganzen Ideen, die wir in etlichen Telefonaten und Treffen hatten.

Ein weiterer großer Dank geht an Michael und Jürgen für die tolle Unterstützung in der Arbeit, euer immenses Fachwissen, das erweitern meines Horizontes in so vielen Belangen, das offene Ohr und die wunderbaren Abende mit vielen kühlen Getränken.

Die Unterstützung und der Austausch mit unseren Wuppertaler Kollegen und Freunden hat die Arbeit deutlich vereinfacht und zu einer tollen Zeit gemacht. Danke

Dennis, Jörg, Ievgenii, Karl-Heinz und Christian für die tolle Zusammenarbeit und die Erinnerungen die ein Leben lang erhalten bleiben. Jörg, Christian, danke für die tollen Gespräche, eure ansteckende Freude an der Arbeit und die herausragende Zeit auf diversen Reisen und Strahlzeiten! Bei jeder erfolgreichen Mars Landung werde ich jetzt an Christian und seine Begeisterung für das Unmögliche denken müssen, die ich mit ihm teile.

Ein spezieller Dank geht auch an Norbert, Ingo, Pierre-Alain, David und Christian für unglaublich gute Zusammenarbeit und die Unterstützung in der Vorbereitung und Durchführung der zahlreichen mCBM Strahlzeiten und deren Auswertungen.

Ich bedanke mich des weiteren bei der kompletten HADES wie auch der TRB und CBM Kollaboration für die tolle Zeit. Ein besondere Dank geht hier an Adrian für die Hilfe während des ECAL und RICH upgrades, dessen Inbetriebnahme und den ganzen Spaß den wir dabei hatten. Danke Jurek für die häufige Hilfe, die detaillierte Justierung der RICH Kühlung und deinen unermüdlichen Einsatz.

Eine große Unterstützung in Firmware Details des DiRICH ist mir durch Ingo zu gekommen. Danke für die detaillierte Arbeit, Hilfe und Unterstützung. Ich bedanke mich bei Peter für die Unterstützung in EPICS Angelegenheiten und die interessanten Gespräche, sowie bei Thorsten für die hervorragende Zusammenarbeit bei Magnet Messungen und darüber hinaus. Des weiteren geht ein besonderes Dank an Semen, Sergey und Jörn für die Hilfe in Sachen Software, Event Builder und allem was zusätzlich angefallen ist.

Ein großer Dank geht auch an all meine Freunde, die mich nun über so viele Jahre im Leben begleiten, mich unterstützen und mein Leben bereichern.

Den letzten und wichtigsten Dank widme ich den wichtigsten Menschen in meinem Leben: Meiner ganzen Familie. Danke für die unermüdliche Unterstützung über all die Jahre. Egal wie schwer die Zeit war, ich habe immer volles Vertrauen und die volle Unterstützung in meinem Handeln gespürt. Auch wenn ich euch mit unerträglichen Technikdetails genervt habe, habt ihr mir trotzdem ein offenes Ohr geschenkt. Ohne euch und eure Unterstützung wäre ich nie so weit gekommen. Danke.